Site GT1: layered cumulate gabbros and deep fault zones[1]

Kelemen, P.B., Matter, J.M., Teagle, D.A.H., Coggon, J.A., and the Oman Drilling Project Science Team[2]

Keywords: Oman Drilling Project, OmanDP, Samail ophiolite, Zihlmann-Muller Fault Zone, Wadi Gideah, layered cumulate gabbros, deep fault zones, lower crustal gabbros, Site GT1, Hole GT1A

Chapter contents

[1] Kelemen, P.B., Matter, J.M., Teagle, D.A.H., Coggon, J.A., and the Oman Drilling Project Science Team, 2020. Site GT1. *In* Kelemen, P.B., Matter, J.M., Teagle, D.A.H., Coggon, J.A., et al., *Proceedings of the Oman Drilling Project*: College Station, TX (International Ocean Discovery Program. https://doi.org/10.14379/OmanDP.proc.106.2020
[2] OmanDP Science Team affiliations.

MS Oman-106
Published 24 April 2020

Site GT1

Site GT1 (22.890°N, 58.520°E) is hosted in lower crustal layered gabbros. This site is considered ideal for investigation of vertical variation of igneous mineral chemistry, mid-ocean magma chamber processes, cooling rates over a variety of temperature intervals, mineralogical and geochemical indices of alteration, crystal lattice-preferred orientations, and a spectrum of overprinting deformational, alteration, and weathering process that have occurred from the ancient ridge crest to the present (see the **Introduction to the Oman Drilling Project** chapter). The resulting data will address ongoing uncertainty regarding the processes that form and cool oceanic lower crust. A 400 m diamond cored hole was sited to target a known fault zone that crops out exposing greenschist facies alteration and Cu mineralization that appears to be of mid-ocean-ridge origin. This feature, when intersected, would be a good example of the little-studied focused fluid flow zones in the Samail lower crust, which could have been the locus of hydrothermal alteration and advective cooling of the lower oceanic crust as it was forming at the ridge crest (e.g., Coogan et al., 2006).

Geological setting

Site GT1 is located ~3 km south of the contact, thrust in places, between the mantle peridotites and the lower gabbros (Figs. **F1**, **F2**) of the Samail ophiolite. The drill site was positioned on a wadi terrace at the end of a ridge where the southward-draining wadi changes abruptly to an east–west trend (Fig. **F3**). The modal and grain size layering in the gabbros dip gently to moderately to the southeast (s/d 056/24°SE) either conformable with or slightly steeper than the crust/mantle boundary. Geological exposure in the area is of mixed quality; most steep slopes are covered with desert-varnished, strongly jointed small outcrops or rubble. Common white scars on many of the slopes hint at abundant zones of deformation and strong alteration or weathering, probably related to minor faults (Fig. **F2**).

Two small northwest-trending gullies have formed on the eastern slopes of Wadi Gideah ~300 m north of Site GT1 (Fig. **F4**). From the dirt road next to the campsite south to the base of the gullies, pieces of cupriferous slag are commonly found in the wadi gravels. Climbing the larger, more southern gully reveals a ~1 m thick platy chlorite-epidote–rich fault gouge that anastomoses around heavily altered and strongly veined clasts of deformed and brecciated layered gabbro (Zihlmann et al., 2018). The principal shear sense appears to be normal, although there is evidence for reverse sense reactivation with the partial stacking of gabbro boudins. Lozenges of pyrite 10–15 cm long with subordinate chalcopyrite

occur within the chlorite-epidote fault gouge. A platy chlorite-rich fabric is developed in the footwall gabbros immediately adjacent to the fault gouge zone. The host gabbros are highly altered for >4 m in both the footwall and hanging wall.

A wide array of secondary materials are present in the fault clasts and host wall rocks that document hydrothermal alteration from moderate (~300°C) to low (<100°C, zeolites, carbonates) temperatures. The presence of chlorite-epidote with pyrite and chalcopyrite suggests that at least some of the alteration and mineralization occurred at greenschist facies conditions similar to those estimated for black smoker fluid reaction zones (e.g., Seyfried et al., 1991; Alt, 1995). Although there are later stages of lower temperature secondary mineral precipitation, most of the deformation, fluid flow, and mineralization appears to have occurred in the fault zone when these rocks were at the mid-ocean ridge. For the purposes of this report, this fault is named the Zihlmann-Müller Fault Zone (ZMFZ), and it is one of the best examples of a fault within the layered gabbros that is most convincingly of a mid-ocean-ridge origin (Fig. F5; see also Coogan et al., 2006). Sampling a fault zone in the lower layered gabbros that formed at the ancient mid-ocean ridge-crest is one of the primary targets of the Oman Drilling Project. Consequently, Wadi Gideah was surveyed to find a suitable site for diamond coring to penetrate through the ZMFZ with a 400 m deep diamond cored hole.

The surface trace of the ZMFZ can be followed for a few tens of meters across the small ridge into which it is incised. The southern extension of this trend to where it reintersects the wadi course coincides with a 10 m wide zone of strongly carbonated and clay-rich highly weathered gabbro draped by layered carbonate travertine (Figs. F6, F7) and overlain by a ~1 m thick carbonate-cemented polymict wadi boulder terrace indicative of "modern" groundwater flow. Although a direct connection to the northern side of the ridge can only be assumed, the co-linearity of these features gives some confidence that the ZMFZ is a significant feature with along-strike dimensions of >200 m with possibly the same order of continuity downdip to the southeast.

A relatively flat area was identified for a potential drill pad on a ~5 m high terrace above the wadi bed in the inside corner of the southwest–east dogleg in Wadi Gideah ~150–200 m perpendicular to the strike of the ZMFZ. Given an average measured dip of 54° ± 9° (2σ) for the ZMFZ, it was predicted that a vertical borehole would cross the downdip extension of the fault at ~210 m with a 2σ range of 145–310 m, clearly within range of a 400 m vertical borehole (Fig. F8). Development of this site and the deployment of a drill rig required significant road diversion to bring heavy equipment along the wadi bed to Site GT1.

Operations

All times are reported as local time in Oman (UTC + 4 h).

An overview of all holes drilled is given in Table T3 in the Methods chapter. Drilling operations and core curation information for Site GT1 are reported in Table T1.

Hole summary

- Spud-in: 22/01/2017, 07:50 h
- First core on deck: 22/01/2017, 08:29 h
- HW surface casing installed: 22/01/2017, 2.5 m
- HW surface casing extended: 23/01/2017, 12 m
- NW casing installed: 02/02/2017, 254.2 m
- Final core on deck: 08/02/2017, 15:45 h
- Total depth of borehole: 403.15 m

Geology summary

- Beautiful layered gabbros and olivine gabbros, sometimes very coarse grained.
- No layering between ~60 and 100 m.
- Occasional troctolite intervals.
- Subvertical white laumontite veins very common.
- Veins of prehnite, epidote, clinozoisite, chlorite, serpentine, and amphibole.
- Several fault zones as thick as ~1 m including ultramylonites and cataclasites.

Technical issues

Deviation of hole during extension of surface casing through fault zone at ~10–10.4 m. Discovered two different lengths of drill rods in stock (see below **Drill rod length differences explained**). No other major technical issues.

Drilling summary

- 22 Jan 2017: spud-in at 07:50 h, pull 2 cores. 13:13–14:15 h: rig stopped for inspection and engine service by 2 men from "BEC." Fault encountered at ~10.0–10.4 m depth; agreed with chief driller Wali to install HW casing to 12 m. Tripped pipe after Core 8Z then reamed and installed 2.5 m of HW surface casing by end of day.
- 23 Jan 2017: morning reaming and casing installation, ending at total depth (TD) 12 m. Started coring from ~10.4 m. Cores 9M–11M recovered to 17.7 m (M = miscellaneous because they overlap previous cores and are similar to Cores 6Z–8Z). Pieces in Core 9M and top of 10M show the outer drill marks/scar from previous core, indicating that we drilled a new hole at ~10.4–17.7 m subparallel to that drilled on 22 Jan. Our interpretation is

that the hole drilled previously deviated from vertical at ~10–10.4 m depth, where we encountered highly altered olivine gabbro in which the core was falling apart. Reaming this morning experienced difficulties at ~10.4 m and we pulled out of hole (POOH) the HW string and found some pieces of altered gabbro in the shoe bit. Casing from ~10–12 m was slower. The most satisfactory explanation for these observations is that the HW casing deviated from the original hole at ~10.4 m and continued subparallel to the original hole (Fig. F9). Wali is confident that the new hole is true vertical and the original hole is off-vertical, based on the fact that the casing is much more rigid than the HQ drill string and therefore less likely to bend.

- 24 Jan 2017: resumed coring "fresh" olivine-gabbro. Last core pulled at 15:24 h—lightning and thunder overhead while washing core at core deck. Wali made decision to stop drilling (derrick and drill string are basically a giant lightning rod!); BI and JC approved decision. Began to rain heavily, so science team curated Core 19Z, packed up, and made sure all equipment was secured and (where necessary) raised above ground level.
- 25 Jan 2017: rain yesterday did not have an adverse effect on equipment; everything seems to have remained water-tight. POOH at ~15:00 h after Core 26Z to change bit. New bit is different cutting structure—better suited to very hard rocks.
- 16:30 h: new bit reached bottom of hole (BOH).
- 26 Jan–1 Feb 2017: routine coring to 254.2 m, reached on 1 Feb. Started POOH HQ drill string in preparation for change to NQ coring.
- 2 Feb 2017: finished POOH HQ drill string and ran in hole (RIH) with NW temporary casing in early morning. Started inserting NQ drill string to 254.2 m at noon. First NQ core on deck at 14:50 h. Discovered not all rods are same length (see below, **Drill rod length differences explained**)
- 3 Feb 2017: pulled 3 cores, then drill team left for Friday prayers.
- 4 Feb 2017: routine coring.
- 5 Feb 2017: routine coring in morning; 13:30 h: started tripping pipe to replace the bit; 14:55 h: bit on deck and changed; 15:20 h: started tripping in; 16:30 h: finished tripping in; drilling operations finished for the day.
- 6 Feb 2017: mostly routine coring, except for Core 128Z, which was not fully recovered in first core barrel trip and required second trip to retrieve full advance drilled. In the afternoon the drilling team pumped out mud pits and after last core of the day was pulled they cleaned the rig using a high-pressure hose.
- 7 Feb 2017: routine coring.
- 8 Feb 2017: routine coring until 15:45 h, when final core of this hole was brought on deck. Hole complete!
- 9 Feb 2017: science team completed core flow for remaining cores drilled yesterday while drill team demobilized. Took down tarp and packed up all kit except scanner and tent for move to Site GT3.
- 10 Feb 2017: tent down, kit packed up, and everything moved to Site GT3. Science team set up tent at GT3.

Drill rod length differences explained

At Site GT2, all rods were 3.05 m (10 ft). Two lengths of HQ rods exist in stock: 3.00 m (× 51) and 3.05 m (10 ft) (× 50). The 10 ft rods are being used first.

So at Site GT1, HQ drilling is

$$50 \text{ rods} \times 3.05 \text{ m} + 33 \text{ rods} \times 3.00 \text{ m} = 251.5 \text{ m} + 2.61 \text{ m} = 254.11 \text{ m}. \quad (1)$$

NQ drilling is

$$83 \text{ rods} \times 3.05 \text{ m} = 253.15 \text{ m} + 2.61 = 255.76 \text{ m}. \quad (2)$$

$$255.76 - 254.11 = 1.65 \text{ m}. \quad (3)$$

Resulting updates to DIS for Site GT2: all 3.00 m advances are actually 3.05 m. For Site GT1, the first 50 advances at 3.00 m should be 3.05 m.

Igneous petrology

Major rock types

The downhole variations of rock types in Hole GT1A are shown in Figures F10 and F11 and Table T2. The primary observational data are available in Excel worksheets in **Supplementary material** > **E_Tabulated VCD data**. The main lithology is olivine gabbro (65.9%), followed in abundance by olivine-bearing gabbro (21.5%) and olivine melagabbro (3.9%). Minor rock types include orthopyroxene-bearing olivine gabbro (2.4%), oxide-bearing olivine gabbro (1.5%), gabbro (1.1%), anorthositic gabbro (1%), troctolitic gabbro (0.8%), orthopyroxene-bearing gabbro (0.5%), gabbronorite (0.3%), and dunite (0.3%).

Igneous units

Unit I

Igneous intervals: 1–36
Sections GT1A-4Z-1, 0 cm, to 14Z-4, 33 cm
Depth: 4.90–26.62 m Chikyu curated depth (CCD)
Lithology: medium-grained granular olivine gabbro

The main rock type in Unit I is medium-grained olivine gabbro with minor fine-grained intercalations or patches of the same lithology and some domains of troctolitic gabbro and olivine-bearing gabbro. All these gabbros show granular to nearly equigranular texture. This unit is also generally characterized by increasing modal abundance of olivine downhole (~3%–60%).

Unit II

Igneous intervals: 37–46
Sections GT1A-14Z-4, 33 cm, to 37Z-1, 6 cm
Depth: 26.62–88.16 m CCD
Lithology: medium-grained granular olivine gabbro and olivine-bearing gabbro

The transition from Unit I is identified by a generally lower modal abundance in olivine in Unit II. The main rock type of Unit II is medium-grained olivine gabbro with minor coarse-grained intercalations (Section 21Z-2) and two pegmatitic layers (Sections 29Z-3 and 29Z-4 to 30Z-1). Three more felsic layers (classified as anorthositic gabbro) are present in Sections 18Z-3, 19Z-2, and 25Z-3. Although the general texture is granular and equigranular, the rocks exhibit varitextured grain size distributions and poikilitic textures in Igneous Intervals 40–42 (Sections 29Z-4 to 31Z-3). These intervals are characterized by coarse-grained clinopyroxene oikocrysts (up to 2 cm in grain size) with inclusions of plagioclase.

Unit III

Igneous intervals: 47–51h
Sections GT1A-37Z-1, 6 cm, to 45Z-2, 43 cm
Depth: 88.16–104.72 m CCD
Lithology: medium-grained olivine melagabbro, disseminated oxide gabbro, olivine gabbro, and olivine-bearing gabbro

The transition from Unit II to III is identified by a distinct increase in the modal abundance of olivine, although the actual contact between these two units was not recovered. The main rock type in Unit III is medium-grained olivine melagabbros (olivine + clinopyroxene > 65%) with granular textures and equigranular grain size distribution. The middle of the unit includes disseminated oxide gabbros (Igneous Interval 49, 1% oxides with grain size up to 4 mm). The modal abundance of olivine decreases toward the bottom of the unit (Igneous Intervals 50–51h), the grain size distribution becomes more varitextured with subophitic textures, and the layering intensity increases.

Unit IV

Igneous intervals: 51i–53
Sections GT1A-45Z-2, 43 cm, through 63Z-3
Depth: 104.72–154.04 m CCD
Lithology: medium-grained granular olivine gabbro and olivine-bearing gabbro

Unit IV is relatively homogeneous and comprises medium-grained olivine gabbros and olivine-bearing gabbros with granular textures and equigranular grain size distributions. The modal abundance of olivine decreases slightly toward the center of the unit (Igneous Interval 52: olivine-bearing gabbro) and increases again toward the bottom. The layering intensity is stronger in the olivine gabbros, where layering is characterized by the intercalation of several-centimeter-wide fine-grained and coarse-grained gabbroic bands within the medium-grained olivine gabbros. The olivine-bearing gabbros at the middle of Unit IV do not have these coarse-grained layers.

Unit V

Igneous intervals: 54–57
Sections GT1A-63Z-3 through 86Z-4
Depth: 154.04–215.22 m CCD
Lithology: medium-grained granular olivine gabbro, olivine-bearing gabbro, olivine melagabbro, and fine-grained gabbro

The Unit IV–V transition is identified by the appearance of fine-grained gabbros, but the major rock types in Unit V are medium-grained olivine gabbros with minor olivine-bearing gabbros and olivine melagabbros, all of which exhibit granular textures and equigranular grain size distribution. The modal abundance of olivine generally increases toward the bottom of the unit and is more irregularly distributed than Unit IV. The layering intensity increases downhole, and the lower part of the unit (Igneous Interval 57) is characterized by the appearance of multiple fine (0.5 cm wide) olivine-rich bands (in the visual core description (VCD) comments commonly termed “tiger layers”).

Unit VI

Igneous intervals: 57–60
Sections GT1A-86Z-4 through 121Z-3
Depth: 215.22–306.94 m CCD
Lithology: medium-grained granular olivine gabbro, olivine-bearing gabbro, orthopyroxene-bearing gabbro, and gabbronorite

The major rock type in Unit VI is medium-grained olivine gabbro with minor olivine-bearing gabbros, orthopyroxene-bearing gabbros, and gabbronorite, all of which exhibit granular textures and equigranular grain size distribution. The onset of Unit VI is marked by appearance of orthopyroxene rimming olivine grains, but orthopyroxene is only present to Igneous Interval 60. The top part of the unit, up to the bottom of Igneous Interval 57, exhibits fine (0.5 cm wide) olivine-rich bands. Below this, the spacing of the layering exceeds the length of the core sec-

tions and therefore is not immediately apparent when describing the core section by section.

Unit VII

Igneous intervals: 60–62
Sections GT1A-121Z-4 through 156Z-2
Depth: 306.94–403.37 m CCD
Lithology: fine- to medium-grained granular olivine gabbro and olivine-bearing gabbro

The major rock types in Unit VII are fine- to medium-grained olivine gabbros with minor olivine-bearing gabbros and olivine melagabbros, all of which exhibit granular textures and equigranular grain size distribution. The transition from Unit VI to VII is marked by a decrease in the modal abundance of olivine and olivine grain size.

Core descriptions

Modal variations

Modal abundances of the primary magmatic phases were estimated visually on the most representative part of the core section. Olivine-bearing gabbros are 1–4 vol% olivine, 20–80 vol% plagioclase, and 20–80 vol% clinopyroxene (Fig. F12). Olivine gabbros are 5–40 vol% olivine, 10–80 vol% plagioclase, and 15–75 vol% clinopyroxene. Orthopyroxene-bearing olivine gabbros are 5–24 vol% olivine, 10–60 vol% plagioclase, and 20–70 vol% clinopyroxene.

The downhole modal variations are highly scattered, but the upper 105 m has a wider range in olivine and clinopyroxene modes compared to lower in the hole. This is well displayed by plotting an average mode for every 10 m interval downhole (Fig. F12). The modal abundance of olivine and clinopyroxene varies widely throughout Units I–III in the upper 105 m of the hole, whereas modal variation remains <20 vol% for olivine and 20–40 vol% for clinopyroxene in the lower 300 m of the hole.

Contacts

A total of 64 lithologic contacts and changes in lithology were recognized in Hole GT1A. Because of recovery gaps (36% of the total), many contacts were not observed directly other than as a change in rock type across a gap in recovery. The contacts recovered were classified as either lithologic or structural. Lithologic contacts were further classified based on variations in either modal mineralogy or grain size, whereas structural contacts are related to the juxtaposition of different rock types by intrusion or faulting (Fig. F13). Lithologic and structural contacts constitute 91% and 8% of the total observed, respectively.

The nature of both lithologic and structural contacts is that they may be either sharp (Fig. F13C) or gradational (Fig. F13B). Gradational lithologic contacts are gradual changes in either grain size or modal abundance of constituent minerals or both. Figure F13B shows an example of gradational contact where grain sizes of constituent olivine, plagioclase, and clinopyroxene gradually increase upsection without significant change in modal proportions. In addition to grain size and modal abundance, sharp contacts were observed at the margins of shear zones or faults (Fig. F13C).

Three types of contact geometry were observed: "planar," "curved," and "irregular." Planar and curved contacts are either concordant and discordant to the structures of the adjacent two lithologies. Figure F13A (intervals 45Z-1, 69–72 cm, and 77–81 cm) shows a planar modal contact across which the modal abundance of olivine increases significantly upsection. This contact may be a result of precipitation or in situ crystallization of primary olivine from magma with the appearance or disappearance of olivine from the liquidus of the crystallizing melt. In contrast, discordant crosscutting relationships of the host foliation and layering and the engulfment of the host rocks within the invaded rock can result in contacts that follow the outlines of grain boundaries and grains in the invaded rock that are not broken to make room for the invading magma (e.g., Fig. F13D; interval 107Z-3, 23–25 cm). One interpretation is that a melt intruded a partly consolidated crystal mush so that grains of the invaded country rock were easily separated from one another during intrusion. Alternatively, these textures could be ascribed to rapid sedimentation of large crystals that disturbed the lower crystal mush layer. Sheared contacts commonly display weak foliation adjacent to the contact in one or both bordering lithologies, and in many cases cataclastic deformation is developed along the contact (Fig. F13C; see **Structural geology**). Sheared contacts imply that a fault zone (whether deforming in a ductile or brittle regime) has juxtaposed differing lithologies that may not have been in contact originally.

Grain size variations

The average grain size of rock samples ranges from fine (<1 mm) to medium (1–5 mm) except for rare varitextured pegmatitic (>30 mm) intervals at 68.6–70.4 mCCD (Igneous Intervals 39–40). Besides the pegmatitic intervals, the maximum lengths of clinopyroxene and plagioclase do not change with depth and generally fall within the range of medium grain size (Fig. F14). Olivines tend to be finer grained and are more varied in length from <1 to 15 mm deeper than 130 m. Macroscopically identified coarse-grained olivine crystals are elongate to tabular in shape and under the microscope consist of olivine subgrains aligned subparallel to the foliation defined by surrounding plagioclase and clinopyroxene (see **Thin section descriptions**).

There are weak positive correlations between maximum lengths of plagioclase and clinopyroxene, and between olivine and orthopyroxene, although the correlation is less clear for smaller grain sizes (<5 mm) of all rocks (Fig. F15). The maximum lengths of plagioclase and clinopyroxene do not correlate with olivine length.

The maximum length attained by clinopyroxene is 35 mm, and clinopyroxene is generally larger than plagioclase for grains >10 mm. In contrast, olivine is generally <10 mm. This results from the presence of large clinopyroxene oikocrysts that are larger than the surrounding clinopyroxene crystals (see **Thin section descriptions**).

Textures

Most rock samples have undergone metamorphic (hydrothermal) alteration along veins and shear zones that partly obscures the original igneous (and/or structural) textures. In addition, cataclastic shearing, crystal-plastic deformation, and partial recrystallization overprint some of the original magmatic features (see **Structural geology**), some of which occurred at high temperatures. However, primary igneous textures are still well preserved in most of the least deformed and least altered samples. Almost all gabbroic rocks have a granular texture except two core sections that show "poikilitic" and "ophitic" textures (Fig. F16). However, within a granular matrix, ophitic or poikilitic clinopyroxene oikocrysts are commonly present in most core samples (see **Thin section descriptions**).

Olivine occurs mostly as anhedral tabular to elongate crystals, although subhedral equant to subequant crystals are also present. Plagioclase forms anhedral to subhedral tabular to subequant crystals partly or totally enclosed by large clinopyroxenes. Clinopyroxene is commonly anhedral to subhedral with subequant to tabular habit and generally encloses tabular plagioclase (totally or partially) and, less commonly, olivine. The rare pegmatitic rocks are characterized by the presence of clinopyroxene oikocrysts as large as 2 cm. When brownish orthopyroxene is present, they form film-like coronae around olivine. Tiny oxide crystals are also present in most rocks as inclusions in olivine and clinopyroxene.

Igneous layering

Igneous layering generally occurs in all igneous units. However, in order to describe the strong lithologic differences between the different layers, for example in Igneous Interval 37 (Unit II) and Igneous Interval 51 (Unit III), some intervals were divided into different subintervals and the lithologic features of each subinterval were described individually. As a result, the layering in these intervals is underestimated by plotting layer thickness and layer intensity rank downhole (Fig. F17). Additionally, in some intervals, the scale of layering exceeds the length of described sections, and these layers also cannot be represented by the numbers for layer thickness and layer intensity rank, which are given for each section (or subinterval). However, if layering on such a large scale was observed, this was noted in the VCD comments.

In order to give a better representation of the actual layer thickness downhole, a single value for layer thickness was assigned for each section layer (even though this section was divided into different subintervals), and layer thicknesses were added across sections where they exceeded the length of a single section.

Although igneous layering generally occurs in all igneous units, it appears to be most strongly developed in Unit III and is not observed in the lower part of igneous Unit II below 60 mCCD (Igneous Intervals 39–50). Layer contacts are planar in almost all layers.

The nature of layering is mainly modal or combined modal and grain size for Unit I, but pure grain size layering was not observed (Fig. F18). Layering in Unit II is mainly modal; grain size layering is absent. Unit III shows rather gradational layer contacts, and the nature of layering is modal. Layering in Units IV, V, and VI is dominated by gradational transitions and a combination of grain size and modal layering. In contrast, layering in Unit VII is dominated by sharp contacts and the nature of layering is different grain sizes.

Thin section descriptions

Principal lithologies

The igneous petrology team described 70 thin sections from Hole GT1A. Brief summaries of thin section descriptions are shown in Table T3, and the detailed description of each thin section or thin section domain is available in Excel worksheets in **Supplementary material** > **B_Thin section descriptions**. The most common rock types observed in the thin sections of Hole GT1A are olivine gabbro and olivine-bearing gabbro; both rock types principally display medium-grained granular textures.

Euhedral olivine is not present in Hole GT1A. Anhedral, elongated olivine crystals are most common at depths shallower than ~150 m in Hole GT1A (Units I–IV; Fig. F19A). Elongated olivine displays kink bands and subgrain development (Fig. F20A, F20B). The directions of olivine elongation and plagioclase laminations define planar magmatic foliations. Some samples rarely display thin orthopyroxene films rimming olivine crystals (Fig. F20C), but orthopyroxene is not present as discrete crystals. Olivine commonly contains equant sulfide grains, mostly pyrite. The volume percent of replacement (= degree of alteration) of olivine is more variable at depths shallower

than ~120 m, but complete alteration of olivine is still common in many samples deeper than ~120 m (Fig. F19B). Variation of modal olivine has peaks at ~20 and 104 m depths (Fig. F19C). The result is comparable to that of modal analysis in the VCD (Fig. F12). Around the peaks of modal olivine, the olivine habit tends to be elongated. In the downhole horizon richest in olivine (~90–120 m; Sections 38Z-3 to 50Z-1), the volume of replacement of olivine is relatively lower (2%–40%, with the exception of one sample in which olivine has completely altered).

Plagioclase occurs as subhedral to euhedral grains. Planar magmatic foliations are defined by weak to moderate plagioclase (and olivine) shape-preferred orientation. Plagioclase crystals commonly contact each other with 120° triple junctions throughout the hole. Zoning of plagioclase is only weakly developed in most sections of Hole GT1A and poorly developed to absent in samples from 100–130 m CCD.

Clinopyroxene is present as subhedral grains in most samples. It contains a few small inclusions of plagioclase laths and commonly exhibits subgrain development. Large clinopyroxene oikocrysts occur at some cores as described in the next section.

Detailed observations and special features

Clinopyroxene and olivine oikocrysts

Large clinopyroxene oikocrysts (>1 cm) occur only in a few intervals (e.g., 30Z-4, 45–49 cm) where they are present in the medium-grained olivine gabbro matrix (Figs. F21, F22). Clinopyroxene oikocrysts commonly surround plagioclase and olivine chadacrysts. The plagioclase chadacrysts are generally much smaller than those in the surrounding olivine gabbro. Consequently, the grain size distribution of plagioclase in the clinopyroxene-oikocryst–bearing rocks is bimodal. Clinopyroxene oikocrysts show partial subgrain development, and plagioclase chadacrysts are abundant along the subgrain boundaries of the oikocryst (Fig. F21). There are rare bent plagioclase and kinked olivine chadacrysts within the clinopyroxene oikocrysts. The aspect ratios of plagioclase chadacrysts are generally larger than those of plagioclase crystals in the matrix olivine gabbro.

Clinopyroxene oikocrysts have also been found in layered mafic intrusions (e.g., Somerset Dam, McIntosh, and Eulogie Park Intrusions in Australia; Rum Intrusion, Scotland; Mathison, 1987; Leuthold et al., 2014) and oceanic layered gabbros from Hess Deep, East Pacific Rise (Gillis et al., 2014a, 2014b). In contrast to Hole GT1A, clinopyroxene oikocrysts in Hess Deep occur in the troctolite matrix and contain only plagioclase as the chadacryst phase.

Large oikocrystic olivine (up to 10 mm) is also present in Hole GT1A but only occurs in a narrow depth interval (Cores 33Z–34Z, Igneous Interval 45; 80.3–83.4 m CCD). These oikocrystic olivines are some of the largest olivine grains present in Hole GT1A. They contain plagioclase inclusions, but plagioclase chadacrysts occur only near the rim of the oikocrysts (Fig. F23). The oikocrystic olivines commonly exhibit kinking.

Fine-grained gabbroic layers

Fine-grained gabbroic layers are interbedded into medium-grained layered gabbros in some sections (e.g., 45Z-1, 47Z-1, 47Z-2, and 48Z-3). Two thin sections of the lower contact of fine-grained gabbroic layers with medium-grained gabbros were described. At a microscopic scale the lower contact is sharp and both the modal composition and grain size change discontinuously at the contact (Fig. F24). In the contact boundary, an interfingering texture between clinopyroxene of the fine-grained olivine gabbro and olivine of the medium-grained olivine gabbro is observed (Fig. F24C). This suggests that both minerals grew almost simultaneously. The original modal olivine contents of the fine-grained gabbroic layers are 4–5 vol%, generally much lower than those of the surrounding medium-grained olivine gabbros (Table T3).

Alteration

Hydrothermal alteration is ubiquitous throughout Hole GT1A, and all rocks have undergone water-rock reactions. These reactions occurred under a range of temperature conditions and fluid compositions and over the lifespan of the Oman ophiolite from the Tethyan ocean-ridge crest and ocean floor through obduction to exposure today in the mountains of Oman. Hydrothermal alteration in Hole GT1A manifests as alteration of the host rock as secondary mineral replacements of primary phases in the background host rocks, isolated patches, halos surrounding veins, and in zones related to deformation and through the precipitation of secondary minerals in veins. The alteration is highly variable in terms of types and intensity on the scale of a single ~1 m section. All four of the above categories plus hydrothermal veins are present and reflect the complex history that these rocks have undergone.

During macroscopic core description, the alteration description team identified and logged 647 intervals of alteration that indicated different styles or intensities of alteration (see Alteration sheet in **Supplementary material** > **E_Tabulated VCD data**). An alteration interval was defined as an interval in a core section where the alteration assemblage, style, and intensity was similar. Downhole overviews of alteration and veins are shown in Figures F25, F26, and F27. Alteration intensity is highly variable downhole, and total alteration ranges 10%–100% (mean =

~60%) (Fig. F25). Within this broad range are several depth intervals where the alteration intensity is observed to increase downhole (e.g., 0–50, 50–80, and 100–200 m). Deeper than 200 m, the distribution of alteration intensity is more variable with no clear trends with depth.

Background alteration

Background alteration is ubiquitous throughout Hole GT1A, occurring in 93% of the 647 defined alteration intervals (Fig. F26). The average proportion of an interval represented by background alteration is 83%. Background alteration intensity ranges 10%–98% (mean = 51%). Background alteration texture is predominantly classified as pervasive or patchy; banded background alteration is the least common type. Background alteration colors are variable; the most common colors are light gray, medium gray, or gray-green (Fig. F28). Background alteration color is related to the background alteration intensity and secondary mineral assemblage. Background intensity of 0%–25% alteration minerals is generally associated with medium to light gray; 25%–40% with medium gray to greenish; 50%–80% with gray-green, and rocks with background intensity >80% exhibit a wide range of colors. The secondary mineral assemblage of background alteration is dominated by albite + chlorite throughout Hole GT1A (Fig. F27) with the different background alteration colors generally reflecting a change from albite dominated to higher chlorite abundances. Amphibole is also present in the background alteration assemblage but is not common until deeper than ~90 m. Albite is associated with partial to complete replacement of plagioclase. Chlorite replaces olivine, clinopyroxene, and plagioclase. Amphibole generally replaces clinopyroxene. Following albite, chlorite, and amphibole, epidote is the next most abundant secondary mineral observed in the background but is only observed in five depth regions (0–50, ~100, ~175, ~275, and ~340 m). Fe oxyhydroxides are present in the background only in the uppermost 25 m of the hole.

Patches

Alteration patches are present in 16% of the 647 defined alteration intervals, and on average they represent 13% of an interval. Patch alteration intensity ranges 40%–100% (mean = 84%). Alteration patches are found throughout Hole GT1A, although their abundance is generally low in the uppermost 100 m (Fig. F26). Deeper than 100 m, they are more abundant. Alteration patches are generally irregular in shape and 3–6 or >6 cm in size (Fig. F29). The most common colors of alteration patches are light gray to milky white, white, and green. The secondary mineral assemblage of alteration patches commonly contains 3–4 different minerals. The most abundant minerals are (from most to least abundant) albite, chlorite, amphibole, and epidote. Clinozoisite, quartz, and Fe oxyhydroxides are also present in some patches, but the latter phase is only present in the uppermost 70 m of Hole GT1A. Although quartz is not a particularly common phase in patches, when quartz is present it is commonly in high abundance. Alteration patches commonly appear to be related to primary differences in the igneous modal abundances and grain size (Fig. F28C). Rare examples of extensive secondary mineral precipitation consume the width of the core and could be interpreted as either large patches or a large vein halo whose host vein does not intersect the cut surface. Examples of this phenomena include a large interval of anhydrite in interval GT1A-108Z-4, 12–29 cm (Fig. F29).

Halos

Alteration halos are the second most prevalent alteration feature after background alteration and are present in 70% of the 647 defined alteration intervals, on average representing 18% of an interval. Halo alteration intensity ranges 55%–100% (mean = 85%). Alteration halos are associated with ~8% of the total number of veins (1087 vein halos logged) and are found throughout Hole GT1A (Fig. F26). There is a slightly higher abundance of irregularly shaped halos than symmetric halos around veins. Alteration halo color is highly variable; examples include white, light gray, dark gray, light green, green, dark green, yellow-green, light gray-pink, and black spots (Fig. F30). The most abundant halo colors are white and dark gray. Variability in color is a reflection of the variable secondary mineral assemblage and alteration intensity present within the alteration halos. Secondary minerals present in halos include albite, amphibole, chlorite, clinozoisite, epidote, Fe oxyhydroxides, laumontite, prehnite, pyrite, quartz, and zeolites. Albite, chlorite, and amphibole are generally ubiquitous in alteration halos, and epidote is present in a large number of features. The other minerals listed previously are present irregularly with Fe oxyhydroxides, mostly in the upper 80 m.

The most abundant halo type, white halos, is found throughout the hole and are generally <5 mm in width, although examples up to 40 mm are present deeper than 300 m. These halos are associated with a range of vein compositions, most commonly with chlorite + prehnite veins. The next most abundant halo type is gray/dark gray and is only present deeper than 100 m. These halos are predominantly <2 mm wide with rare examples up to 10 mm and are associated with <0.5 mm amphibole veins. Dark green and light green halos are found deeper than 75 m, and they are generally 1–10 mm in size with rare examples up to 40 mm. These halos are predominantly associated with chlorite + prehnite veins. Yellow-green halos are rich in epidote and are found around epidote veins. These halos are also com-

monly compositionally zoned and show a decrease in alteration intensity away from the vein toward the edges of the halos.

Deformation-related alteration

Deformation-related alteration is present in 16% of the 647 defined alteration intervals and on average represents 50% of an interval. Deformation-related alteration intensity ranges 80%–100% (mean = 84%) and has the narrowest range of the four defined alteration categories. This alteration type is the most variable in terms of scale, composition, and complexity (Fig. F31). Deformation-related alteration ranges from 2–3 cm scale bands to >1 m and is generally associated with brecciation, cataclasis, and fault zones. Deformation-related alteration is present throughout Hole GT1A (Fig. F26). The highest proportions of deformation-related alteration (80%–100% of an alteration interval) are found at discrete depths that relate to the major fault zones identified in Hole GT1A. The dominant secondary mineralogy is similar to the other alteration types with chlorite + amphibole + epidote + albite found in most examples of deformation-related alteration. In contrast with background, halo, and patch alteration, quartz is one of the more abundant secondary minerals and is present in >55% of all deformation-related alteration occurrences, although quartz only appears below 80 m in Hole GT1A. Deformation-related alteration also includes secondary minerals that are not observed elsewhere in Hole GT1A. Gypsum is found in fault zones at 231 and 273 m. Calcite is also found in deformation intervals, although it has a relatively low abundance and generally occurs as a thin coating along veins. Some of the deformation intervals contain a high abundance of fine-grained green material that is likely ground-up hydrothermally altered host rock.

The high degrees of alteration in the deformed intervals are difficult to consider in isolation from the hydrothermal veins because the veins commonly form a large component of these intervals (mean abundance = 38%, but up to >80%). Vein material in deformation zones occurs in a variety of forms: as early veins that have been fragmented and deformed, as syntectonic veins, and later as veins that crosscut the deformation. The vein mineral assemblage in the deformed zones is always dominated by chlorite + prehnite. The 3 main assemblages found in the Hole GT1A deformed zones are

- Chlorite + prehnite + quartz (most common),
- Chlorite + prehnite + epidote, and
- Chlorite + prehnite + clay.

Veins

Hydrothermal veins are abundant throughout Hole GT1A. A total of 12,453 veins were logged individually, and a further 2,217 veins were counted in deformed zones and in vein nets. Downhole, vein density is highly variable and ranges 2–204 veins/m (mean = 37 veins/m; Fig. F32). Veins make up ~6% of the total core surface area and are clearly an important component of the hydrothermal evolution of Hole GT1A (Fig. F33). Vein density is observed to increase toward some of the main fault zones (e.g., at 170 m), and the highest vein densities (>100 veins/m) are always associated with fault zones (Fig. F32). The most frequently observed secondary minerals in veins are chlorite + prehnite. These two minerals generally occur together as mixed veins with an average vein density of 20–26 chlorite + prehnite veins/m. Some intervals have as many as ~100 veins/m (Fig. F34). Chlorite + prehnite vein intensity increases between 0 and 150 m, and below 150 m their abundance is constantly high (~40 veins/m) until the lowermost 50 m, where they decrease. Laumontite veins have the second highest vein density after chlorite + prehnite, and >80% of laumontite occurs in veins with chlorite as a lining. Laumontite veins are most abundant at 0–80 m and rare at 100–150 m. Deeper than 150 m, their density increases again with discrete horizons dominated by laumontite veins (e.g., ~325 m). Amphibole veins are only observed deeper than 50 m but are otherwise found throughout the rest of Hole GT1A. Amphibole veins are generally <1 mm wide and are accompanied by 1–2 mm gray halos. Quartz is the only other secondary mineral found continuously throughout Hole GT1A and displays intensities up to ~60 quartz veins/m. Only one-third of all quartz-bearing veins are composed solely of quartz. The remaining two-thirds is found in assemblages with a variety of other secondary minerals, the most common of which are quartz + chlorite and quartz + chlorite + prehnite. Epidote and zoisite veins are found irregularly throughout Hole GT1A at maximum vein densities of 30–40 veins/m. Both epidote and zoisite occur either as single-phase veins or commonly with each other or chlorite. Both calcite and Fe oxyhydroxide veins are present at the top of Hole GT1A, show a pronounced decrease with depth (Fig. F33), and are not present deeper than 50 and 80 m, respectively. At depths greater than 100 m, calcite and Fe oxyhydroxide are only found in discrete horizons.

Alteration halos are developed around ~8% of hydrothermal veins and are described in the Halos, above. Crosscutting vein relationships were observed throughout Hole GT1A; a total of 716 crosscutting relationships were recorded. Crosscutting relationships vary from clear crosscuts with intersecting veins at contrasting orientations to more anastomosing relationships where two (or more) veins share a more complicated geometry. Most but not all of the secondary minerals observed in Hole GT1A have crosscutting relationships (Figs. F35, F36).

XRD results

To aid mineral identification, X-ray diffraction (XRD) analysis was completed on 79 samples from Hole GT1A (Table T4). These results were integrated into the downhole secondary mineral plots and recorded in the alteration and vein logs where appropriate.

Relative timing

From the crosscutting vein relationships and overprinting halos, the relative timing of each of the secondary minerals can be deduced. From earliest to latest, the following sequence is present:

- Amphibole,
- Epidote + zoisite + quartz,
- Chlorite + prehnite + quartz, and
- Calcite, laumontite, anhydrite, and gypsum.

This sequence reflects a generalized trend from high-temperature alteration to lower temperature alteration and is similar to observations in the modern ocean crust (e.g., Alt et al., 2010). Amphibole is definitely the earliest phase because it does not crosscut any other mineral. Unfortunately, there are no intersecting occurrences of calcite, laumontite, anhydrite, and gypsum where the relative timing of these lower temperature phases can be deduced. As a result, these are all shown equally as "latest" in the above sequence. Quartz was likely precipitating over a longer time span and range of temperatures because it has more complicated crosscutting relationships; it both cuts and crosscuts some mineral phases.

Structural geology

In Hole GT1A, drilled through part of the layered gabbro section of the Samail ophiolite in Oman, numerous structures were observed and recorded, including well-developed magmatic fabrics and layering, very limited crystal-plastic deformation, heavily veined and fractured intervals, and several fault zones exhibiting both normal and reverse sense of shear. Below is a summary of major findings, beginning with the highest temperature structures and ending with the lowest temperature structures.

Magmatic structures

Magmatic contacts

The majority of magmatic contacts in the core are those that define the magmatic layering. These are typically planar and sharp, defined by modal, phase, and grain size variations, and are discussed in more detail in Magmatic layering. Crosscutting or irregular intrusive contacts are present but rare (e.g., 107Z-3, 23–25 cm), although sharp, planar, tectonic contacts are present throughout the core.

Magmatic layering

Magmatic layering is common throughout the core and is dominantly defined by variations in mineral proportions (ratio layering) and mineral assemblages (phase layering) commonly in combination with variations in grain size (Fig. F37). Pure grain size layering is less common. Layers exhibiting grain size or modal grading are only rarely present (e.g., 47Z-2, 53–83 cm). Layer boundaries are typically sharp and planar but may also be gradational and less commonly curved.

Complicated and possibly folded layering may be present in interval 46Z-3, 8–71 cm. Magmatic banding defined as a weaker, more diffuse type of layering is also present but less common in the core (Fig. F38).

The dip of the layering varies 0° to ~40° (mean = 18°), and there is a hint of a slight increase in dip with depth (Fig. F39B). A total of 863 layers were measured in the core, and layer thicknesses vary and range from <1 cm to 3.3 m (mean = 24 cm). However, the centimeter-scale layers dominate (thickness mode ~ 3 cm) (Fig. F40).

Magmatic foliation

Magmatic foliation is ubiquitous throughout the core, and nearly 90% of the core shows foliation (Fig. F39A). The foliation mostly dips 0°–40° (mean = 19°). Overall, the dip of the foliation gently increases with depth downcore from a mean of ~10° near the top of the core to ~28° near the bottom of the core. The orientation of the foliation is commonly parallel to the magmatic layering (Fig. F39).

The magmatic foliation itself is defined by aligned and elongate plagioclase, olivine, and more rarely pyroxene crystals and varies in strength from not present through weak to strong (Figs. F41, F42, F43). Weak foliations are more prevalent than strong foliations. The strongest foliations have more elongate crystals and plagioclase crystals having aspect ratios as large as 4:1 (Fig. F38C), subgrained olivine crystals with aspect ratios up to 5:1 (Fig. F42A), and pyroxene crystals with aspect ratios of 2:1 (Fig. F43C). The foliations are most commonly planar, although rarely they may curve to become parallel to the layering or parallel to the later faults. Rare folded foliation is found in contiguous intervals 38Z-3, 0–68 cm, and 38Z-4, 0–67 cm.

Commonly, plagioclase crystals show evidence of annealing and equilibration (Fig. F43C), although rare plagioclase deformation twins are present (Fig. F43D). The elongated olivine crystals always show subgrain development.

Magmatic veins

Magmatic veins are extremely rare in the core, and only dioritic veins and a single anorthositic vein

were recorded. The dioritic veins are found in Units IV and V, are 1–2 cm wide, dip steeply (59°–90°), and are therefore discordant to the magmatic layering and foliation (Fig. F39B). Two veins have planar margins and two have irregular margins. All have moderately coarse grain size (2–4 mm). An example of a dioritic vein with a planar margin can be found at interval 61Z-1, 60–61 cm, and one with an irregular margin at interval 65Z-1, 22–39 cm. The anorthositic vein is 3 cm wide, has planar margins, and dips 83° (94Z-2, 57–74 cm). This vein is also cut and offset by brittle faults. It is located in Unit VI.

Discussion

The dip of the layering and foliation measured around the drill site is ~20°–40° to the south-southeast, and the region dips southwest; both are similar to the magnitude of the dip of the layering and foliation measured in the core reference frame, implying that the layering and foliation are approximately subparallel to the paleo-Mohorovicic discontinuity (Moho).

In detail, the variation of the layering and foliation dip with depth exhibits two distinctive features. First, there are rare localized and isolated excursions to dips as high as 90° (Fig. F39). These excursions are caused by rotation of the layering/foliation due to drag on late brittle faults (Figs. F44, F45); however, these excursions do not appreciably affect the overall variation in magmatic fabric dip. Second, the overall variation of dip with depth appears to vary systematically, exhibiting cycles of gradually increasing and decreasing dip over length scales of ~50–75 m (Fig. F45). The origin of this cyclic "fanning" of the layering/foliation is unclear, although it appears to be a primary magmatic feature and not a later tectonic feature.

Crystal-plastic deformation

In Hole GT1A, no significant and continuous subsolidus crystal-plastic fabrics (CPFs) are observed except for narrow domains with incipient low-temperature crystal-plastic deformation that was logged in the brittle deformation log with a note as such. These CPF domains are mostly 3–35 mm wide but can be wider close to highly fractured zones. These features were mainly recovered at the margins of zones with intense cataclasis, at the contact with sheared veins, or in intervals with abundant secondary alteration minerals or related to zones with very fine grain size (see Brittle structures). At macroscopic scale, the incipient fabric is characterized by anastomosing, ultra-fine-grained light brown to beige seams surrounding broken submillimetric fragments of the host gabbro and in many cases fragments of epidote from alteration veins. At microscopic scale, these domains show transitional features between foliated cataclasite and low-grade protomylonite with S-C microstructures and rotation of the incipient foliation. Plagioclase and olivine show undulose extinction, tapered twins, and subgrain development and bent grains. In general, crystal-plastic deformation mostly affects secondary subgreenschist alteration minerals such as prehnite and chlorite.

Examples of brittle-plastic fabric include one shear zone in partly altered gabbro in interval 34Z-4, 50–64 cm (Fig. F46), and one sheared vein of anhydrite 2–3 cm wide that cuts cataclasite in a fault zone in interval 108Z-4, 11–26 cm (Fig. F47). In thin section, anhydrite exhibits brittle-plastic fabric and dynamic recrystallization. The plastic component formed the elongate, sigmoidal crystals, and the brittle component formed block boundins, the boudin necks filled with secondary anhydrite (Fig. F47). Other examples of brittle-plastic zones are in intervals 22Z-4, 24–31 cm; 34Z-4, 70–86 cm; 90Z-1, 33–44 cm; 34Z-1, 74.3–77.5 cm, and Section 119Z-1.

Microstructures were also used to check the sense of shear of some structures.

Brittle structures

Brittle structures are well developed throughout Hole GT1A, and they were logged in all sections (see Brittle log sheet in **Supplementary material** > **E_Tabulated VCD data**). More than 500 brittle features, including features involving both brittle and incipient crystal-plastic deformation, were logged. In addition, >12,000 veins were described by the alteration specialists (see the Alteration sheet in the Hole GT1A core description workbook). In some cases, whole sections or even cores are formed entirely of fault rocks (e.g., Cores 80Z and 131Z). Cataclastic deformation intensity rankings in Hole GT1A (see **Structural geology** in the Methods chapter) ranges mostly 1–4 with minor intensities of 0 and 5.

The most intense brittle structures are represented by discrete cataclastic zones and fault zones, including hydraulic or hydrothermal breccias, shear veins, and minor shear zones. Commonly, veins are sheared or fractured (e.g., epidote veins in Fig. F48). Shear veins are commonly accompanied by incipient brecciation or less frequently by protomylonitic fabric defined by alteration minerals (see Structure and Brittle log sheets in **Supplementary material** > **E_Tabulated VCD data**); shear zones are rare and mostly brittle-ductile shear zones.

In Hole GT1A, cataclastic zones and fault zones exhibit variable thickness (from millimeter to decimeter scale), heterogeneous grain sizes (mostly submillimeter to centimeter scale), various degrees of alteration, and different associated vein densities (see **Alteration**). The succession of vein formation and mineral filling vs. brittle deformation is complex and multiphase. In most fault zones, late veins of low-temperature subgreenschist minerals such as

prehnite, zeolites, clays, and carbonate crosscut earlier deformation. Cataclastic zones have textures ranging from narrow millimeter-spaced networks of fractures to centimeter-wide intensely comminuted zones to variably brecciated rocks at the decimeter scale. The fault zones tend to be indurated and cohesive, making them more dense than the adjacent altered gabbro (Fig. **F49**).

Fault rocks show a wide range of grain sizes and compositions with different grades of cohesiveness and alteration (see **Alteration**). Offsets, rotation of fragments, disaggregation of primary fabrics and layering, and formation of secondary veins are observed in cataclasite. Fault breccias have centimeter to decimeter subrounded clasts of gabbro (e.g., Sections 80Z-1, 80Z-2, and 131Z-4; Fig. **F50**).

Foliated cataclasite and ultracataclasite are also common. At least 10 narrow (5–20 mm thick) zones of ultracataclasites were recovered, associated with both wider fault zones and quartz or epidote veins or localized in less fractured host rocks mostly in the upper part of the hole (to 125 m; e.g., 14Z-1, 46–65 cm, 28Z-4, 0–10 cm, and 48Z-4, 2–26 cm) (Figs. **F48**, **F51**, **F52**). Ultracataclasites show very fine grain size (micrometer scale) with transgranural fracturing and intense comminution of the host rock, cataclastic and granular flow, and multiple superposed sharp slip surfaces (e.g., 32Z-2, 25–41 cm; Fig. **F53**).

Intervals of hydrothermal breccia with signs of dynamic dilational processes, injections, and implosion associated with intense fracturing, grain size reduction, and corrosive wearing of the wall rocks occur in intervals 133Z-0, 25–41 cm, and 141Z-1, 26–55 cm (Fig. **F54**). These features were most common at ~357 m and are associated with epidotic background or deformation-related alteration.

General overview

Numerous intervals with incipient to well-developed fracturing were recovered in material from Hole GT1A. On the basis of (1) disruption of primary magmatic fabrics, (2) brittle fabric intensity, (3) background alteration intensity, and (4) peaks in vein density for various compositions, more than 20 well-defined fault zones were identified and characterized. Figure **F55** shows the location of the fault zones grouped into 7 major and 14 minor fault zones and the damage zones associated with the main fault zones.

Main fault zones are characterized by single or multiple core zones with related damage zones and background alteration. The mean dip angle of the slip zones measured in the faulted interval is ~50°–55° with minor steeply dipping and associated low-angle minor structures (Fig. **F56**). This dip magnitude is very close to that of the fault zones that crop out at the surface near the drill site (see Figs. **F4**, **F5**). If we take into account the dip angle of 50°–55°, the thickness of the recovered damaged rocks around main fault zones has been estimated to be 2–10 m.

Cataclasis and shearing are localized in narrow millimeter- to centimeter-scale zones (mostly in the uppermost 120 m of Hole GT1A; Fig. **F55**) where the brittle fabrics range from foliated cataclasite to ultracataclasite. A total of 154 structures showing sense of shear were logged in the Brittle deformation worksheet. For 42 of these features, the orientations of associated lineations were also measured. Senses of shear are mostly normal (57% of measurements) and reverse with mostly dip-slip and oblique-slip movements. Strike-slip movements are uncommon (~15% of measurements) (Fig. **F56**). Commonly, the crosscutting relationships show reverse sense of shear structures overprinting normal sense of shear structures. Reverse senses of shear are mostly localized to the upper 270 m of Hole GT1A.

Fault zone and brittle-ductile shear zones commonly nucleate on strain-weakened precursors such as veinlets of secondary minerals (most commonly prehnite or chlorite), alteration halos surrounding veins, or at the contact between different rock types, such as dunitic layers/gabbro, orthopyroxene-bearing gabbronorites/olivine-rich gabbro, or olivine gabbro/anorthositic magmatic veins.

Most of the brittle structures show evidence of multiple phases of reactivation. Cataclastic zones and fault zones show repeated cycles of tectonic slip within a single deformational event. In places, the syntectonic fluid infiltration and interaction with the host rock is intense and accompanied by alteration and metasomatic recrystallization (see **Alteration**).

Crosscutting relationships are complex. Structures with normal sense of shear cut epidote and chlorite veins and are accompanied by prehnite, and normal incipient shear zones are accompanied by clinozoisite, whereas reverse fractures are commonly associated with quartz, zeolite, prehnite, and laumontite.

Veins

The orientations of 2987 veins were measured. Compositions range from epidote to clay (**Alteration**; also see the GT1A Vein log in **Supplementary material** > **E_Tabulated VCD data**). All fractures were completely filled or partially filled with vein material with no purely open fractures. Therefore, no fractures or joints were logged.

Vein dip distribution

The range in vein dip is large, from subhorizontal to subvertical with no pattern downhole (Fig. **F57**). The frequency distribution of the dips peaks near 45°, in-

dicating a random distribution based on borehole sampling bias (see **Structural geology** in the Methods chapter). However, there are some patterns in dip magnitude with depth. For example, 30–130 m contains a relative lack of steeper features, whereas 250–340 m contains few gently dipping veins. Overall, when all vein compositions are considered together, the dip magnitude downhole is random.

Sense of shear

Of the almost 3000 veins measured, 185 had identifiable slickenfibers or slickenlines. The plunge of the lineations is gentle to moderate with little variation downhole (Fig. **F58**). The angle between the plunge of the slickenfibers and the dip of the vein is typically low to moderate, indicating mostly dip-slip motion with minor oblique-slip (Fig. **F58**). There are rare examples of strike-slip indicators. Slickenlines have three main compositions: (1) actinolite ± prehnite, (2) chlorite, and (3) chlorite with clay (e.g,. saponite) (Fig. **F59**).

Of 121 identified shear sense indicators (Fig. **F60**), 42 are slickenfibers and the rest are pull-apart veins. The sense of shear recorded by these indicators is mostly normal or reverse; only three indicators show only sinistral or dextral components. The majority of shear sense indicators are normal (n = 69; 57%). The 49 reverse sense of shear indicators mostly occur in the upper two-thirds of the hole; normal sense of shear indicators dominate in the bottom one-third. Nearly half of the reverse sense shear sense indicators are slickenfibers, whereas only ~25% of normal sense indicators are slickenfibers. However, the majority of slickenfibers identified do not have a clearly defined sense of shear.

The relationship between shear sense indicators can be complicated. In many cases, slickenfibers and/or pull-apart veins occur as discrete structures and do not overlap. In the case of fault zones, as described above, reverse shears crosscut normal shears. There are some examples where veins that record a normal sense of shear occur very close to veins of similar composition with a reverse sense of shear (Fig. **F61**).

The majority of reverse sense of shear indicators are slickenlines (25 reverse, 15 normal). The majority of normal shear sense indicators are pull-apart veins. However, several pull-apart veins indicate a reverse sense of shear. Contraction-related structures are recorded as both pull-apart veins and slickenlines, whereas extension-related structures are mainly recorded as pull-apart veins. The type of shear sense indicator also changes downhole. For example, in the upper half of the hole the shear sense indicators are almost exclusively from steps in slickensides/slickenlines. In the lower part of the hole, the majority of slip sense indicators are pull-apart veins.

The composition of the vein does not seem to preclude any sense of shear. Both normal and reverse sense of shear are recorded by chlorite, prehnite, and laumontite veins. However, quartz veins almost exclusively record normal sense of shear.

Crosscutting relationships

Veins may have crosscutting relationships either by one growing over the other or one offsetting the other. The latter is discussed here. Most vein types, including chlorite, prehnite, laumontite, epidote, and clinozoisite, are crosscut by later veins. The main compositions that are crosscut are epidote, clinozoisite, and prehnite. Veins that crosscut previous veins are typically composed of quartz and laumontite and to a lesser extent chlorite, epidote, and clinozoisite. The most common observation is epidote and/or clinozoisite veins offset by prehnite veins and prehnite veins offset by other prehnite veins ± chlorite (Fig. **F62**). Gypsum and/or zeolite-filled veins crosscut/fill all other veins and do not seem to be offset themselves.

Vein offset was measured on 35 veins. The offset, which is limited to the scale of the core diameter, ranges 1–20 mm. Twelve (34%) of the offsets have a reverse sense of shear and 21 (60%) have normal sense of shear. The remaining 6% include one dextral offset and one sinistral offset.

Conclusions

Magmatic layering and foliation has a mean dip of 18°–19° and is subparallel to the paleo-Moho. The overall variation of dip of the magmatic fabrics with depth downcore varies systematically, exhibiting cycles of gradually increasing and decreasing dip over length scales of ~50–75 m. The origin of this cyclic "fanning" of the layering/foliation is unclear, although it appears to be a primary magmatic feature and not a later tectonic feature. Faulting causes the magmatic fabrics to locally rotate with dips up to 90°.

There are 7 main fault zones and 14 minor fault zones defined by deformed and altered gabbro consistent with (1) disrupted magmatic fabrics, (2) increases in background alteration intensity, and (3) peaks in vein density for various compositions.

The fault identified on the surface with an orientation of (D/DDir) 52/251 is most likely the fault encountered near ~190 m.

Structures show both normal and reverse senses of shear, with the normal sense of shear structures crosscut by reverse sense of shear structures, possibly indicating reactivation.

Geochemistry

Geochemical analyses were carried out on Hole GT1A cores on board the *Chikyu*, and on-site samples were analyzed at the University of St. Andrews prior to ChikyuOman Phase 1. Analyses were performed on 56 samples (33 olivine gabbros, 10 olivine-bearing gabbros, 2 orthopyroxene-bearing gabbros, 2 mela-olivine gabbros and 1 oxide melagabbro, 1 anorthositic gabbro, 1 dunite, and 7 samples of altered olivine and olivine-bearing gabbro). Samples were selected based on discussion with representatives from the ChikyuOman Phase 1 visual core description teams to identify representative areas of plutonic rock and areas where alteration patches and halos were large enough to sample for shipboard geochemistry. In addition, 20 samples were cut from the core on site during drilling every 20 m and analyzed by X-ray fluorescence (XRF) prior to ChikyuOman Phase 1.

XRF was used to quantify major elements on glass beads and trace elements on pressed powder pellets, along with inductively coupled plasma–mass spectrometry (ICP-MS) following alkali fusion acid digestion of rock samples to characterize trace and rare earth elements (REE) (see **Geochemistry** in the Methods chapter). Gas chromatography was used to measure total S, C, N, and H in dried rock powder samples. Data are shown on Figures **F63**, **F64**, **F65**, **F66**, **F67**, **F68**, and **F69** and reported in Table **T5** and Supplemental Table **ST1**. Major oxide data are reported as volatile free, and trace elements are reported as recalculated after subtraction of loss on ignition (LOI) as a measure for volatile loss (although mass gain through oxidation of ferrous iron to Fe^{3+} likely varies between samples). This recalculation was done to allow direct comparison between XRF and ICP-MS trace element data because ICP-MS analyses were carried out on ignited powders.

Inorganic geochemistry

Major, trace, and rare earth elements

Olivine gabbros, olivine-bearing gabbros, melagabbros (some oxide bearing), orthopyroxene-bearing gabbros, and one dunite and one anorthositic gabbro were sampled for geochemical interrogation. Here we use Mg and Ca numbers (Mg# = molar ratios of $Mg/(Mg + Fe^{Total}) \times 100$, and Ca# = molar ratio $Ca/(Ca + Na) \times 100$, and the concentrations of trace metals such as compatible (Cr and Ni) and incompatible (Y) elements to investigate chemical differentiation. Olivine gabbros are the most common rock type in Hole GT1A and display the widest range of differentiation in Mg# (74.8–83.7) and Ca# (95.2–98.3) and the widest range in Cr and Y concentrations (116–1974 and 1.3–6.8 ppm, respectively) (Fig. **F63**). Olivine melagabbros display a narrower range of differentiation (Mg# = 78.2–83.2; Ca# = 97.1–99.2) and have among the highest Cr and Ni concentrations (676–1942 and 152–685 ppm, respectively), but only 3 samples were analyzed. Olivine-bearing gabbros have the lowest Mg and Ca numbers (Mg# = 74.2–82.1; Ca# = 98.0–94.9) and are not as primitive as olivine gabbros or olivine melagabbros, have lower modal abundances of olivine, and have the highest Y contents (2.3–8.4 ppm). Only 2 orthopyroxene-bearing gabbros were analyzed; these have moderately differentiated Mg# (77.3–77.7) and Ca# (98.4–96.2) and relatively low Ni and moderate Cr concentrations (101–188 and 555–905 ppm, respectively) compared with other rocks from Hole GT1A.

The dunite (107Z-3, 24–29 cm) and anorthositic gabbro (19Z-3, 13–18 cm) show contrasting major element compositions; FeO* of the dunite sample is high at 22.7 wt%. Mg# and Ca# values are 70.9 vs. 72.1 and 97.8 vs. 95.6 for dunite and anorthositic gabbro, respectively, and Cr concentrations in both rock types are low (23 and 18 ppm for dunite and anorthositic gabbro, respectively). The dunite has an abnormally low Mg# (70.9), which may be attributed to the near-complete replacement of original olivine and clinopyroxene with serpentine and amphibole, talc, and chlorite observed in thin section, which may have resulted in silica gain.

In Hole GT1A across all gabbro lithologies, CaO ranges 10.2–18.6 wt% and Al_2O_3 spans a wider range (7.6–28.3 wt%), where one anorthosite unit has higher Al_2O_3 at 32.6 wt%. CaO and Al_2O_3 contents of the dunitic unit are 1.92 and 1.86 wt%, respectively, and melagabbros range 10.2–16.8 wt% and 7.6–14.2 wt%, respectively; when plotted against MgO they follow a vector characteristic of olivine accumulation. In contrast, olivine gabbros that have >19 wt% Al_2O_3 follow a trend indicative of plagioclase accumulation (Fig. **F64**). Similarly, plagioclase accumulation trends can be discerned for samples with <10 wt% MgO at FeO* < 7.1 wt% and TiO_2 < 0.34 wt%. For samples where there is no evidence for accumulation of olivine or plagioclase, the range of CaO and Al_2O_3 contents of olivine gabbro in Hole GT1A is 13–19 wt% and 11–18 wt% for CaO and Al_2O_3, respectively, at MgO contents of 6–8 wt% (Mg# = 75–84).

Trace and rare earth elements (REEs) are normalized to primitive mantle (Hoffman, 1988) to assess the systematic behavior of these elements during melting of mantle and further differentiation. Here we show that the concentration of REEs is highest in olivine-bearing and mela-olivine gabbros and lowest in olivine gabbros, as would be expected if olivine-bearing gabbros are more differentiated relatives of olivine gabbros. All samples analyzed, apart from the dunite and an altered vein halo, have an Eu anomaly comparable to lavas, indicating removal of plagioclase through crystal fractionation. The light REEs are depleted relative to primitive mantle, indicating that these rocks are primitive cumulates derived

from magmas formed by partial melting of the mantle (Fig. F65). First-generation vein (V1) lavas from Oman (Einaudi et al., 2003; Godard, et al., 2003) have ~10× higher REE concentrations, as would be expected with further fractionation of melt (more so than fractionation during crystal fractionation).

The igneous rocks in Hole GT1A are divided into 7 igneous units (see **Igneous petrology**). Differences downhole are at a finer scale than the defined igneous units because they sampled a range of different rock types from each unit; however, the geochemical variability is generally within the same broad ranges within each unit (Fig. F66). Samples from Unit I are all olivine gabbros and show limited variability in concentrations of Al_2O_3, TiO_2, Cr, Ni, and V and have among the highest Ca# and Mg# of rocks sampled in Hole GT1A. In Unit II, 5 samples of olivine gabbro, an olivine-bearing gabbro, and an anorthositic gabbro were sampled; due to sampling these different rock types there is greater geochemical variability in this unit. The highest Al_2O_3 concentrations of Hole GT1A are in Unit II, decreasing grading down into Unit III. Unit III is composed of mela-olivine gabbros and mela-oxide olivine gabbros with maximums in olivine and minimums in plagioclase modal abundances logged coinciding with the highest concentrations of Cr and Ni and highest Mg# and Ca# and lowest Al_2O_3 concentrations. Seven samples of olivine gabbro and one olivine-bearing gabbro were taken from Unit IV; this unit displays the lowest Cr and Ni concentrations and higher Al_2O_3 contents than Unit III with a narrower, lower range of Al_2O_3 concentrations than Unit II (Fig. F66). Unit V is also composed of olivine and olivine-bearing gabbros and is geochemically similar to Unit IV but with slightly decreasing Al_2O_3 and increasing TiO_2 concentrations with depth and higher Cr concentrations and Mg#. Unit VI is dominated by samples of olivine-bearing gabbro with two orthopyroxene-bearing gabbros, a mela-olivine gabbro, and a dunite. These differences in rock units are reflected in the geochemical data; this unit has the lowest Al_2O_3 concentrations and most variable V and TiO_2 concentrations. The most geochemically uniform unit is Unit VII; it is similar to Unit V in being composed mostly of olivine gabbro and olivine-bearing gabbro with similar ranges in concentrations of SiO_2, Al_2O_3, Ni, and V but lower concentrations of Cr and higher average Mg# and Ca#. General downhole trends that can be extrapolated across lithologic units are a decrease in Al_2O_3 between Unit I and Unit VI and an increase in TiO_2 from Unit I to Unit V (Fig. F66).

Volatile content

The volatile content of samples was measured by elemental analysis CHNS during ChikyuOman Phase 1 (see **Geochemistry** in the Methods chapter). Water content measured by CHNS analyzer is on average ~0.2 wt% higher than that measured by LOI (Fig. F67), indicating that mass gain during ignition due to oxidation of Fe^{3+} to Fe^{2+} occurred. There is no relationship between LOI and CO_2 contents measured by CNHS; CO_2 contents are generally <0.2 wt% in olivine gabbros. Nitrogen was below detection limits in all samples analyzed.

Water, carbon dioxide, nitrogen, and sulfur contents

Samples recovered from Hole GT1A contain 0.7–11.8 wt% H_2O (average = 2.5 wt%; median = 2.1 wt%). Olivine gabbros and olivine-bearing gabbros sampled as "fresh" representative samples of units have higher H_2O contents in identified fault and fault damage zones where these samples contain above median H_2O contents (>2.1 wt%) indicating stronger hydrothermal alteration (Fig. F68). Samples collected from away from fault or fault damage zones have below median H_2O contents of generally <1 wt%. Samples taken from visibly altered rocks to assess mass change have considerably higher H_2O contents, up to 7.5 wt%, and the one dunite sampled has the highest H_2O content of 11.8 wt%, reflecting its almost complete replacement by serpentine and amphibole (see **Thin section descriptions**).

CO_2 concentrations, calculated from TOC, in samples from Hole GT1A range 0.02–0.69 wt% (average = 0.11 wt%; median = 0.08 wt%). Representative olivine and olivine-bearing gabbro samples have highest CO_2 contents within the vicinity of fault or fault damage zones where CO_2 concentrations range from average values to 0.7 wt%. The lowest CO_2 concentrations (<0.13 wt%) are detected in the minor fault zones and undeformed sections. Of the altered samples analyzed, different alteration styles are apparent throughout Hole GT1A (Fig. F68). For example, altered Sample 46Z-1, 78–83 cm (107.18 m CCD), has 6× higher CO_2 and 2× higher H_2O than background. In contrast, Sample 69Z-5, 0–12.5 cm (172.27 m CCD), has 3.5× higher H_2O but CO_2 the same as background levels. This indicates that alteration in a fault zone in Core 69Z is dominated by hydration processes, corresponding to clay gouge formation, whereas alteration in a vein halo where pyroxene is replaced by amphibole and carbonate is precipitated experiences both CO_2 and H_2O addition.

Sulfur concentrations in olivine gabbros are highly variable (<0.022–0.22 wt%), largely due to the nugget effect of sulfides in these rocks. Generally, the depths at which CO_2 and H_2O are highest in relation to major fault zones correspond with the greatest sulfur contents (Fig. F68).

The proportion of inorganic carbon (TIC) to organic carbon (TOC) in most samples ranges ~0.5–1 wt%

with no definable trend downhole (Fig. F68). This ratio deviates significantly in samples of altered olivine gabbro, particularly in vein halos where there has been carbonate alteration. The altered fault zone Sample 69Z-5, 0–12.5 cm (172.27 m), has elevated sulfur and water contents, but carbon contents are no different from background values. However, this sample has an elevated TIC/TOC ratio indicating that there has been carbonate mineralization, but because the organic carbon content is low, the overall carbon concentration of the altered rock is no different from background.

Altered samples

Six samples of altered core were taken for geochemical analyses to assess mass changes, and in most cases a representative "fresh" sample was also taken for comparison. Generally most altered samples have lower Na_2O and higher LOI than the paired fresh sample, but to assess true mass change without dilution/concentration due to relative changes in elemental composition and total mass change we use Gresen's equation (Grant, 1986):

$$C_i^A = M^O/M^A(C_i^O + \Delta C_i), \quad (4)$$

where

- C_i^A = concentration of component *i* in the altered rock,
- M^O = mass of original unaltered sample,
- M^A = mass in altered sample,
- C_i^O = concentration in original, and
- ΔC_i = change in concentrations between original and altered samples.

As mass of the original and altered samples is unknown, we use an immobile component such as TiO_2, Al_2O_3, or REEs to assess overall changes so M^O/M^A becomes C_x^A/C_x^O where *x* is an immobile component. Using these equations we show losses of up to ~65% mass of Na_2O and gains of up to ~45% CaO and ~63% SiO_2. In some instances there are gains in Na_2O and losses in CaO. Gains are generally up to ~350% by mass of H_2O and 200% by mass of CO_2, although in one instance there is apparent mass loss of CO_2, but in this instance the most altered sample is a clay-rich fault zone that has a different alteration style from background alteration sampled from the rest of the core (Fig. F69). This is shown graphically in two isocon diagrams that compare nearby "fresh" and "altered" representative samples from Sections 19Z-3 and 20Z-2 and Sections 139Z-4 and 140Z-2 (Fig. F69).

X-ray fluorescence core scanning

Sample selection and analysis

Seven cores were selected for nondestructive XRF chemical analysis of archive-half cut surfaces using the mapping mode of the XRF core scanner (CS-XRF) on board *Chikyu* (Table T6). As the criterion for selection, we chose cores with as flat a cut surface as possible and avoided regions with significant secondary alteration. Selected samples include 1 interval from Unit III, 3 intervals from Unit VI, and 1 from the top of Unit VII (Table T6; Fig. F70). Standard measurement conditions were used, following calibration experiments described in **X-ray fluorescence scanning** in the Methods chapter (high voltage = 30 kV, beam current = 0.04 mA, counting time = 60 s, spot size = 7 mm, spacing between spots = 5 mm; Table T46 in the Methods chapter). The intensity in counts measured at individual spots are tabulated in Tables T7, T8, T9, T10, T11, T12, and T13. The average compositions of the intervals are listed in Table T14 with standard deviations.

Analytical results

Downcore compositional variations of major elements and the compatible trace elements Cr and Ni for the intervals of 7 core sections are shown in color-contoured images in Figures F71, F72, F73, F74, F75, F76, F77, F78, F79, F80, F81, F82, and F83. In the following section, "X" indicates a distance along the core from the top of the section, whereas "Y" indicates a distance across the core.

Interval GT1A-38Z-3A, 13–40 cm. This Unit III interval (93.08–93.35 m) is melagabbro (X = 27 cm, Y = 2.5 cm; Table T7; Fig. F71). The elongation of minerals on the flat surface is oblique to the Y-axis of the core at dips of ~60°. Thus, the apparent "true" thickness of the core on the cut surface of the core is ~17 cm. This distance does not fully account for the real attitude of the magmatic foliation and causes some error in estimating "true" thickness of the scanned core. The interval is characterized by higher concentrations of MgO (>20 wt%), higher Mg# (>0.91), and lower SiO_2 (<44 wt%), Al_2O_3 (<12 wt%), and CaO (<15 wt%) relative to other cores measured by CS-XRF (Table T14). The downhole variations of SiO_2, TiO_2, Al_2O_3, CaO, and Cr show similar patterns with wavelengths of ~30–35 cm (equivalent to compositional layering of 19–22 cm after dip correction), indicating that they are controlled by the modal amounts of common minerals. Clinopyroxene contains these elements in certain amounts and may be responsible for these systematic variations. Moreover, the downhole variations of Ni and MgO show similar patterns to each other. Olivine and clinopyroxenes may be the candidates that control the abundances of both elements. The concentration patterns observed for SiO_2, TiO_2, Al_2O_3, CaO, and Cr are opposite to those for Ni and MgO, which display mirror-image relationships. Hence, the downhole compositional variations of melagabbro are mainly controlled by the amount of olivine and clinopyrox-

ene with much less influence from plagioclase, due to its relatively low abundance. These features are also observed in the color-coded map (Fig. F71).

Interval GT1A-53Z-4A, 30–60 cm. This continuous section of Unit IV (130.5–130.8 m) is olivine gabbro and olivine-bearing gabbro (X = 30 cm, Y = 4.5 cm; Table T8; Fig. F72). The elongated direction of minerals on the flat surface is oblique to the Y-axis of the core by ~30°. Thus, the apparent "true" thickness of the core is ~26 cm. This interval is characterized by relatively high average compositions of SiO_2 (47.7 wt%) and high Al_2O_3 (21.3 wt%) (Table T14). There is a distinct difference in grain size between the upper and lower parts of the section: the uppermost part of the section (30–37 cm) is coarse grained (2–5 mm in grain size), whereas the lower part is more fine grained. The boundary between these two parts occurs 37 cm from the top of the section. Because of large grain size in the upper part, the analytical data of individual spots are largely scattered in most elements. In the lower part, measured TiO_2, Al_2O_3, and CaO concentrations show waveform patterns. The variation patterns of TiO_2 and CaO contents are similar to each other, indicating modal control of these elements by clinopyroxene. The variation pattern of Al_2O_3 content is opposite to those of TiO_2 and CaO, a mirror relationship. These results suggest that the modal amount of plagioclase is negatively correlated with the clinopyroxene mode. The contents of Fe_2O_3, MnO, Ni, and MgO vary similarly with gradual decreases downhole from 30 cm followed by an abrupt increase at 41 cm. Again, they gradually decrease toward 51 cm downhole. The variation of these elements may be controlled by the modal abundance of olivine, although no visible contrast is observed at 41 cm in the core.

The color-coded image clearly shows the compositional variations along the core (Fig. F73) and is consistent with the observations described above.

Interval GT1A-90Z-1A, 45–80 cm. This Unit VI interval (223.15–223.5 m) is orthpyroxene-bearing gabbro (X = 37 cm, Y = 3.5 cm; Table T9, Fig. F74). The elongated direction of minerals on the flat surface is oblique to the Y-axis of the core by ~10°. Thus, the apparent "true" thickness of the core is ~36.4 cm. The average composition of this interval is characterized by relatively high SiO_2 (47.7 wt%) (Table T14). The compositional ranges of each element are limited to narrow ranges relative to other cores. However, downhole rhythmic patterns are recognized in some elements (i.e., Al_2O_3, CaO, and Fe_2O_3) at wavelengths of ~6 cm (equivalent to layering of 6 cm after dip correction). For example, low concentrations of SiO_2 and Al_2O_3 occur at 52.5, 59, 66, 72, and 78 cm, intervals of ~7 cm. On the other hand, the concentrations of Fe_2O_3, MnO, Ni, and MgO slightly increase at the same positions, probably indicating that the amount of olivine increases. These features are also observed in the color-coded map (Fig. F75).

Interval GT1A-100Z-3A, 4.5–60 cm. This Unit VI interval (252.97–253.52 m) is orthopyroxene-bearing gabbro (X = 55.5 cm, Y = 3.5 cm; Table T10, Fig. F76). The elongated direction of minerals on the flat surface is oblique to Y-axis of the core by ~15°. Thus, the apparent "true" thickness of the core is ~53 cm. This interval is characterized by high SiO_2 (48.1 wt%) and high Al_2O_3 (21.8 wt%) contents (Table T14). As shown in Figure F76, significant compositional variations are observed in this 55.5 cm interval at wavelengths of 30–35 cm (equivalent to layering of 29–34 cm after dip correction). Most of the scanned interval is a relatively Si rich gabbro (SiO_2 = ~48 wt%), whereas lower concentrations of SiO_2, TiO_2, CaO, and Cr and higher Fe_2O_3, MnO, Ni, and MgO concentrations occur at 14–24 cm and from 53 cm to the bottom of the section. Variations in Al_2O_3 concentrations do not follow those of other elements. These variations indicate that this interval includes compositional layering between a more abundant relatively Si rich gabbro (probably an orthopyroxene-bearing gabbro) intercalated every 10–30 cm with minor amounts of Si-poor gabbro (probably olivine gabbro).

The color-coded composition map for the interval also indicates significant variation of each element (Fig. F77). The boundaries between each compositional layer are easily defined by changes in color. It is noted that the interval 24–34 cm has relatively low MgO, Fe_2O_3, and Ni concentrations, indicating low modal proportions of olivine. In contrast, the same interval displays the highest Al_2O_3 contents, indicating high modal proportions of plagioclase. This zone is located immediately below the olivine-rich part that occurs ~20 cm from the top of the section.

Figure F84 shows a diagram of Al_2O_3 vs. CaO for the 4.5–60 cm interval. Individual analyses and average values at each section profile are compared with mineral compositions for olivine, plagioclase, and clinopyroxene. Most data plot within the triangle formed by three minerals at the apex. This diagram implies the presence of troctolite in this interval. The interval 10–20 cm from the top of the section is characterized by low CaO and high Al_2O_3 and may be a candidate for "troctolite." However, visual core description of this section did not report troctolitic rocks. Further investigations are required to test this possibility.

Interval GT1A-118Z-4A, 15–35 cm. This Unit VI interval (298.04–298.24 m) is olivine gabbro (X = 20 cm, Y = 3.5 cm; Table T11, Fig. F78). The elongated direction of minerals on the flat surface is oblique to the Y-axis of the core by ~40°. Thus, the apparent "true" thickness of the core is ~15 cm. Although this interval is relatively short, the compositional varia-

tion is significant: Al_2O_3 content gradually decreases from 20 to 10 wt% and MgO content increases from 10 to 20 wt% with increasing distance from the top of the interval at a wavelength of 10 cm (equivalent to layering 7–8 cm after dip correction). This variation indicates higher modal abundance of plagioclase in the upper part of the interval relative to the lower part, where the modal abundances of olivine and clinopyroxene increase.

SiO_2, TiO_2, CaO, Fe_2O_3, and MnO contents are mostly constant over the interval with slight depletion of SiO_2 associated with slight enrichment of TiO_2, CaO, Fe_2O_3, and MnO at 19 and 28 cm from the top of the section. This may indicate that the modal amount of olivine spontaneously increases at these positions.

On the color-coded map of major elements, Cr and Ni indicate that the compositions of most elements abruptly change at 6–9 cm with a boundary oblique to the core (Fig. F79). The amount of plagioclase and olivine may drastically change through this boundary.

Interval GT1A-122Z-3A, 34–54 cm. This Unit VII interval (309.4–309.6 m) is olivine-bearing gabbro (X = 20 cm, Y = 3.0 cm; Table T12; Fig. F80). The elongated direction of minerals on the flat surface is oblique to the Y-axis of the core by ~10°. Thus, the apparent "true" thickness of the core is ~20 cm. Although it is a relatively short interval, there are large variations in some elements such as CaO and Al_2O_3. Downhole variation patterns of SiO_2 and Al_2O_3 are similar to each other and display antithetic relationships with TiO_2 and CaO on a 10 cm wavelength (equivalent to layering of 10 cm after dip correction). At 42 cm from the top of the section, TiO_2 and CaO contents show small peaks associated with depletions in SiO_2 and Al_2O_3. These variations may be controlled by modal variations of plagioclase and clinopyroxene. These features are also observed in the color-coded map (Fig. F81).

Interval GT1A-143Z-2A, 3–50 cm. This Unit VII interval (366.0–366.5 m) is olivine gabbro (X = 47 cm; Y = 3.5 cm; Table T13; Fig. F82). The elongated direction of minerals on the flat surface is oblique to the Y-axis of the core by ~30°. Thus, the apparent "true" thickness of the core is ~41 cm. The compositional range in this interval is relatively narrow compared to the other sections studied. However, most elements display small zigzag patterns at a wavelength of ~5–6 cm. The color-coded map of Al_2O_3 clearly shows this feature—Al-enriched and -depleted parts are repeatedly distributed (Fig. F83).

Summary

All the core intervals studied indicate compositional layering with wavelengths of 6–30 cm. The average compositions of most profiles show smooth and continuous curves along the cores, proving that the average composition measured at 6 points in each depth provides good estimates of bulk compositions. Moreover, compositional mapping by CS-XRF is appropriate to detect the heterogeneity at such length scales. The layering may be governed by modal variations. Determination of mineral compositions is necessary to investigate the change in modal variations. Nevertheless, mapping of the flat core surface by CS-XRF is a powerful tool to identify the presence of fine-scale layering that is difficult to detect by visual observation of the cores.

Paleomagnetism

Remanent magnetization

Measurements of magnetic remanence were made exclusively on discrete 20 mm × 20 mm × 20 mm cube samples taken from the working halves of cores from Hole GT1A because the onboard long-core cryogenic rock magnetometer malfunctioned. A total of 149 discrete samples were measured, of which ~25% were thermally demagnetized and all others were subjected to stepwise alternating field (AF) demagnetization to isolate the characteristic remanent magnetization (ChRM) direction.

Discrete sample remanence results

Natural remanent magnetization (NRM) intensity values range between 8.77×10^{-4} and 10.7 A/m. The lowest values occur in a sample taken from a cataclastic zone (32Z-2, 32–34 cm; 8.77×10^{-4} A/m) and an anorthositic sample (19Z-2, 18–20 cm; 8.15×10^{-3} A/m). Excluding these atypical samples, the lowest NRM intensity is 2.62×10^{-2} A/m (geometric mean of all discrete samples = 0.506 A/m). The vast majority of samples from Hole GT1A are olivine gabbros, and the downhole profile of NRM intensity does not exhibit any simple relationship with lithologic features such as olivine modal abundance (Fig. F85). However, the discrete sample measurements do not provide a continuous record of the magnetic behavior of the cores, and higher resolution measurements may reveal a closer relationship between core mineralogy and magnetic properties. Principal component analysis (PCA) of demagnetization data was used to identify three broad types of remanence components: Component A has a low coercivity or low unblocking temperature that was removed by 5–10 mT or 200°C demagnetization in several samples. A stable remanence (ChRM; Component C) that trends to the origin at the highest field and temperature steps was identified in all samples. An additional Component B with intermediate coercivity or unblocking temperature and a distinct orientation from the

ChRM was also distinguished in a number of samples.

All samples were nearly entirely demagnetized by 600°C with only minor changes in remanence occurring up to 475°C (Fig. F86A). Sharp decreases in remanence intensity occur at 510°–530°C and 550°–580°C. The relative importance of these two unblocking temperature ranges varies from sample to sample (Fig. F86). In a few samples, the remanence directions unblocked in these two temperature ranges are different from each other (Fig. F86A). The high unblocking temperature component was interpreted as the ChRM. Changes in magnetic susceptibility (MS) were observed after various steps during thermal demagnetization, indicating that thermal alteration of the magnetic minerals occurred over the course of the experiments (Fig. F86C). However, these changes were only significant at high temperatures (>475°C) and were not associated with abrupt changes in the remanence vector orientations, indicating that the changes resulting from heating during thermal demagnetization are not likely to have affected the directional paleomagnetic results.

AF demagnetization was also effective at removing nearly all remanence (Fig. F87). Several samples were subjected to a three-axis static AF demagnetization rather than tumbling AF demagnetization; however, this was found to result in acquisition of a spurious anhysteretic remanence at high peak AF fields and so was not subsequently used. The overall absence of large low-coercivity components suggests that the Hole GT1A cores are not significantly affected by drilling-induced overprints. The median destructive field (MDF) values range 11.1–54.4 mT (mean = 24.8 mT; Table T15). The highest MDF was found in a sample from a cataclastic shear zone (32Z-2, 32–34 cm), but several samples from background olivine gabbros also exhibit MDFs > 30 mT. In contrast to thermal demagnetization results, AF demagnetization often revealed continuous changes in remanence directions up to high fields (Fig. F87), suggesting the presence of multiple components with largely overlapping coercivity distributions.

AF demagnetization was also performed on shipboard physical properties samples that were taken next to those used for thermal demagnetization (see **Physical properties** in the Methods chapter), which included heating samples overnight at 105°C. The NRM direction and intensity of the samples after heating at 105°C are very close to the adjacent thermal demagnetization samples (Fig. F88). Thus, low-temperature laboratory heating did not significantly affect the magnetic mineralogy or remanence. In addition, overall similar demagnetization patterns were observed between the AF and thermal demagnetization results (Fig. F88), indicating that the ChRM directions determined by AF and thermal demagnetization results isolated the same remanence component.

Initial interpretation of remanence results

The distribution of inclinations in discrete samples is illustrated in Figure F89, which shows the downhole inclinations of the lowest, middle, and highest unblocking temperatures and coercivities together with NRM inclinations. The orientations of Component A are highly variable, showing both positive and negative inclinations, and are therefore not consistent with a modern-field overprint. Rather, this component may represent a minor drilling-induced overprint that is removed after the first demagnetization steps.

The ChRM vectors generally have shallow and negative inclinations (only 15 of 147 calculated positive inclinations) that are also uniformly shallow, as illustrated in Figure F90 (Component C). Component B was distinctly identified in 62 samples that have similar low-angle negative inclinations. Thus, the difference in orientation between the intermediate components and the stable remanence components lies principally in the horizontal plane. Mean inclinations were calculated using the Arason and Levi (2010) maximum likelihood method (Table T16). This results in a mean inclination for the highest unblocking component of –7.28° (k = 98.0; $\alpha 95$ = 1.18°; n = 147). These low inclinations are similar to the values reported from the outcrop investigations from previous studies (Weiler, 2000; Morris et al., 2016), which found positive inclinations after tilt correction. The entire ophiolite complex is considered to be tilted by ~20° to the south according to mapped field structures of the crust–mantle transition. Therefore, it is possible that some or all of the negative inclinations measured in the Hole GT1A samples would revert to shallow positive inclinations after tilt correction has been applied.

Magnetic susceptibility

Bulk magnetic susceptibility

Bulk MS values range between 24.76 × 10^{-6} and 59,038 × 10^{-6} SI (geometric mean = 2,514 × 10^{-6} SI; (Fig. F85; Table T17). The downhole profile of bulk MS is similar to that of NRM intensity, indicating that variation is controlled by the concentration of magnetic minerals rather than major differences in magnetic grain size and mineralogy.

The Königsberger ratio, Q, in Hole GT1A ranges 0.14–35 (geometric mean = 6.30). Although very few samples have $Q < 1$, nearly all samples exhibit values $Q > 1$ and most are 2.5–10 (Fig. F85; Table T15). These values are comparable to those reported in previous investigations of the Samail ophiolite (Luyendyk and Day, 1982). The values indicate that re-

manent magnetization is more important than induced magnetization in the magnetization of in situ rocks. In addition, there is a general downward trend of increasing Q values throughout the upper 200 m of Hole GT1A (Fig. F85), suggesting some change in either magnetic grain size or mineralogy. The range of Q is approximately constant throughout the lower 200 m of the hole.

Anisotropy of magnetic susceptibility

Anisotropy of magnetic susceptibility (AMS) determinations were performed on all discrete samples prior to stepwise demagnetization to characterize the shape-preferred orientations of magnetic minerals in the core samples (Fig. F91). Magnetic fabric shapes vary throughout the hole, ranging from strongly oblate (T = 0.95) to strongly prolate (T = –0.97). The samples above ~150 m tend to be oblate (average T = 0.10), whereas the samples below tend to be prolate (average T = –0.34) (Fig. F91A). However, nearly all magnetic fabrics are triaxial in character (Table T17; Fig. F91C).

K_{min} orientations are generally clustered near the core axes, whereas those of K_{max} are consistently shallow and define a near-horizontal magnetic foliation. K_{int} orientations are highly scattered (Fig. F92). K_{max} inclinations are typically <40°, which is approximately the same range of magmatic foliations observed (see Structural geology). K_{min} orientations do not exhibit any regular variation with depth except at ~100–200 m, where the K_{min} inclinations are consistently steep (Fig. F91A). A strong correlation exists between the degree of anisotropy, P_j, and bulk susceptibility (Fig. F91B). This relationship indicates that samples containing greater quantities of magnetic particles also tend to be more anisotropic, which may reflect a strong preferred orientation of secondary magnetite during growth in altered olivine grains (see Magnetic mineralogy).

ChRM directions were used to rotate the AMS fabric into a paleomagnetic reference frame. After this rotation, AMS fabrics for Hole GT1A display a good clustering of principal susceptibility directions when plotted on a stereoplot relative to a reference ChRM declination of 000. K_{min} directions cluster roughly around the core axis, whereas K_{max} directions are distributed across a girdle also oriented parallel to the core axis. K_{max} directions cluster around two subparallel axes, both shallowly dipping in opposite directions and oriented roughly normal to the reference ChRM vector direction and roughly parallel to the modal layering in the core (Fig. F93A). This result indicates that the angle between the principal susceptibility axes and the ChRM vector does not vary by a large amount throughout the hole. An exception to this is seen in the lower part of Hole GT1A, where one set of these K_{max} axes in the paleomagnetic reference frame displays a small but consistent change in declination deeper than ~250 m (Fig. F93B). These variations cannot be interpreted in terms of changes in either magnetic fabric orientations or magnetic remanence directions until absolute reorientation of each core has been performed.

Magnetic mineralogy

The high values of susceptibility and the dominance of unblocking temperatures near 580°C and coercivities <100 mT are consistent with nearly stoichiometric magnetite as the primary magnetic mineral in the Hole GT1A samples. The presence of lower unblocking temperatures may result from differences in the predominant grain size or from slight variations in magnetite composition such as cation substitution or solid solutions with other spinel group phases (Moskowitz et al., 1998). To better understand the carriers of magnetic remanence and susceptibility in the Hole GT1A samples, reflected light microscopy observations were made on a small number of representative thin sections. A small number of opaque particles were identified in several samples that contain primary oxide minerals, generally together with yellowish sulfides (probably pyrite) (Fig. F94A). The most notable oxide occurrences are in the mesh-textured networks of opaque material in altered olivine grains (Fig. F94B–F94F). Abundant bright phases in reflected light, which are likely magnetite or similar Fe oxides, often occur in long strings or bands (Fig. F94D) and vary between very fine isolated particles to larger oxide particles that may be aggregates of smaller grains. The broad range of observed oxide grain sizes is consistent with previous interpretations that the magnetization of the lower crustal section of the Samail ophiolite was pervasively overprinted by fluid-induced alteration that produced secondary magnetite with a range of coercivities that overlap those of the primary magnetic minerals (Feinberg, 1999; Morris et al., 2016).

Physical properties

Physical properties of gabbroic rocks from Hole GT1A were characterized through a series of measurements on whole-round sections, split halves, section-half pieces, and discrete samples (see Physical properties in the Methods chapter; Table T18). All whole-round sections were run through the X-ray computed tomography (XCT) scanner before splitting. We measured MS and natural gamma radiation (NGR) with the whole-round multisensor core logger (MSCL-W), point magnetic susceptibility (MSP) and reflectance spectroscopy and colorimetry (RSC) with the color spectroscopy logger (MSCL-C), thermal conductivity on section-half pieces, and compressional wave velocity, density, and porosity on discrete samples. The rock names reported in data ta-

bles correspond to the primary rock names assigned by the igneous petrology team (Tables T19, T20).

Whole-round and section-half measurements

A total of 547 core sections from Hole GT1A were measured. All data except for XCT measurements are summarized in Supplemental Tables ST2 and ST3 and Figure F95. MS and NGR were measured with the MSCL-W. Gamma ray attenuation (GRA) density was not measured for Hole GT1A cores.

X-ray computed tomography

XCT images were continuously logged for all whole-round core samples obtained from Hole GT1A. Figure F96 shows examples of XCT images from Sections 104Z-3 and 108Z-4. CT value is a function of the density and chemical composition of the sample in a voxel. Hence, data from plutonic rocks, such as gabbro, result from a combination of their mineral composition and porosity structure. Intact gabbro and veins tend to have CT values of ~3800. In Figure F96, altered zones, for example at 65–89 cm, show relatively low CT values (~3000) because of their more porous nature and the presence of low-density secondary minerals (e.g., serpentine, chlorite, and clay minerals). In contrast, epidote veins (e.g., 77 and 86 cm) show elevated CT values because of the high density of epidote (~3.4 g/cm^3).

Magnetic susceptibility

MS was measured on both the MSCL-W with an 80 mm loop sensor and the MSCL-C with a contact sensor probe for MSP.

MS is generally low (Fig. F95), reflecting the absence or low amount of magmatic oxides in the recovered rocks. Higher values generally correspond to the occurrence of secondary magnetite associated with serpentinization in olivine-rich intervals.

Natural gamma radiation

NGR is generally low (<1 count/s on average) in Hole GT1A cores except in a few sections where narrow intervals or veins display significantly higher counts (up to ~10 counts/s) (Fig. F95). This is similar to other gabbroic cores from International Ocean Discovery Program (IODP) expeditions (e.g., Expedition 360; MacLeod et al., 2017). Negative values were frequently recorded, probably because the background radiation noise was determined by taking measurements on a water-filled calibration core and the Oman Drilling Program gabbroic core has higher shielding ability than the water. More background radiation was detected through the water-filled calibration core than the Hole GT1A cores. This background was subtracted from the actual measurement during the calibration.

Reflectance spectroscopy and colorimetry

RSC data were obtained for 449 archive-half sections from Cores 1Z–130Z (Fig. F97). RSC and MSP were measured using the MSCL-C. Reflectance and chromaticity a*, b*, and L* range –5.75–5.5, –4.65–13.49, and 6.28–76.59, respectively. The "specular component included" (SCI) setting was used for measurement of Hole GT1A cores. This setting provides data that are closer to the actual color than that of the "specular component excluded" (SCE) setting (see Physical properties in the Methods chapter). Figure F98 is an example of how reflectance and chromaticity values change as a function of lithology in a core section.

Discrete sample measurements

Density and porosity

Bulk density, grain density, and porosity were calculated from measurements on 137 cubic (2 cm × 2 cm × 2 cm) and 3 irregular-shape samples taken from the working-half sections of Hole GT1A (Table T19; Figs. F99, F100, F101). Average bulk and grain densities of cube samples are 2.93 and 2.94 g/cm^3, respectively, with bulk density values ranging 2.61–3.19 g/cm^3 and grain density values ranging 2.75–3.19 g/cm^3. Porosity of cube samples is generally very low, ranging 0.04%–4.2% (mean = 0.7%). There is a systematic bias in our measurements toward less porous material in Hole GT1A because cube samples were taken from relatively homogeneous intervals with no cracks or veins. Three irregular-shape samples were taken from damaged serpentine-rich intervals to measure their density and porosity (Table T19). Those three samples show high porosity (7.9%) and low density (2.68 and 2.83 g/cm^3 for bulk and grain densities, respectively).

Bulk density of Hole GT1A gabbroic samples roughly correlates with porosity; lower densities correspond to higher porosities (Fig. F100B). Grain density is not correlated to olivine mode (Fig. F100D).

P-wave velocity

P-wave velocity was measured on 137 cube samples along the three principal directions *x*, *y*, and *z* in the core reference frame. Results are listed in Table T19 and plotted in Figures F99, F100, and F101. *P*-wave velocity ranges 5.2–7.3 km/s (average = 6.8 km/s). The apparent anisotropy varies at 0%–14% but is generally low (mean = 3.5%). As detailed in Physical properties in the Methods chapter, the precision of our V_P measurements is on the order of 1.5%. Hence, the lowest measured apparent anisotropies should be treated with caution.

Results for Hole GT1A samples are plotted in Figure F101 and include V_P and density measurements made during Integrated Ocean Drilling Program Expeditions 304, 305, and 345 and IODP Expedition

360 on gabbroic and troctolitic samples from slow-spreading oceanic crust at Atlantis Bank and Atlantis Massif and from fast-spreading crust at Hess Deep. V_P values from Hole GT1A are consistent with previous measurements on gabbroic rocks at Atlantis Bank and Hess Deep; they show a relatively well defined trend of decreasing densities with decreasing velocity. V_P measurements made on board the R/V *JOIDES Resolution* over time vary notably for Atlantis Bank (Southwest Indian Ridge), Hess Deep (East Pacific Rise), and Atlantis Massif (Mid-Atlantic Ridge). The latter seems to be characterized by significantly lower velocities.

Measured velocities at room pressure show a well-defined inverse correlation with porosity (Fig. **F100A**). There is no obvious relationship between sample V_P and background alteration or olivine mode (Fig. **F100C**). Because the propagation of acoustic waves is primarily controlled by porosity, the measured velocities and apparent anisotropies cannot be simply related to mineral modes and crystallographic-preferred orientations.

Thermal conductivity

A total of 63 measurements were taken on 54 core pieces from Hole GT1A, mostly from the working halves (Table **T20**; Fig. **F102**). Thermal conductivity ranges 1.7–3.4 W/m·K, and the standard deviation of the average of 6–12 measurements for each piece ranges 0.02–0.14 W/m·K. Thermal conductivities are noticeably lower in the upper 100 m, probably due to weathering and higher proportions of clay minerals (Fig. **F102**). Anorthositic gabbro has the lowest thermal conductivity (1.70 W/m·K), and disseminated oxide olivine melagabbro shows the highest value (3.41 W/m·K). The average thermal conductivity is 2.58 W/m·K. No clear relationship is evident between (primary) olivine mode and thermal conductivity, although olivine melagabbro (olivine > 50 vol%) shows higher thermal conductivities (mean = 3.08 W/m·K; Fig. **F103**). The range of measured values is wider than that of gabbroic cores from Expeditions 304/305, 345, and 360 (Blackman et al., 2006; Gillis et al., 2014; MacLeod et al., 2017).

Imaging spectroscopy

All sections from Hole GT1A were imaged on board *Chikyu* during Leg 2. In total, 556 sets of images (visible and near-infrared [VNIR] + short-wave infrared [SWIR]) were acquired, comprising 3.7 TB of data over 7 days. Fifteen SWIR images of key core sections were selected in consultation with the alteration description team and processed with reflectance on board, and preliminary mineral maps were generated (Table **T21**). The remainder of the images will be processed and more robust mineral maps will be generated at the California Institute of Technology (Caltech, USA) after the completion of analyses on *Chikyu*. The figures in this section show the high data quality and the ability to discriminate key mineralogies with this imaging spectroscopy data set. Minerals identified through a quick examination of these 15 images include chlorite, epidote, zeolites, prehnite, amphibole, pyroxene (augite and/or diopside), gypsum, serpentine, and phyllosilicates (e.g., Clark et al., 1990). Other minerals are likely to be identified through more extensive analysis of the full Hole GT1A imaging spectroscopy data set.

Figure **F104** shows the upper portion of Section 111Z-1, which contains large epidote veins. The portion of the sample in this image contains epidote-bearing zones with some of the amphibole-bearing matrix remaining. Also visible is an offset prehnite-bearing vein. The offset is easier to see with the imaging spectroscopy data than through standard visual examination of the core. Section 133Z-2 in Figure **F105** contains hydrothermal breccia and a variety of minerals. Epidote-rich zones occur near the upper portion of the section, and amphibole, prehnite, and zeolite occur in the lower portion. One gypsum vein cuts across the full core. Similar analyses will be completed for the full core over the next year.

Downhole measurements

Downhole logging and hydrogeological testing operations and acquisition parameters for each borehole are available in Table **T56** and **T57** in the Methods chapter. Raw and processed data from all downhole logs are available in **Supplementary material** > **L_Wireline logging** and in the ICDP Oman Drilling Project online data repository.

References

Abers, G.A., and Hacker, B.R., 2016. A MATLAB toolbox and Excel workbook for calculating the densities, seismic wave speeds, and major element composition of minerals and rocks at pressure and temperature. Geochemistry, Geophysics, Geosystems, 17:616–624. doi: https://doi.org/10.1002/2015GC006171

Adachi, Y., and Miyashita, S., 2003. Geology and petrology of the plutonic complexes in the Wadi Fizh area: multiple magmatic events and segment structure in the northern Oman ophiolite. Geochemistry, Geophysics, Geosystems, 4(9):8619. doi:10.1029/2001GC000272

Alabaster, T., Pearce, J.A., and Malpas, J., 1982. The volcanic stratigraphy and petrogenesis of the Oman ophiolite complex. Contributions to Mineralogy and Petrology, 81:168–183. doi: 10.1007/BF00371294

Alt, J.C., 1995. Subseafloor processes in mid-ocean-ridge hydrothermal systems. In Humphris, S.E., Zierenberg,

R.A., Mullineaux, L.S., and Thomson, R.E. (Eds.), Geophysical Monograph, 91.

Alt, J.C., Laverne, C., Coggon, R.M., Teagle, D.A.H., Banerjee, N.R., Morgan, S., Smith-Duque, C.E., Harris, M., and Galli, L., 2010. Subsurface structure of a submarine hydrothermal system in ocean crust formed at the East Pacific Rise, ODP/IODP Site 1256. Geochemistry, Geophysics, Geosystems, 11(10):Q10010. https://doi.org/10.1029/2010GC003144

Arason, P., and Levi, S., 2010. Maximum likelihood solution for inclination-only data in paleomagnetism. Geophysical Journal International, 182:753–771. https://doi.org/10.1111/j.1365-246X.2010.04671.x

Blackman, D.K., Ildefonse, B., John, B.E., Ohara, Y., Miller, D.J., MacLeod, C.J., and the Expedition 304/305 Scientists, 2006. Proceedings of the Integrated Ocean Drilling Program, 304/305: College Station TX (Integrated Ocean Drilling Program Management International, Inc.). https://doi.org/10.2204/iodp.proc.304305.2006

Clark, R.N., King, T.V.V., Klejwa, M., Swayze, G.A., and Vergo, N., 1990. High spectral resolution reflectance spectroscopy of minerals. Journal of Geophysical Research, 95:12653–12680.

Coogan, L.A., Howard, K.A., Gillis, K.M., Bickle, M.J., Chapman, H., Boyce, A.J., Jenkin, G.R.T., Wilson, R.N., 2006. Chemical and thermal constraints on focussed fluid flow in the lower oceanic crust. Am. J. Sci., 306:389–427. doi:10.2475/06.2006.01

Einaudi, F., Godard, M., Pezard, P., Cocheme, J.-J., Brewer, T., Harvey, P., and Coulon, C., 2003. Magmatic cycles and formation of the upper oceanic crust at spreading centers: Geochemical study of a continuous extrusive section in the Oman ophiolite. Geochemistry Geophysics Geosystems, 4(6):8608. doi:10.1029/2002GC000362

Feinberg, H., Horen, H., Michard, A., and Saddiqi, O., 1999. Obduction-related remagnetization at the base of an ophiolite: paleomagnetism of the Samail nappe lower sequence and of its continental substratum, southeast Oman Mountains. Journal of Geophysical Research: Solid Earth, 104(B8):17703–17714.

Gillis, K.M., Snow, J.E., Klaus, A., Abe, N., Adrião, Á., Akizawa, N., Ceuleneer, G., et al., 2014a. Primitive layered gabbros from fast-spreading lower oceanic crust. Nature, 505.7482:204. doi:10.1038/nature12778

Gillis, K.M., Snow, J.E., Klaus, A., and the Expedition 345 Scientists, 2014b. Proceedings of the Integrated Ocean Drilling Program, 345: College Station, TX (Integrated Ocean Drilling Program). https://doi.org/10.2204/iodp.proc.345.2014

Gillis, K.M., Snow, J.E., Klaus, A., Guerin, G., Abe, N., Akizawa, N., Ceuleneer, G., et al., 2014c. Hole U1415J. In Gillis, K.M., Snow, J.E., Klaus, A., and the Expedition 345 Scientists, Proc. IODP, 345: College Station, TX (Integrated Ocean Drilling Program). doi:10.2204/iodp.proc.345.110.2014

Godard, M., Bosch, D., and Einaudi, F., 2006. A MORB source for low-Ti magmatism in the Semail ophiolite: Chemical Geology, 234:58–78. doi:10.1016/j.chemgeo.2006.04.005

Godard, M., Dautria, J.M., and Perrin, M., 2003. Geochemical variability of the Oman ophiolite lavas: Relationship with spatial distribution and paleomagnetic directions. Geochemistry Geophysics Geosystems, 4(6):8609. doi:10.1029/2002GC000452

Grant, J.A., 1986. The isocon diagram; a simple solution to Gresens' equation for metasomatic alteration. Economic Geology, 81(8):1976-1982.

Hoffmann, A.W., 1988. Chemical differentiation of the Earth: the relationship between mantle, continental crust, and oceanic crust. Earth and Planetary Science Letters, 90:297-314. doi:10.1016/0012-821X(88)90132-X

Kusano, Y., Adachi, Y., Miyashita, S. and Umino, S., 2012. Lava accretion system around mid-ocean ridges: volcanic stratigraphy in the Wadi Fizh area, northern Oman ophiolite. Geochemistry, Geophysics, Geosystems, 13:Q05012. doi:10.1029/2011GC004006

Kusano, Y., Umino, S., Shinjo, R., Ikei, A., Adachi, Y., Miyashita, S., and Arai, S., 2017. Contribution of slab-derived fluid and sedimentary melt in the incipient arc magmas with development of the paleo-arc in the Oman Ophiolite. Chemical Geology, 449:206–225. doi.org/10.1016/j.chemgeo.2016.12.012

Leuthold, J., Blundy, J.D., Holness, M.B., Sides, R., 2014. Successive episodes of reactive liquid flow through a layered intrusion (Unit 9, Rum Eastern Layered Intrusion, Scotland). Contributions to Mineralogy and Petrology, 168(1):1021.

Lippard, S.J., Shelton, A.W., and Gass, I.G., 1986. The ophiolite of northern Oman. Geological Society of London Memoir, 11:178.

Luyendyk, B.P., and Day, R., 1982. Paleomagnetism of the Samail ophiolite, Oman: 2. The Wadi Kadir gabbro section. Journal of Geophysical Research: Solid Earth, 87(B13):10903–10917.

MacLeod, C.J., Dick, H.J.B., Blum, P., and the Expedition 360 Scientists, 2017. Southwest Indian Ridge Lower Crust and Moho. Proceedings of the International Ocean Discovery Program, 360: College Station, TX (International Ocean Discovery Program). https://doi.org/10.14379/iodp.proc.360.2017

MacLeod, C.J., Lissenberg, C.J., and Bibby, L.E., 2013. 'Moist MORB' axial magmatism in the Oman ophiolite: evidence against a mid-ocean ridge origin. Geology, 41:459-462.

Mathison, C.I., 1987. Pyroxene oikocrysts in troctolitic cumulates—evidence for supercooled crystallisation and postcumulus modification. Contributions to Mineralogy and Petrology, 97(2):228-236.

Miyashita, S., Adachi, Y., and Umino, S., 2003. Along-axis magmatic system in the northern Oman ophiolite: Implications of compositional variation of the sheeted dike complex. Geochemistry Geophysics, Geosystems, 4. doi:10.1029/2001GC000235

Morris, A., Meyer, M., Anderson, M.W., and MacLeod, C.J., 2016. Clockwise rotation of the entire Oman ophiolite occurred in a suprasubduction zone setting. Geology, 44(12):1055–1058.

Moskowitz, B.M., Jackson, M., and Kissel, C., 1998. Low-temperature magnetic behavior of titanomagnetites. Earth and Planetary Science Letters, 157(3):141–149.

Pallister, J.S., 1984. Parent magmas of the Semail ophiolite, Oman. In Gass, I.G., et al. (Ed.), Ophiolites and Oceanic Lithosphere: Geological Society Special Publication, 13:63–70.

Pallister, J.S., Hopson, C.A., 1981. Samail Ophiolite plutonic suite: Field relations, phase variation, cryptic variation and layering, and a model of a spreading ridge magma chamber. Journal of Geophysical Research, 86:2593–2644.

Peters, T., El Amin, O., Blechschmid, I., Al-Busaidi, S., 2008. Geological Map Oman 1:50000, Sheet NF 40-8A1. Sultanate of Oman: Ministry of Commerce and Industry.

Seyfried, W.E., Jr., Ding, K., Berndt, M.E., 1991. Phase equilibria constraints on the chemistry of hot spring fluids at mid-ocean ridges, Geochim. Cosmochim. Acta, 55(12):3559-3580. https://doi.org/10.1016/0016-7037(91)90056-B

Umino, S., Miyashita, S., Hotta, F., and Adachi, Y., 2003. Along-strike variation of the sheeted dike complex in the Oman Ophiolite: insights into subaxial ridge segment structures and the magma plumbing system. Geochemistry Geophysics, Geosystems, 4(3):8618. doi:10.1029/2001GC000233.

Weiler, P.D., 2000. Differential rotations in the Oman ophiolite: paleomagnetic evidence from the southern massifs. Marine Geophysical Researches, 21(3–4):195–210.

Zihlmann, B., Müller, S., Coggon, R.M., Koepke, J., Garbe-Schönberg, D, and Teagle, D.A.H., 2018. Hydrothermal fault zones in the lower oceanic crust: An example from Wadi Gideah, Samail ophiolite, Oman. Lithos, 323:103-124. doi:10.1016/j.lithos.2018.09.008

Figure F1. Geological map of the southern end of the Muscat–Ibra transect showing the locations of Oman Drilling Project Sites GT1 and GT2 (modified from Peters et al., 2008).

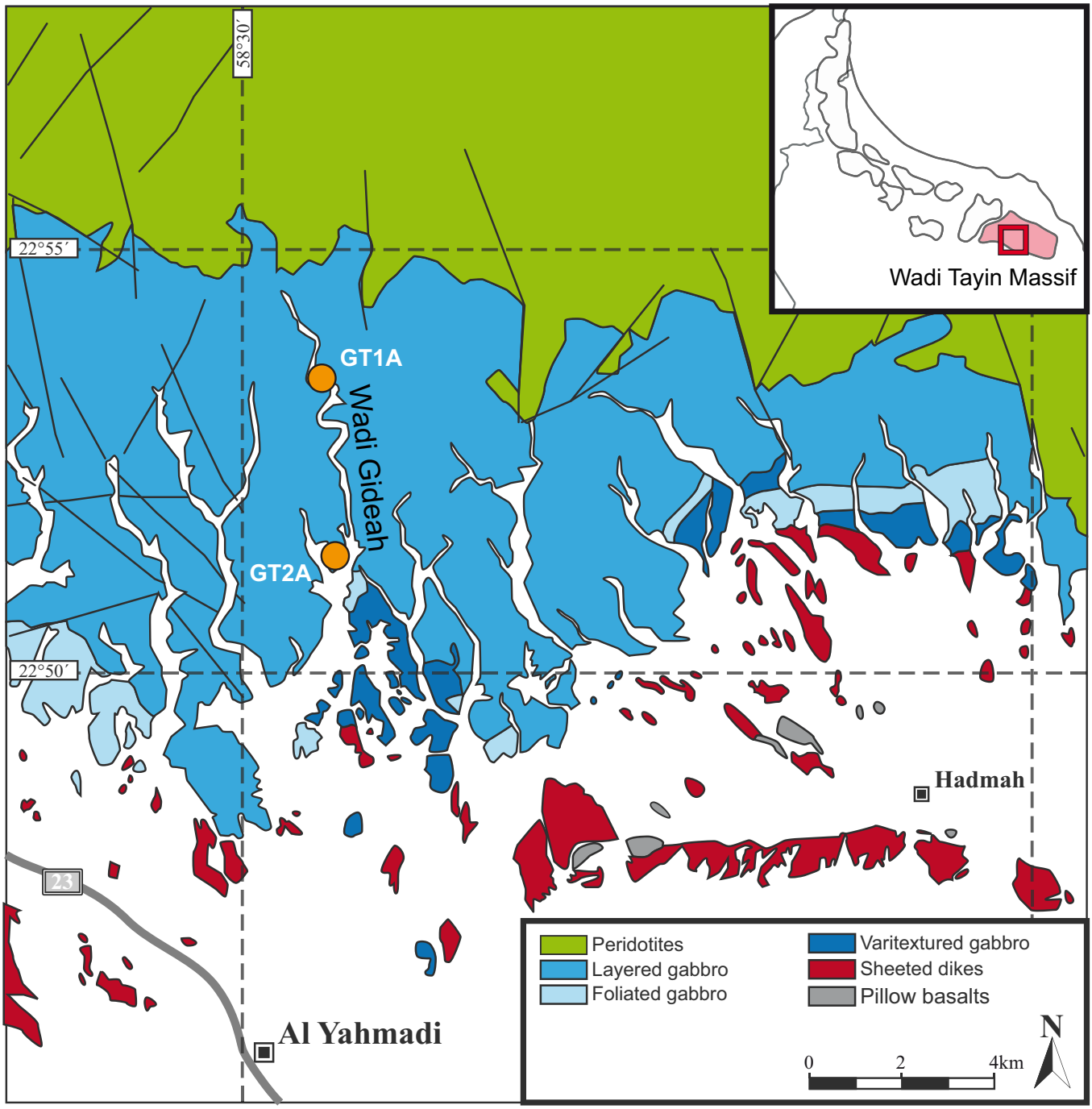

Figure F2. Close-up geological map of the gabbro sequence in the Wadi Gideah region showing the locations of Holes GT1A and GT2A, hydrothermal fault zones, and magmatic layering (after Zihlmann et al., 2018).

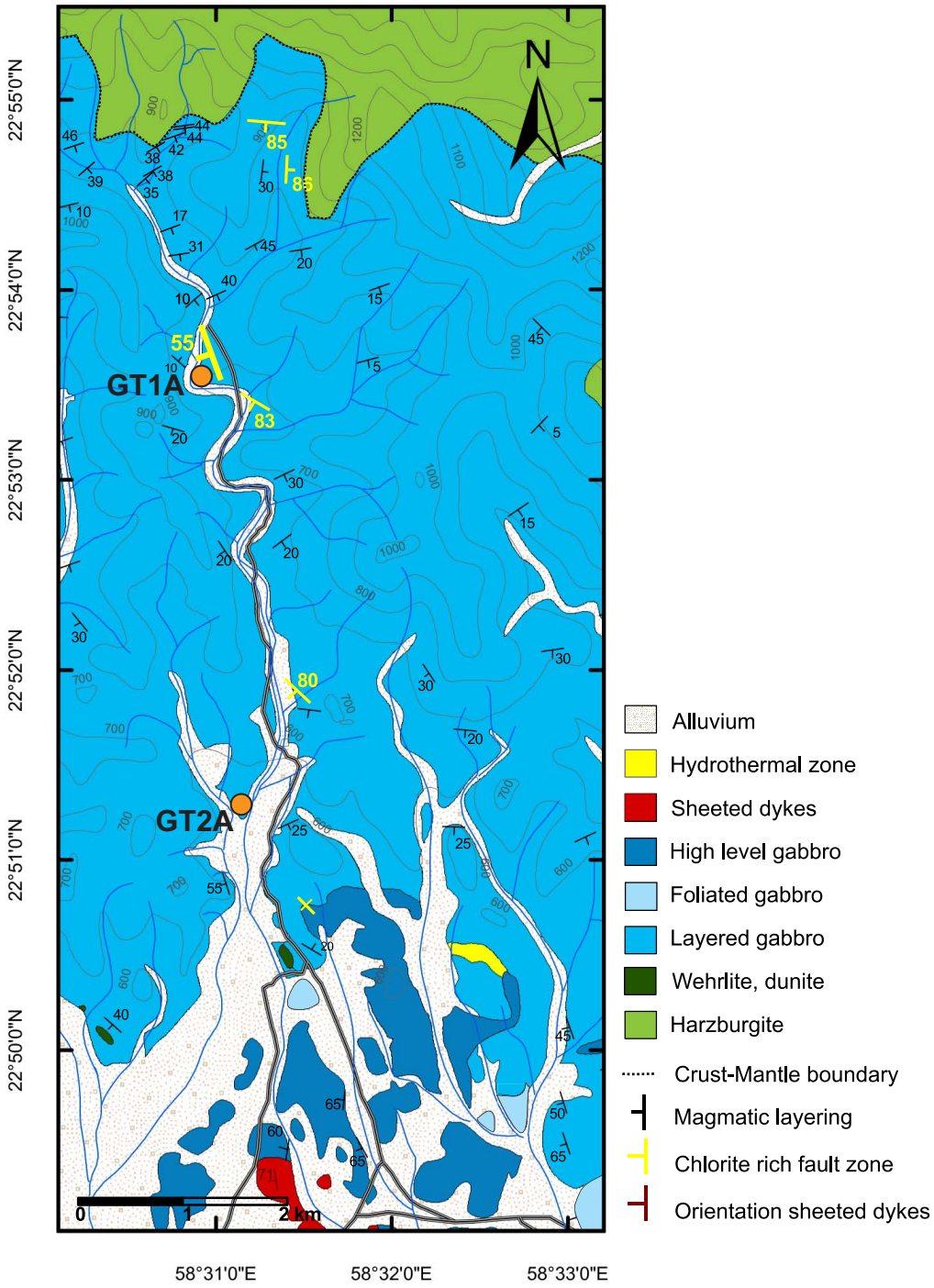

Figure F3. A. Topographic map of the area surrounding Site GT1 displaying magmatic fabrics and the locations of several fault NW-SE–trending minor fault zones (data from Zihlmann et al., 2018). **B.** Aerial photograph of the Site GT1 surroundings.

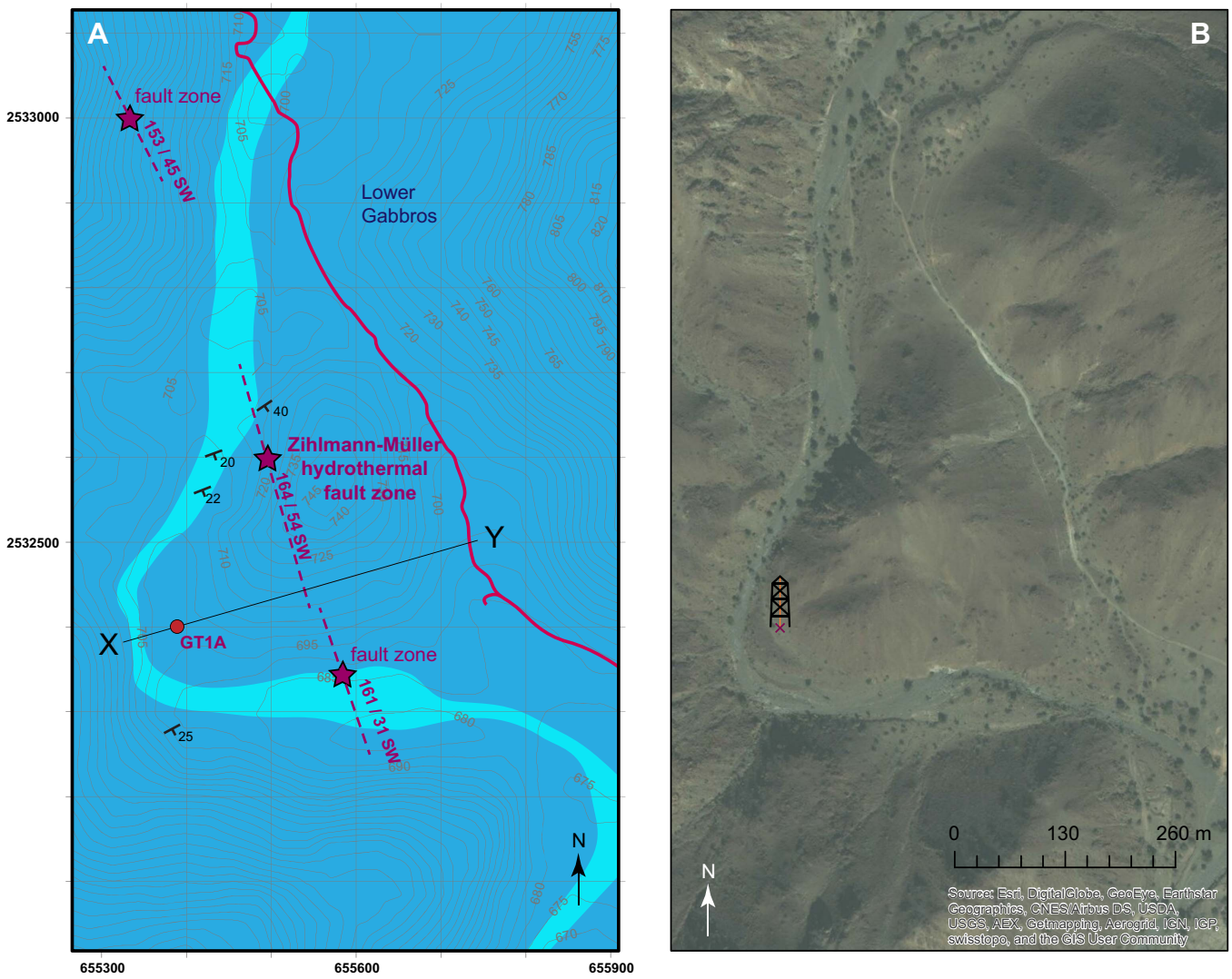

Figure F4. Photograph of two gullies that occur ~300 m north of Site GT1 (22.89226°N, 58.51506°E). The black steeply dipping line highlighted in the white box is fault gouge that is shown in great detail in Figure F5.

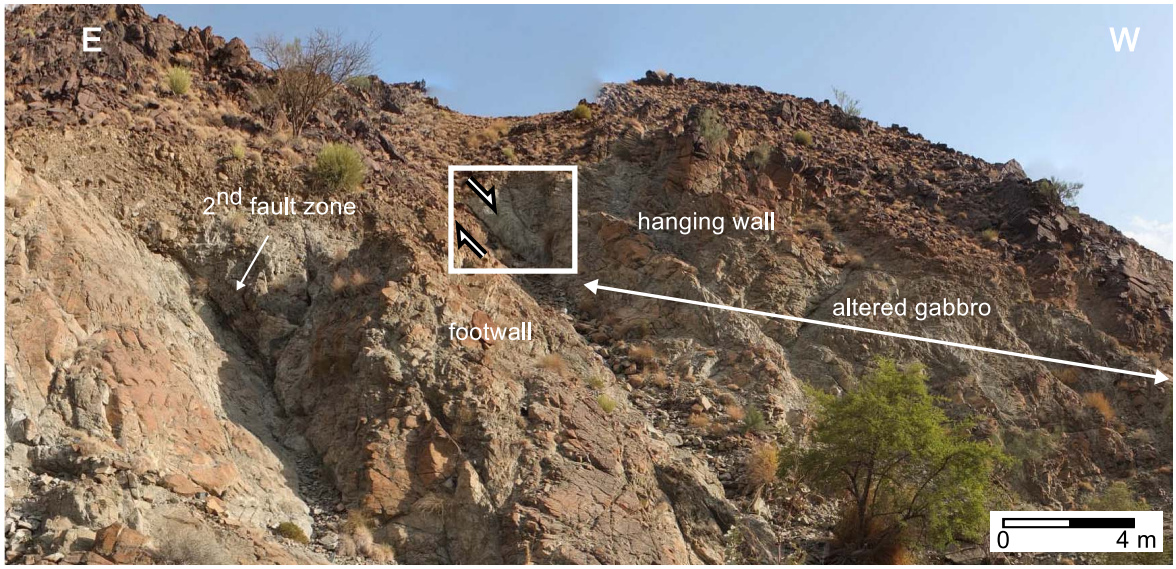

Figure F5. Close-up composite photograph (from Zihlmann et al., 2018) of the Zihlmann-Müller fault zone (22.894210°N, 58.515712°E) showing deformed elongate clasts of altered gabbro within a sheared chlorite gouge. Chlorite-rich fault-parallel platy fabric has developed along 5–10 cm thick wall rock selvages. Within the chlorite gouge are rare lozenges of altered sulfides, some copper-bearing, as evidenced by malachite staining (see Zihlmann et al., 2018).

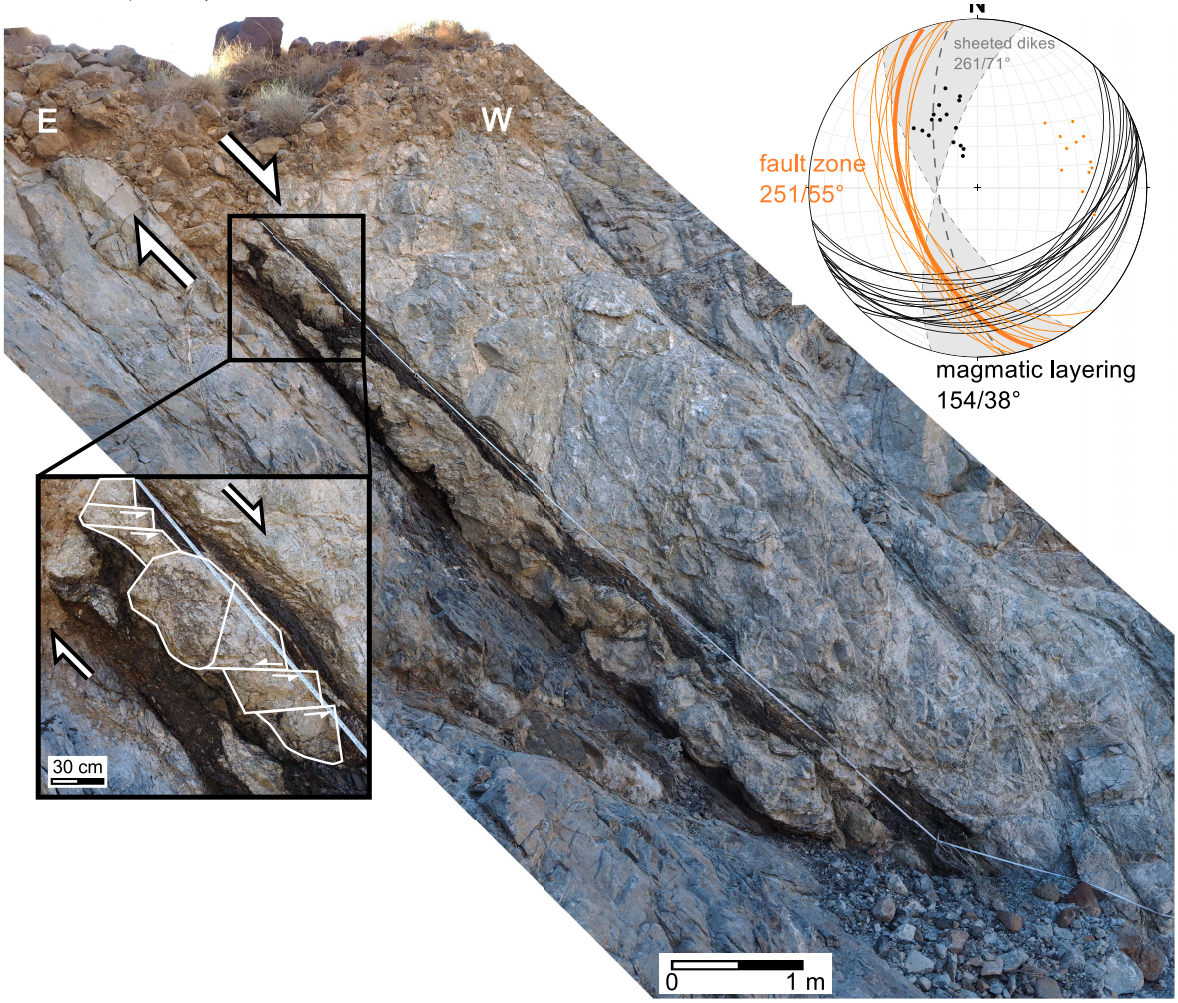

Figure F6. Photographs showing limited outcrops of layered gabbros in Wadi Gideah around Site GT1. **A.** Hole GT1A during drilling. **B.** Hole GT1A drill pad predrilling, with outcrops to south side of wadi. **C.** View toward Zihlmann-Müller Fault Zone from southwest. **D, E.** Layered gabbros in Wadi Gideah, downstream of Site GT1.

Figure F7. Photograph of carbonated gabbros and overlying carbonate-cemented polymict boulders cropping out in Wadi Giddeah along strike from the Zihlmann-Müller Fault Zone.

Figure F8. Predicted cross-section of the intersection of the proposed Site GT1 vertical borehole with the Zihlmann-Müller Fault Zone.

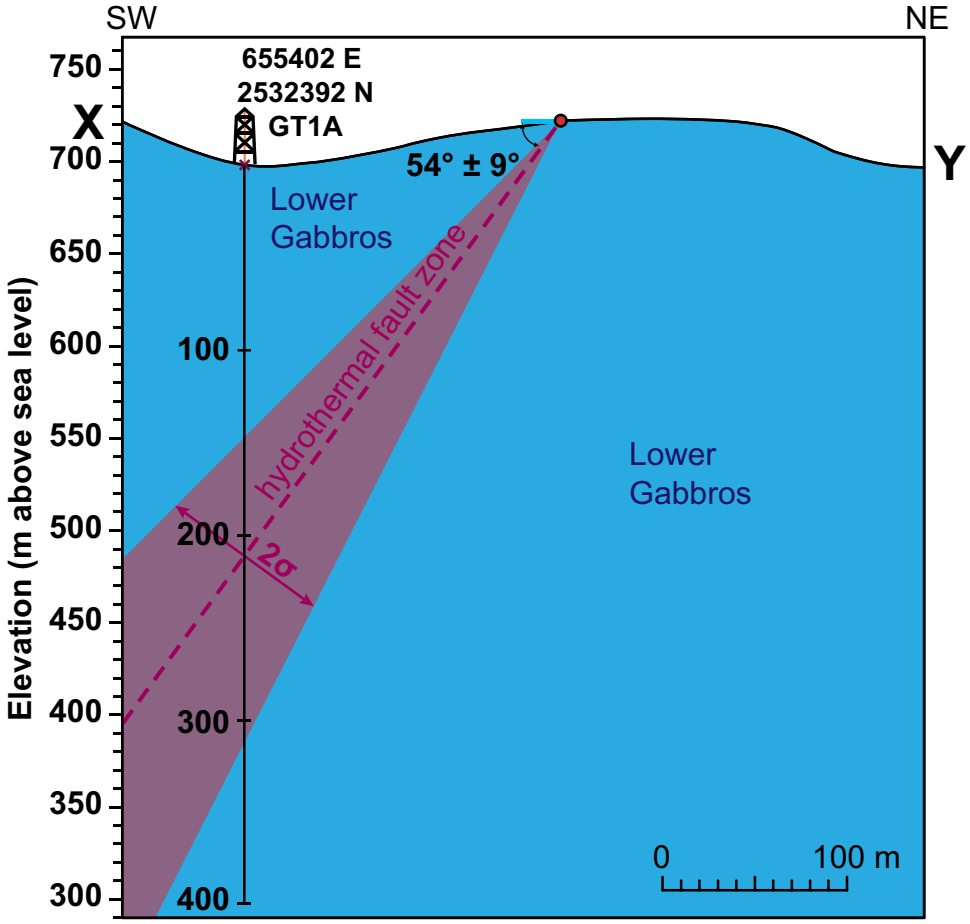

Figure F9. Diagram showing deviation during drilling and casing of Hole GT1A.

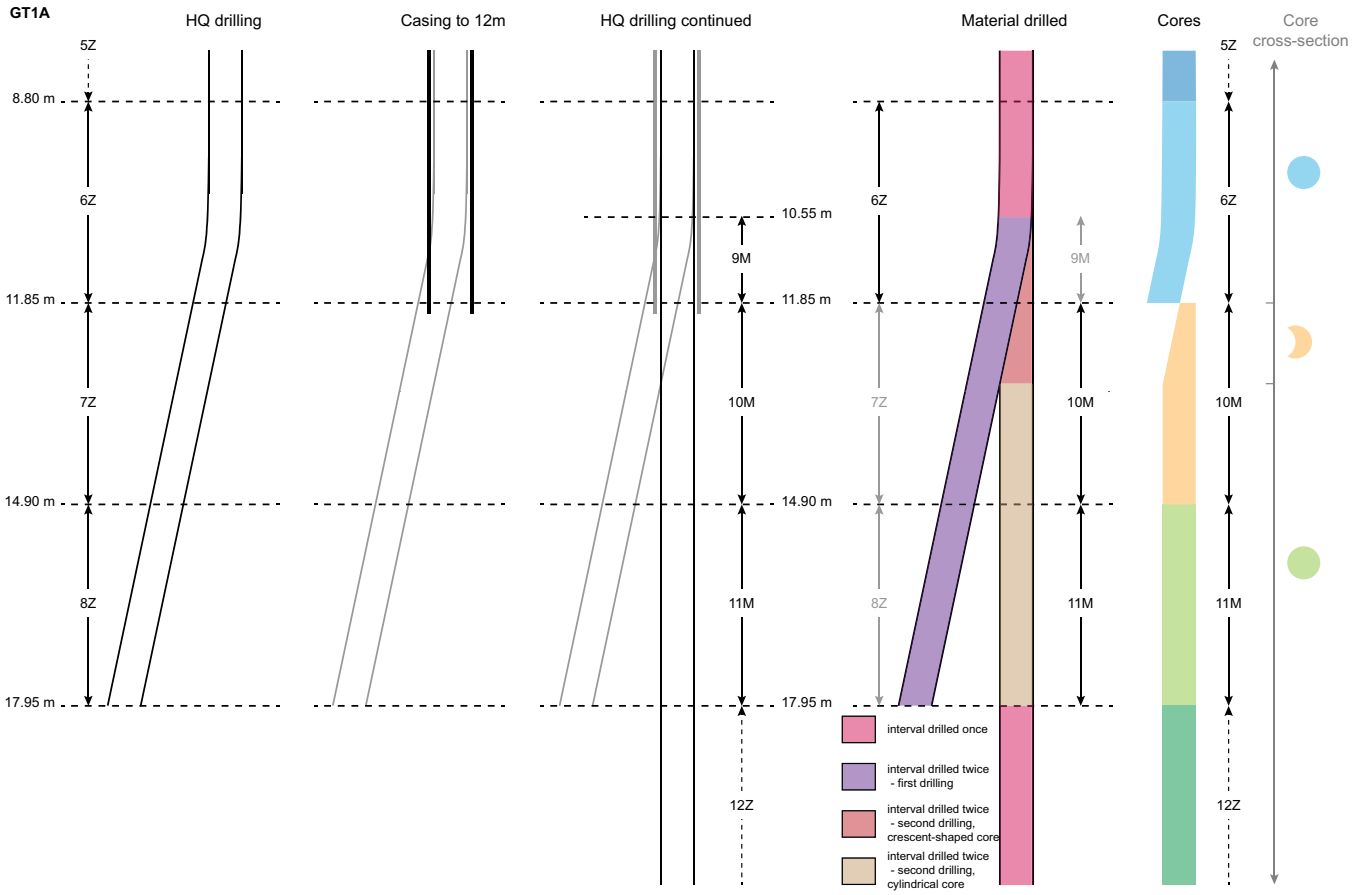

Figure F10. Lithologic variations and Igneous Units I–VII in Hole GT1A. The lengths of the bars do not have specific meanings but are used for better visualization. CAD = Chikyu adjusted depth.

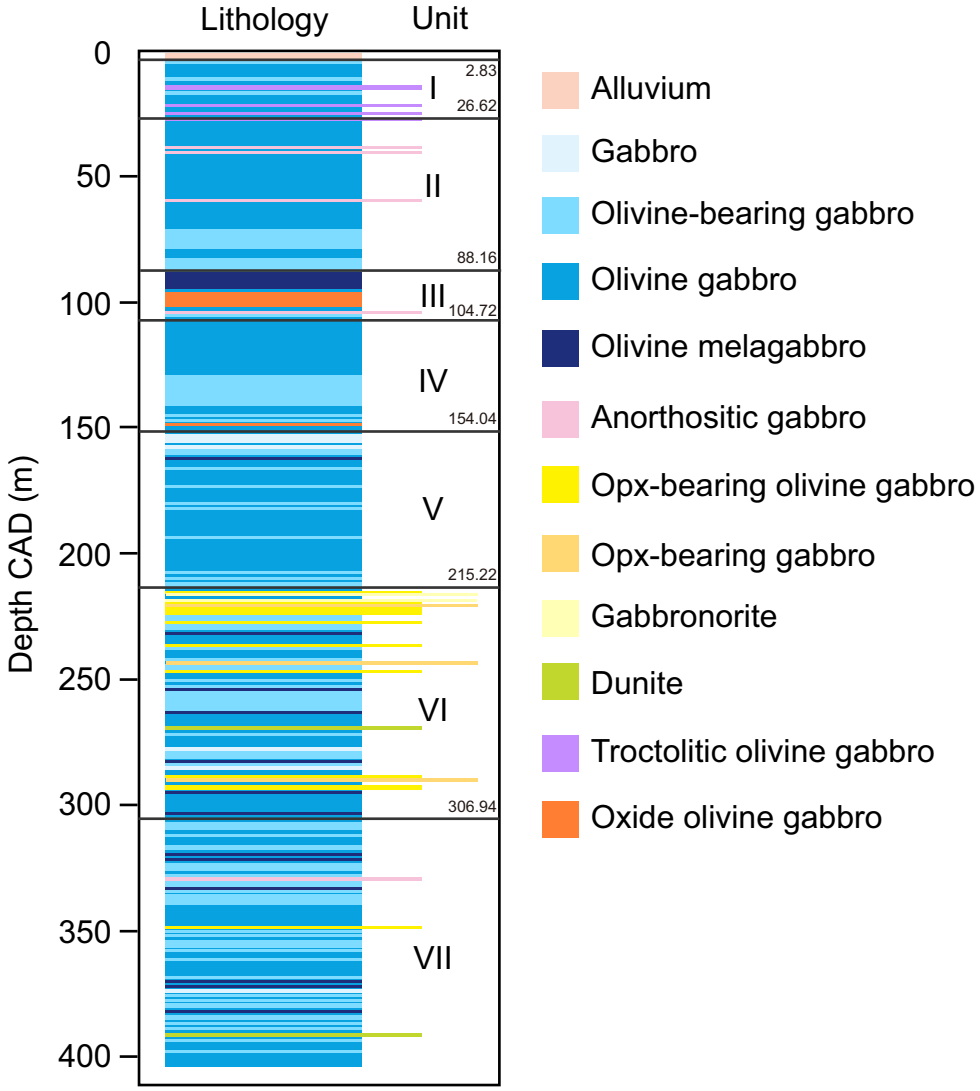

Figure F11. Pie chart of lithologic proportions for Hole GT1A.

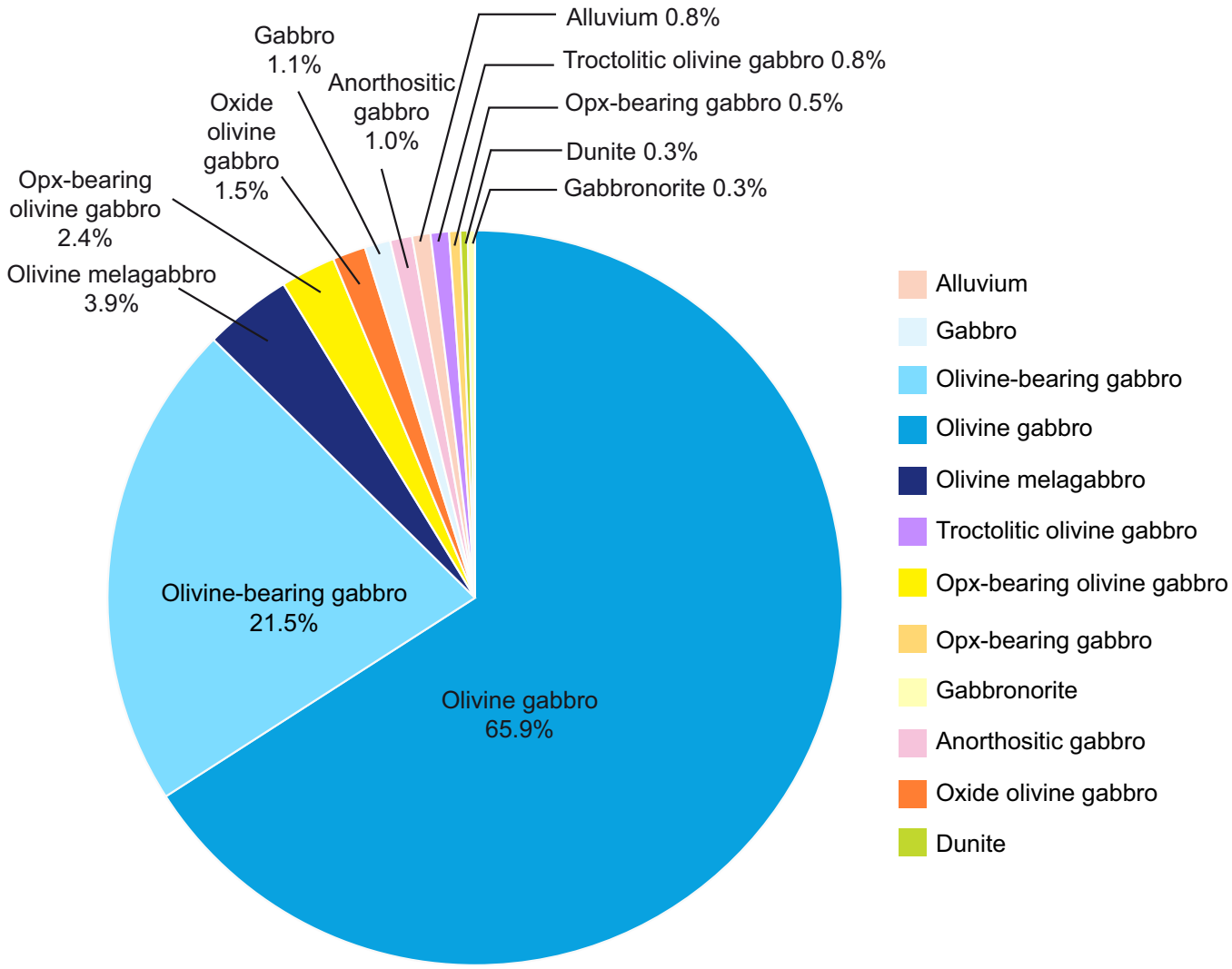

Figure F12. Mineral mode variations with depth, Hole GT1A. Solid and broken lines show the average modal compositions per 10 m long interval.

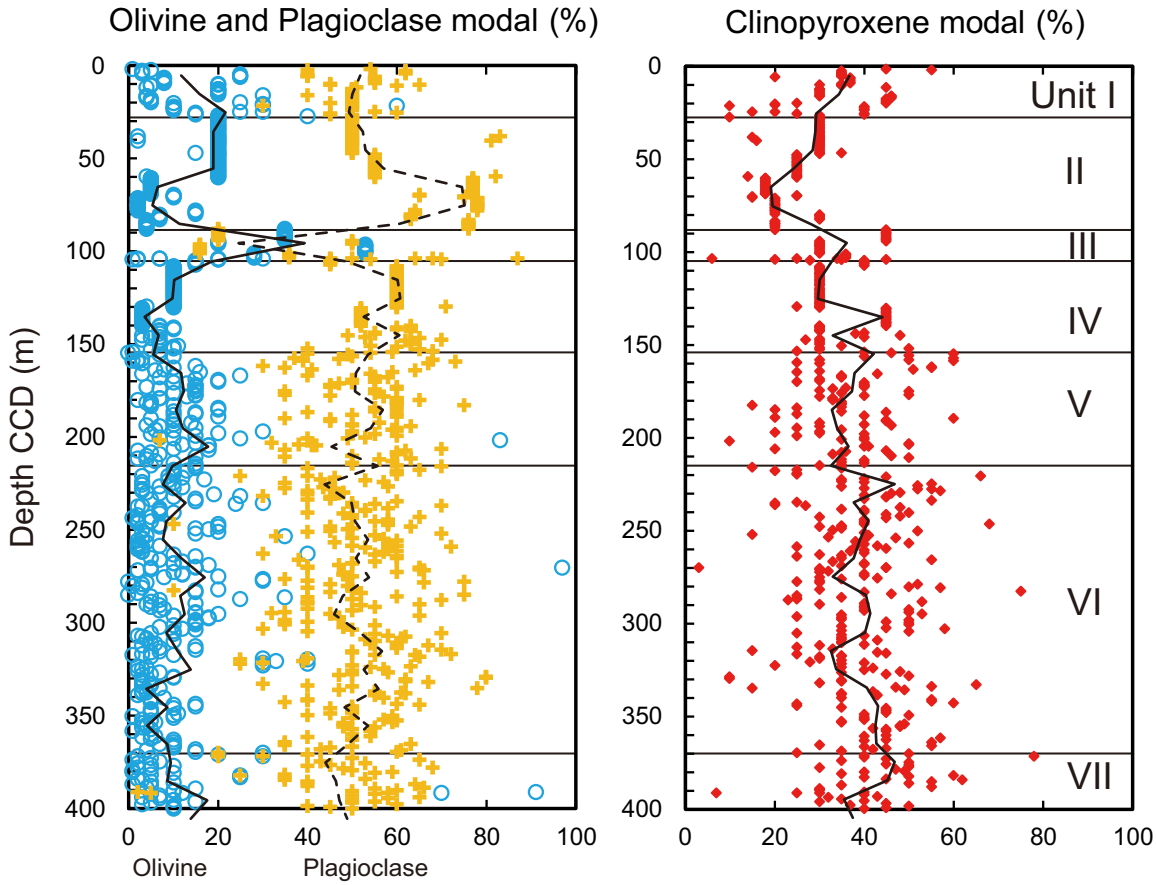

Figure F13. Examples of the variety of contacts observed in Hole GT1A. **A.** Sharp planar and curved modal contacts. **B.** Gradational planar modal contact. **C.** Sheared planar contact. **D.** Sharp irregular modal contact.

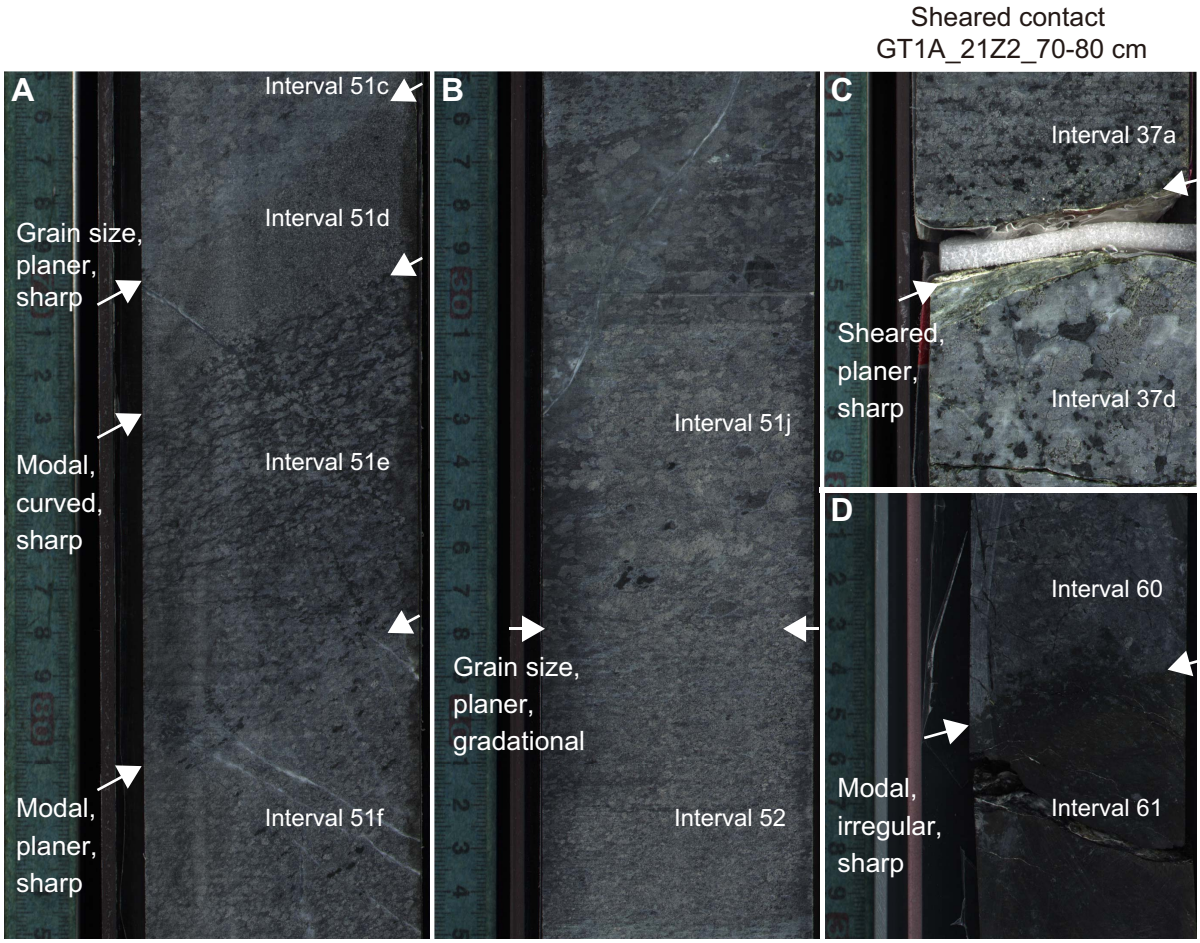

Igneous contact
GT1A_45Z1_65-85 cm

Igneous contact: grain size
GT1A_53Z4_25-45 cm

Intrusive contact
GT1A_107Z3_20-30 cm

Figure F14. Grain sizes of olivine, plagioclase, and clinopyroxene with depth, Hole GT1A. Circles, crosses, and diamonds = maximum lengths; solid lines = modal lengths.

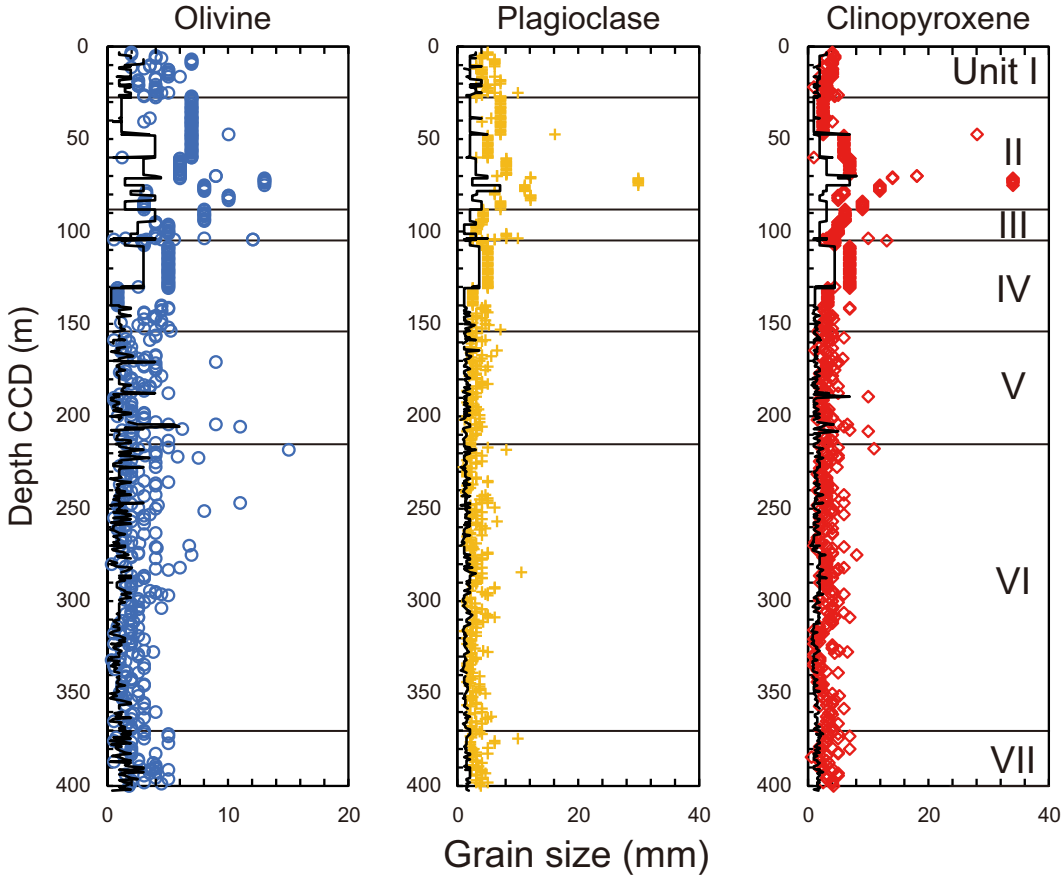

Figure F15. Correlation of grain sizes between plagioclase (Pl) and clinopyroxene (Cpx) and olivine (Ol) in all rocks, Hole GT1A. Linear regression lines and R^2 are shown. There is a positive correlation between olivine and orthopyroxene, but the correlation between maximum lengths of plagioclase and clinopyroxene are weak.

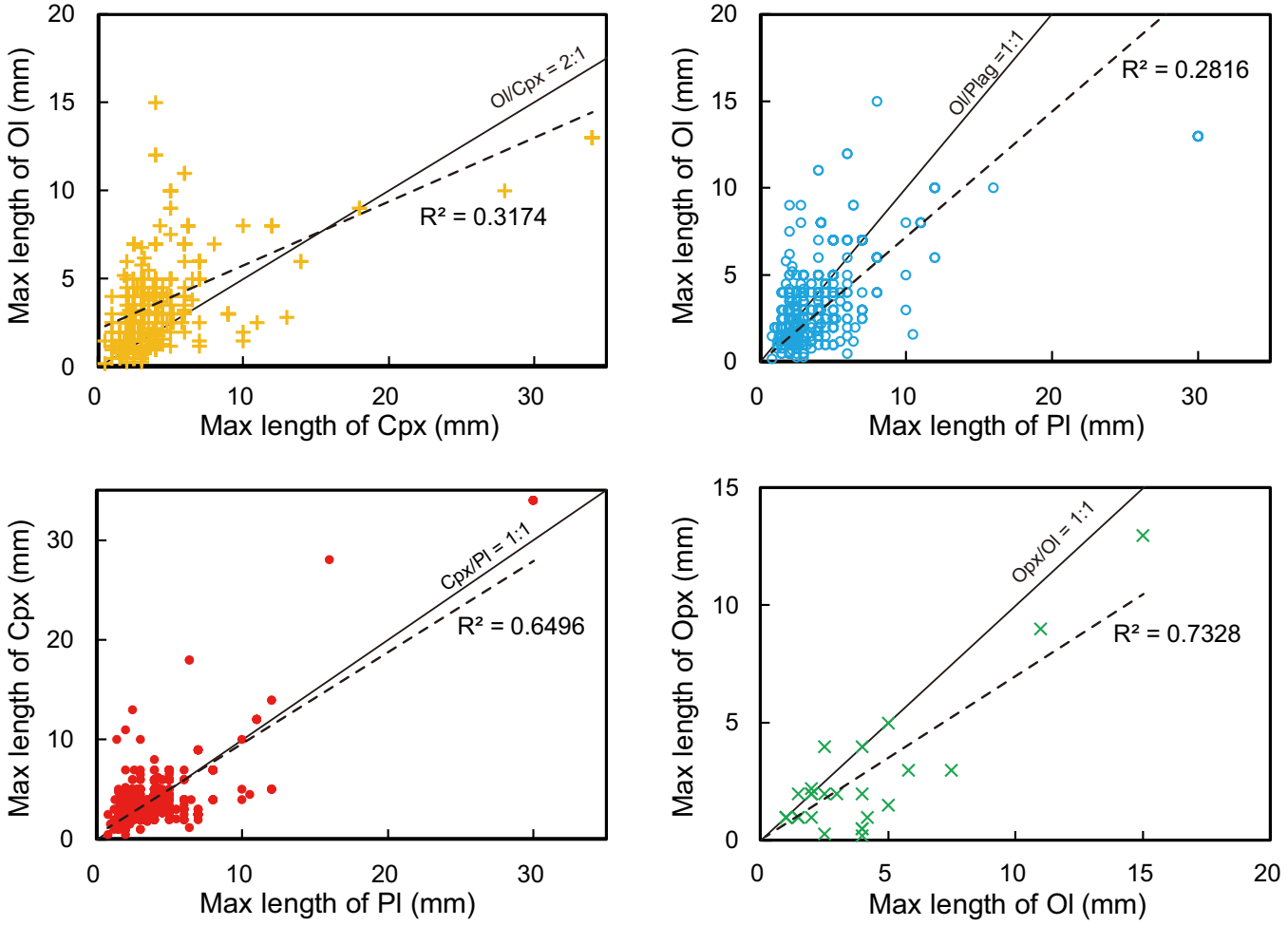

Figure F16. Ophitic and poikilitic textures, Hole GT1A.

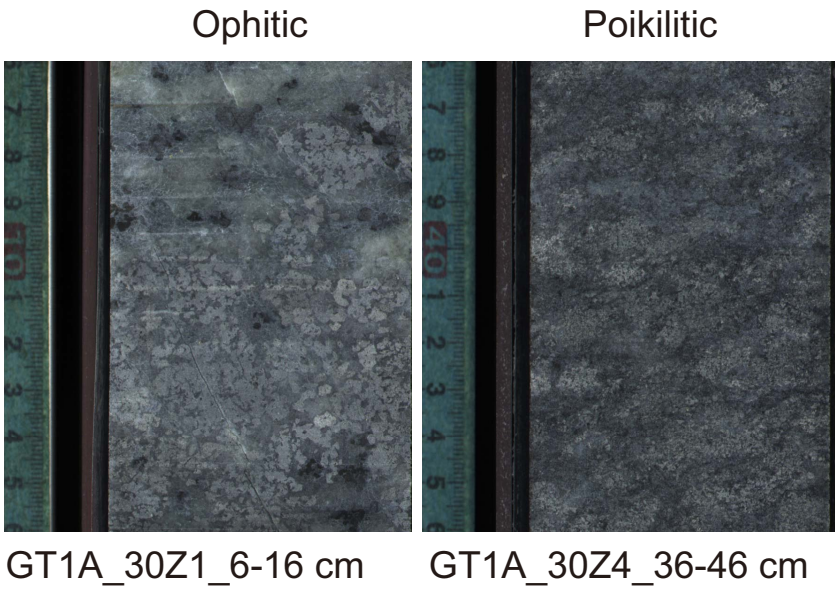

Figure F17. Downhole variations of layer thickness and layer intensity rank, Hole GT1A.

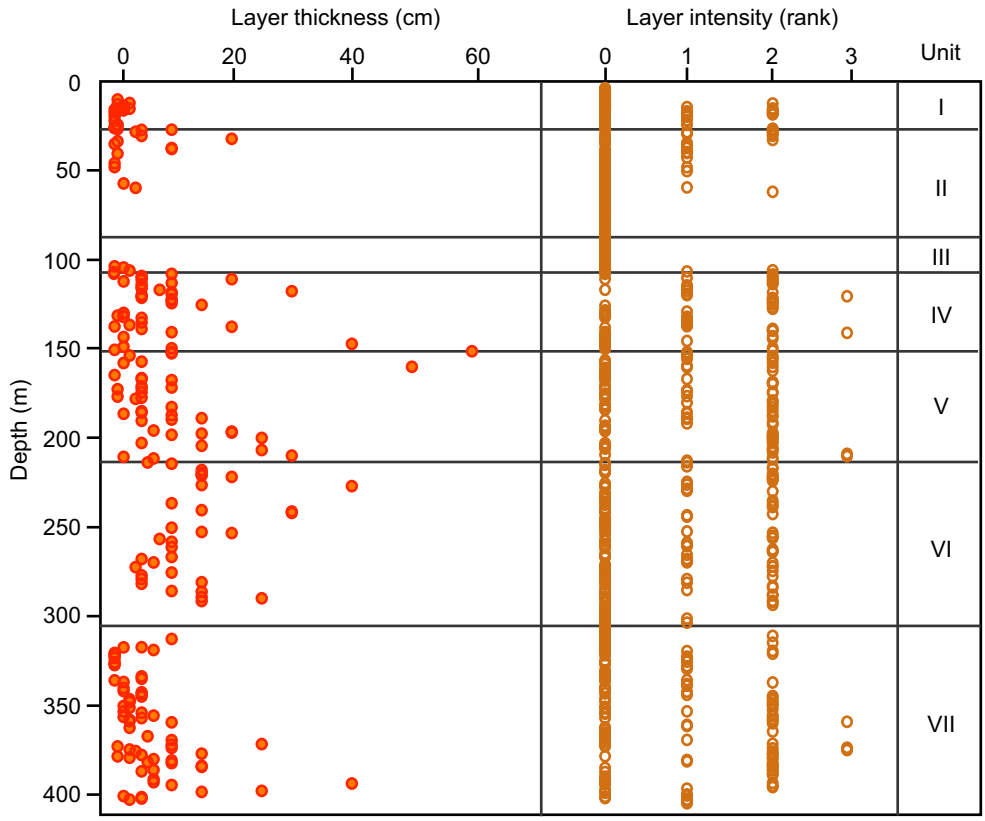

Figure F18. Examples of types of contacts: (**A**) sharp and (**B**) gradational. Nature of layer contacts: (**C**) modal, (**D**) grain size, and (**E**) combined modal and grain size.

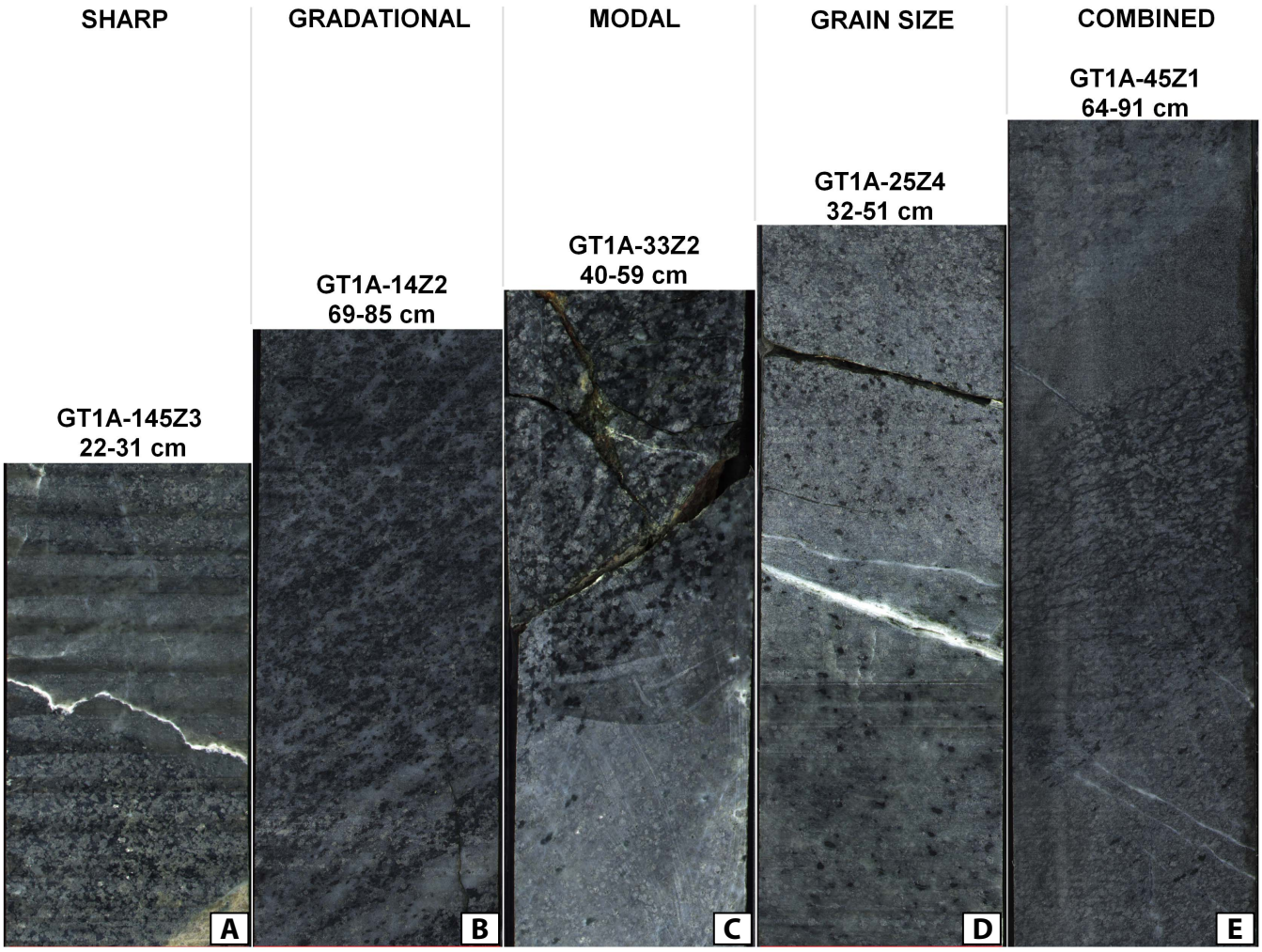

Figure F19. Stratigraphic variations of (**A**) habit, (**B**) volume of replacement, and (**C**) mode of olivine obtained by thin section description. Refer to the **Methods** chapter for explanation of mineral habit.

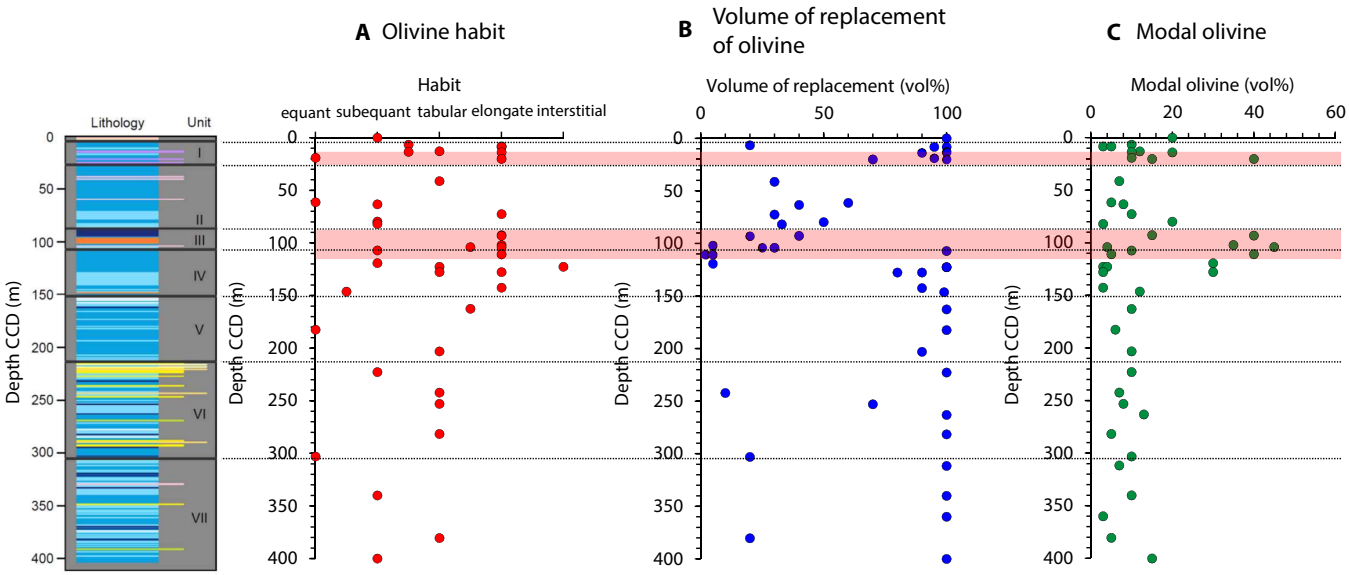

Figure F20. A. Interval 83Z-1, 1–22 cm. **B.** Elongated olivine exhibits subgrain development at 12–15 cm. **C.** Orthopyroxene occurs only with rimming olivine crystal (27Z-1, 13–16 cm).

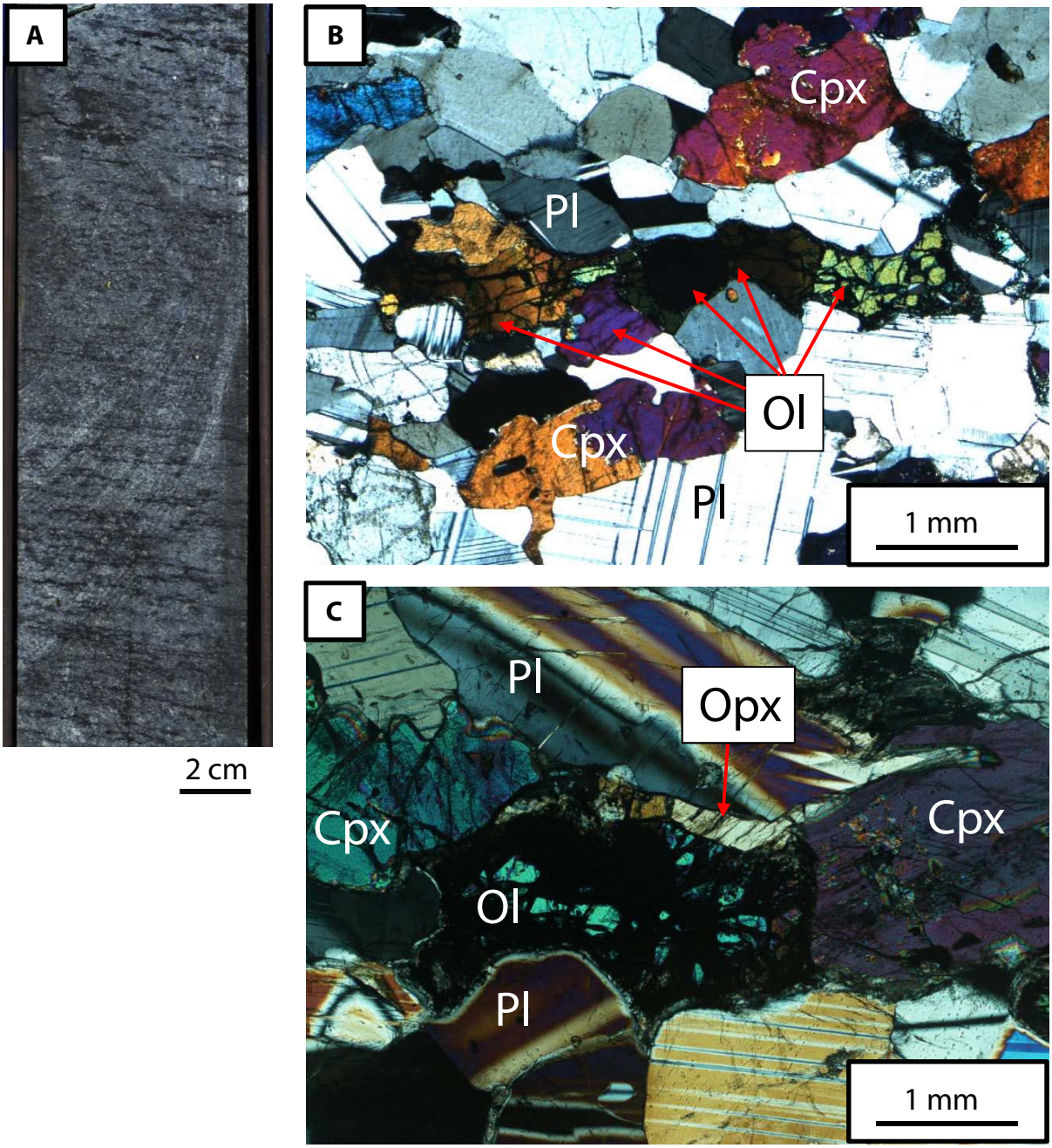

Figure F21. A. Clinopyroxene (Cpx)-bearing olivine (Ol) gabbro (30Z-4, 41–55 cm). **B.** Clinopyroxene oikocryst. Plagioclase (Pl) chadacrysts are randomly oriented. Clinopyroxene oikocryst shows subgrain development.

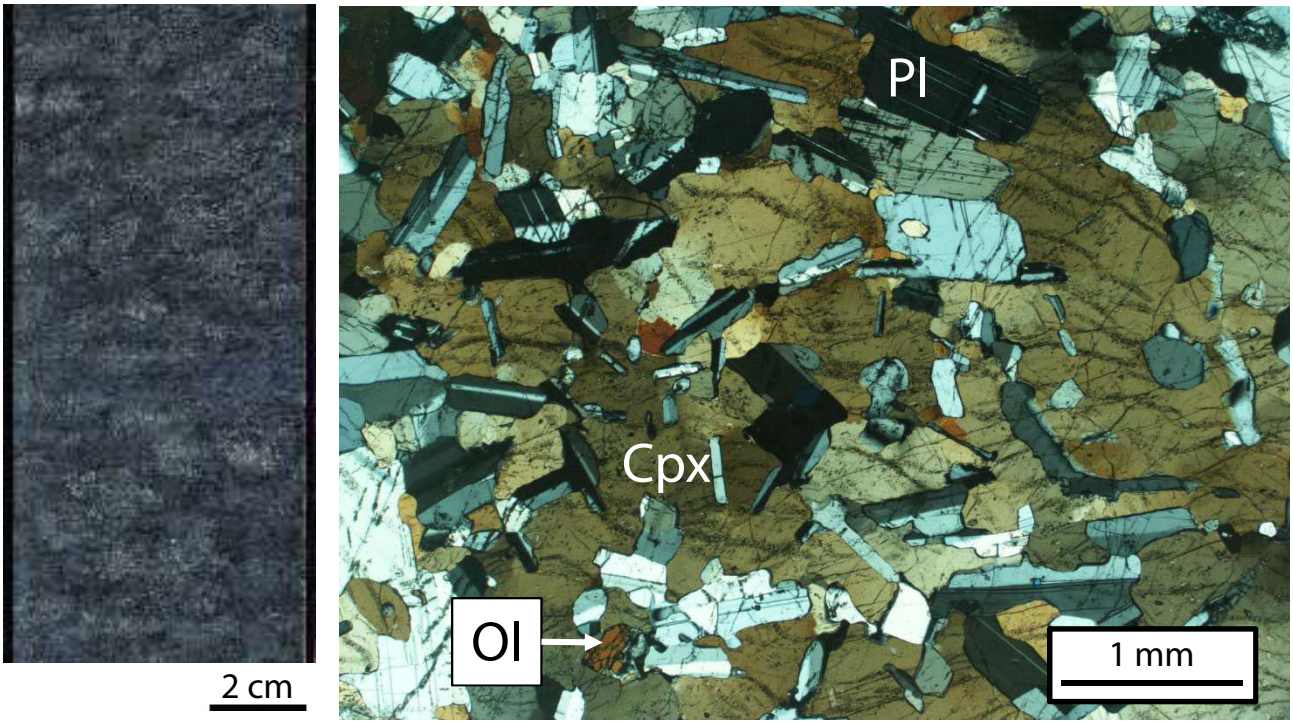

Figure F22. Comparison of clinopyroxene oikocrysts in different settings. **A.** Clinopyroxene oikocryst from clinopyroxene-bearing troctolite in IODP Hole U1415J, Hess Deep plutonic crust, East Pacific Rise (Gillis et al., 2014b). **B.** Clinopyroxene oikocryst in Oman ophiolite (30Z-4, 41–55 cm). Some olivine chadacrysts are kinked.

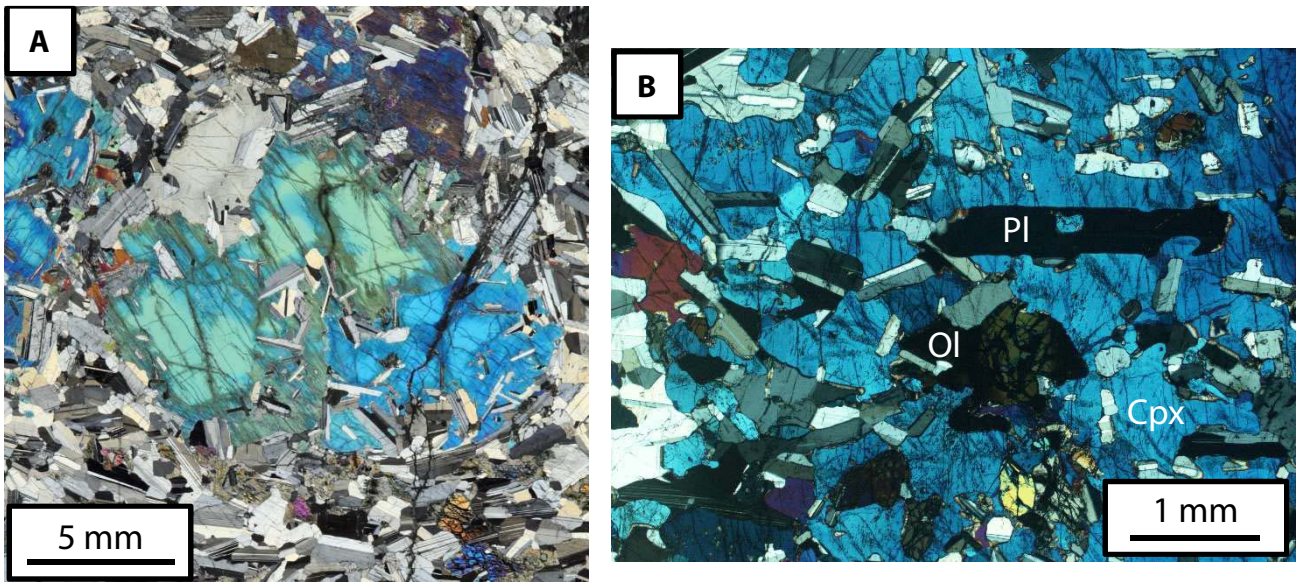

Chadacryst: Plagioclase
Matrix: Troctolite

Chadacryst: Plagioclase, Olivine
Matrix: Olivine gabbro

Figure F23. Oikocrystic olivine, Hole GT1A. **A.** Interval 33Z-4, 44–59 cm (Piece 2). B. Oikocrystic olivine at 33Z-4, 41–55 cm. The core of oikocrystic olivine does not contain chadacrysts. Olivine is kinked.

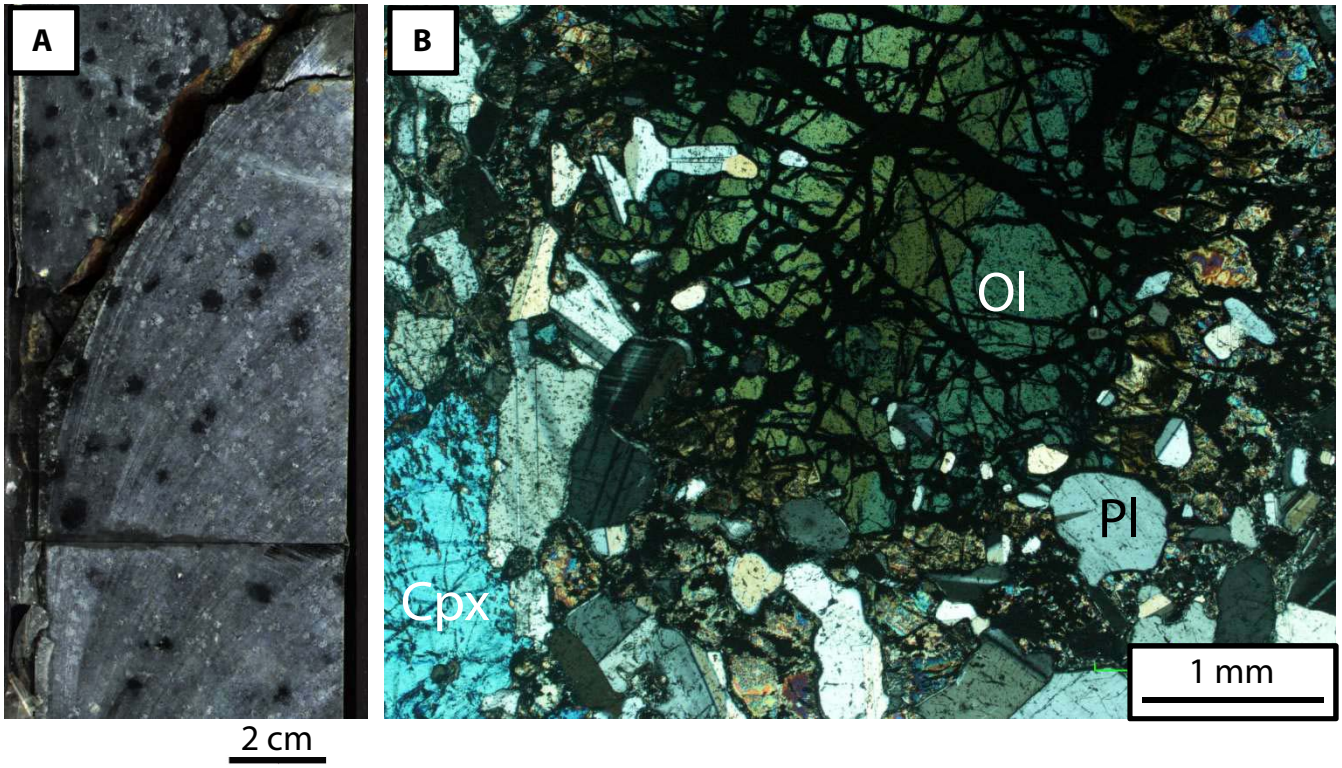

Figure F24. A fine-grained gabbroic layer (brownish part) interbedded into medium-grained layered gabbros. **A.** Interval 45Z-1, 59–75 cm. **B.** Contact between the fine-grained gabbroic layer and the surrounding medium-grained olivine gabbro (cross-polarized light [XPL]). Shape-preferred orientation of minerals of both the fine- and medium-grained gabbros are almost parallel to the direction of boundary. **C.** Contact at 45Z-1, 69–72 cm. Note interfingering between olivine and clinopyroxene.

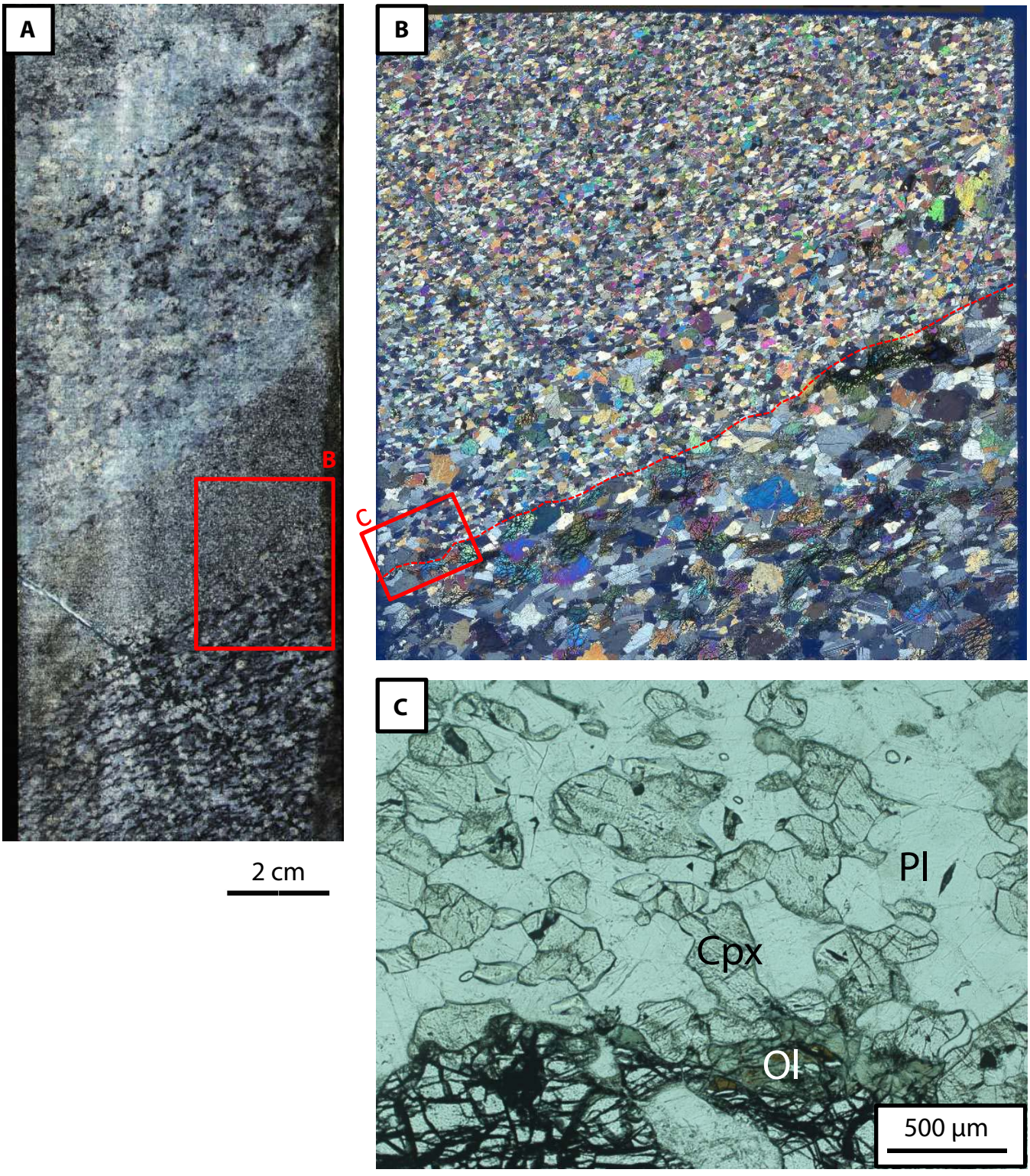

Figure F25. Total alteration intensity downhole.

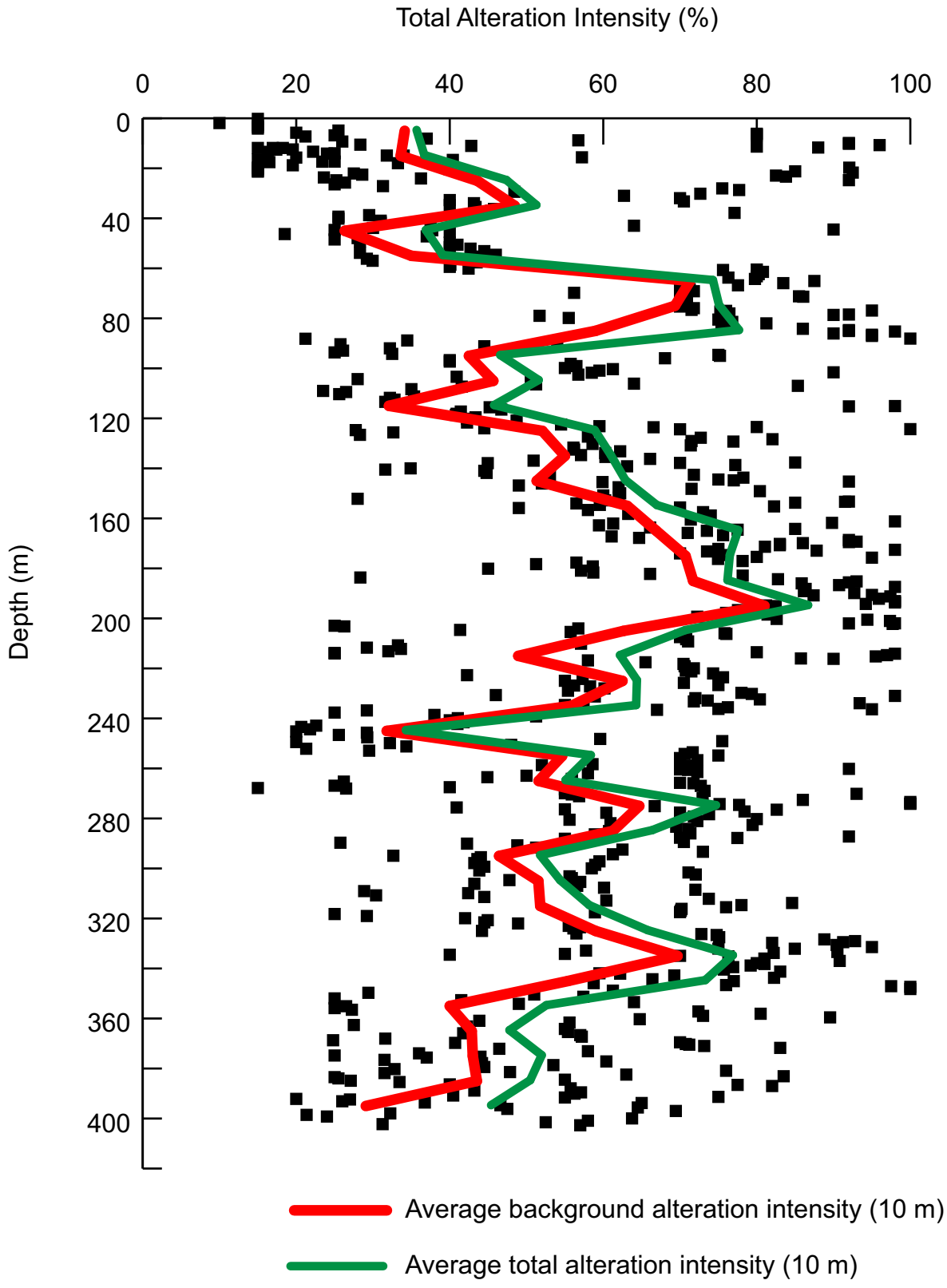

Figure F26. Downhole distribution of the four alteration types.

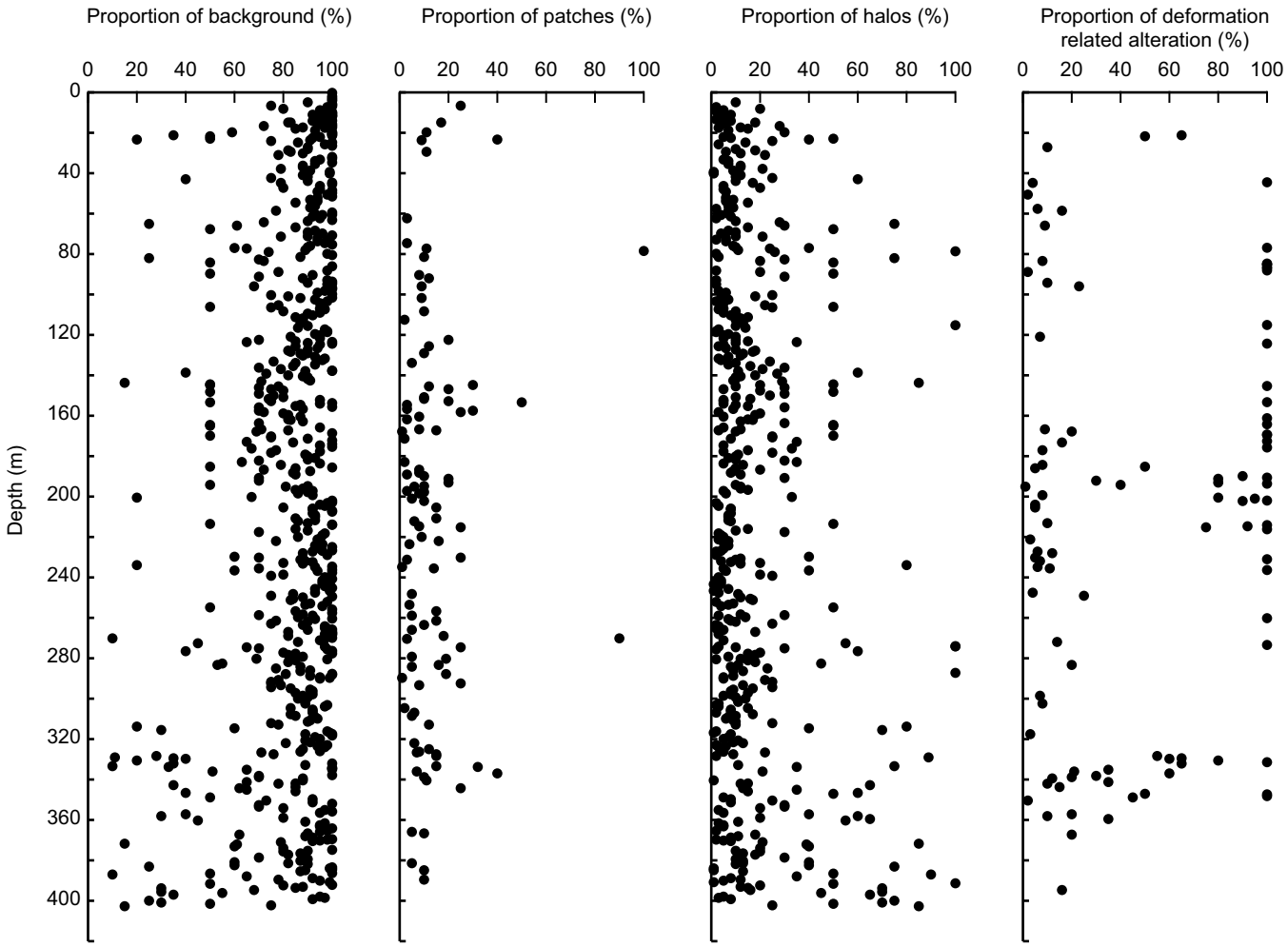

Figure F27. Secondary minerals (in veins and host rock) with depth.

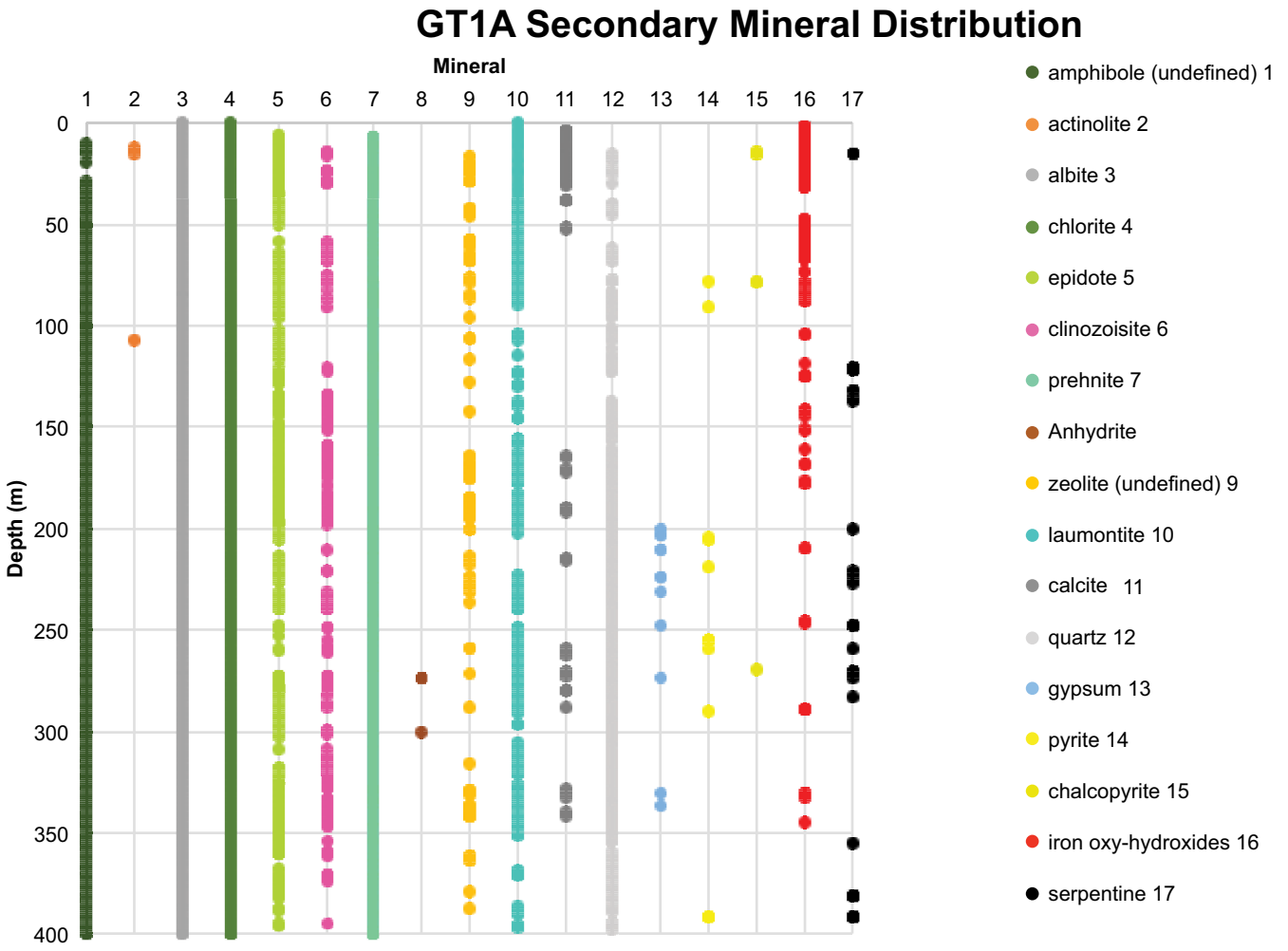

Figure F28. Types of background and patch alteration. **A.** Light gray background alteration with altered olivine (6Z-4, 89–98 cm). **B.** Medium to dark gray background alteration hosting <0.5 mm chlorite ± amphibole veins (51Z-4, 23–29 cm). **C.** Patchy background alteration related to igneous texture (30Z-1, 0–10 cm). **D.** Epidote-rich alteration patch (76Z-2, 62–70 cm).

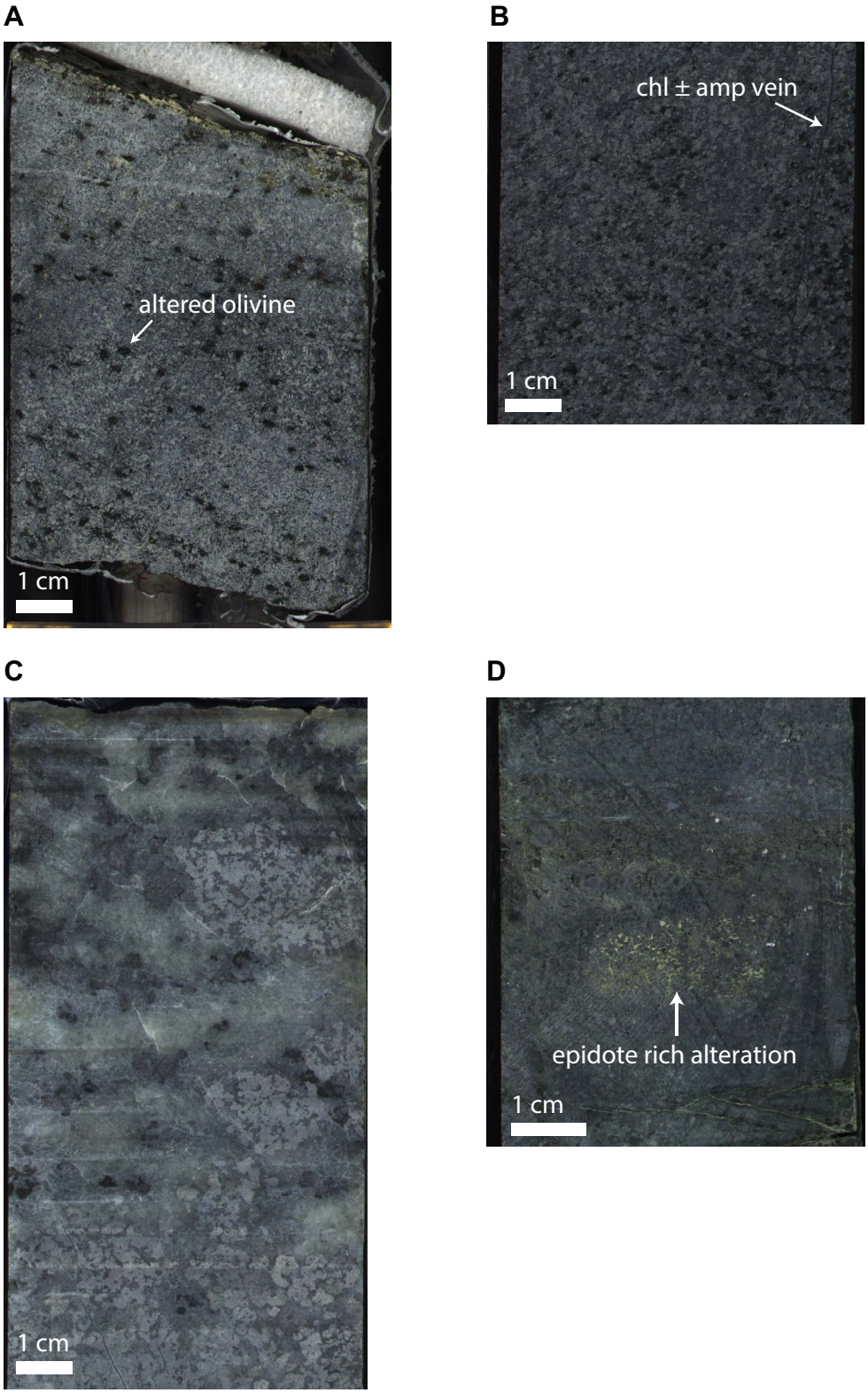

Figure F29. Example of large patch (or vein?) of anhydrite that consumes the width of the core (interval 108Z-4, 9–30 cm).

Figure F30. Types of halo alteration. **A.** Large epidote-rich halo around epidote vein and breccia (140Z-2, 40–70 cm). **B.** Diffuse albite-rich halo around prehnite vein (12Z-1, 25–45 cm). **C.** Sharp albite-rich halo around sheared epidote vein (95Z-2, 63–79 cm). **D.** Small irregular white halo around chlorite + prehnite vein (12Z-2, 53–69 cm).

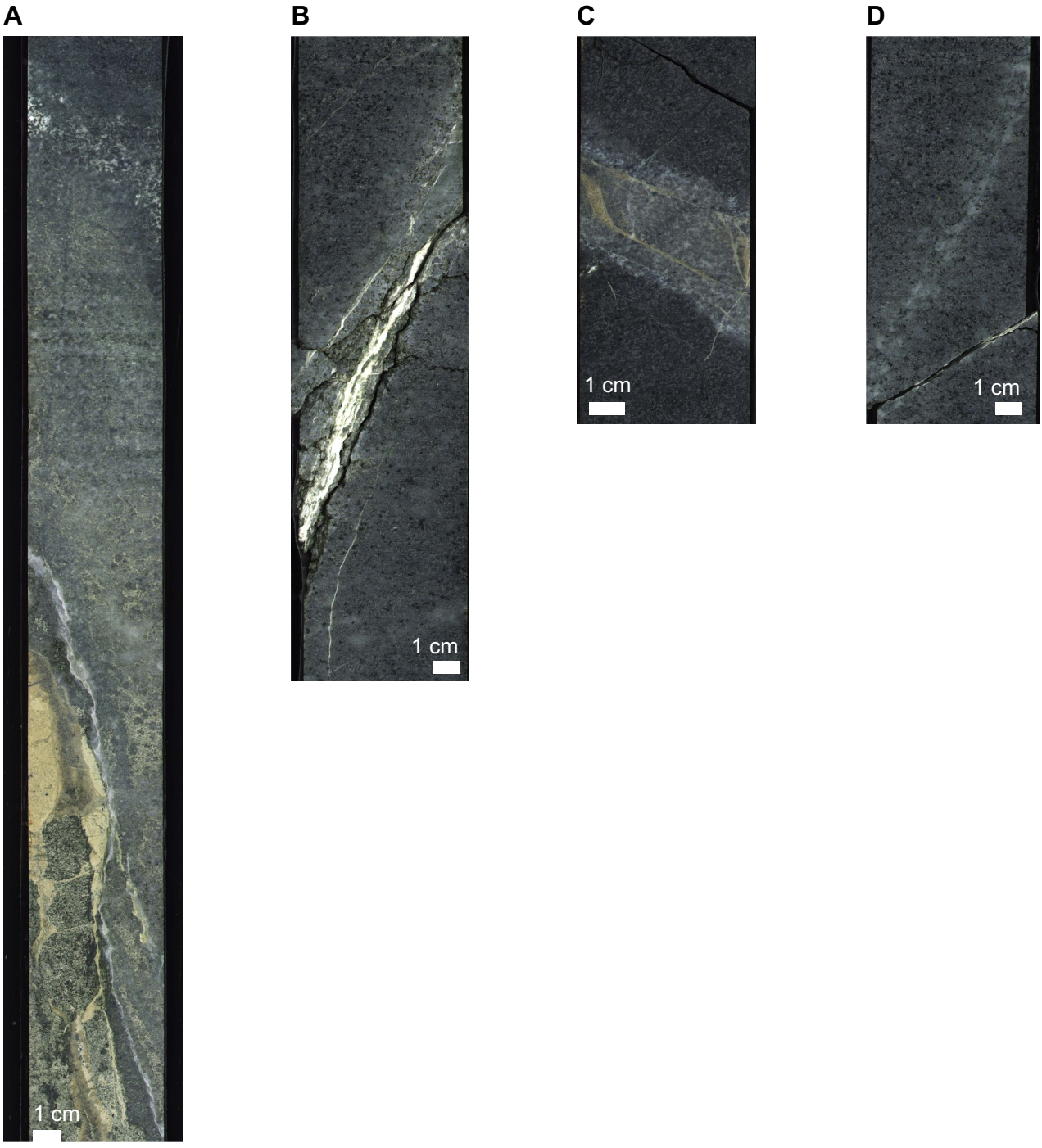

Figure F31. Types of deformation-related alteration. **A.** Incipient brecciation associated with Fe oxyhydroxide–bearing veins (13Z-1, 21–40 cm). **B.** Sheared interval associated with abundant chlorite and prehnite (36Z-1, 0–11 cm). **C.** Silicified sheared band (99Z-2, 0–11 cm).

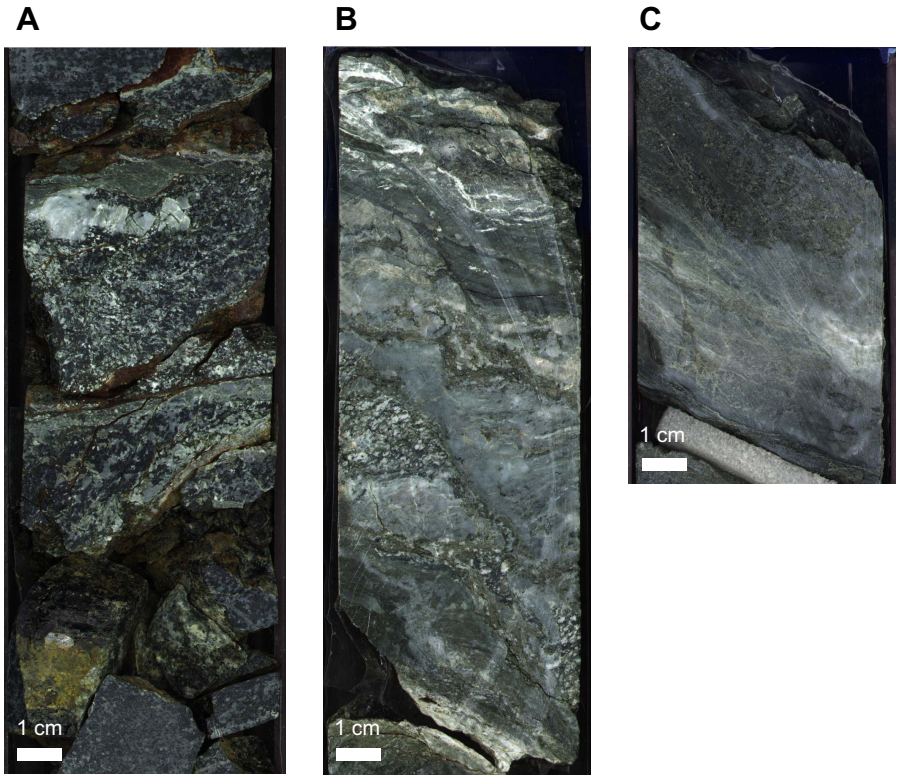

Figure F32. Vein intensity with depth for all veins including those counted in vein nets. Vein density is calculated as veins/meter on a section-by-section basis and shown relative to the igneous stratigraphy and the locations of the main fault zones.

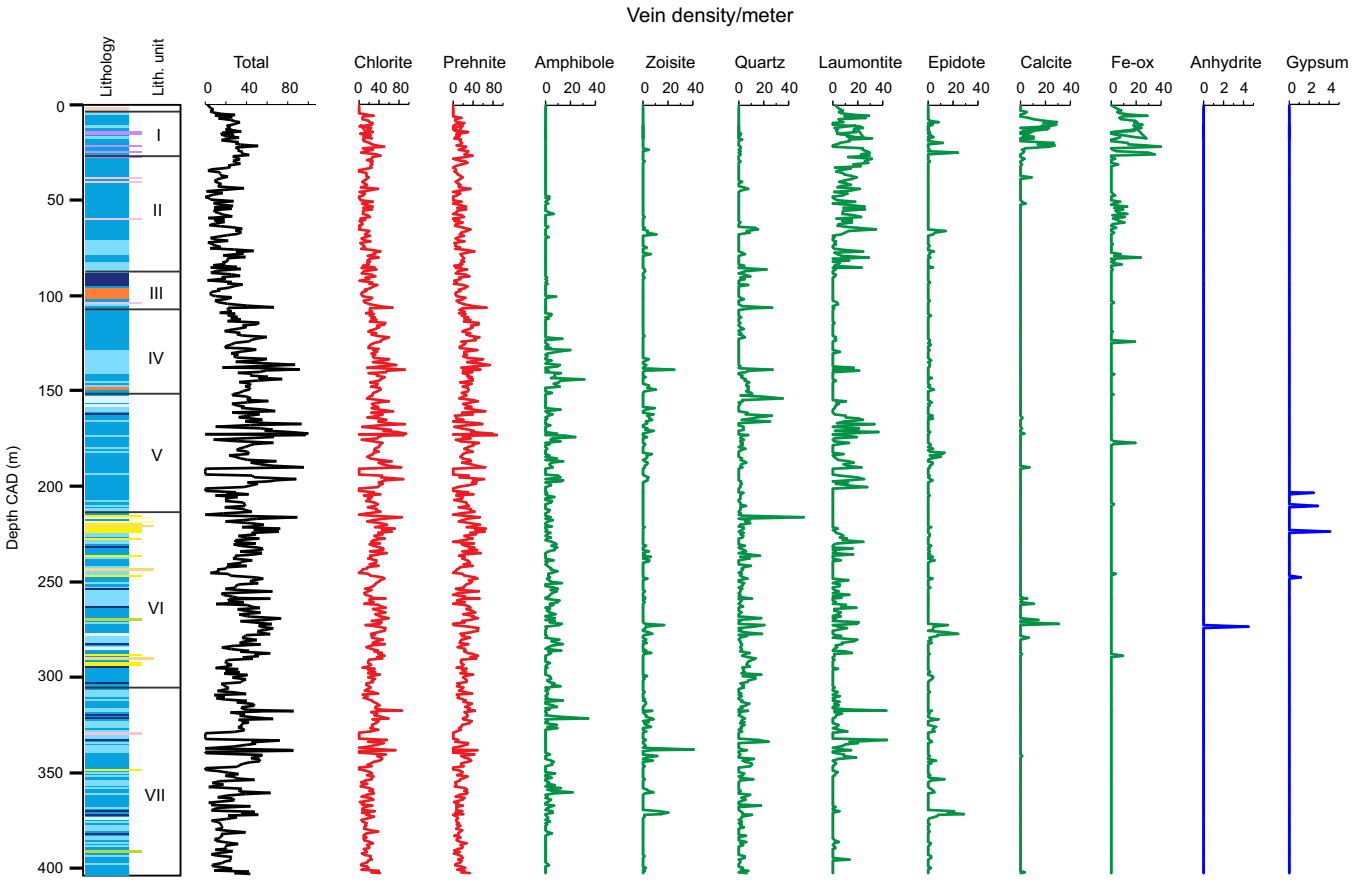

Figure F33. Secondary minerals in veins calculated as area% of core, calculated for each secondary mineral on a section by section basis.

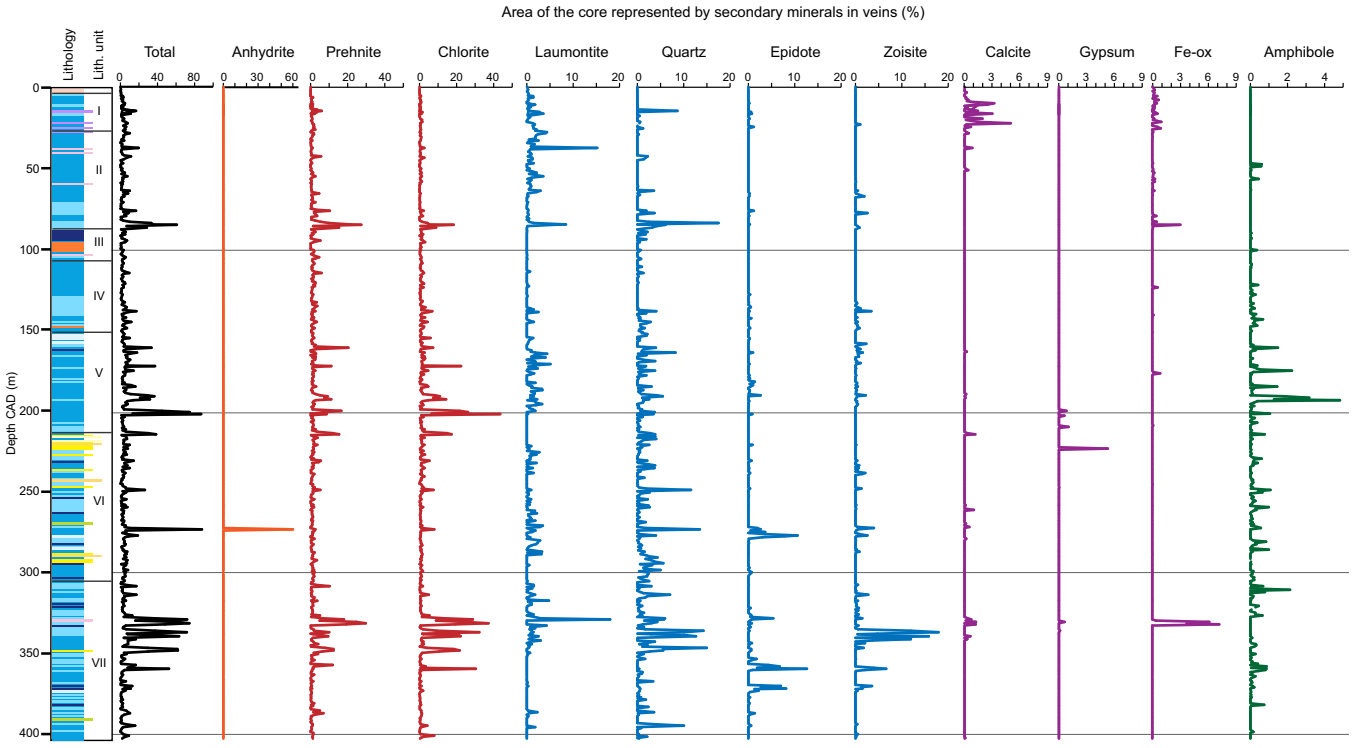

Figure F34. Vein intensity with depth separated by secondary mineral fill. Note vein densities do not include veins hosted in vein nets. Vein density is calculated as veins/meter on a section-by-section basis.

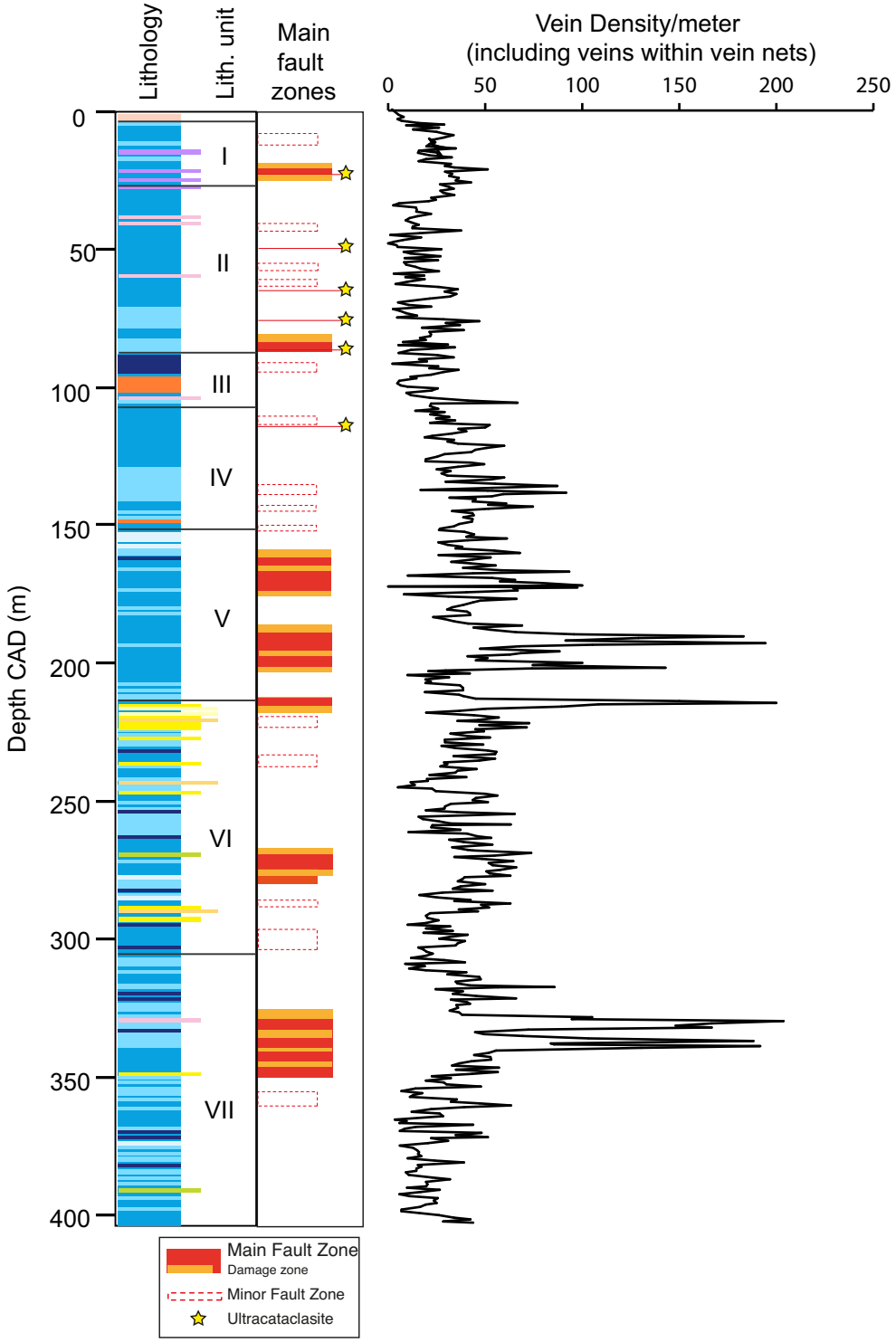

Figure F35. Types of crosscutting relationships. **A.** Earliest amphibole ± chlorite veins (V1) are crosscut by epidote + zoisite (V2), which are then crosscut by chlorite + prehnite (V3). **B.** Epidote veins (V1) are both crosscut and offset by laumontite veins (V2).

GT1A-56Z-1, 0-20 cm

GT1A-69Z-3, 45-52 cm

Figure F36. Types of vein fill.

Amphibole
GT1A_22Z-2, 40-53 cm

Epidote
GT1A-111Z-2, 30-44 cm

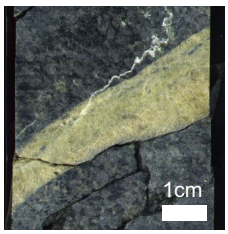

Clinozoisite
GT1A-32Z-4, 36-44 cm

Quartz
GT1A-127A-1, 24-36 cm

Zeolite
GT1A-25Z-4, 36-47 cm

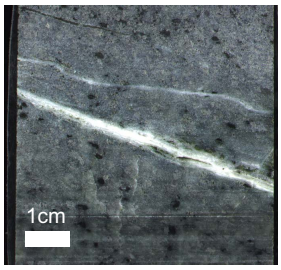

Prehnite + Chlorite
GT1A-21Z-3, 8-26 cm

Laumontite
GT1A 11M-3, 40-56 cm

Anhydrite
GT1A-108Z-4, 46-63 cm

Figure F37. 1–5 cm scale compositional/modal/grain-size layering. **A.** Ratio, phase, and grain-size layering in olivine-bearing and olivine gabbro. **B, C.** Ratio and grain-size layering contact (B: plane polarized light [PPL], C: cross-polarized light [XPL]).

A GT1A_45_1_46_93

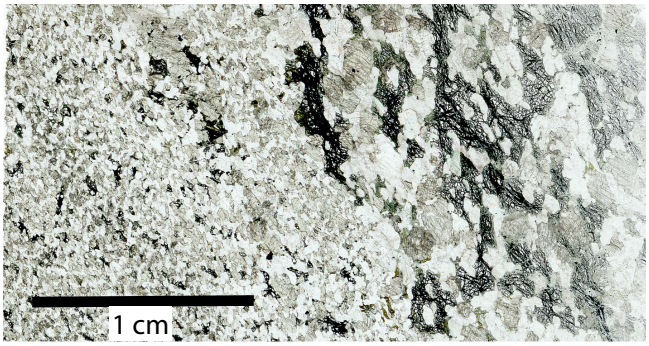

B GT1A_45_1_69_72_PPL_TS#24

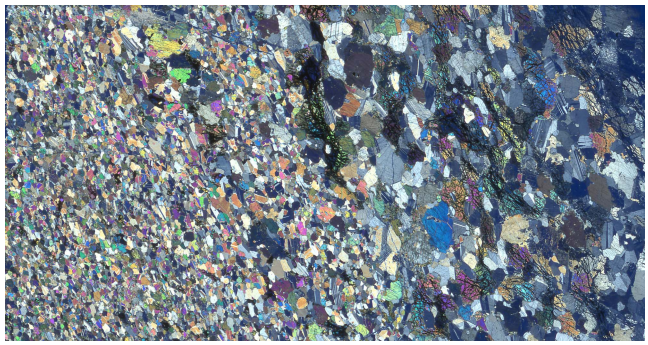

C GT1A_45_1_69_72_XPL_TS#24

Figure F38. Core photograph and thin sections illustrating centimeter-scale diffuse magmatic banding. **A.** Ratio and phase banding in olivine gabbro. **B, C.** Ratio and phase banding.

A GT1A_24_2_65-90

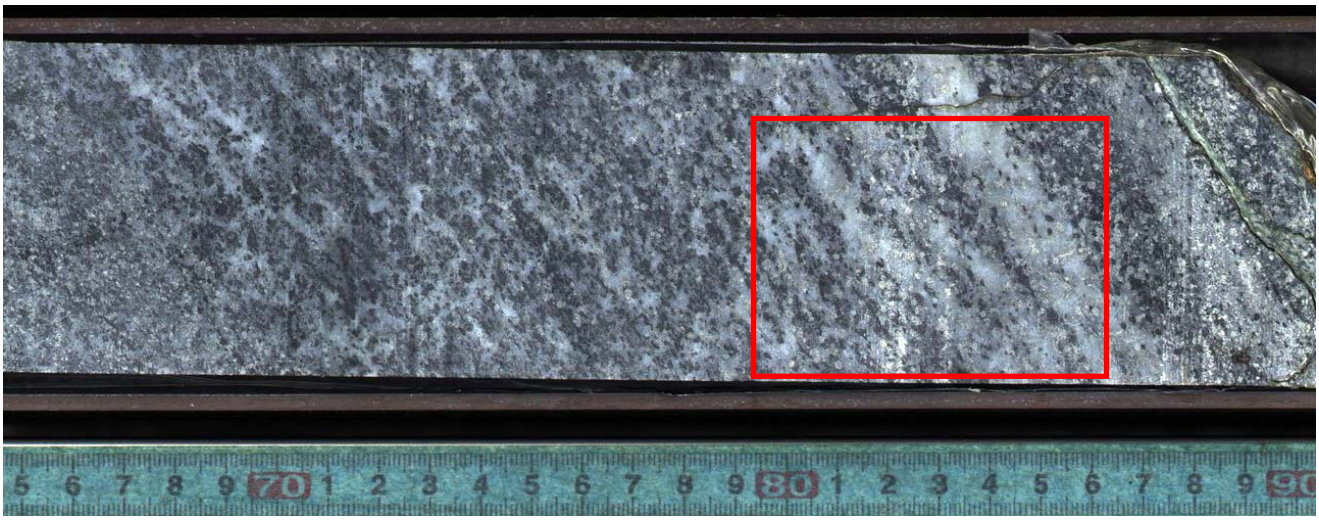

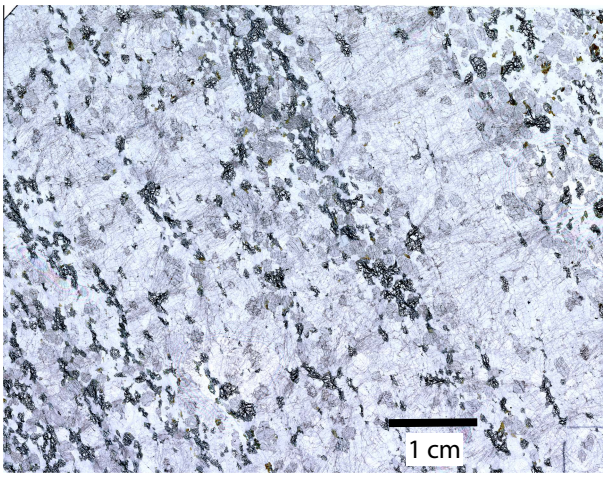

B GT1A_24_2_79_86_PPL_TS#9

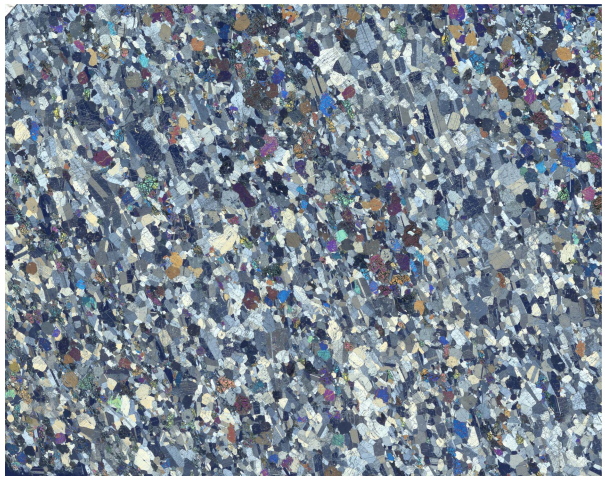

C GT1A_24_2_79_86_XPL_TS#9

Figure F39. Downhole plots of the dip of (**A**) magmatic foliation, (**B**) layering, contacts, and veins, and (**C**) magmatic contacts, layering, and foliation combined.

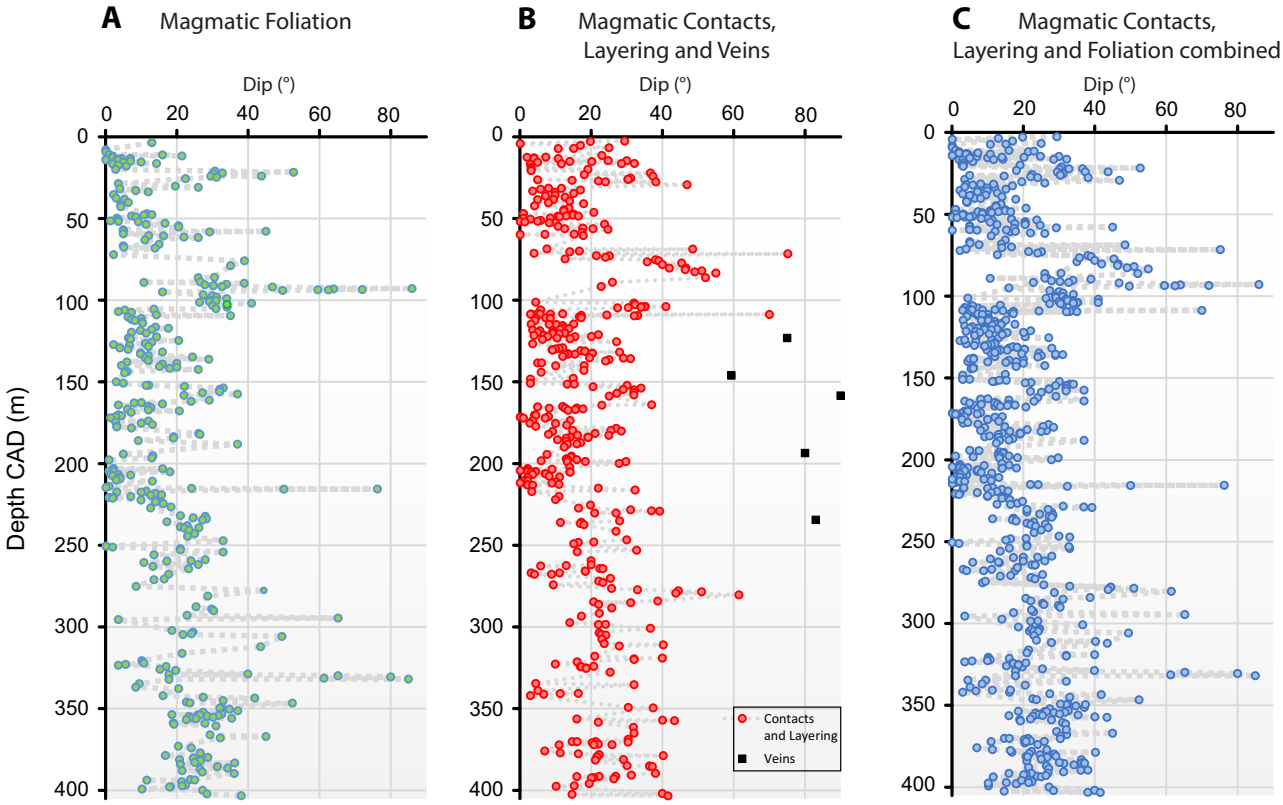

Figure F40. Frequency diagrams of the layer thickness within the core. Layer thickness frequency, by intervals of 5 cm; inset: natural log of layer thickness frequency, by intervals of 0.25.

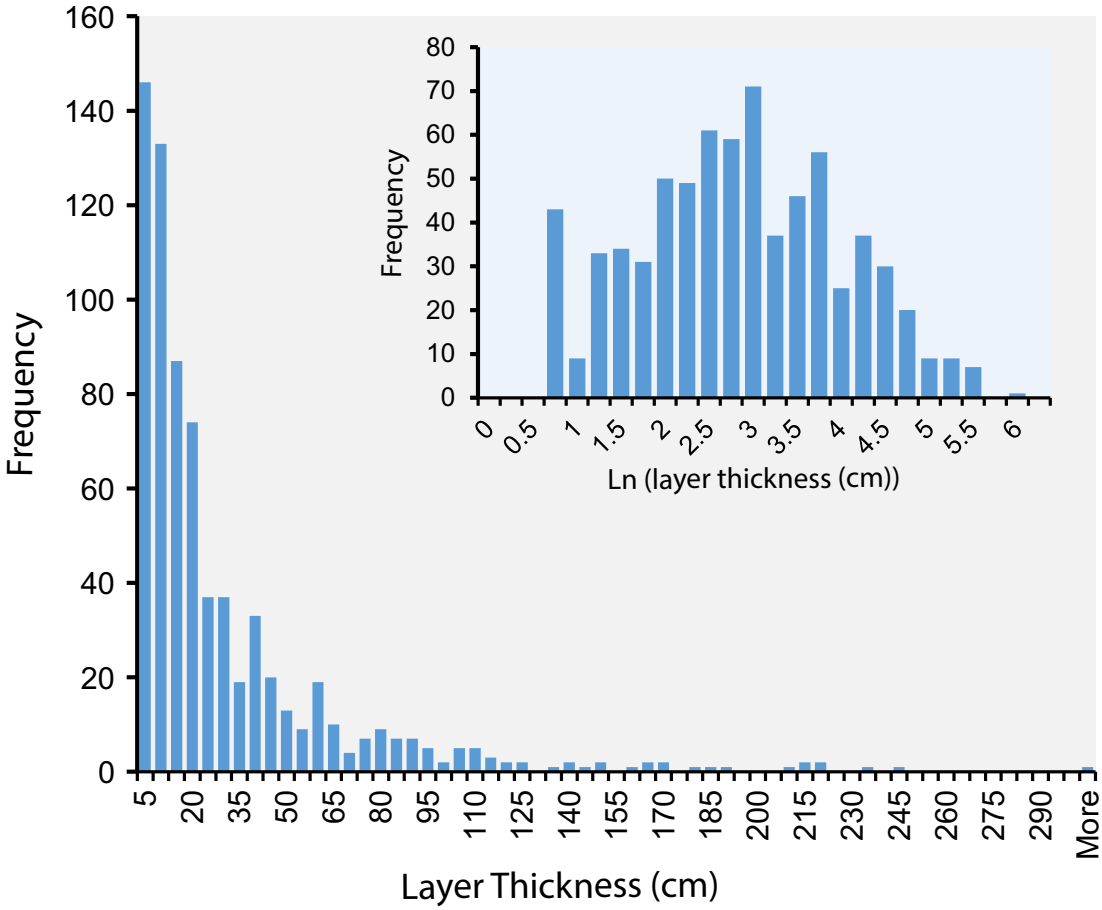

Figure F41. Styles and strengths of magmatic foliation defined by olivine. **A.** Weak olivine foliation defined by sparse, low–aspect ratio olivine crystals. **B.** Weak–moderate olivine foliation. **C.** Strong olivine foliation defined by high–aspect ratio subgrained olivine crystals. **D.** Strong olivine foliation defined by high–aspect ratio subgrained olivine crystals.

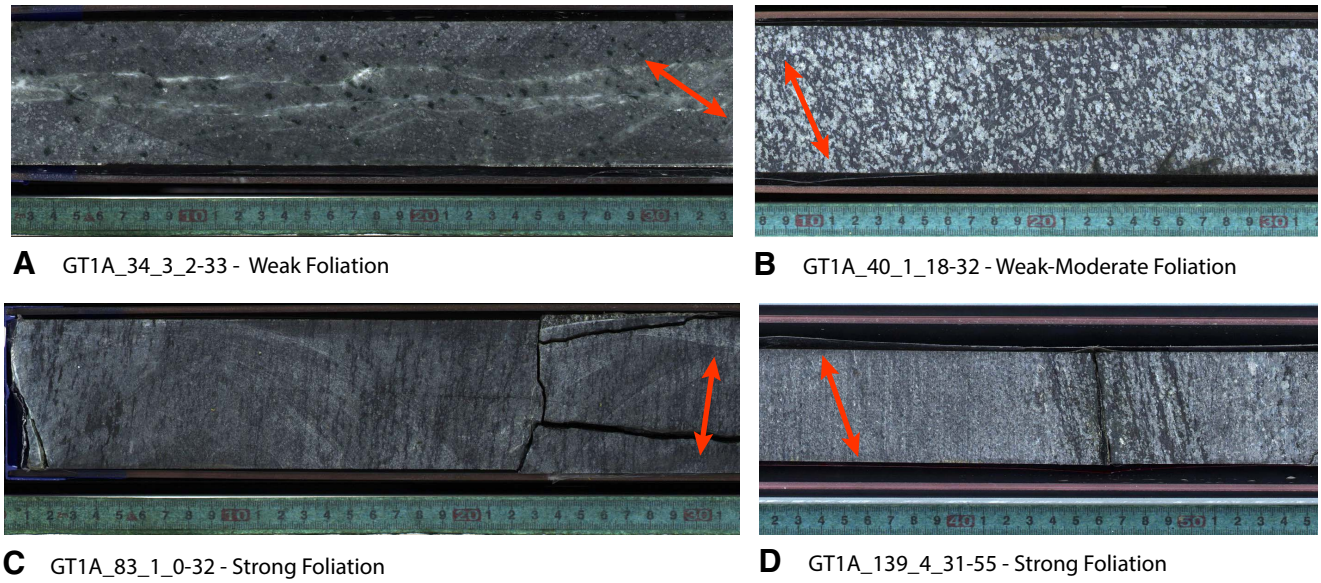

A GT1A_34_3_2-33 - Weak Foliation

B GT1A_40_1_18-32 - Weak-Moderate Foliation

C GT1A_83_1_0-32 - Strong Foliation

D GT1A_139_4_31-55 - Strong Foliation

Figure F42. Examples of magmatic foliation defined by both olivine and plagioclase crystals. **A, B.** Strong foliation defined by moderate–aspect ratio plagioclase and subgrained olivine crystals. **C, D.** Moderate foliation dominantly defined by moderate–aspect ratio plagioclase crystals but also by less common subgrained olivine crystals and low–aspect ratio clinopyroxene crystals. **E, F.** Moderate to weak foliation defined by low–aspect ratio plagioclase crystals, moderate–aspect ratio subgrained olivine crystals, and low–aspect ratio clinopyroxene crystals.

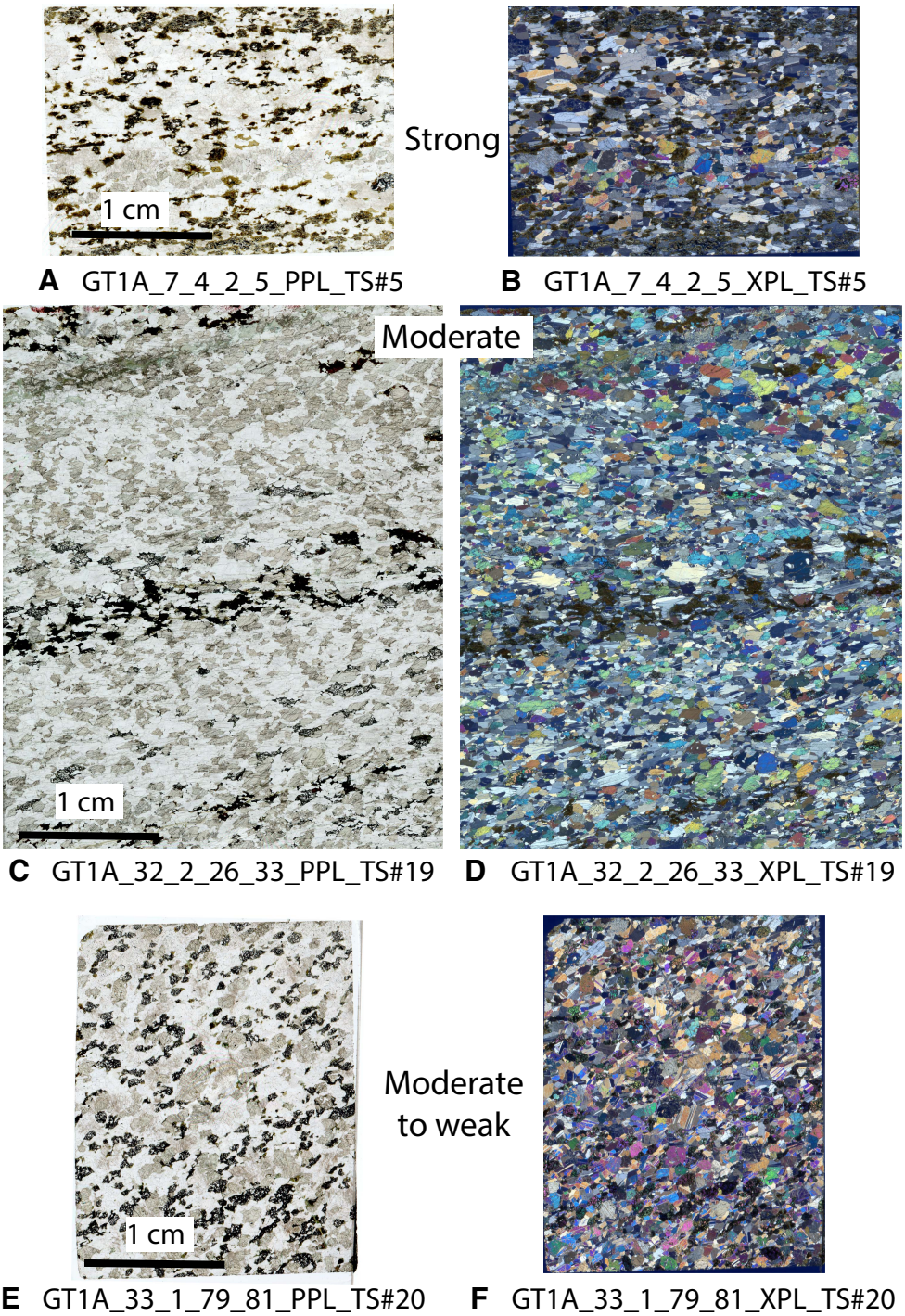

Figure F43. Examples of magmatic foliation defined mostly by plagioclase crystals. **A, B.** Weak foliation defined by low–aspect ratio plagioclase crystals. **C, D.** Moderate foliation dominantly defined by moderate–aspect ratio plagioclase crystals.

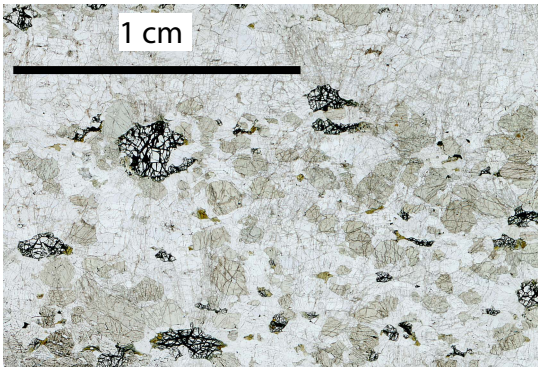

A GT1A_5_3_14_17_PPL_TS#1

Weak

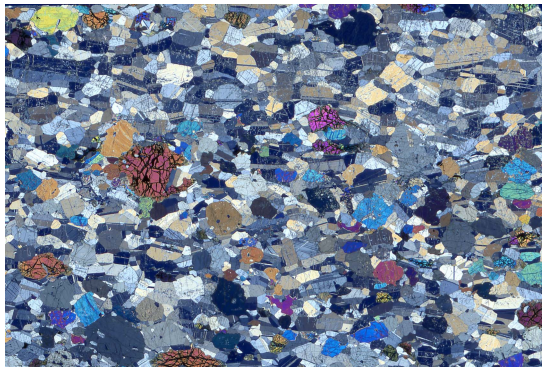

B GT1A_5_3_14_17_XPL_TS#1

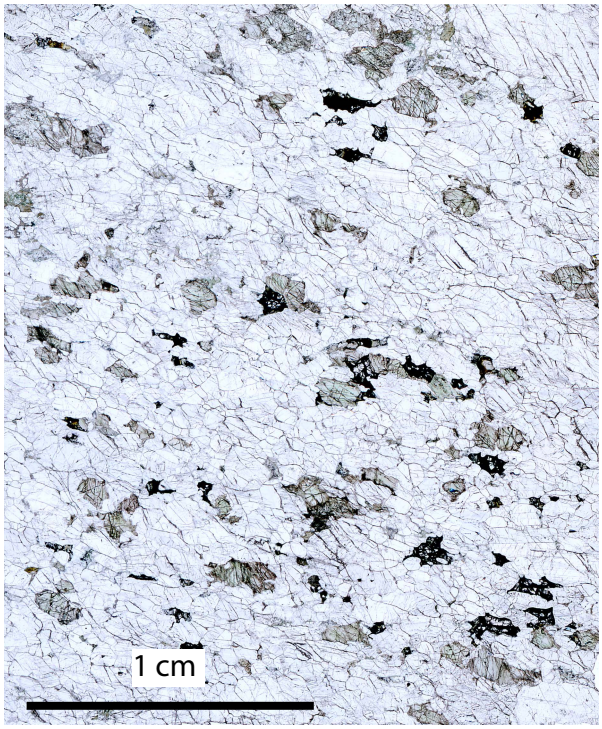

C GT1A_27-1_13_17_PPL_TS#14

Moderate

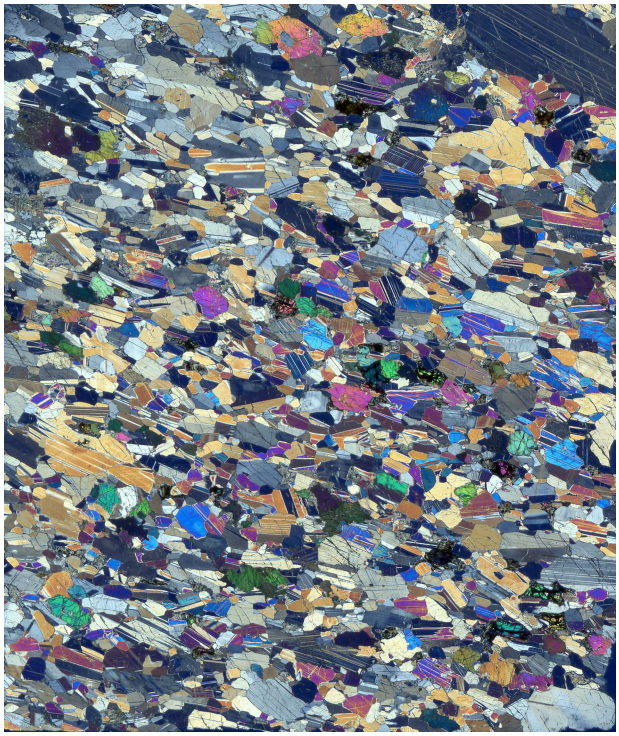

D GT1A_27-1_13_17_XPL_TS#14

Figure F44. Local rotation of the olivine foliation by brittle faulting (blue line). Orientation of the foliation is indicated by red arrows (**A**: not annotated, **B**: annotated).

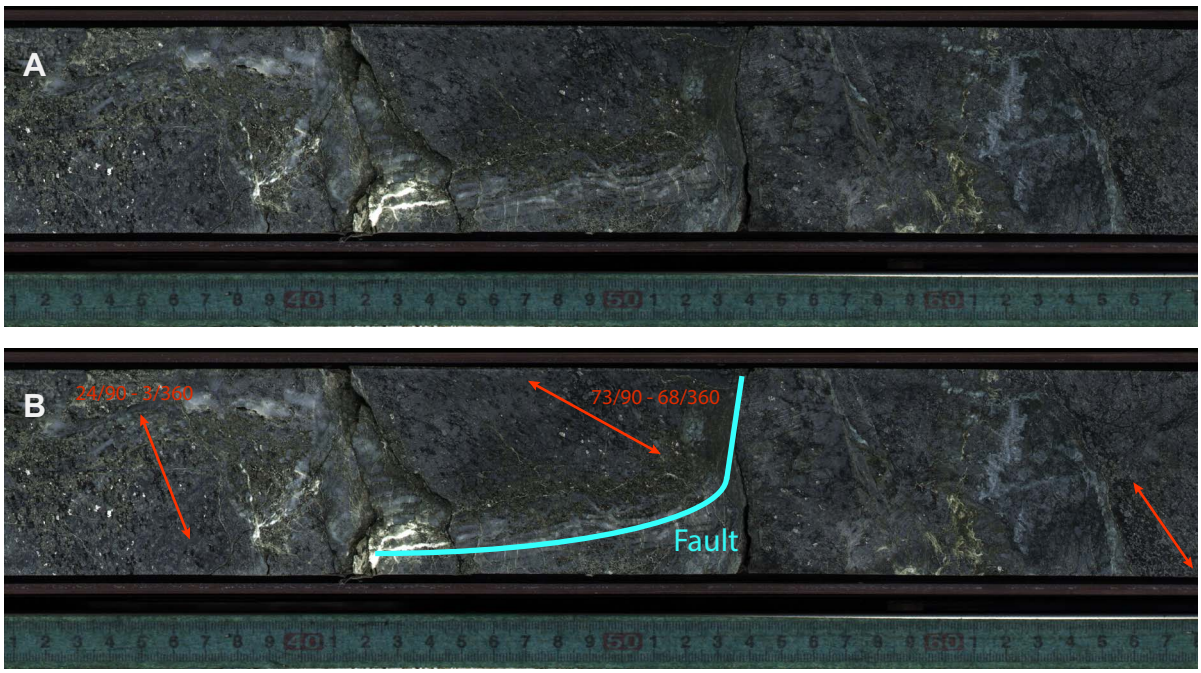

GT1A_87_1_41-58

Figure F45. Lithologic column with igneous units, dip of magmatic contacts, layering, and foliation, and location of the major brittle fault zones. Red lines = interpreted mean variation of magmatic fabric dip vs. depth.

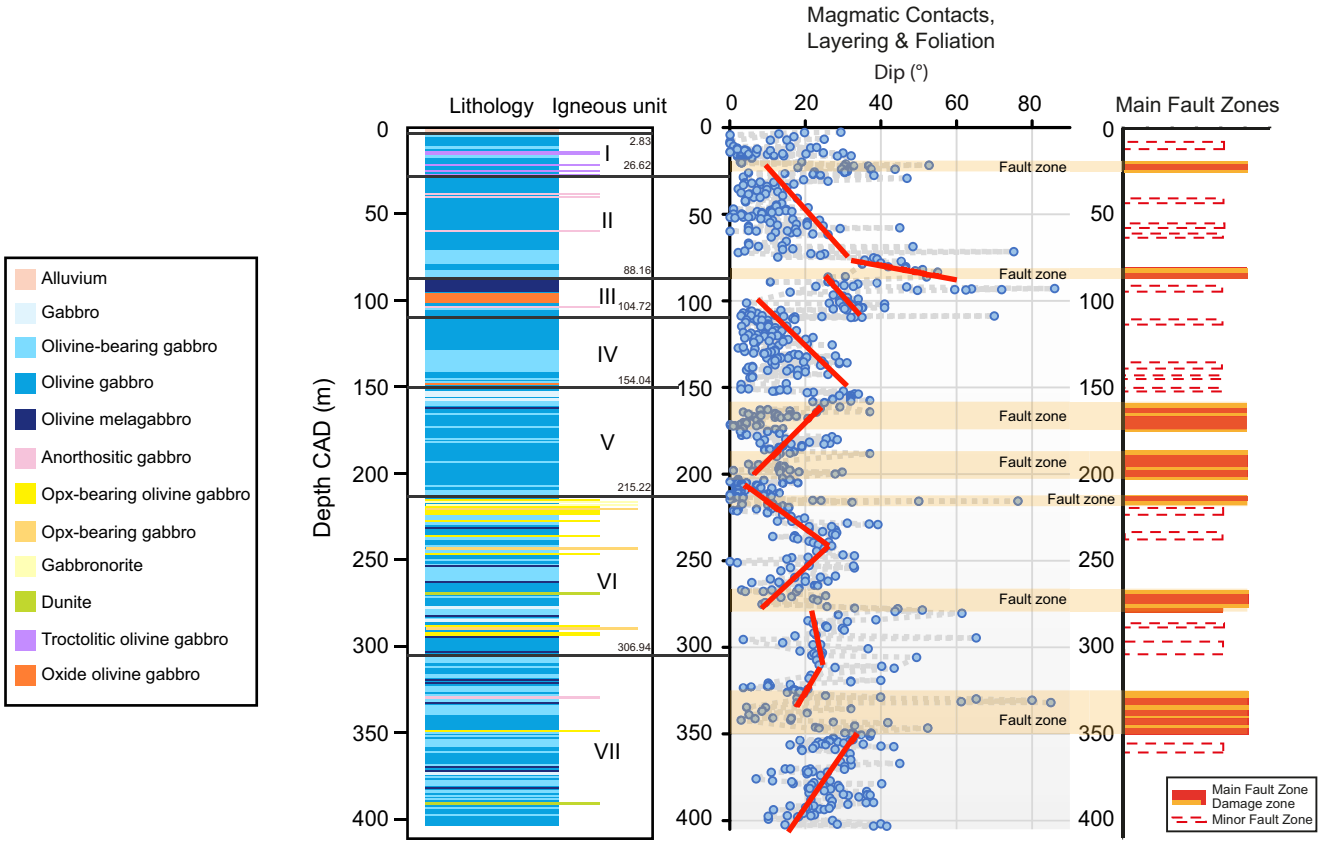

Figure F46. Examples of brittle-plastic fabrics with incipient crystal-plastic fabrics. These zones tend to be fine-grained, altered, and overprinted by brittle structures.

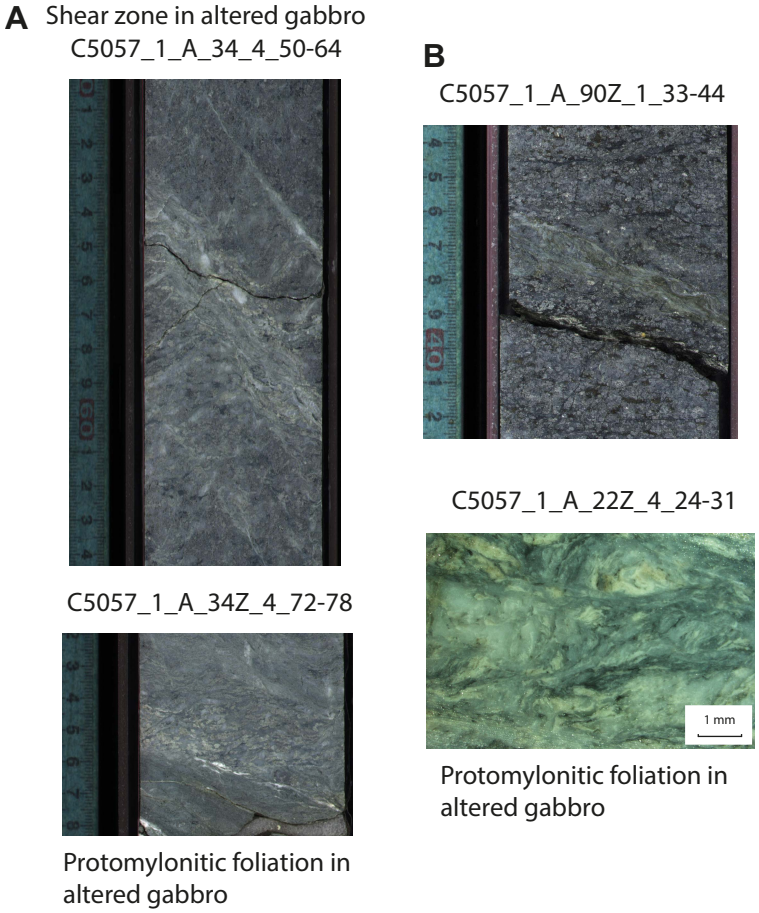

Figure F47. Fault zone with fine- and coarse-grained anhydrite. Anhydrite forms layers parallel to the fault zone indicating syntectonic formation. The XPL photomicrograph shows elongate coarse-grained crystals of anhydrite in a fine matrix of anhydrite. The larger crystals have formed block boudins with the boudin necks filled with fine-grained anhydrite.

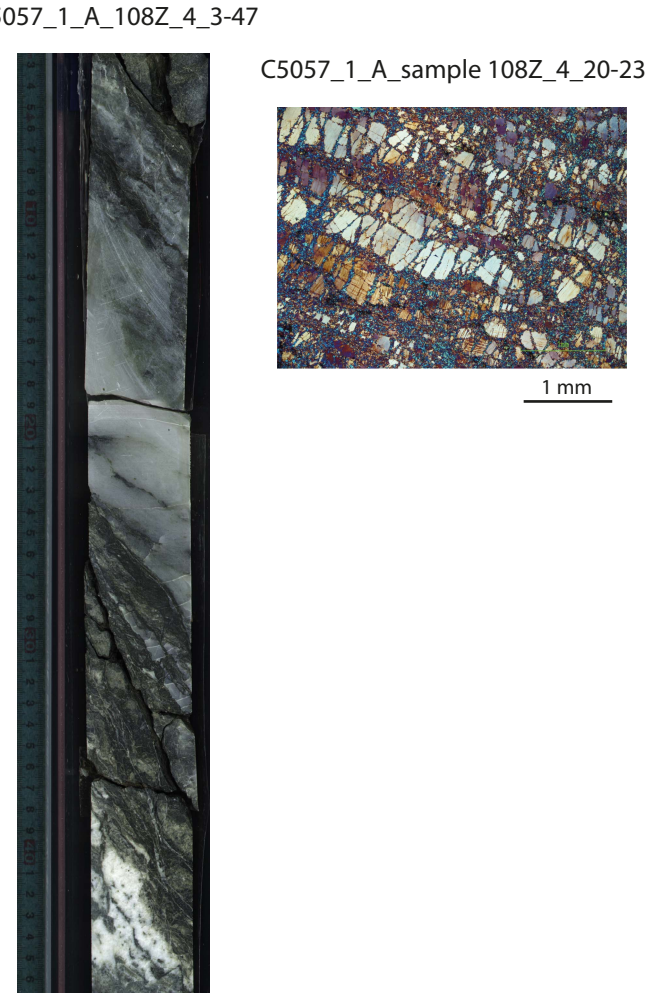

Figure F48. Epidote/clinozoisite veins. **A.** With little deformation. **B.** Sheared and thinned. **C.** Offset by a minor fault. **D.** Close-up of (C) showing how the vein was thinned and sheared before fracturing. **E.** PPL photomicrograph of ultracataclasite with clasts of epidote/clinozoisite.

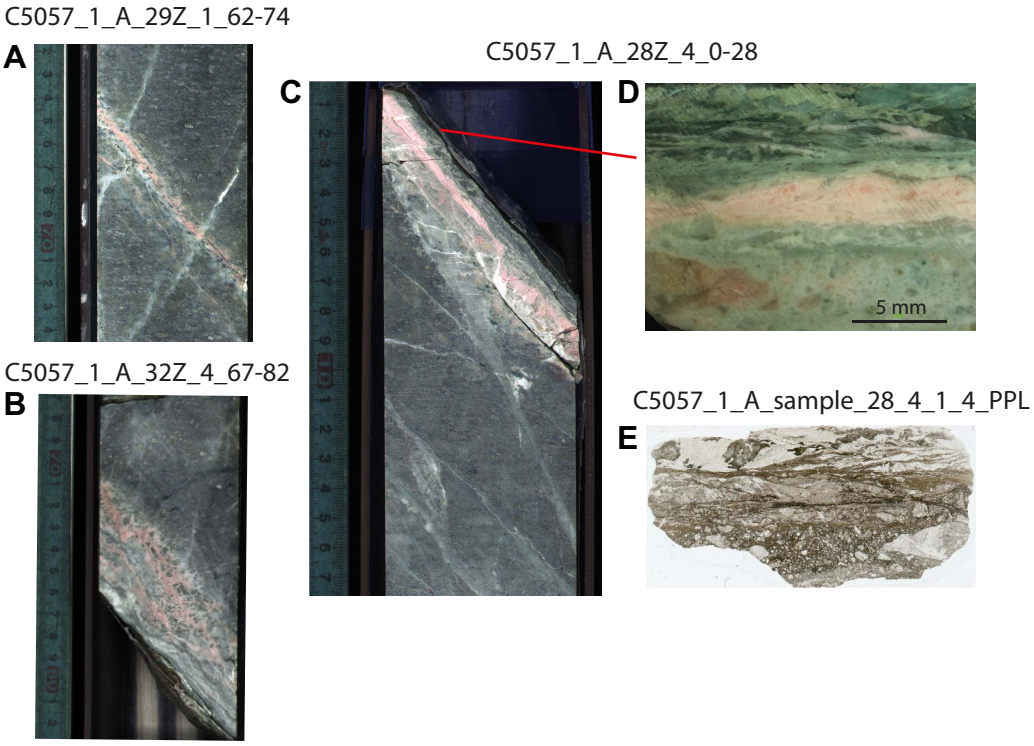

Figure F49. CT and image scans showing an epidote and chlorite fault zone. **A.** Image scan shows yellow epidote and green chlorite. **B.** In the CT scan, epidote is more dense and has a brighter color. The epidote clasts are elongate and form sigma-clasts, an indication a reverse sense of shear. **C.** Perpendicular section CT image showing bands of chlorite and epidote and a bleb of sulfide.

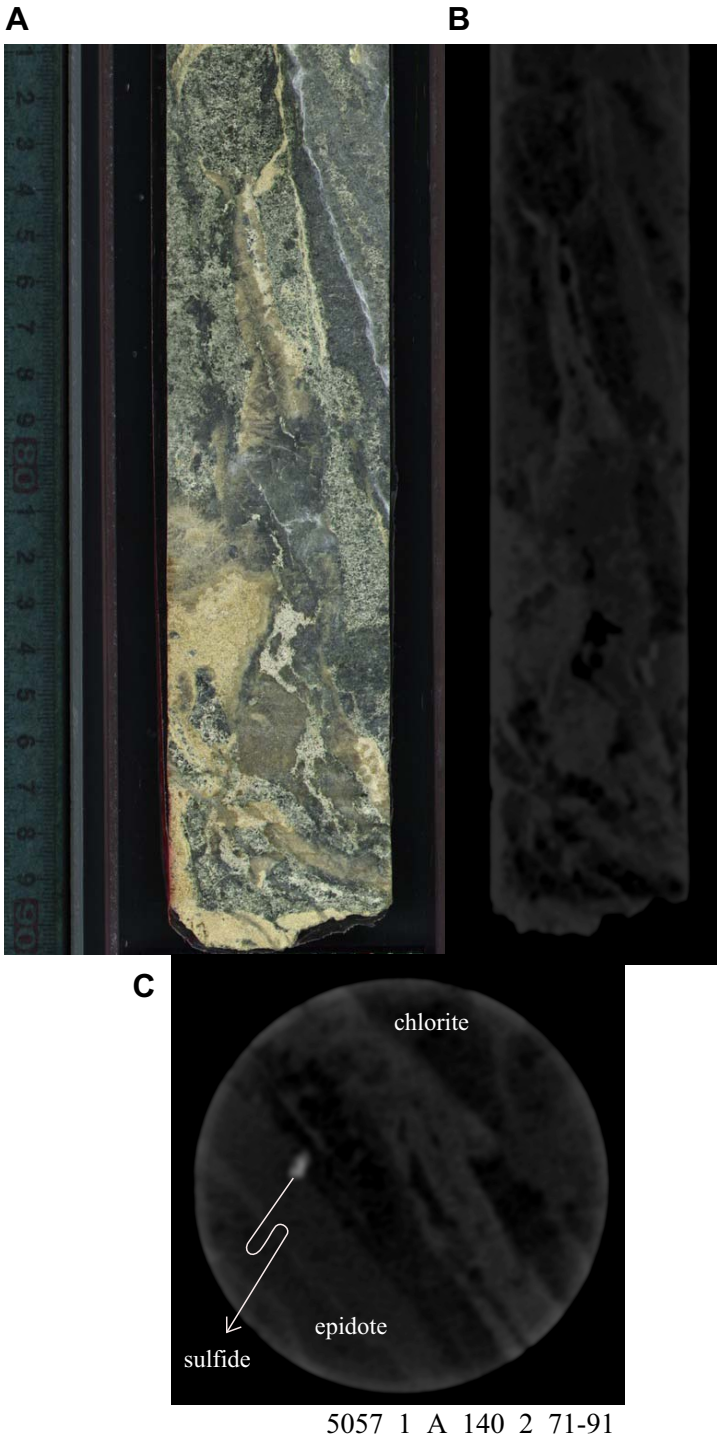

5057_1_A_140_2_71-91

Figure F50. Examples of fault breccias. All of these examples contain clasts of gabbro within a fine-grained matrix of alteration minerals.

Figure F51. Example of narrow and discrete ultracataclastic layers of thickness up to 2–3 cm. **A.** Two logged cataclastic zones (47–49 cm and 59–61 cm). **B.** Close-up of the ultracataclastic zone showing the intense comminution and alteration of the host gabbro. **C.** Ultracataclastic zone shown above (PPL). Multiple sharp slip surfaces cut a fine-grained cataclasite composed of epidote, prehnite, chlorite, clay, and quartz.

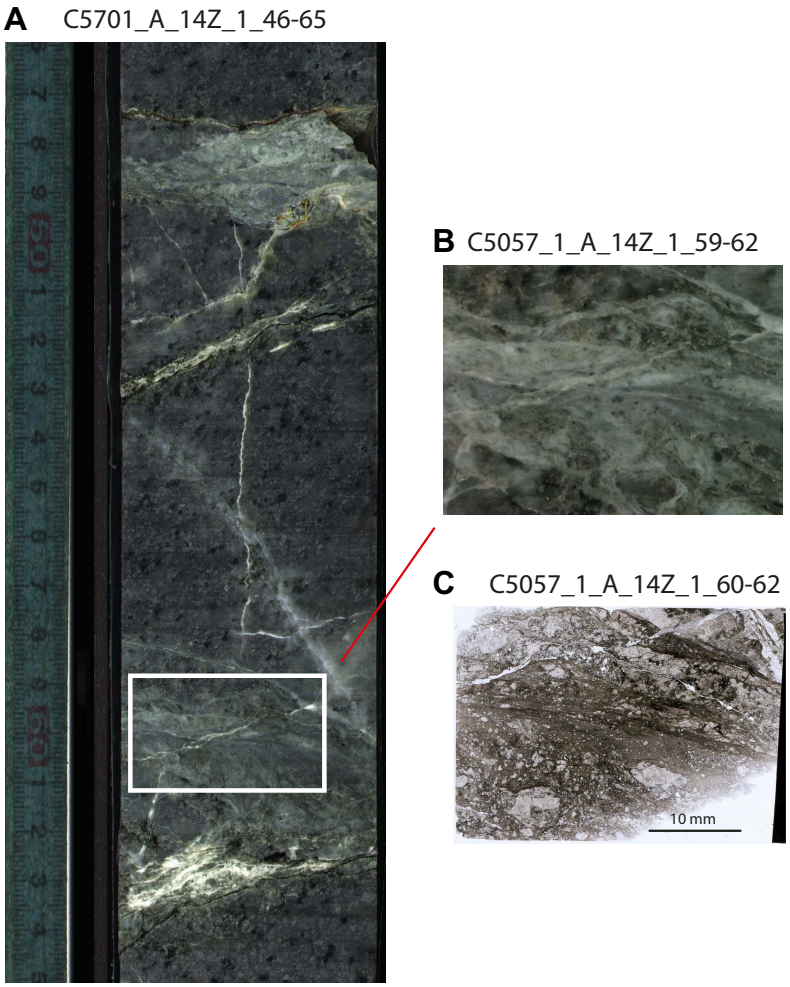

Figure F52. A. Core interval with logged fault zone associated to ultracataclasite and veining. **B.** Close-up of the fault zone showing multiple episodes of crack-and-seal (with prehnite and anhydrite filling) and shearing. **C.** Close-up showing pull-apart microstructure filled with sulfide. **D.** Photomicrograph of the fault zone (48-4, 6.5–11 cm; TS 29; PPL). Foliated ultracataclasite is superposed by en echelon sets of tension gashes.

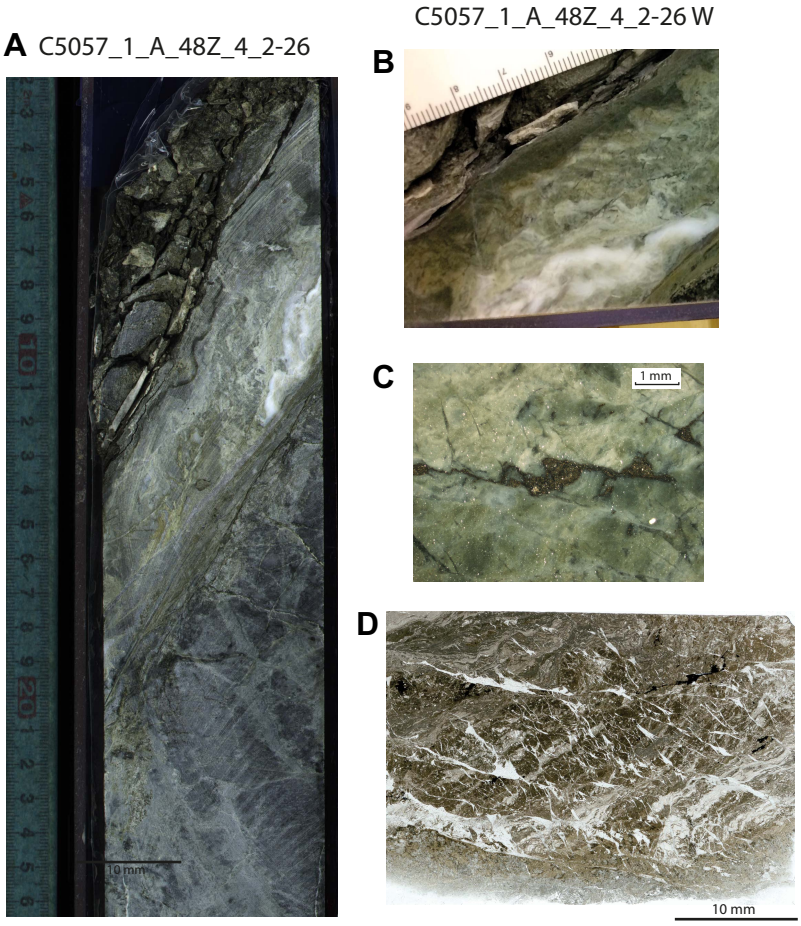

Figure F53. A. Core interval with a multilayered cataclastic fault zone. **B.** Close-up showing the sharp contact between the foliated cataclasite/ultracataclasite and the host gabbro. The gabbro shows intense comminution with blastesis of epidote and prehnite. **C.** Photomicrograph of the fault zone showing superposed layers of mylonite, cataclasite, and fluidized ultracataclasite deformed by shear bands and multiple slip zones (32-2, 26–33 cm; TS 19; PPL).

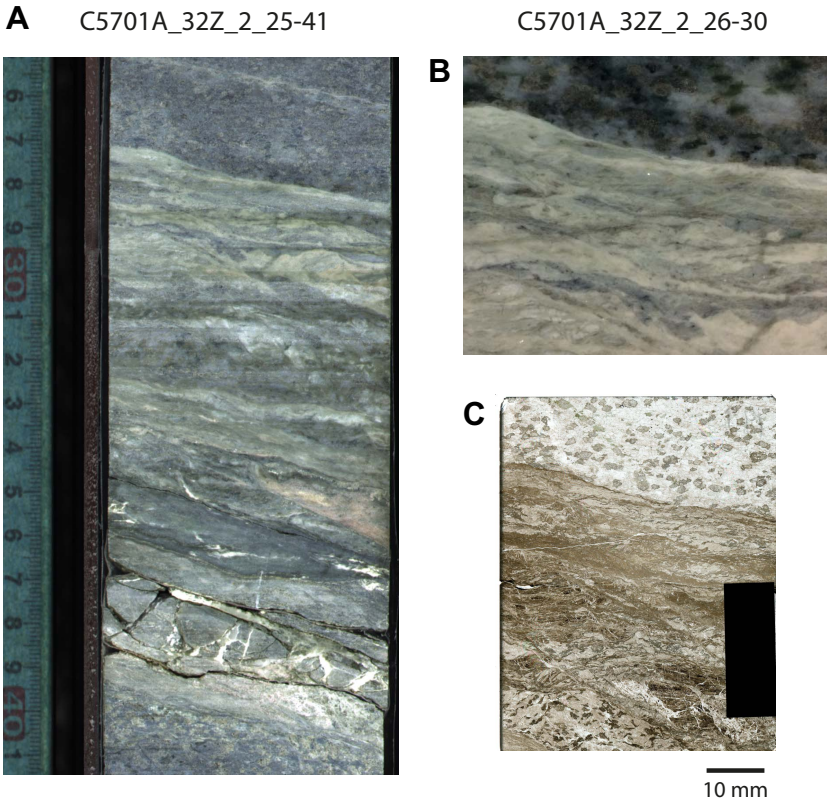

Figure F54. A, B. Two core intervals with hydrothermal breccia/cataclasite in fault zones. **C, D.** Close-up and photomicrograph of fluidized texture of the breccia/cataclasite. The matrix of the breccia contains fragments of wall rocks with different degrees of recrystallization. The matrix is composed mostly of fragments of the host rock, amphibole, epidote, and chlorite (Section 141Z-1; PPL).

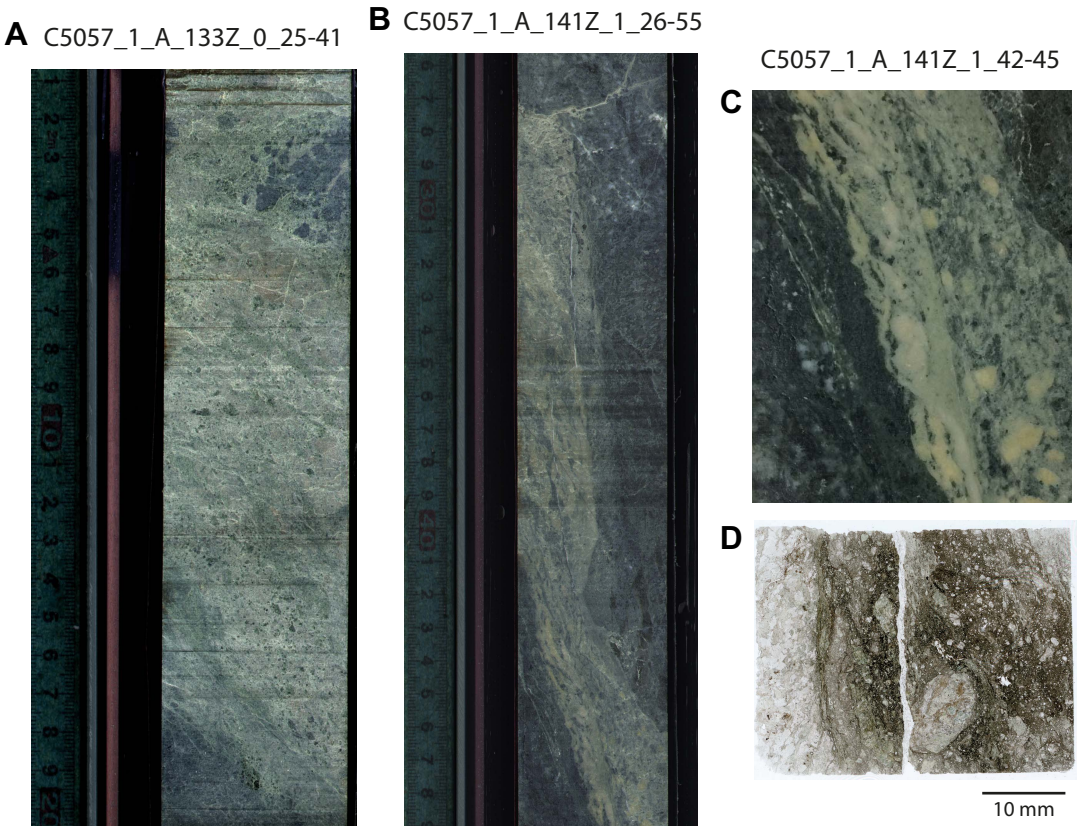

Figure F55. **A.** Location of main fault and cataclastic zones based on the cataclastic deformation intensity. There are 7 main zones of brittle deformation. **B.** Brittle fabric intensity. **C.** Fracture zone thickness. **D.** Preliminary interpretation of major fault zones.

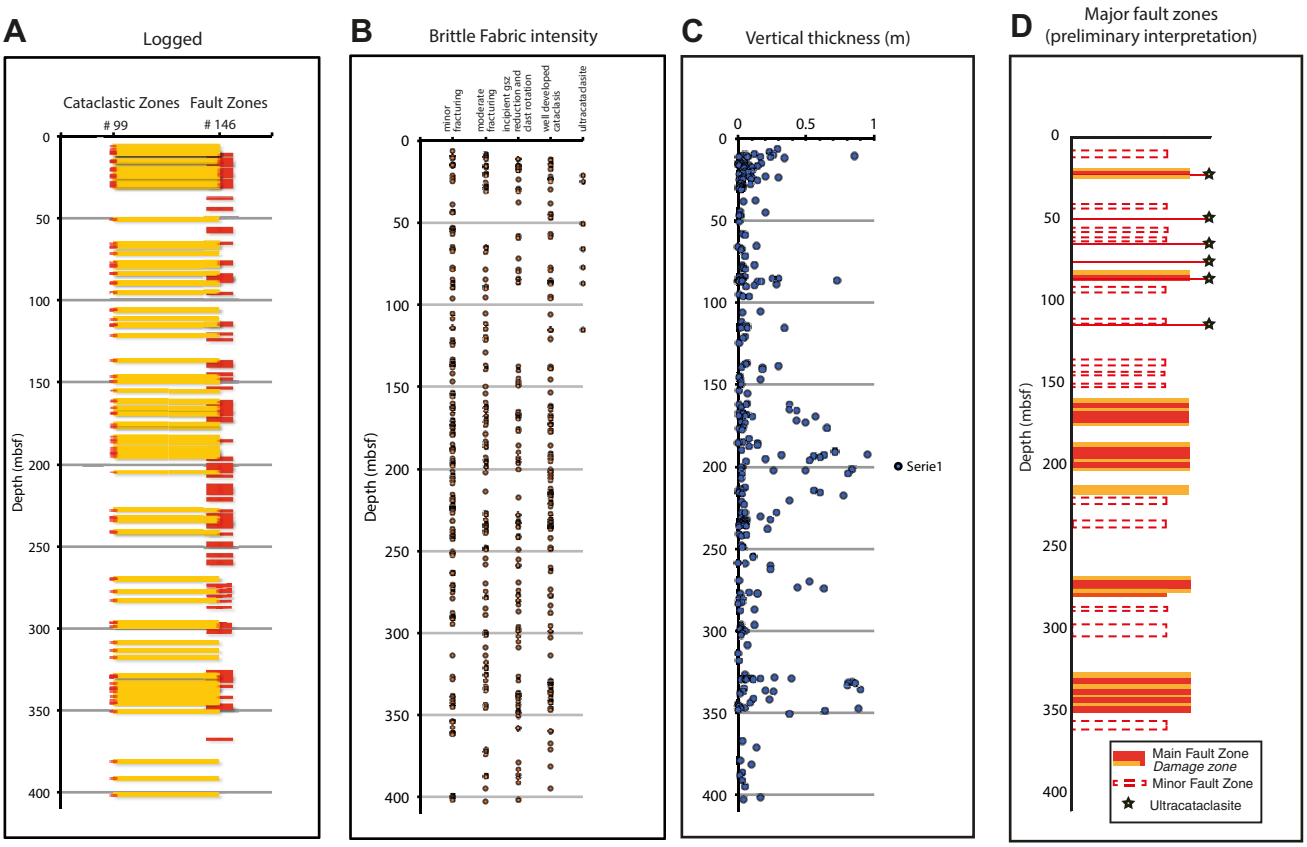

Figure F56. A. Real dip angle with depth. **B.** Rose diagrams of real dip angle. **C.** Sense of shear determined for faults and structures within faults (e.g., veins). **D.** Plunge of slickenfibers plotted vs. dip of slip plane. The majority of structures are dip-slip, to a lesser extent oblique-slip, and even fewer strike-slip.

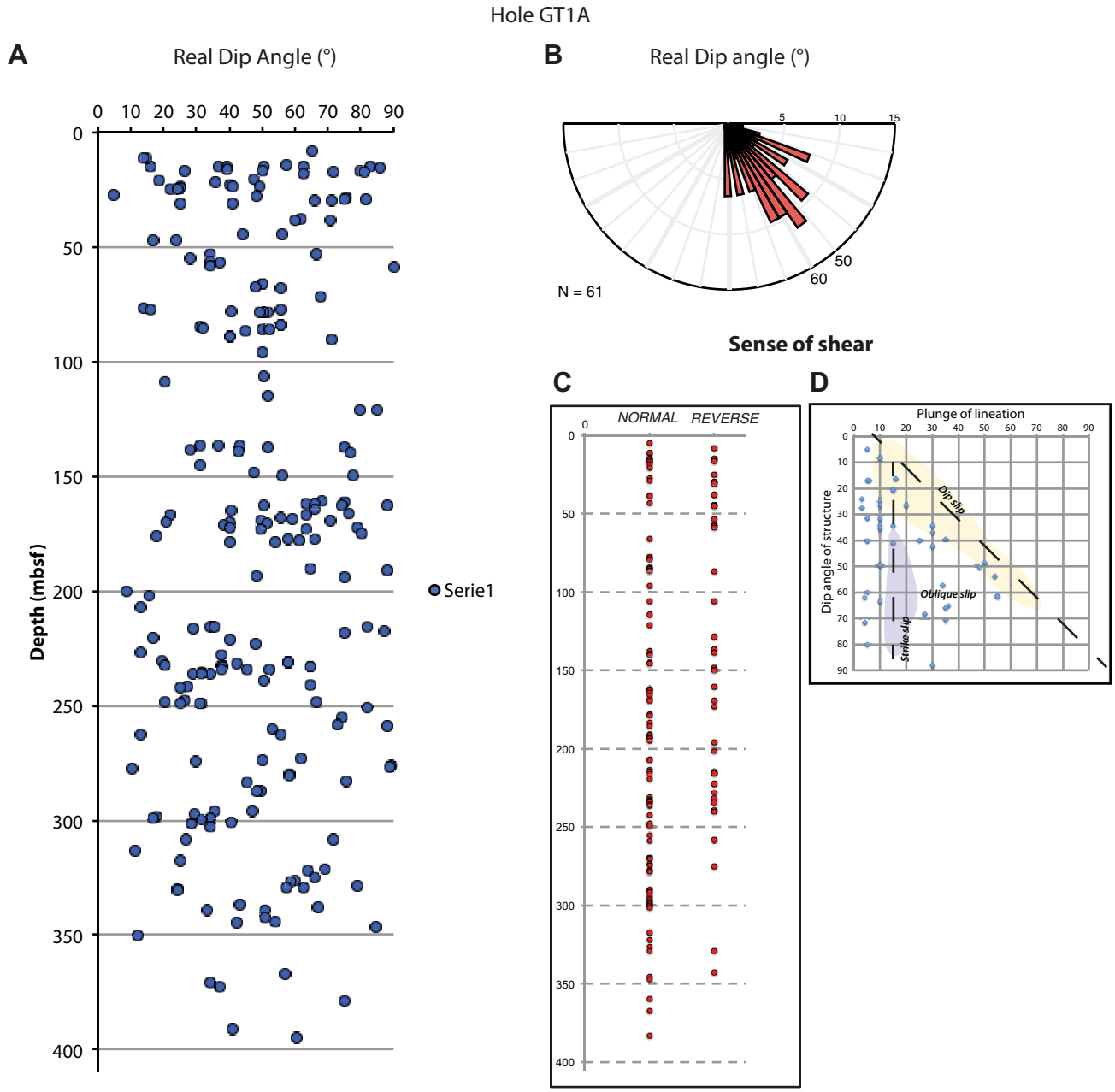

Figure F57. Vein dips with depth and vein dip frequency.

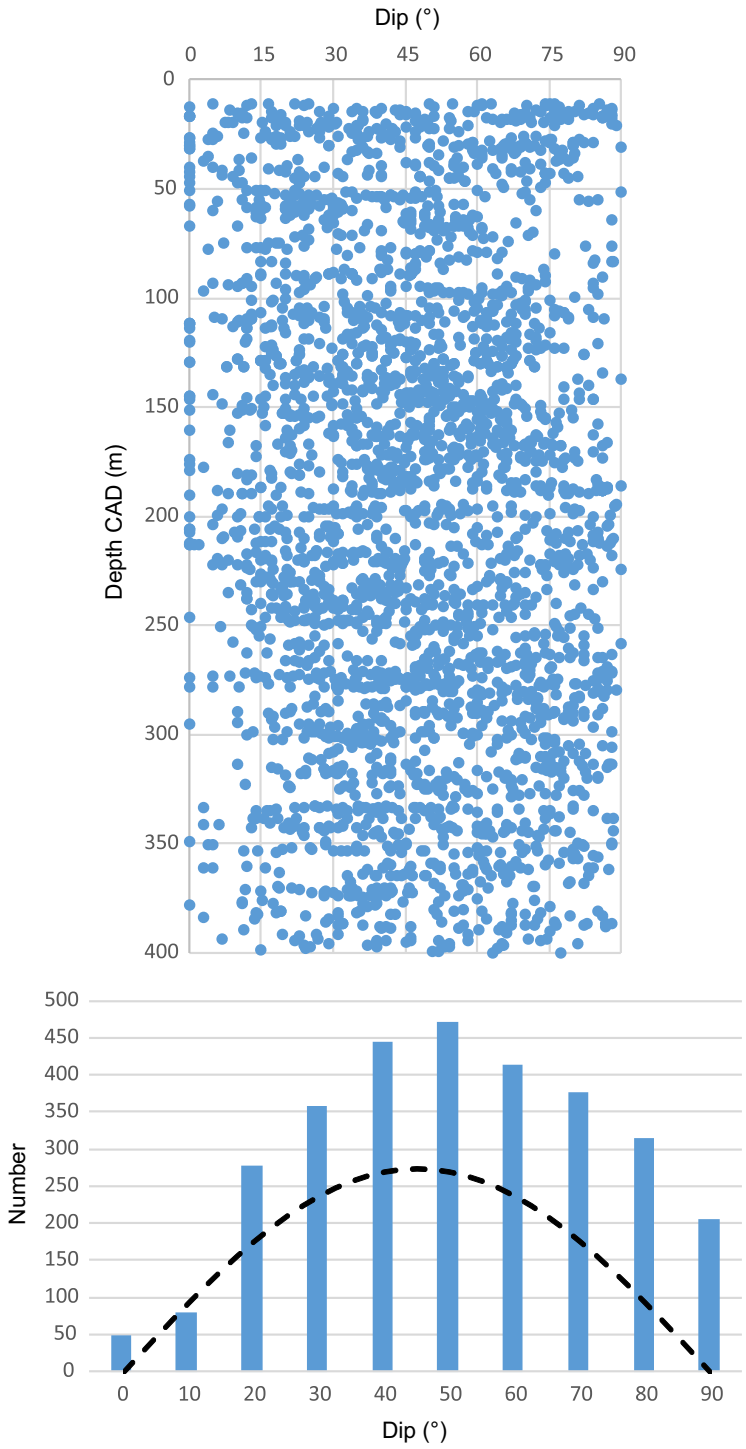

Figure F58. A. Plunge does not change much with depth and tends to be moderate to shallow. **B.** Relationship between dip and plunge angle. Most of the plunges have a magnitude similar to that of dip, indicating most of the veins recorded a dip-slip motion. The other veins mostly recorded oblique-slip motion. **C.** Dip magnitude and plunge magnitude show a similar relation to (B). However, 6 veins record a strike-slip component, mostly in the upper part of the hole.

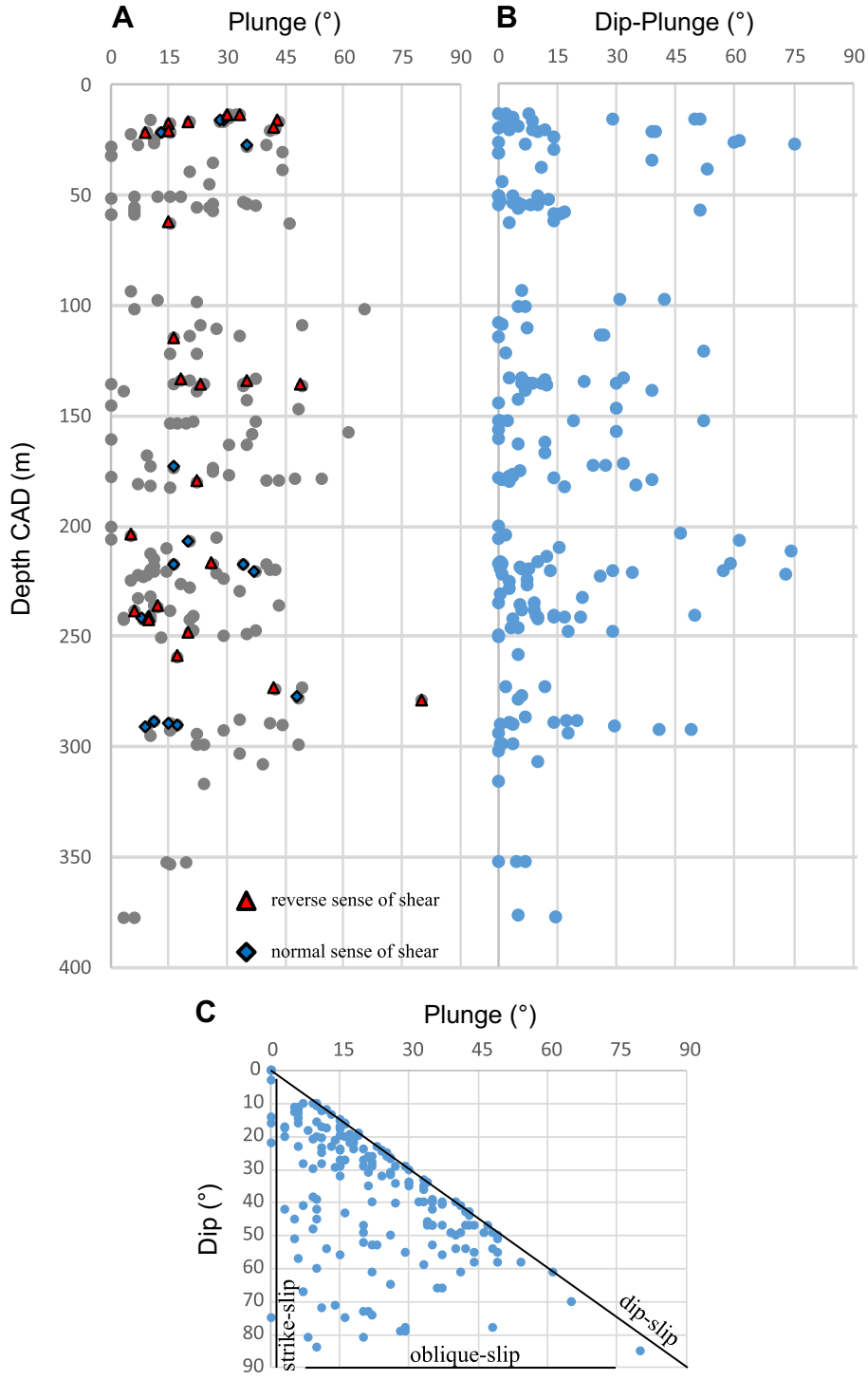

Figure F59. Red lines are parallel to the slickenlines. **A.** Actinolite and prehnite vein with slickenlines. The sense of shear is reverse, sinistral. The top of the core is coming out of the page. **B.** Chlorite vein with slickensides. The ruler scale is in centimeters. The top of the core is to the top of the image. **C.** Chlorite vein with clay on top. The top of the core is to the top of the image.

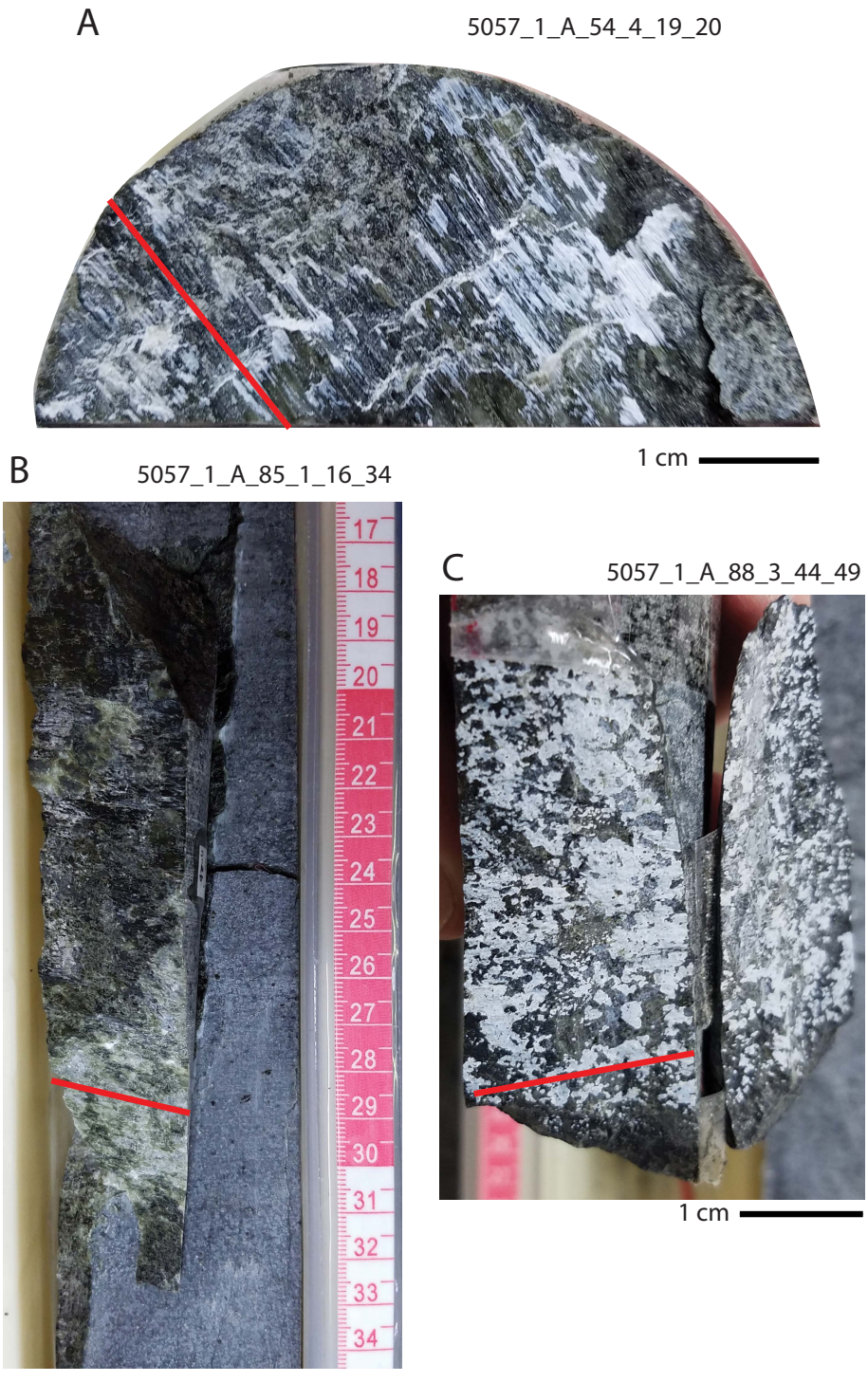

Figure F60. All shear sense indicators recognized in the core. Both normal and reverse sense of shear are recorded throughout the section. The number of slickenlines (open triangles/diamonds) decreases downhole. Reverse sense of shear indicators decrease downhole with the lowermost 75 m dominated by normal sense of shear indicators.

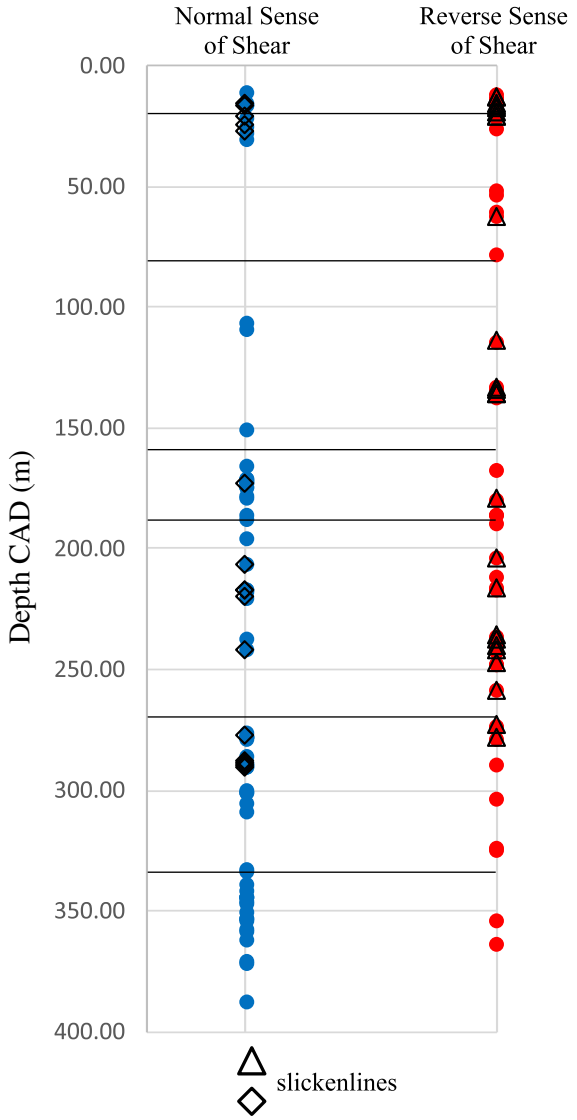

Figure F61. Example of core scan and annotation of core section with both normal and reverse sense of shear. Epidote veins in the upper interval record normal sense of shear, whereas the bottom section records reverse sense of shear. The annotation is enlarged for ease of viewing.

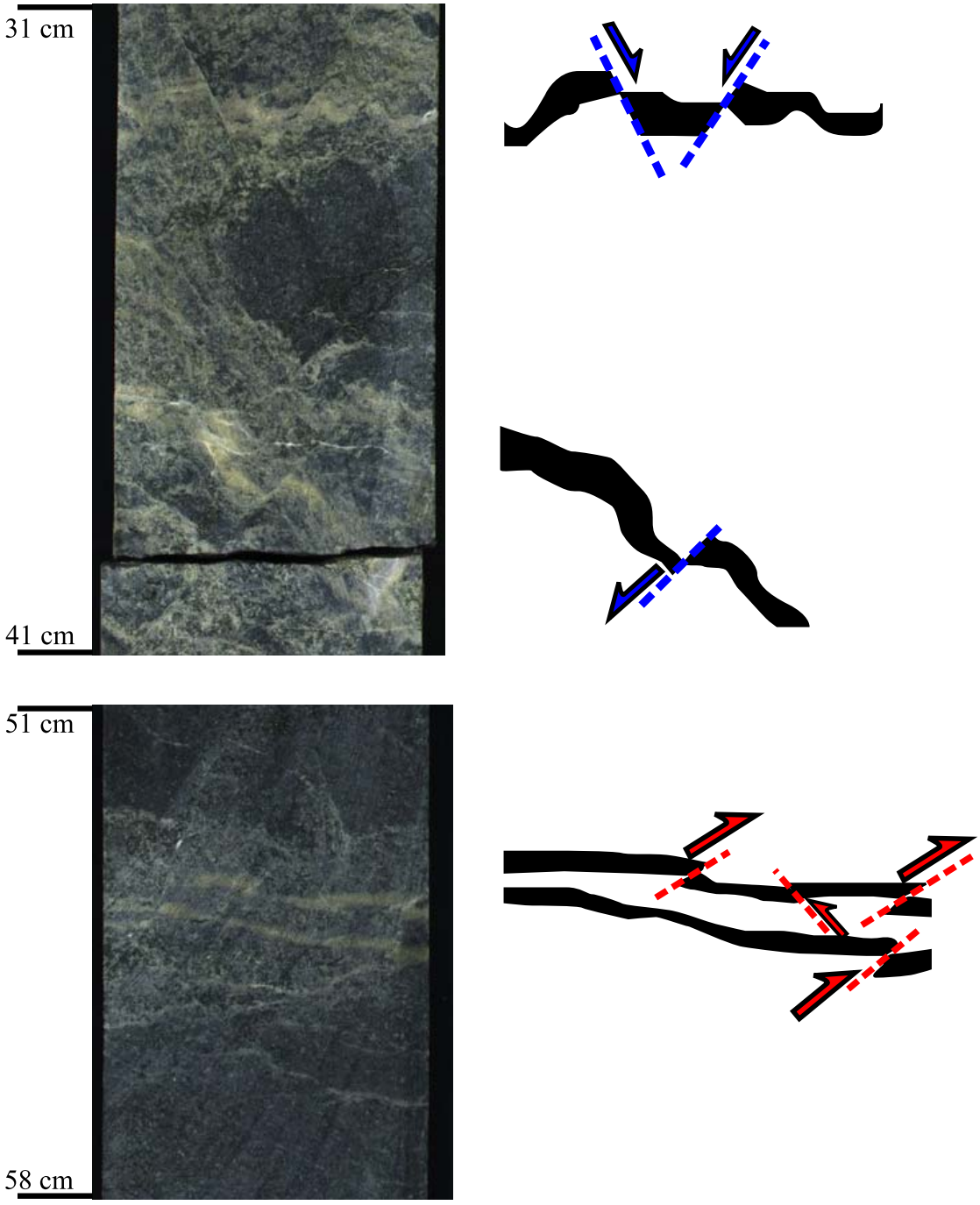

Figure F62. Examples of crosscutting relationships between veins. **A.** Epidote vein offset, with normal sense of shear, by prehnite vein. **B.** Prehnite and chlorite vein offset, with normal sense of shear, by laumontite and chlorite vein. **C.** Clinozoisite vein offset by a vertical prehnite and chlorite vein with sinistral sense of shear. **D.** Prehnite and chlorite vein offset by another prehnite and chlorite vein with a reverse sense of shear.

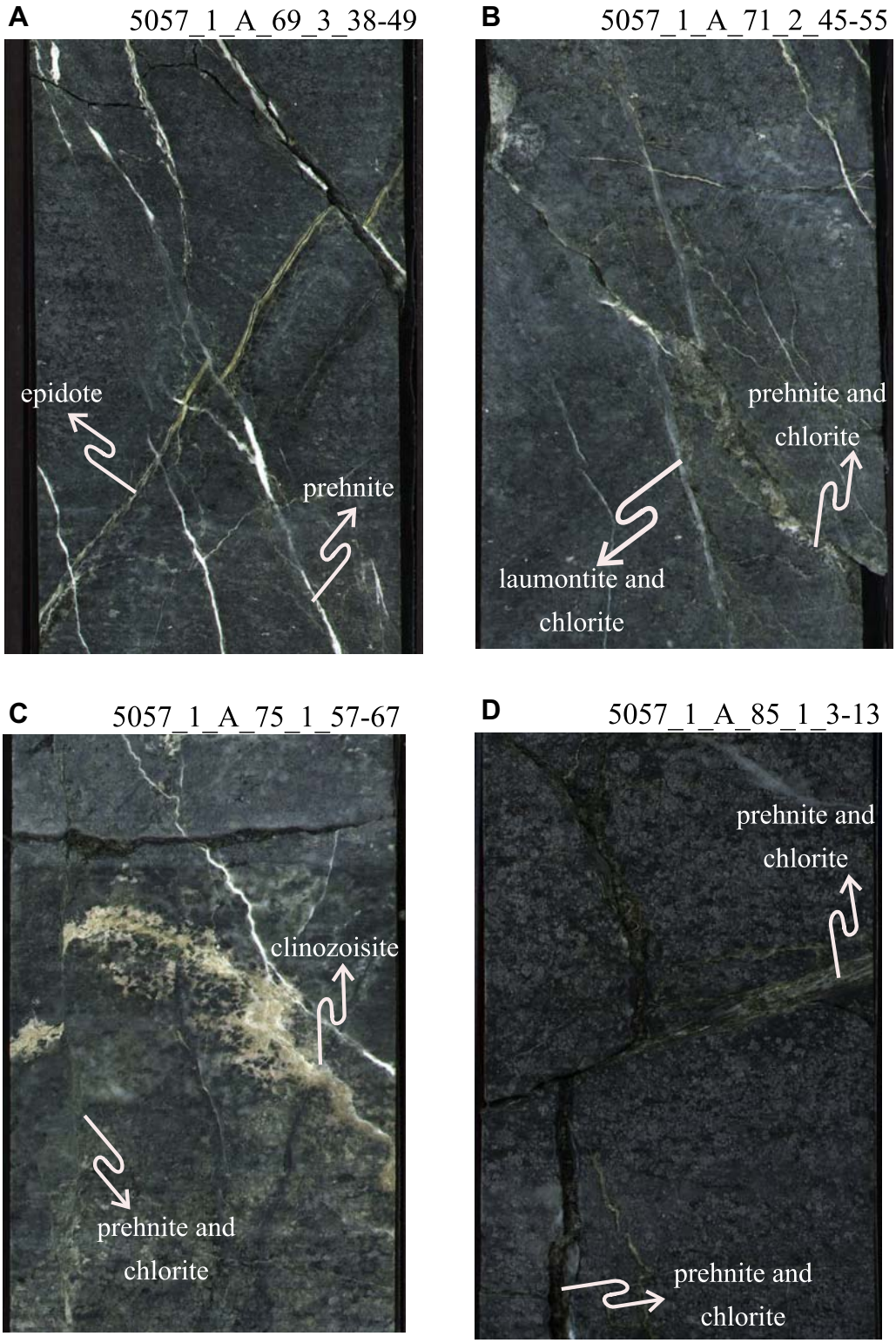

Figure F63. Geochemistry of rocks differentiated by rock type as logged: Mg# vs. Ca#; Mg# vs. Cr; Mg# vs. Y; Mg# vs. Cr. opx = orthopyroxene. Omani lavas are plotted for comparison. Data sources: V1 magmatism (Alabaster et al., 1982; Lippard et al., 1986; Einaudi et al., 2003; Godard et al., 2003, 2006; Kusano et al., 2012, 2017; MacLeod et al., 2013); sheeted dike complex (Miyashita et al., 2003; Umino et al., 2003; MacLeod et al., 2003).

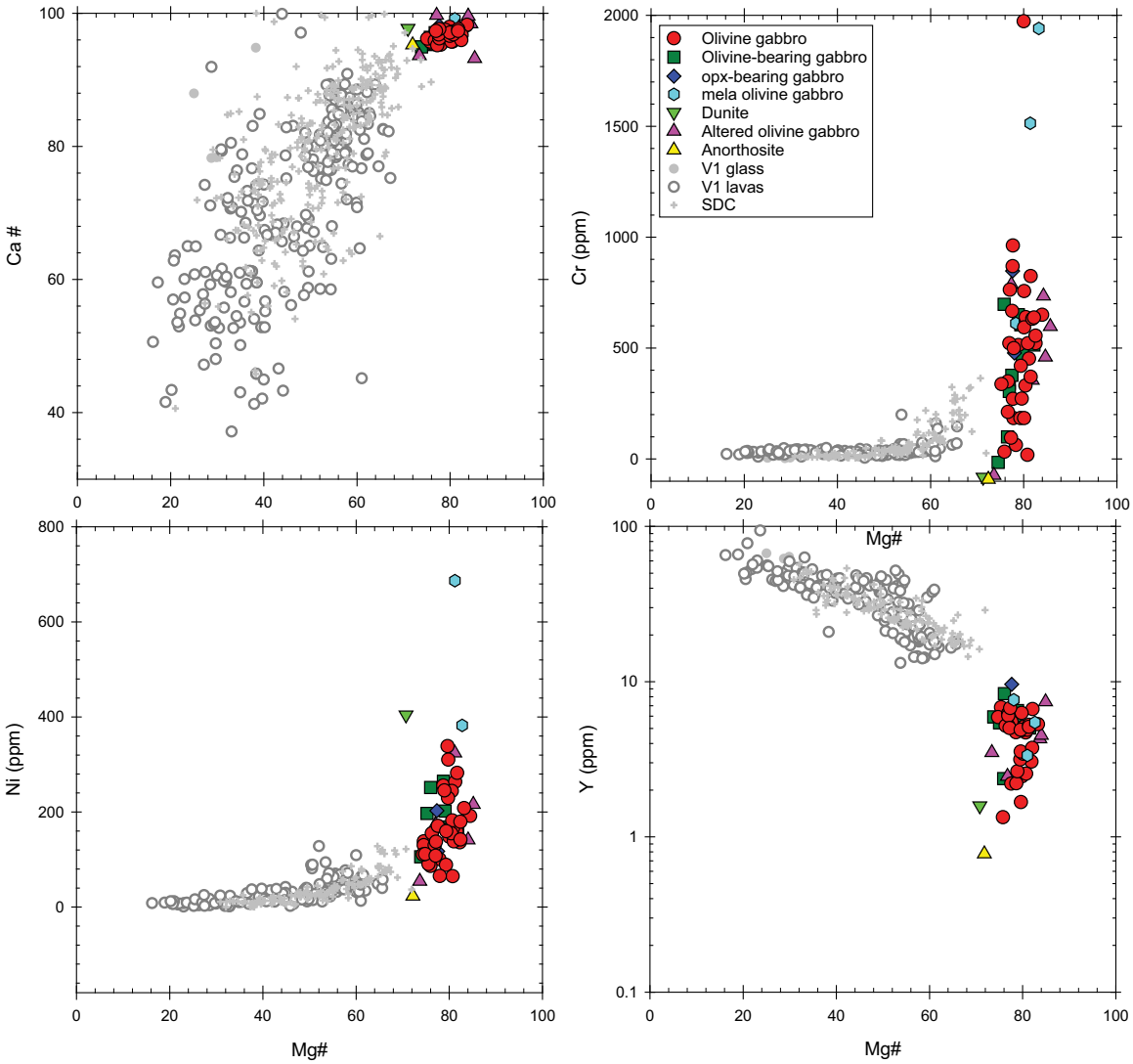

Figure F64. CaO and Al_2O_3 vs. MgO for lithologies recovered in Hole GT1A. Bulk crustal estimates and parental magma composition after Pallister (1984). Mineral chemistry data from Pallister and Hopson (1981), plagioclase plotted range $An_{64.5}$–$An_{88.3}$. Data sources: V1 magmatism (Alabaster et al., 1982; Lippard et al., 1986; Einaudi et al., 2003; Godard et al., 2003, 2006; Kusano et al., 2012, 2017; MacLeod et al., 2013); sheeted dike complex (Miyashita et al., 2003; Umino et al., 2003; MacLeod et al., 2013). V1 fractionation path at 0.4% H_2O modeled using rhyoliteMELTS with similar parameters used by MacLeod et al. (2013).

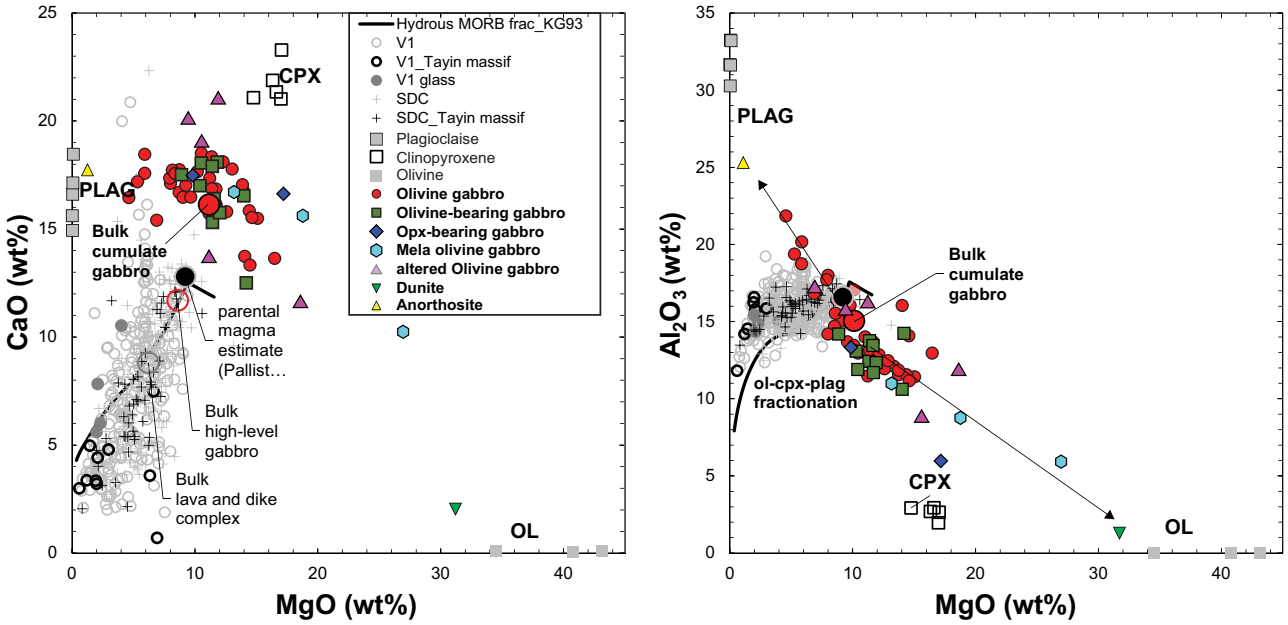

Figure F65. Trace and rare earth elements (REEs) plotted normalized to primitive mantle (Hoffman, 1988). Hole GT1A samples have a light REE–depleted profile and are compared to V1 lavas from Oman (Einaudi, et al., 2003; Godard, et al., 2003) that have flat primitive mantle normalized profiles and higher REE concentrations. All gabbros have higher Sr and display an Sr anomaly that is not present in lavas.

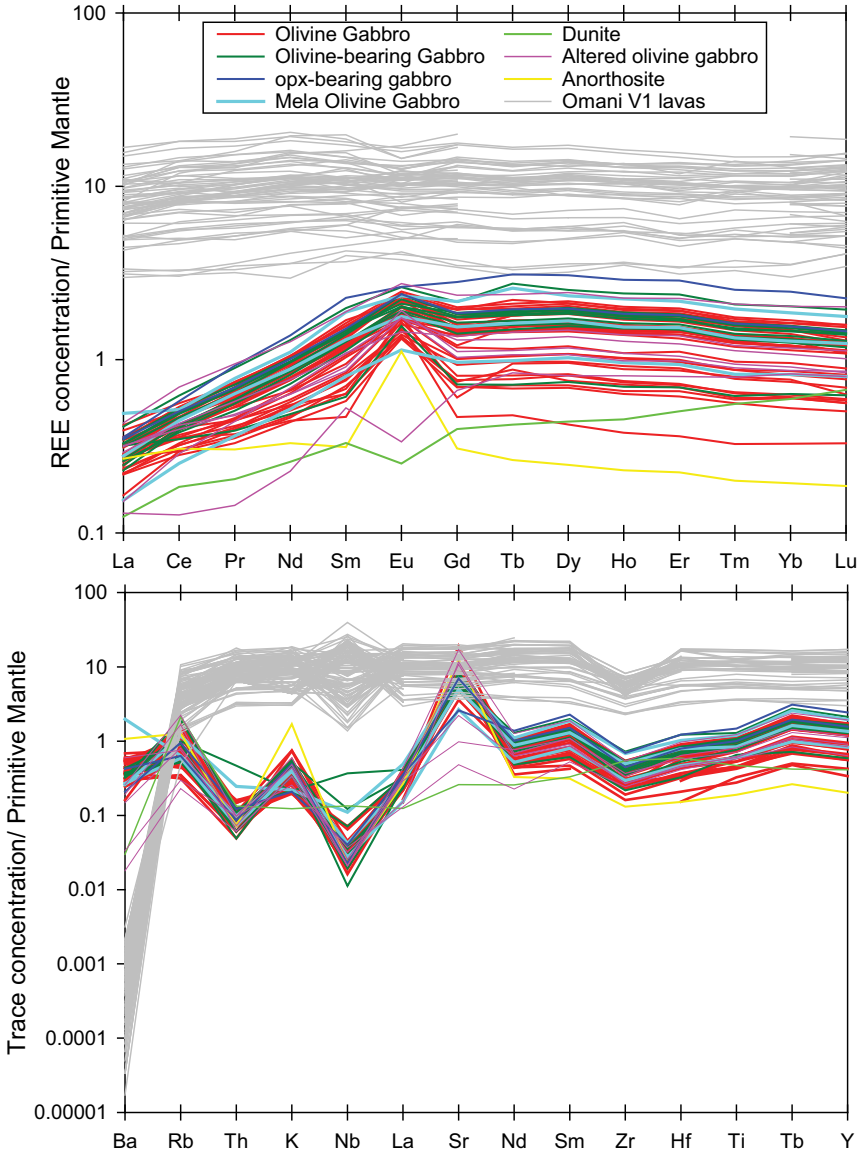

Figure F66. Downhole geochemical variation plotted with modal% olivine, plagioclase, and clinopyroxene. Lithologic unit boundaries labeled I–VII are shown at the depths of the contacts. Altered samples (pink triangles) are not included in the line plot downhole, as these samples have undergone mass change and do not represent the igneous stratigraphy that the profile is compared to. Red circles = olivine gabbro; green squares = olivine-bearing gabbro; blue diamonds = orthopyroxene-bearing gabbro; blue hexagons = mela-olivine gabbro; green triangle = dunite; pink triangle = altered olivine gabbro; yellow triangle = anorthositic gabbro.

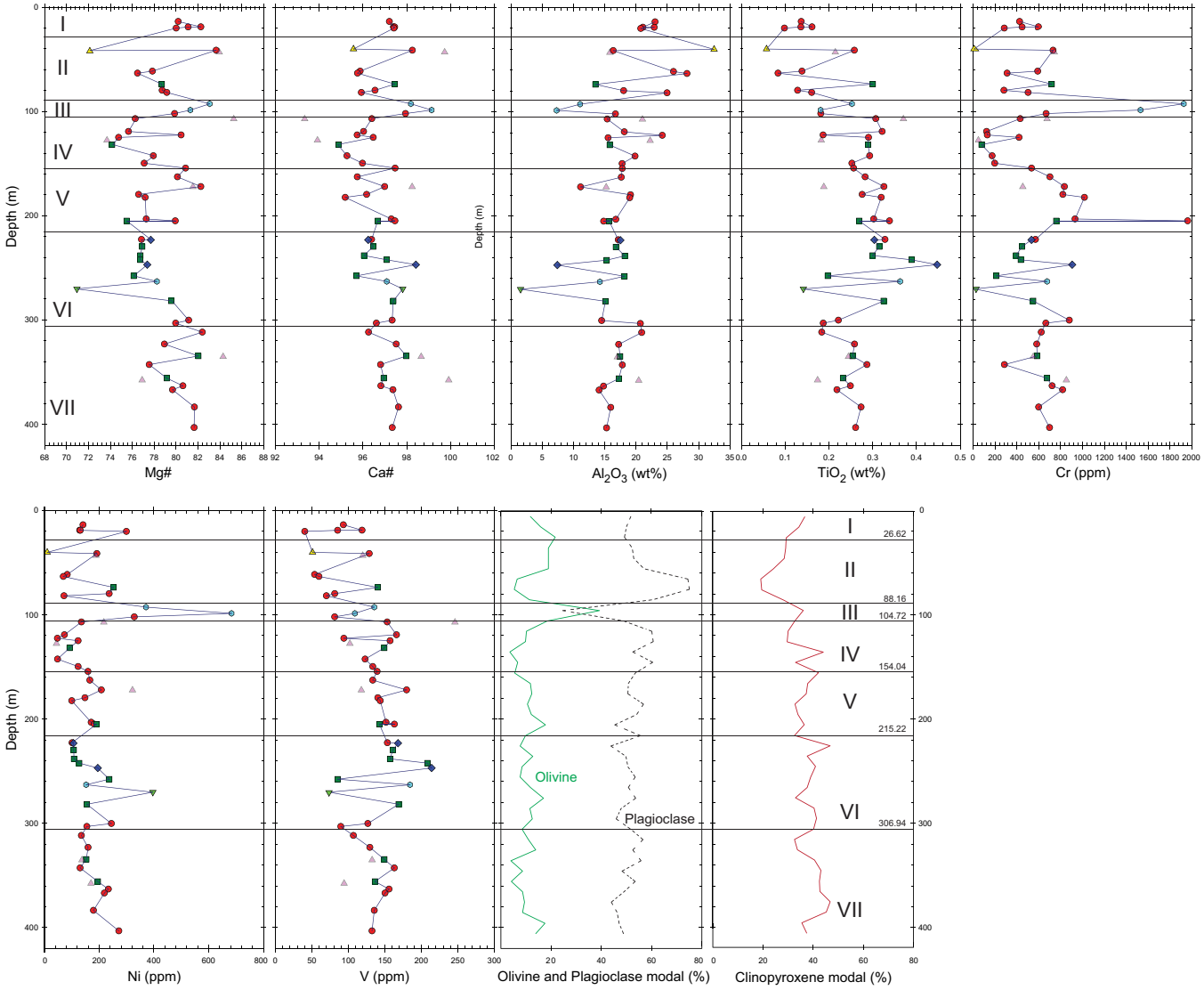

Figure F67. Volatile content of rocks from Hole GT1A, comparison of loss on ignition data with water and carbon dioxide.

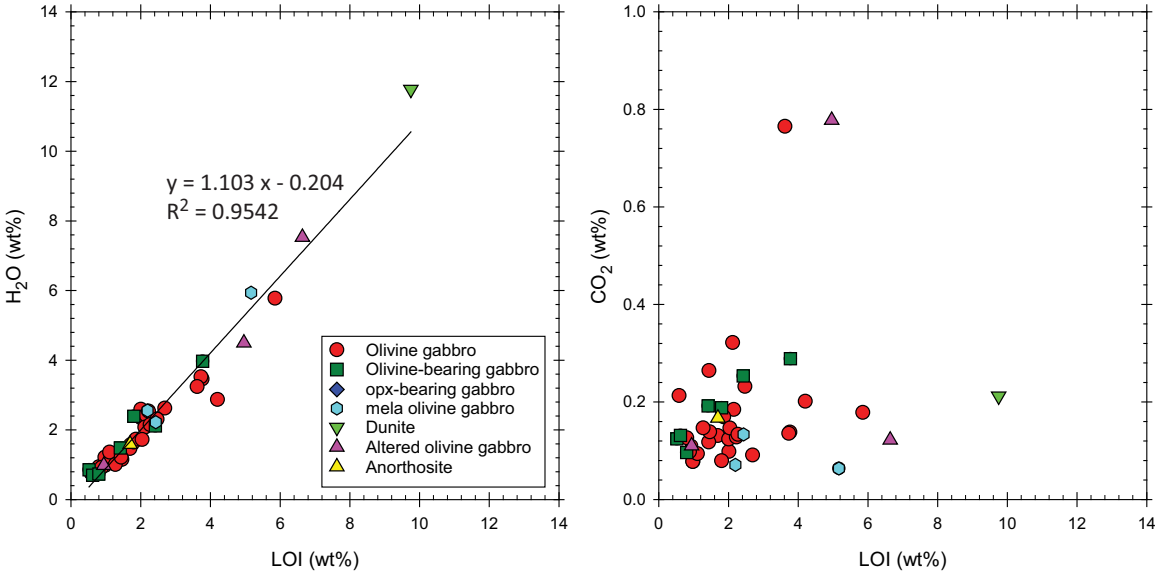

Figure F68. Variation in volatile content (H_2O, CO_2, S, and TIC/TOC) of rocks from Hole GT1A downhole with main fault zones that were identified plotted next to these data.

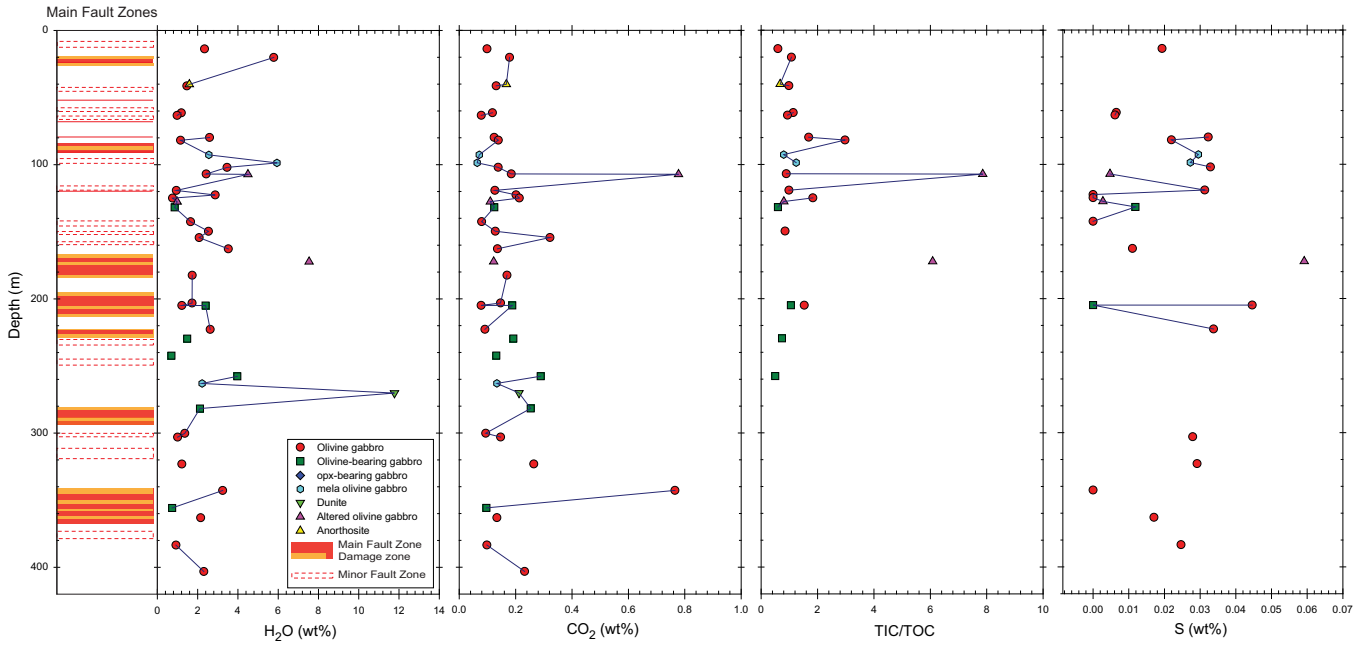

Figure F69. Comparison of "fresh" gabbro and "altered" gabbro from 19Z-3, 45–50 cm (fresh), 20Z-2, 19–33.5 cm (altered), 69Z-3, 76.5–79.5 cm (fresher), and 69Z-5, 0–12.5 cm (altered fault zone). Isocon lines of no mass change are plotted using ΔREE as an immobile reference component. In both examples H_2O, SiO_2, and CaO have increased, whereas Na_2O has decreased. To plot these data, major elements were multiplied by 3–4000 and trace elements 1–3000.

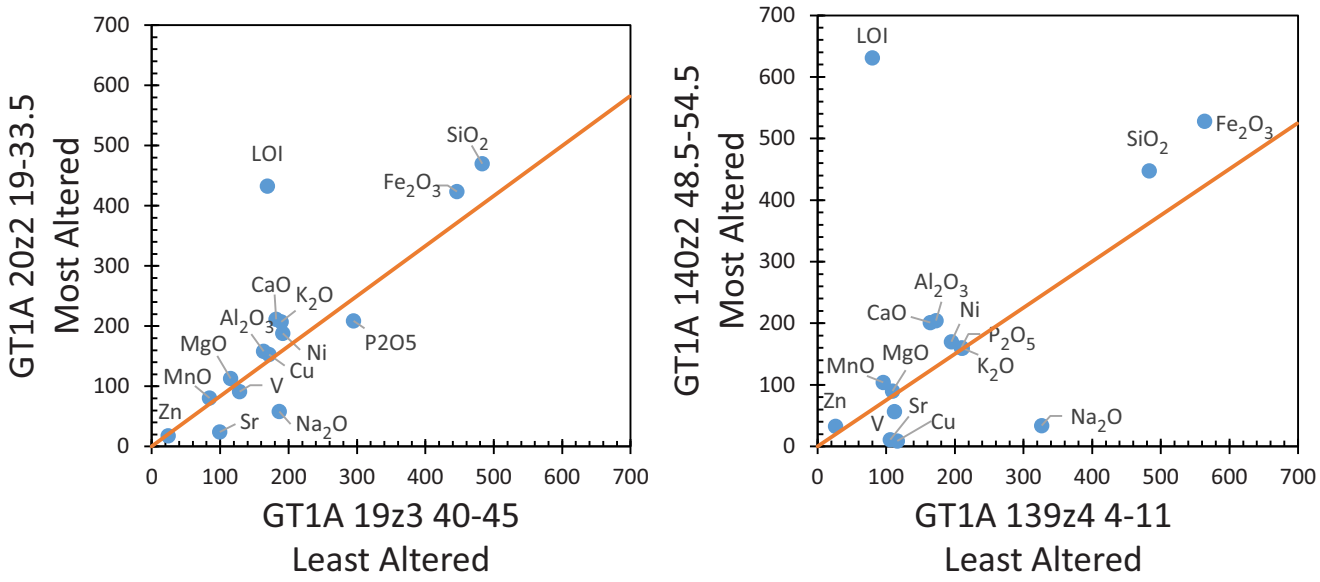

Figure F70. Locations of 7 sections measured by CS-XRF in Hole GT1A.

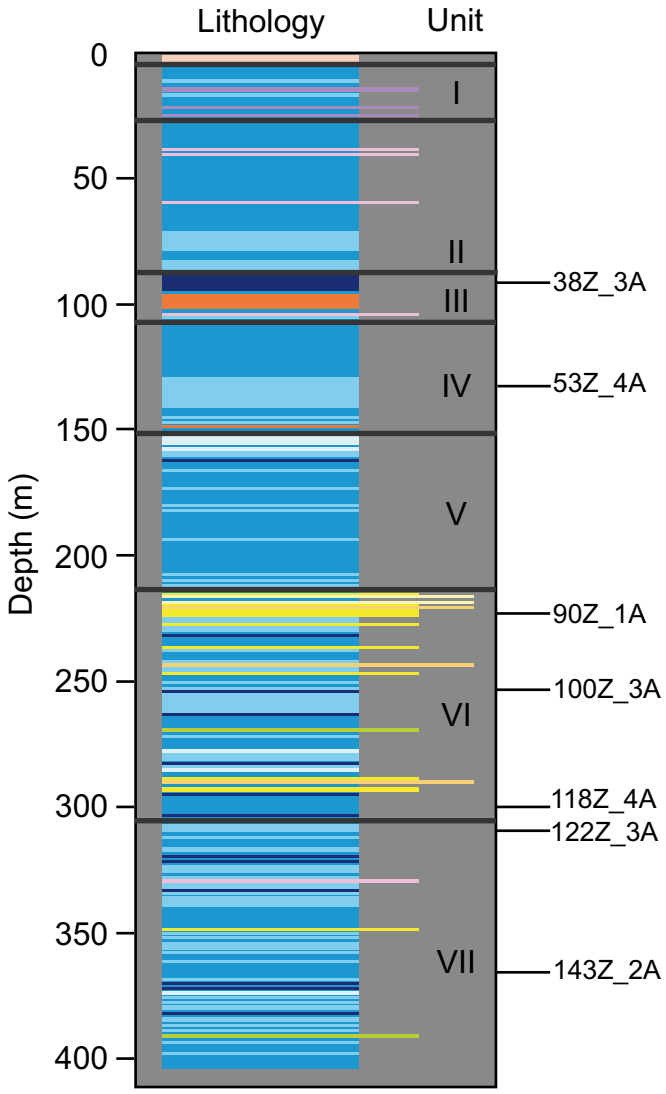

Figure 71. Color-coded images for variations of major elements Cr and Ni (38Z-3, 13–40 cm).

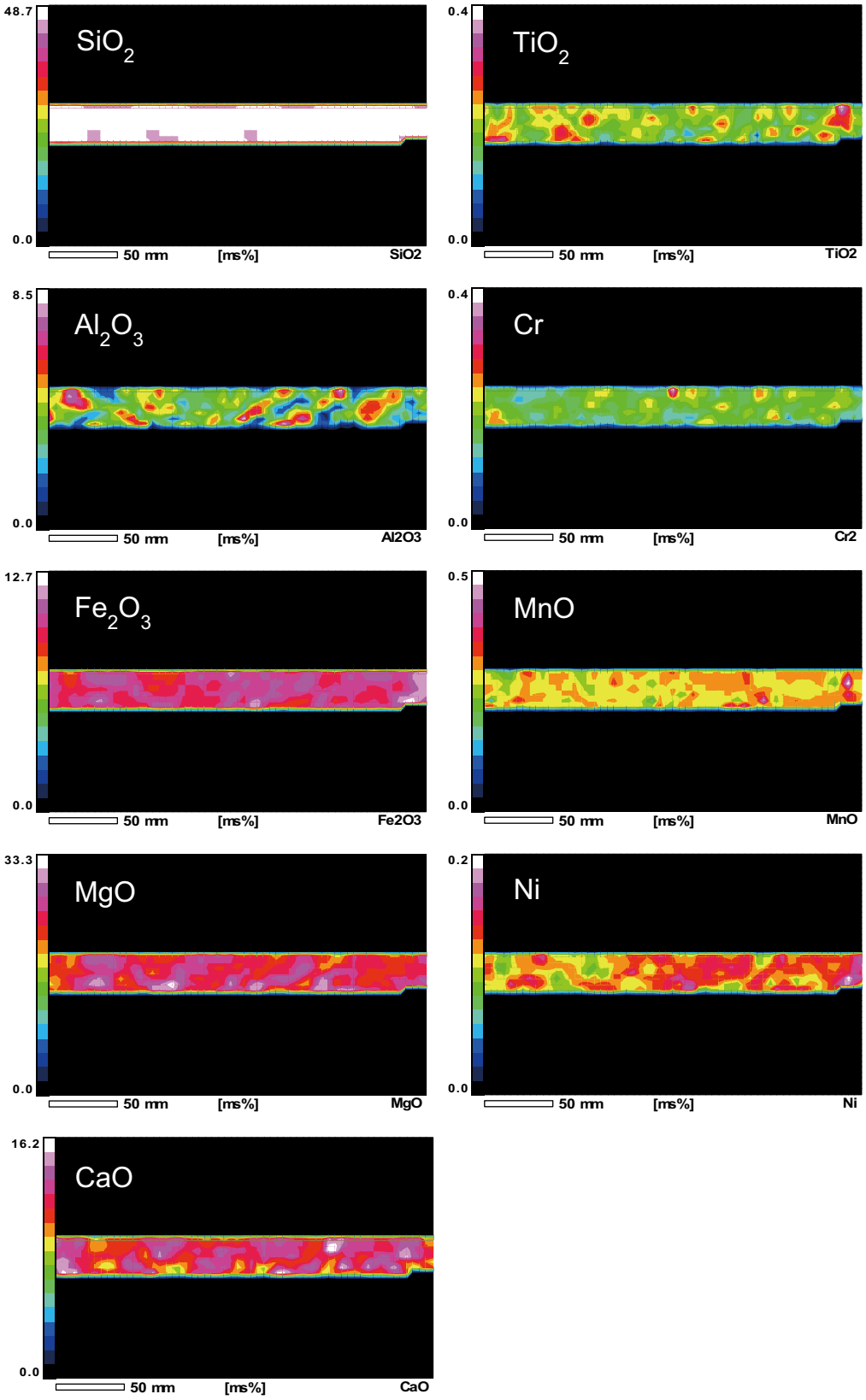

Figure F72. Downhole compositional variations of major elements Cr and Ni (53Z-4, 30–60 cm).

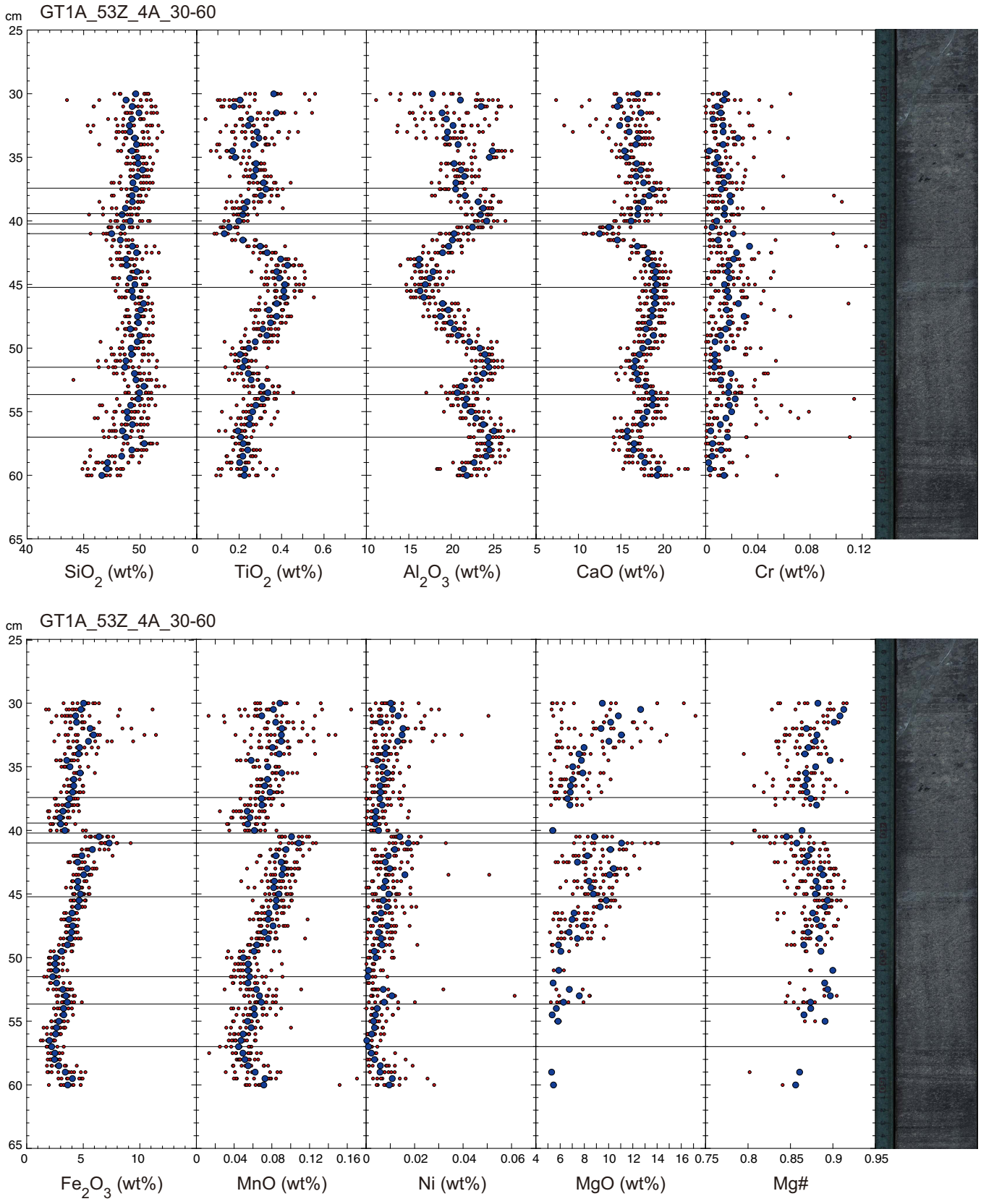

Figure F73. Color-coded images for variations of major elements Cr and Ni (53Z-4, 30–60 cm).

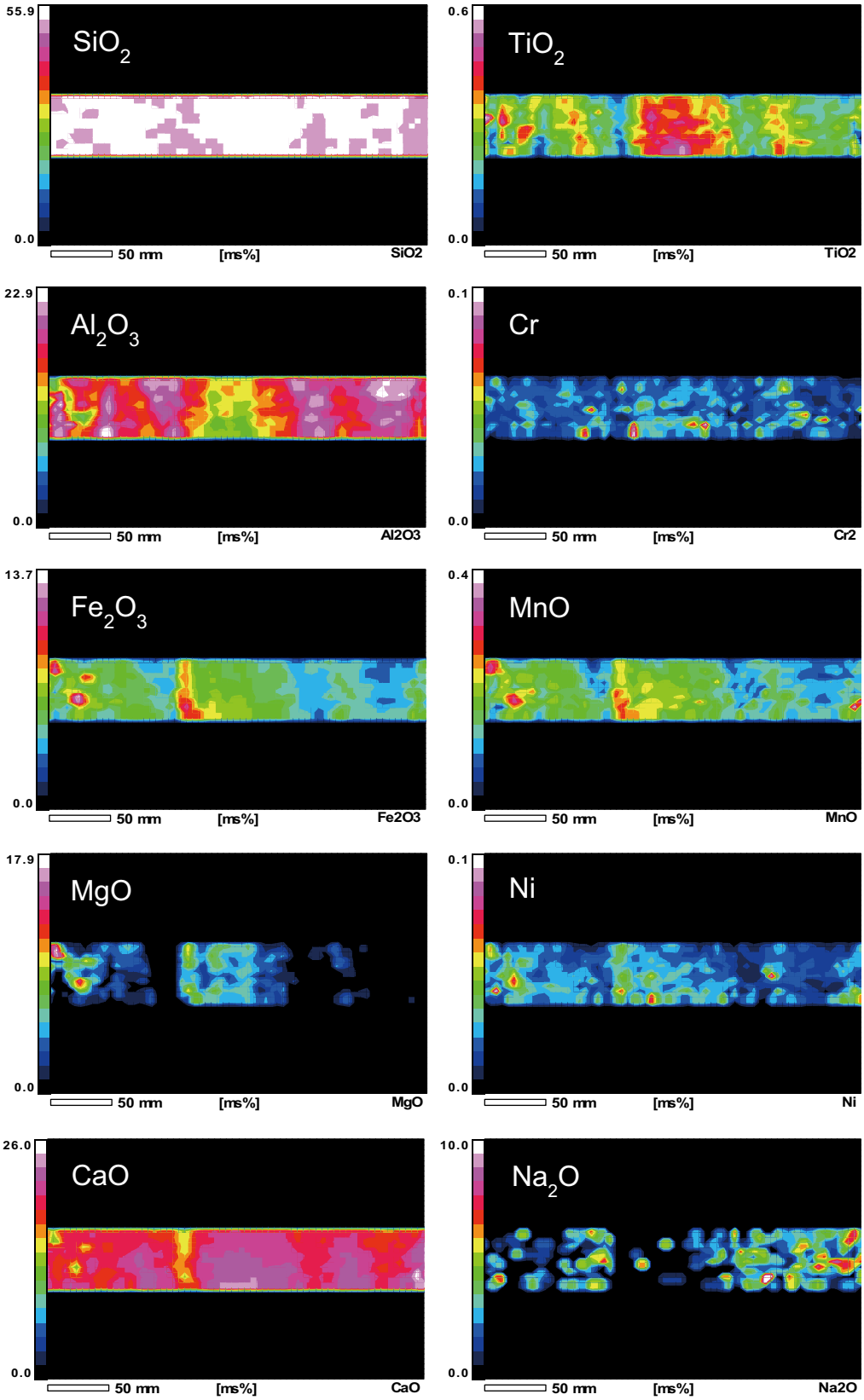

Figure F74. Downhole compositional variations of major elements Cr and Ni (90Z-1, 45–80 cm).

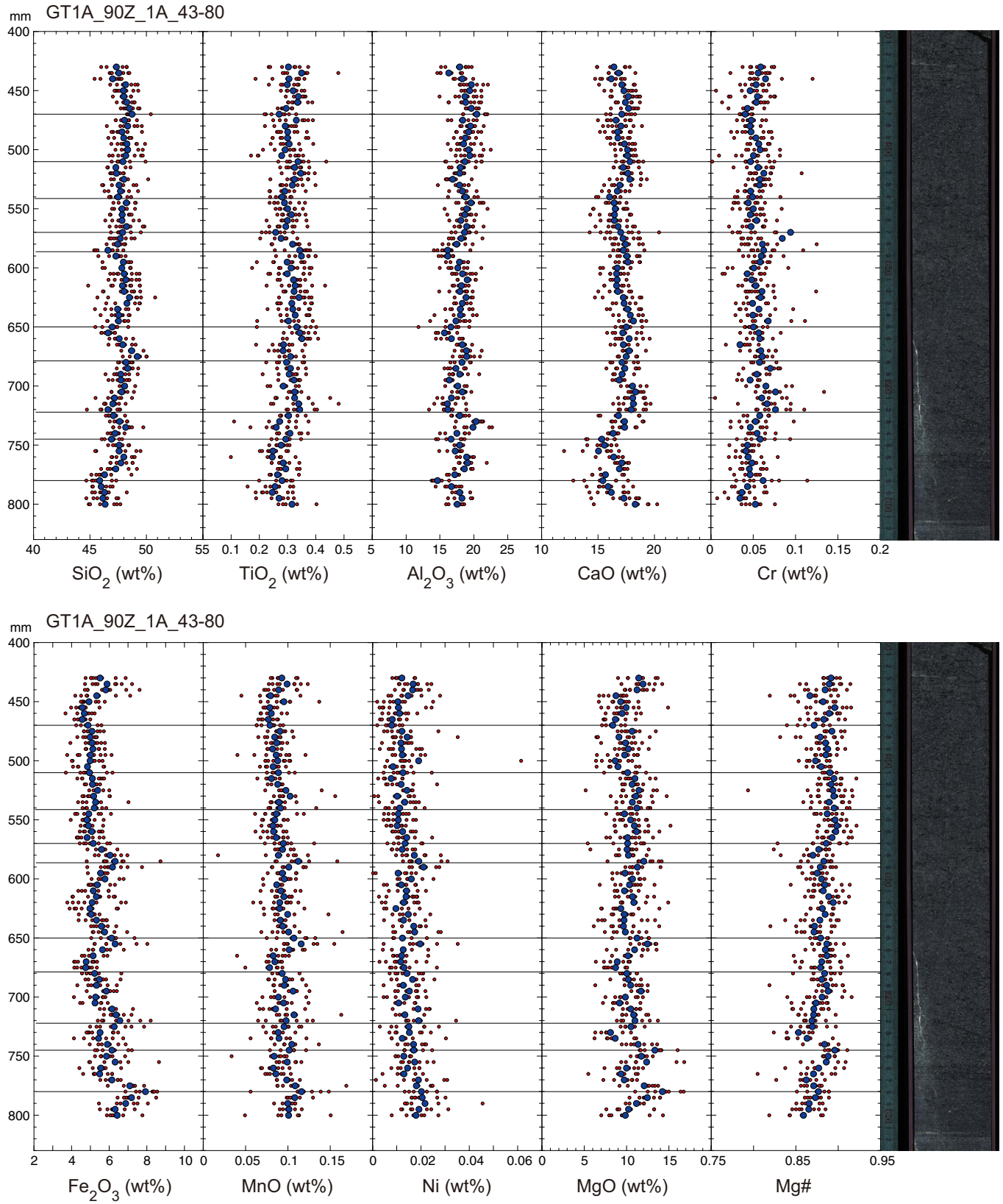

Figure F75. Color-coded images for variations of major elements Cr and Ni (90Z-1, 45–80 cm).

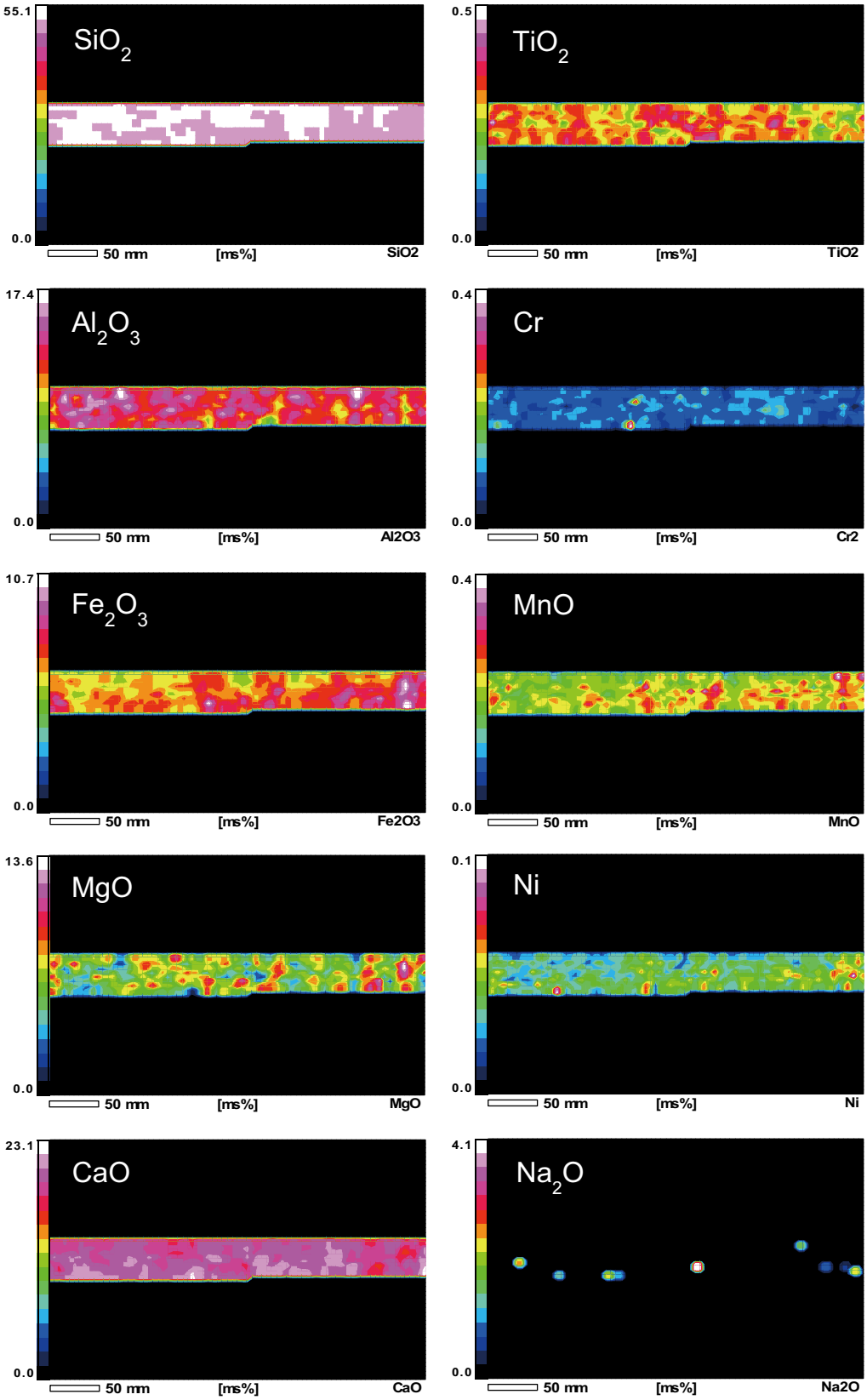

Figure F76. Downhole compositional variations of major elements Cr and Ni (100Z-3, 4.5–60 cm).

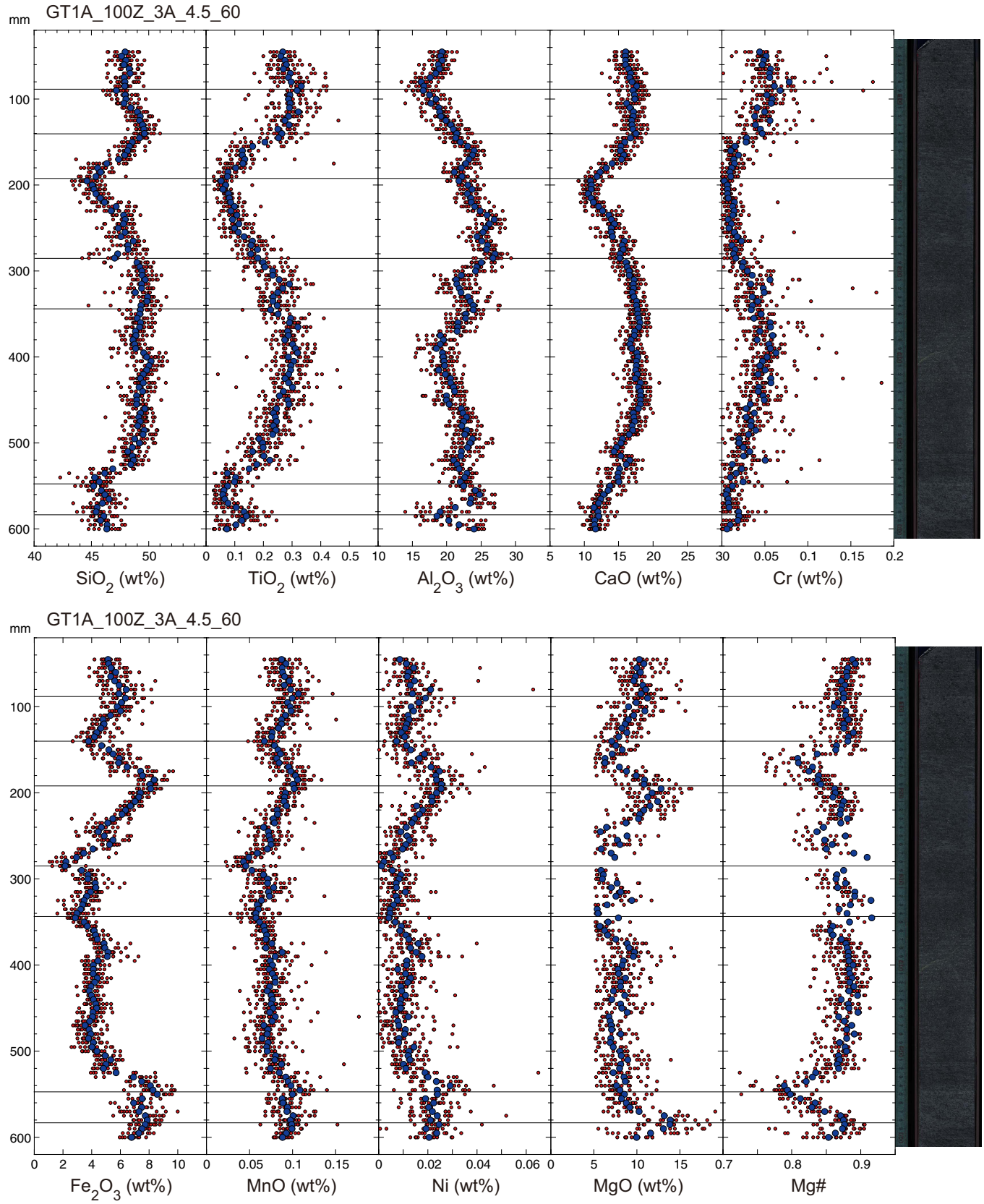

Figure F77. Color-coded images for variations of major elements Cr and Ni (100Z-3, 4.5–60 cm).

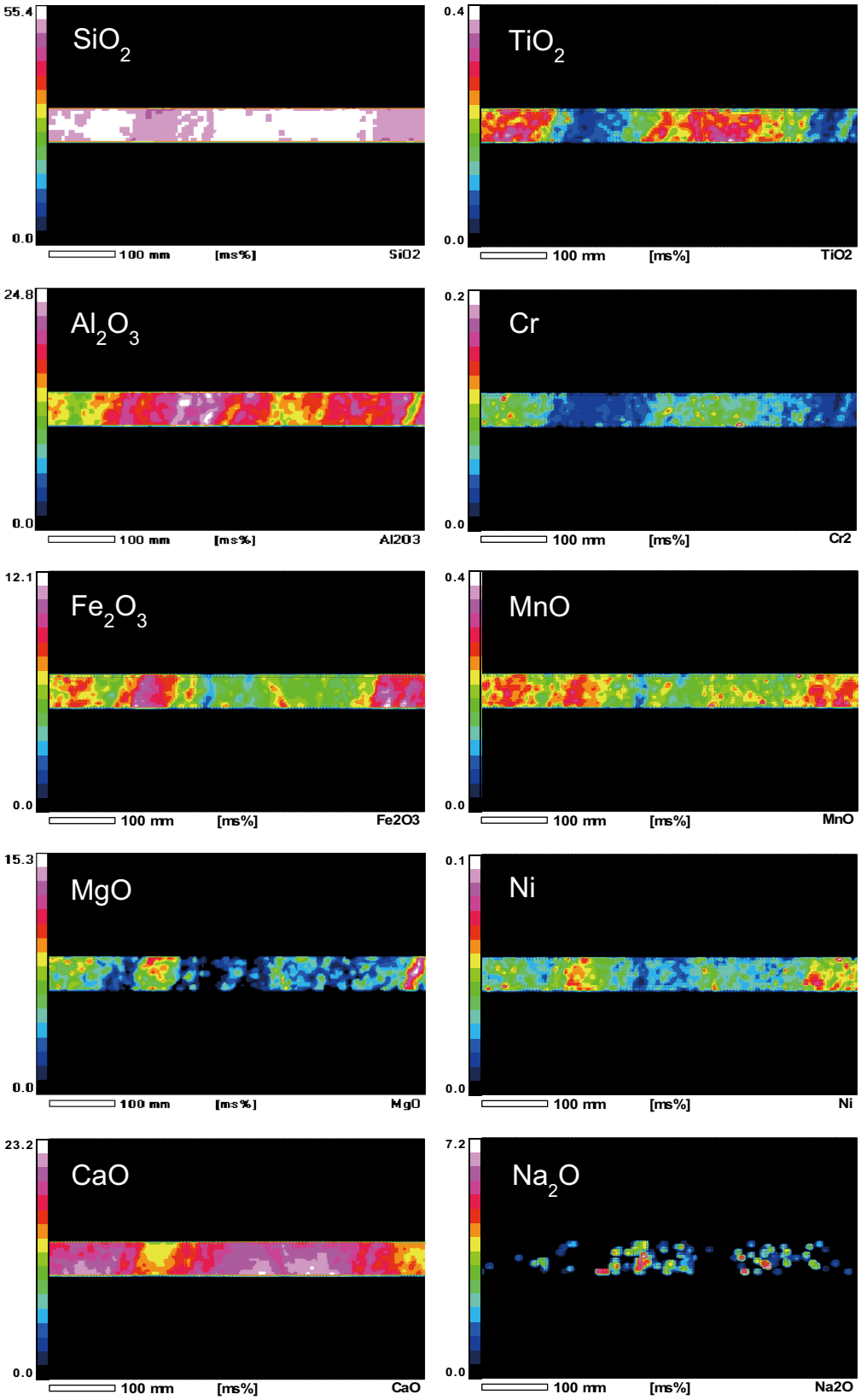

Figure F78. Downhole compositional variations of major elements Cr and Ni (118Z-4, 15–35 cm).

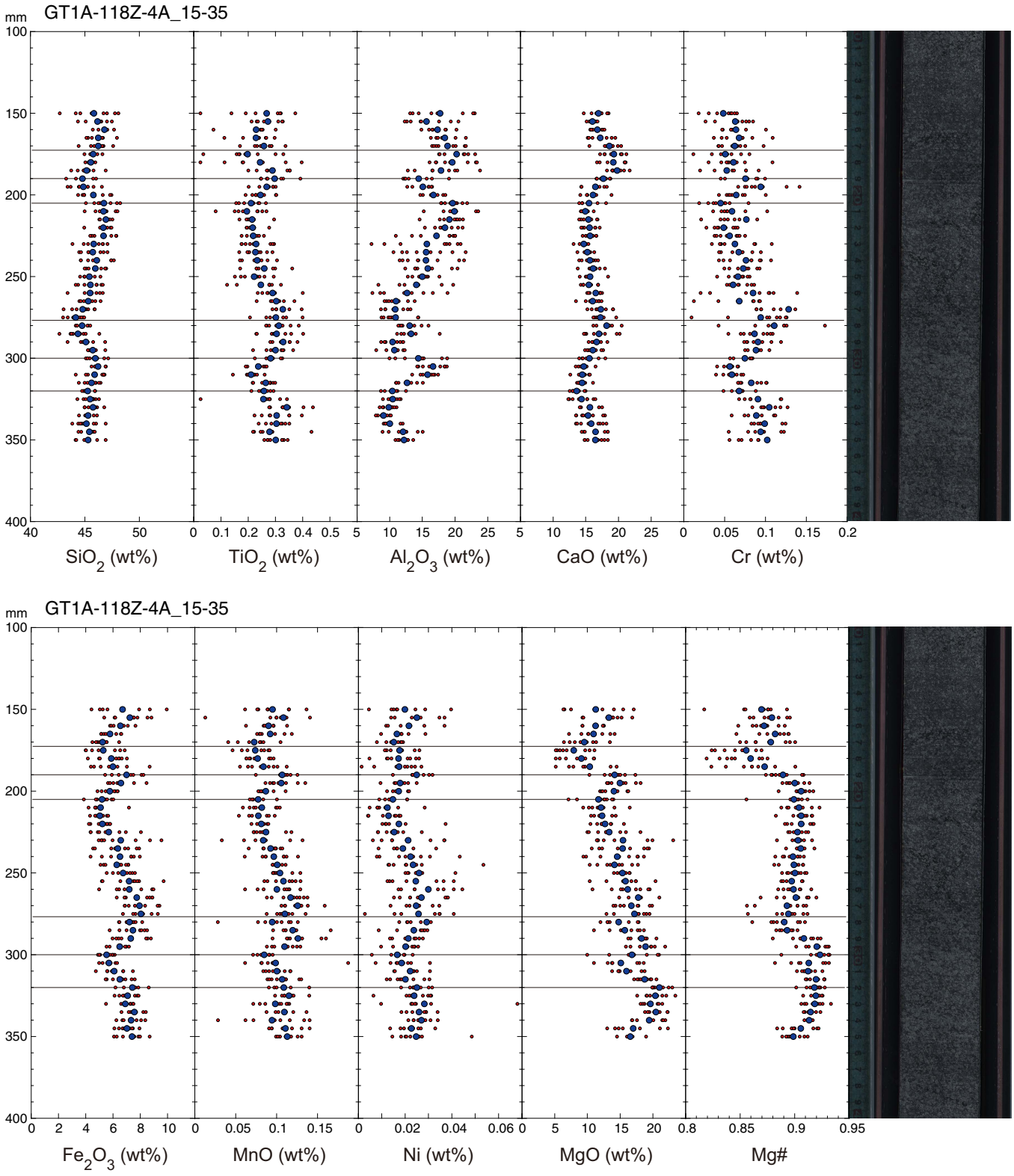

Figure F79. Color-coded images for variations of major elements Cr and Ni (118Z-4, 15–35 cm).

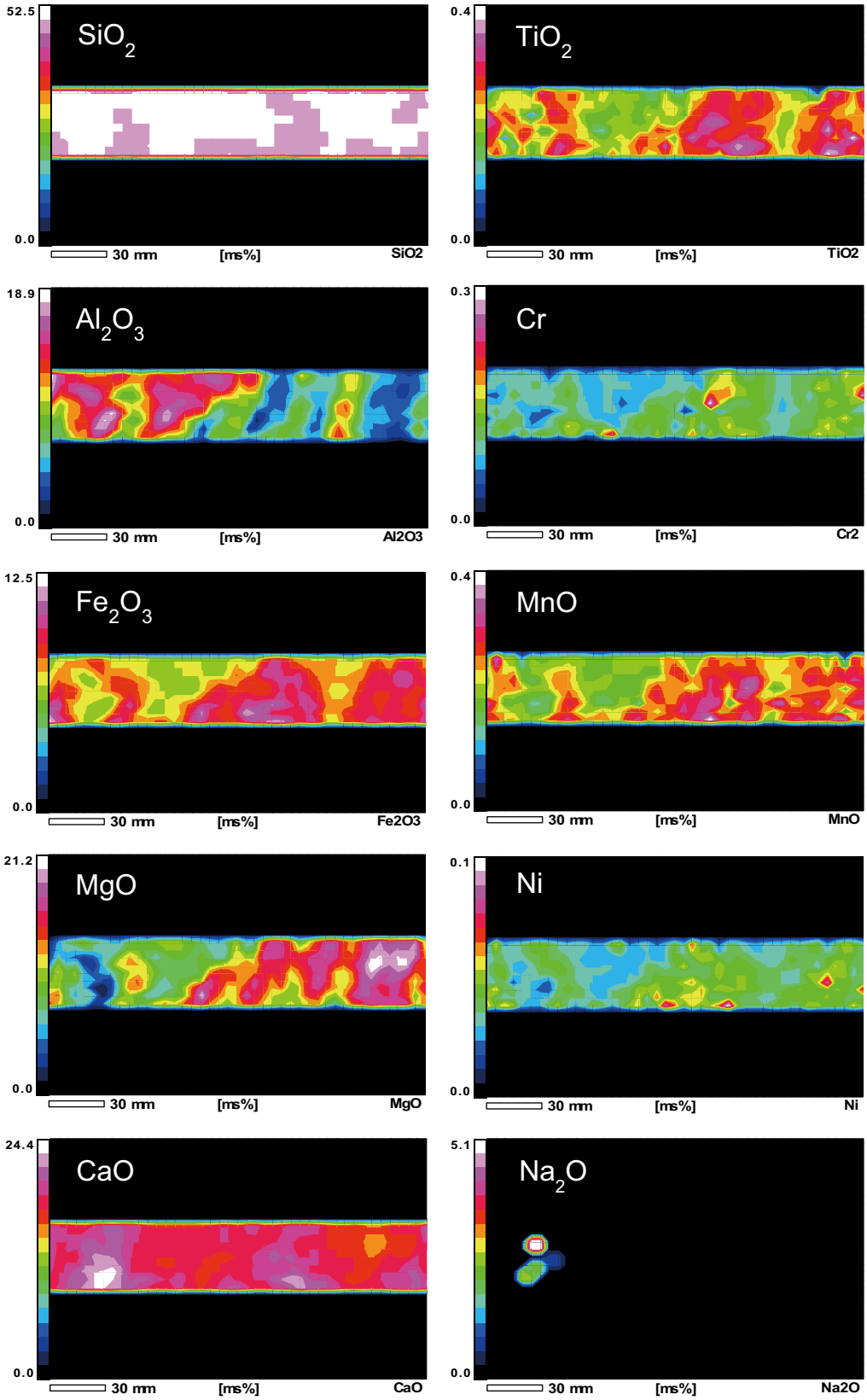

Figure F80. Downhole compositional variations of major elements Cr and Ni (122Z-3, 34–54 cm).

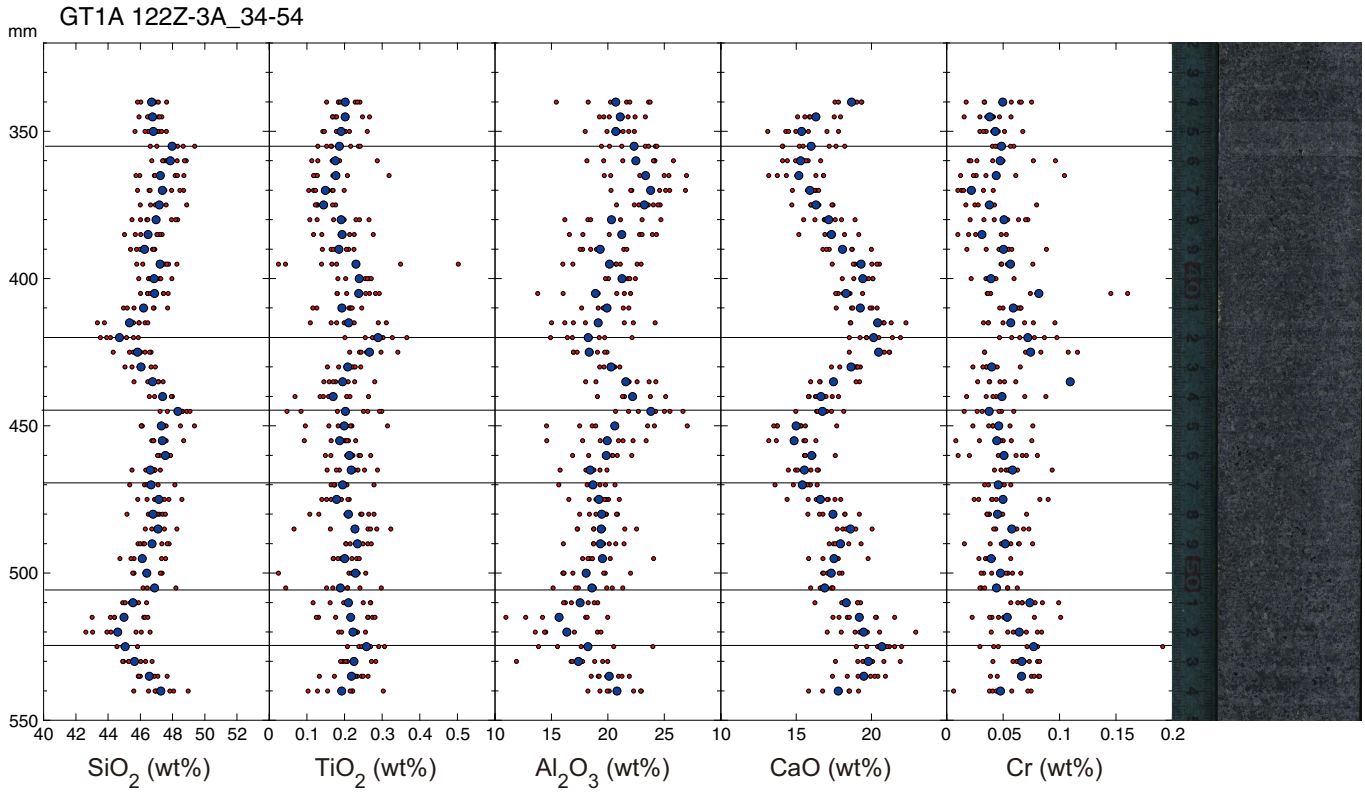

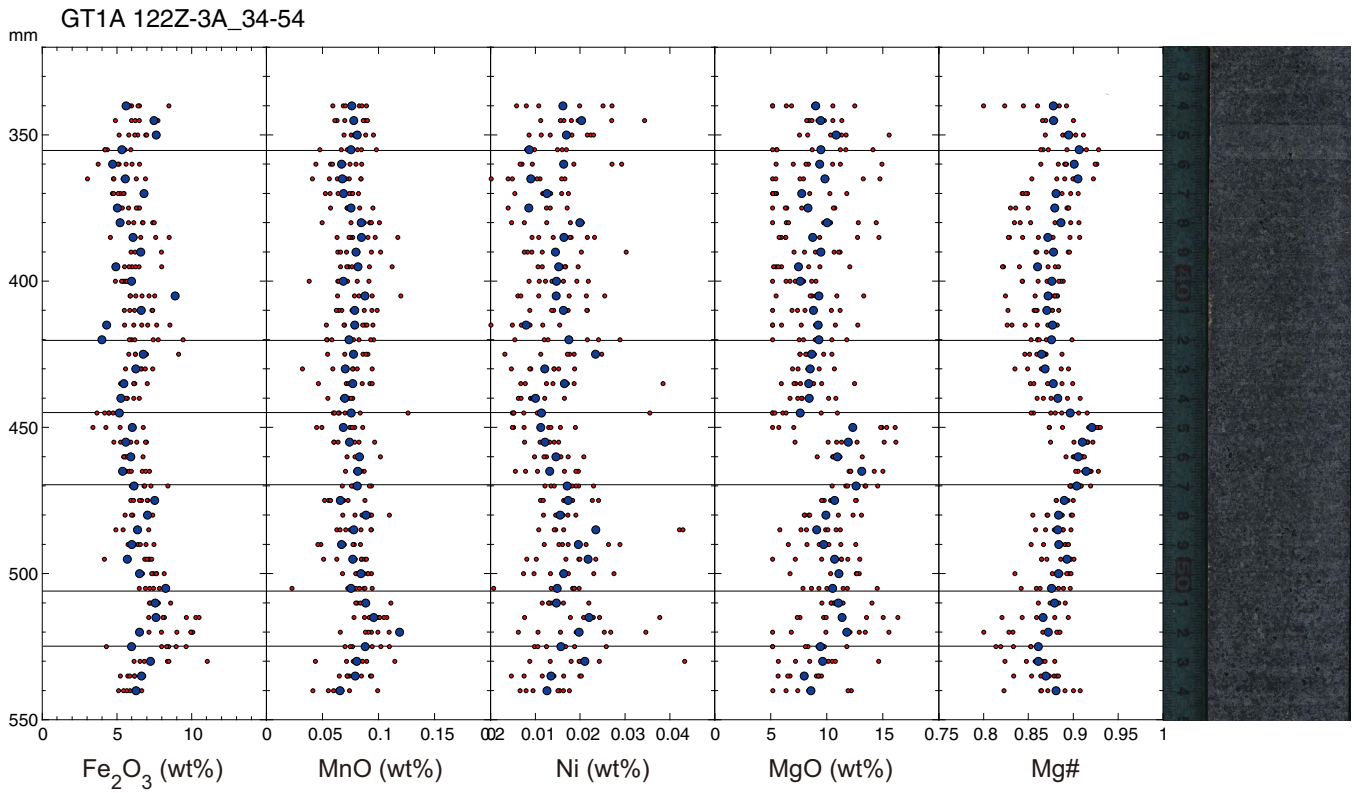

Figure F81. Color-coded images for variations of major elements Cr and Ni (122Z-3, 34–54 cm).

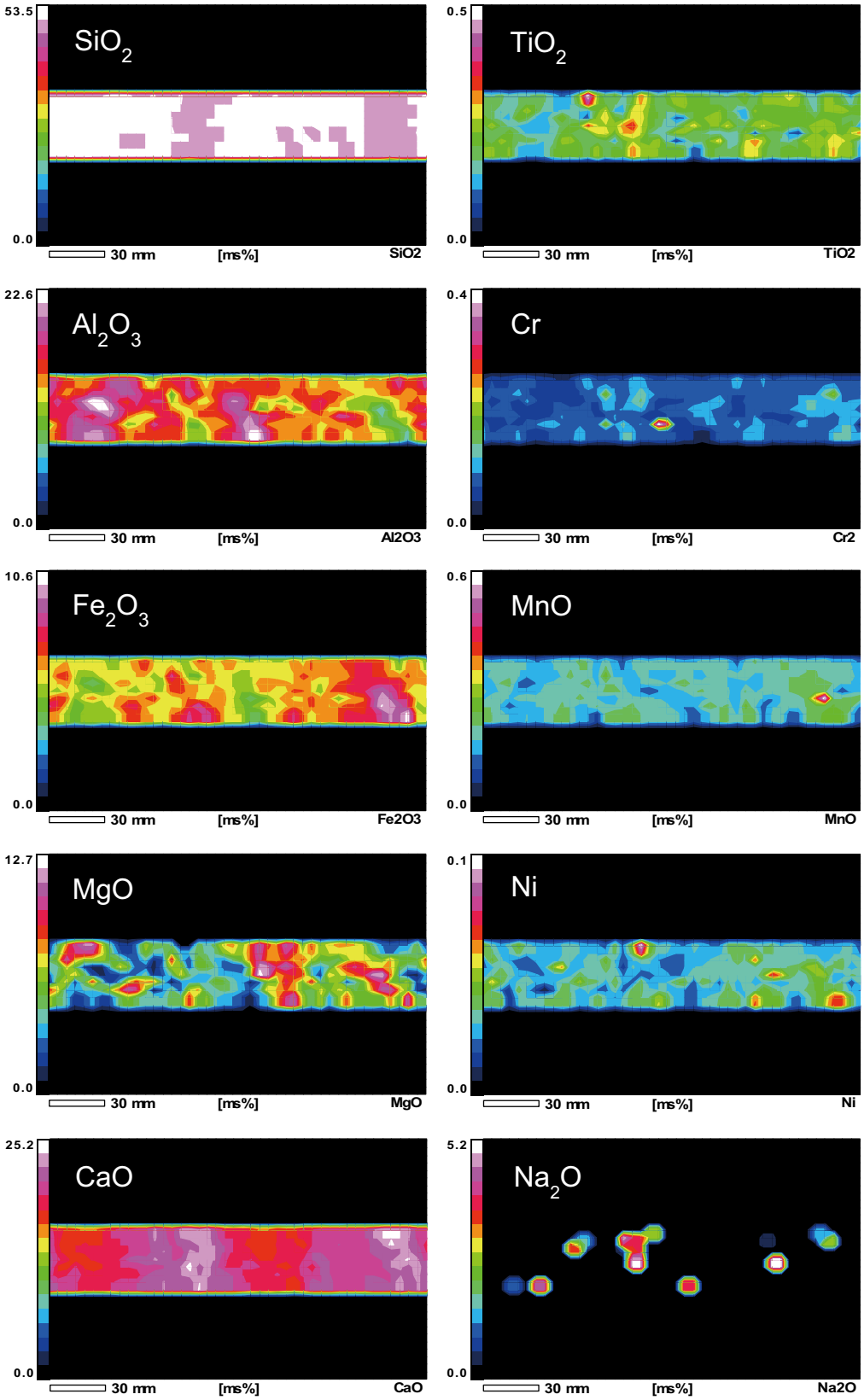

Figure F82. Downhole compositional variations of major elements Cr and Ni (143Z-2, 3–50 cm).

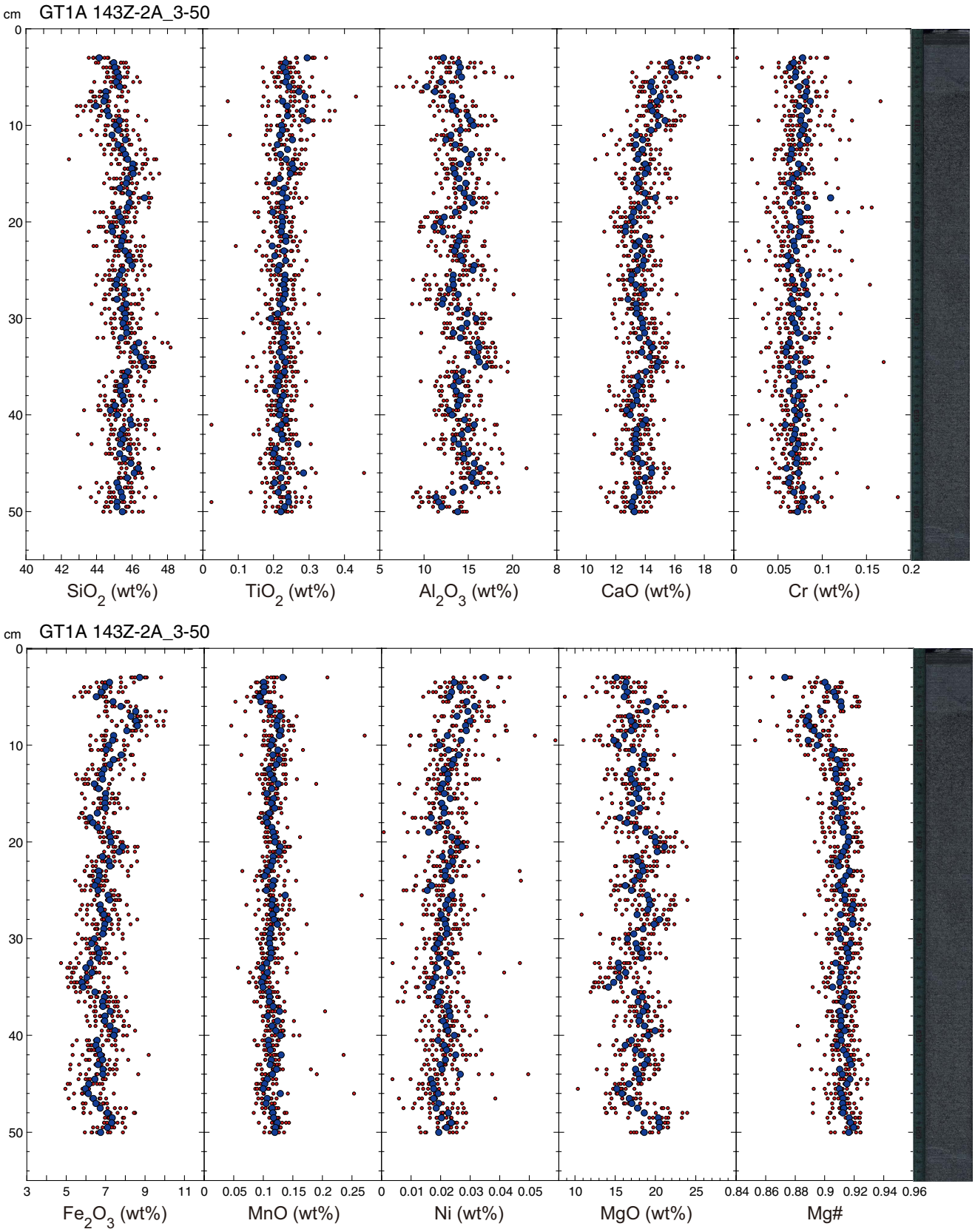

Figure F83. Color-coded images for variations of major elements Cr and Ni (143Z-2, 3–50 cm).

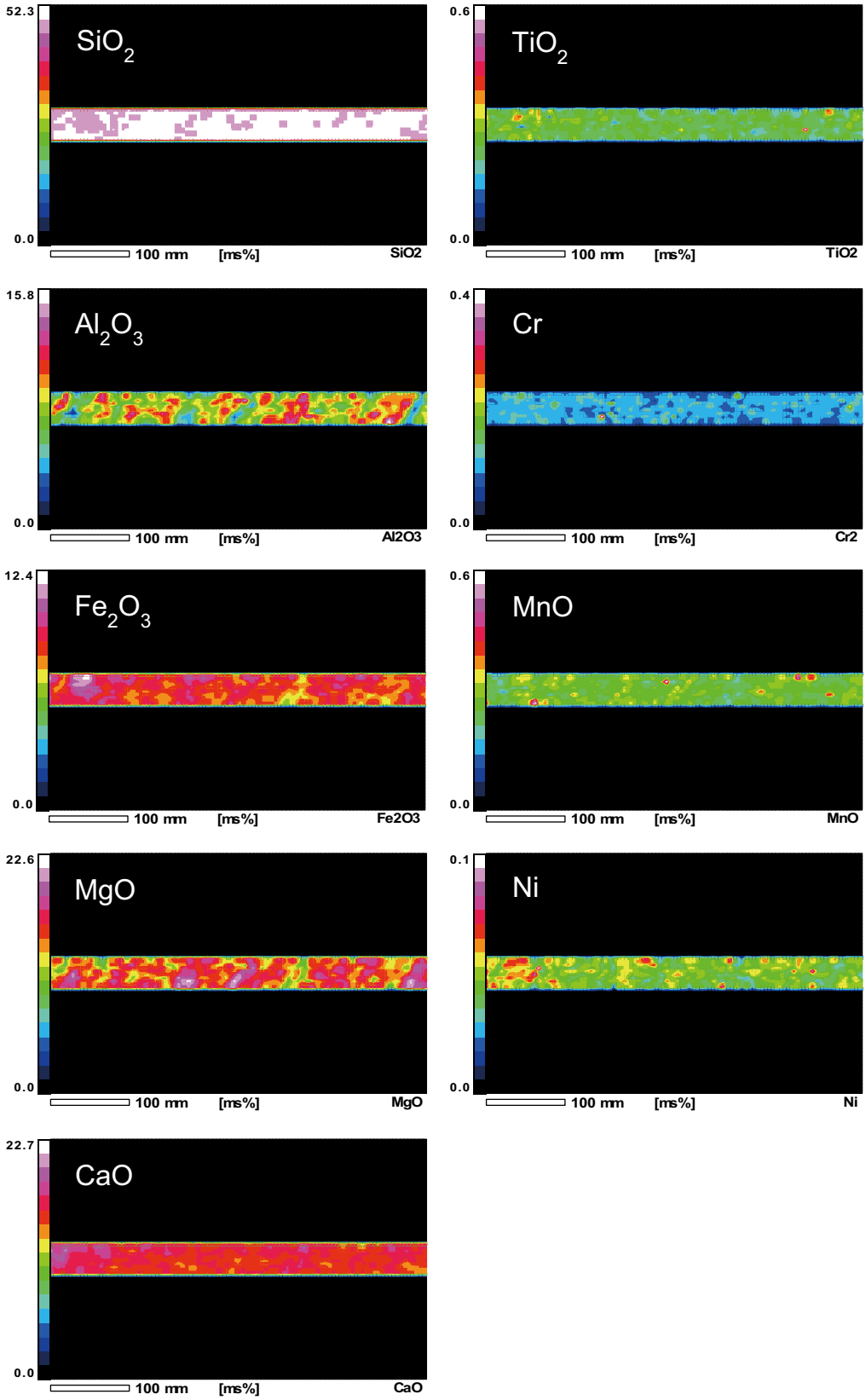

Figure F84. Al_2O_3 vs. CaO plots for interval 100Z-3, 4.5–60 cm. Red circles = individual spots. Blue squares = average values for the data obtained at the same depth of the core. Three large circles indicate approximate compositions for olivine, plagioclase, and clinopyroxene in gabbros with reference to Adachi and Miyashita (2003).

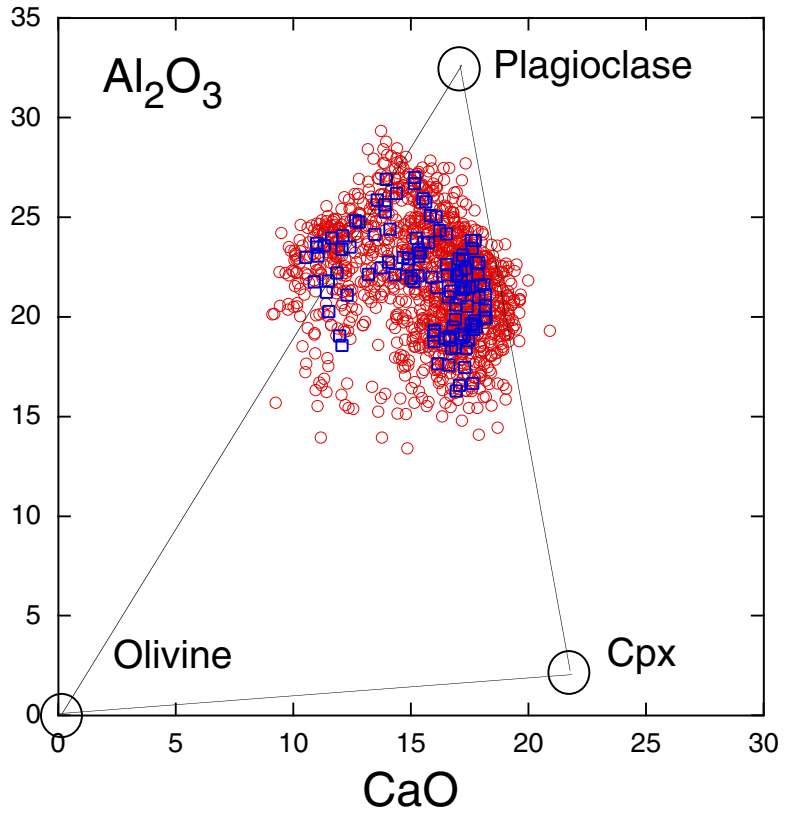

Figure F85. A. Downhole plots of bulk magnetic susceptibility, NRM intensity, and Königsberger (*Q*) ratios measured on discrete samples compared with modal abundances of olivine. **B.** Histograms of bulk susceptibility, NRM intensity, and *Q* values.

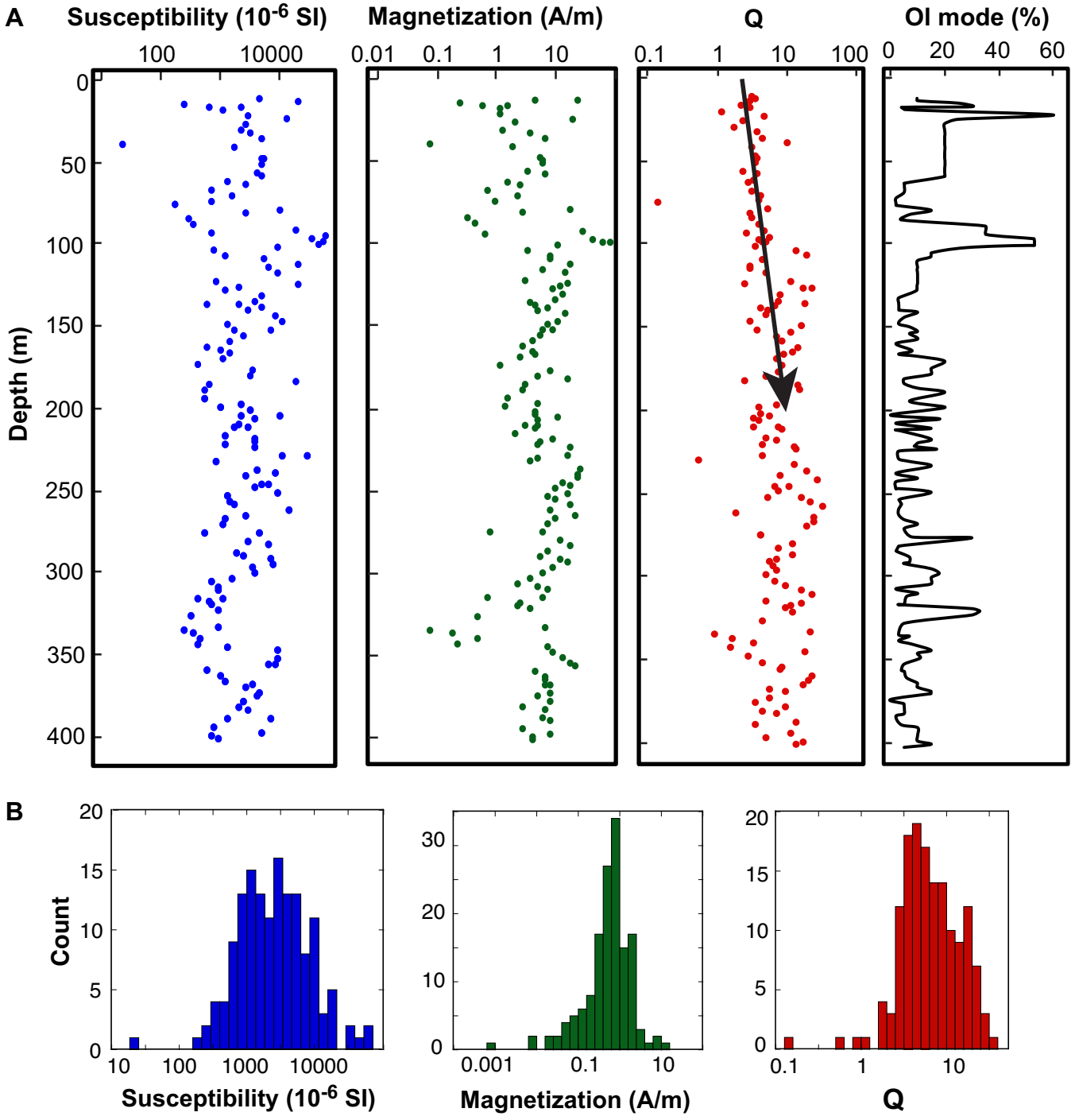

Figure F86. A. Representative orthogonal vector projections displaying behavior of magnetic remanence directions during progressive thermal demagnetization of discrete samples. **B.** Curves of intensity as a function of temperature. **C.** Bulk susceptibility changes during progressive thermal demagnetization.

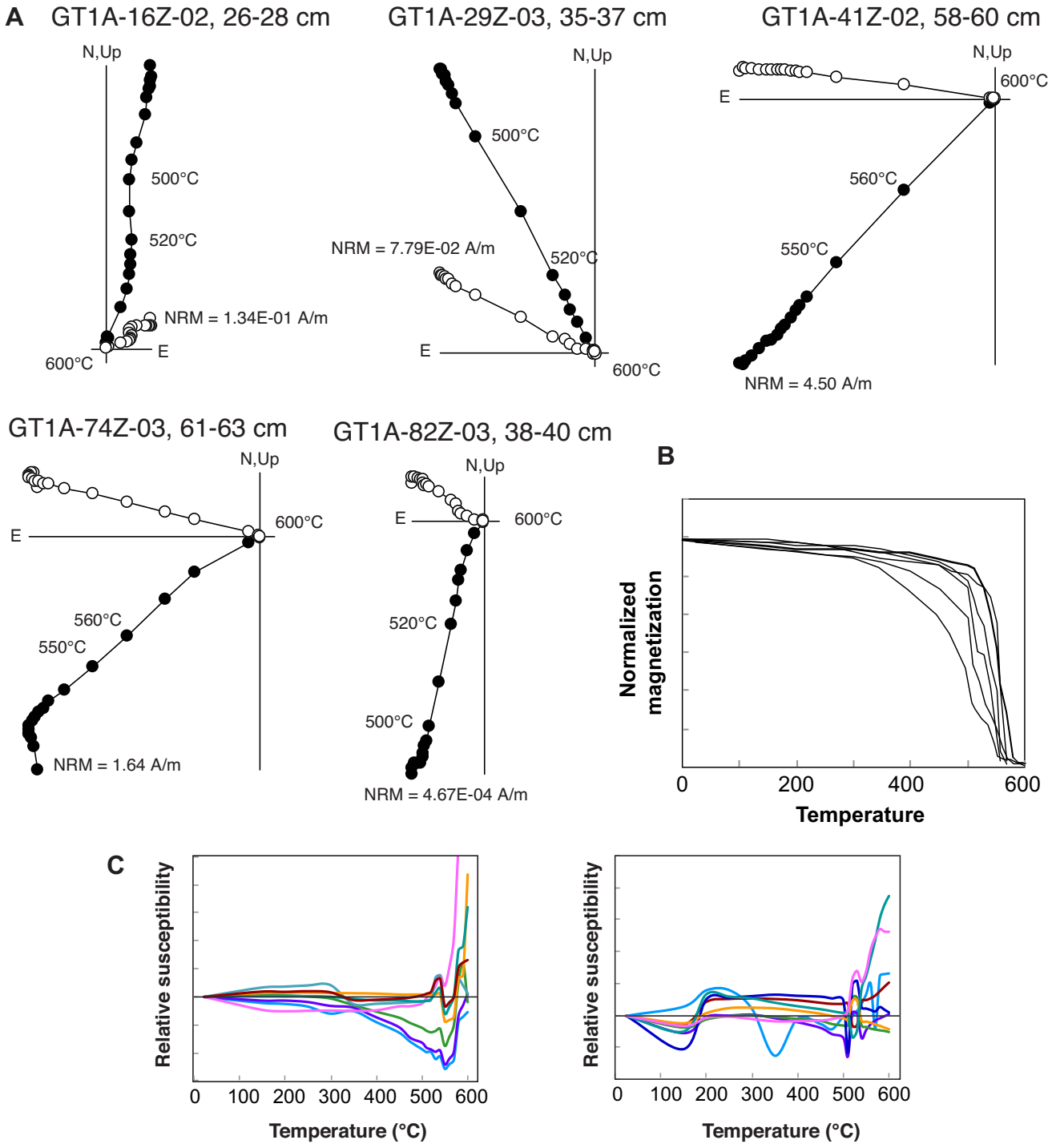

Figure F87. A. Representative orthogonal vector projections displaying behavior of magnetic remanence directions during progressive AF demagnetization of discrete samples. **B.** Curves of intensity as a function of field strength.

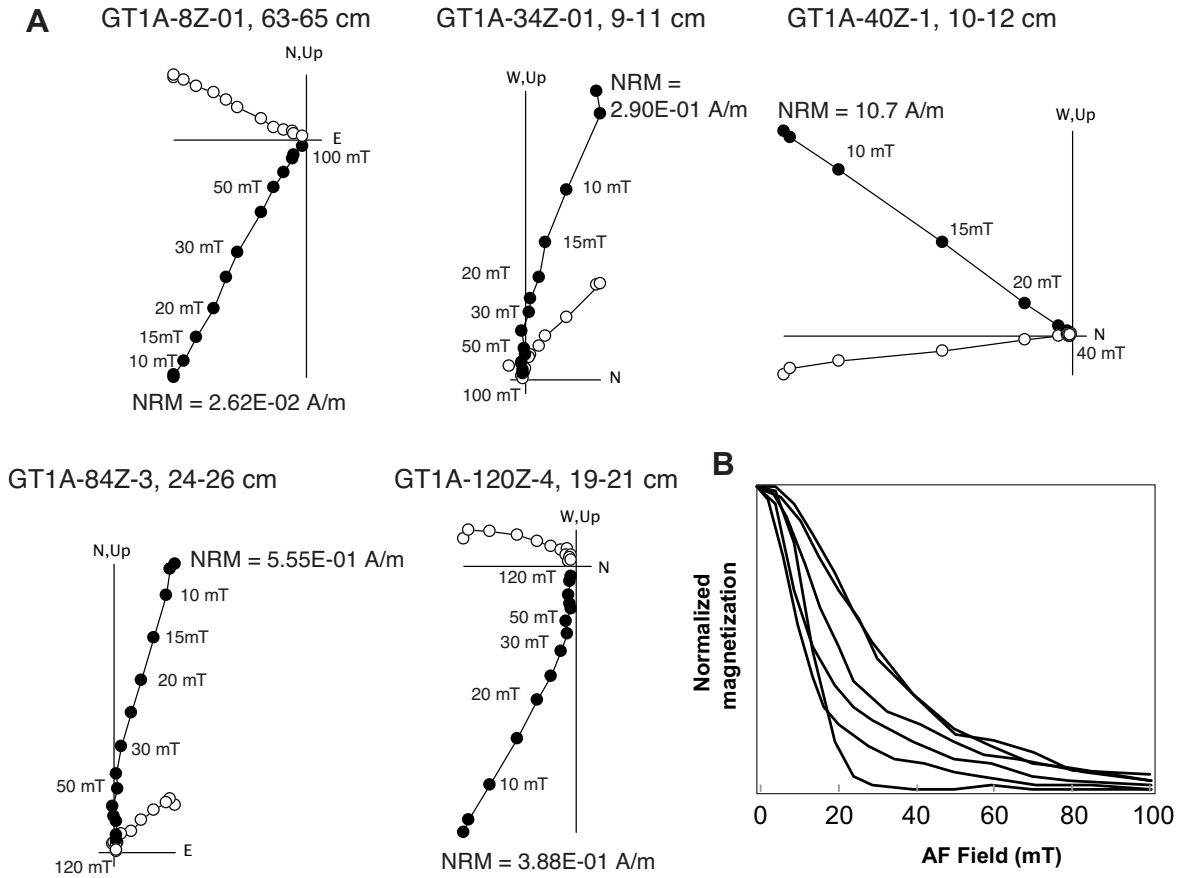

Figure F88. Example comparison of AF and thermal demagnetization results for neighboring discrete samples.

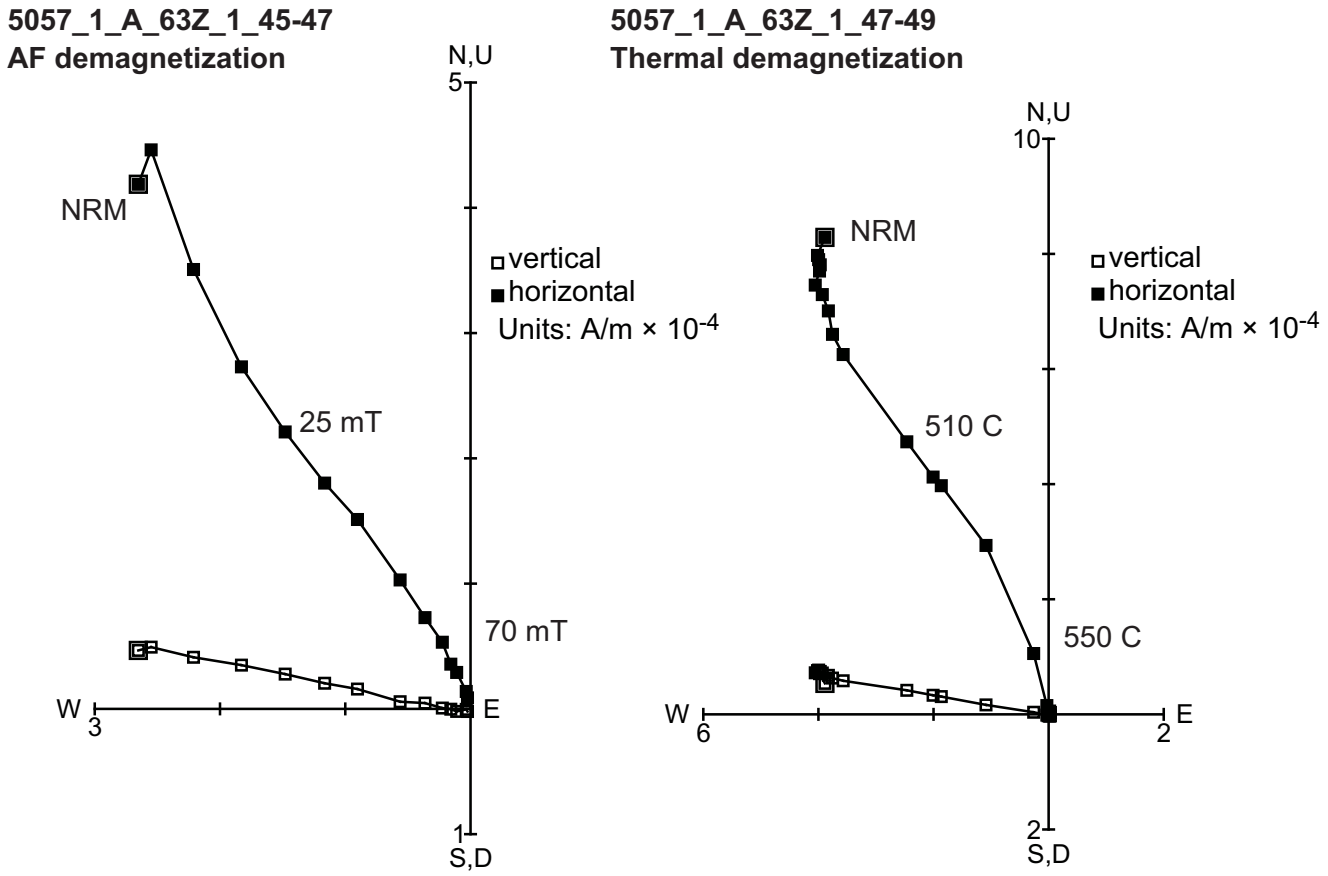

Figure F89. Downhole plot of NRM inclinations and inclinations of the low, intermediate, and stable remanence components determined from principal component analysis.

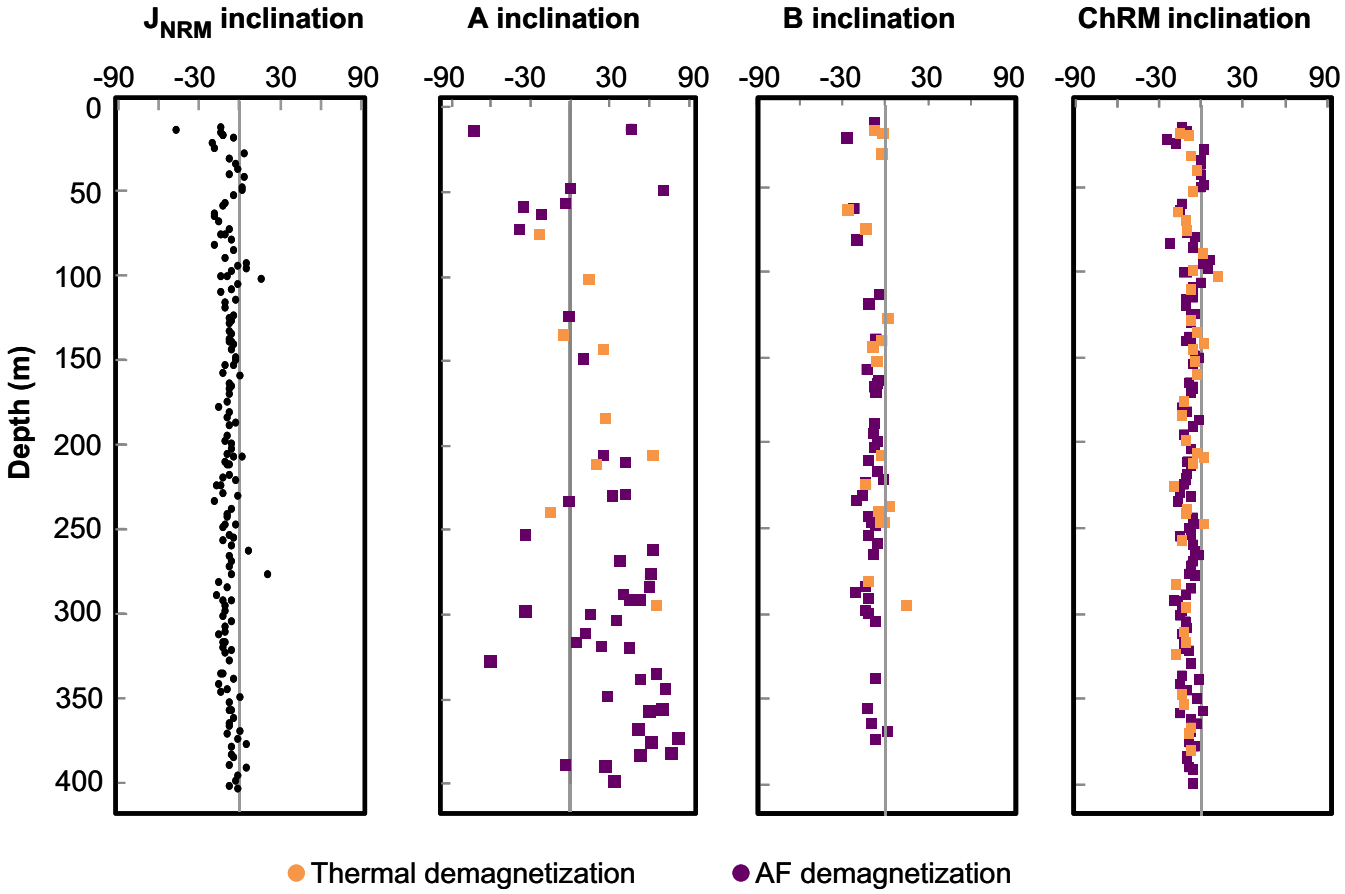

Figure F90. Stereoplots of remanence component orientations identified by principal component analysis. Open (solid) symbols represent upper (lower) hemisphere directions.

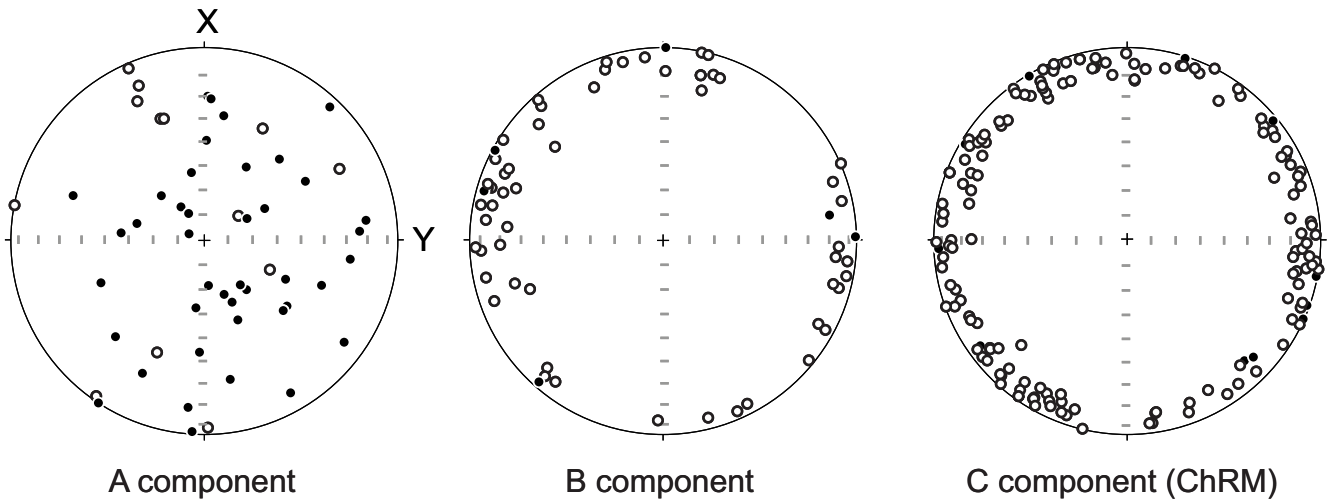

Figure F91. **A.** Downhole plots of magnetic anisotropy intensity, shape, and K_{min} orientation. **B.** Degree of anisotropy as a function of bulk susceptibility. **C.** Shape parameter vs. degree of anisotropy of magnetic susceptibility.

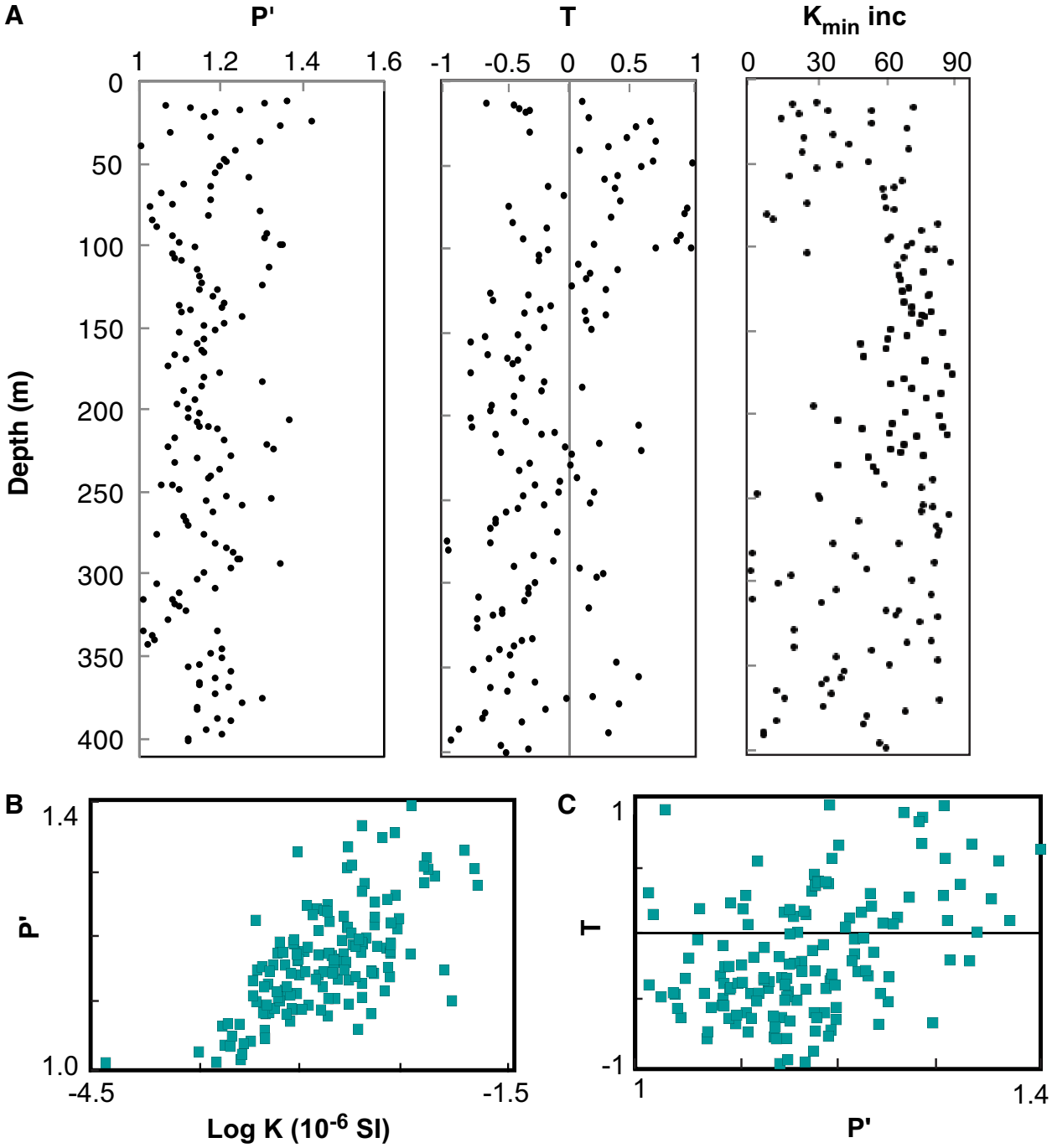

Figure F92. Stereoplots of principal susceptibility axes from anisotropy of magnetic susceptibility measurements plotted on lower hemisphere equal-area projections in the core reference frame.

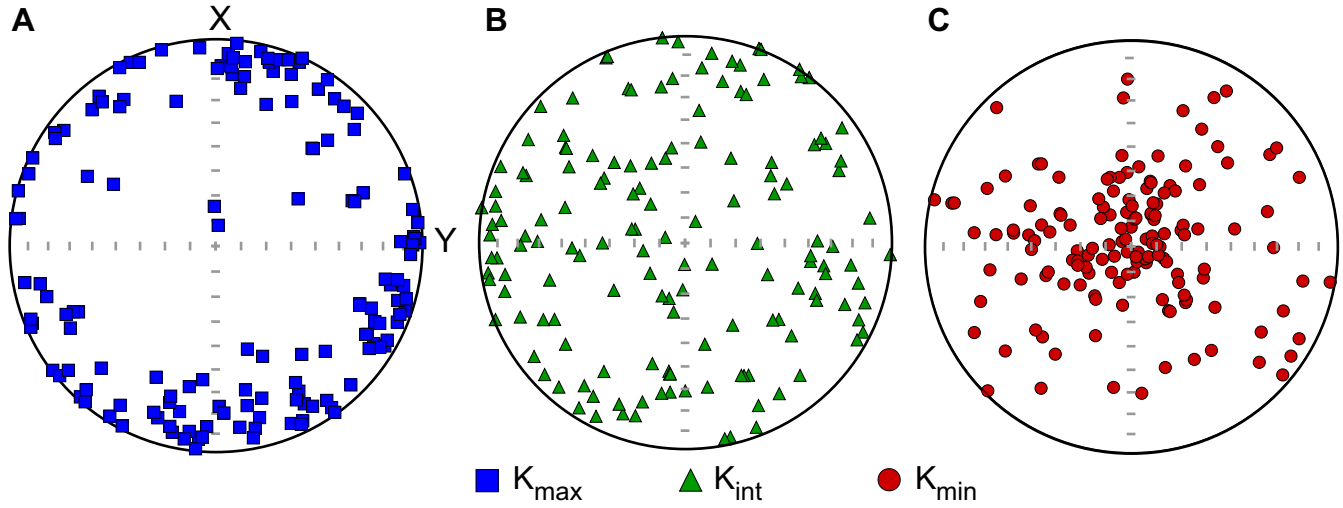

Figure F93. A. Stereoplot of magnetic anisotropy orientations after azimuthal rotation of ChRM declinations around the core axis to a reference paleomagnetic declination. **B.** Downhole plot of rotated K_{max} declinations.

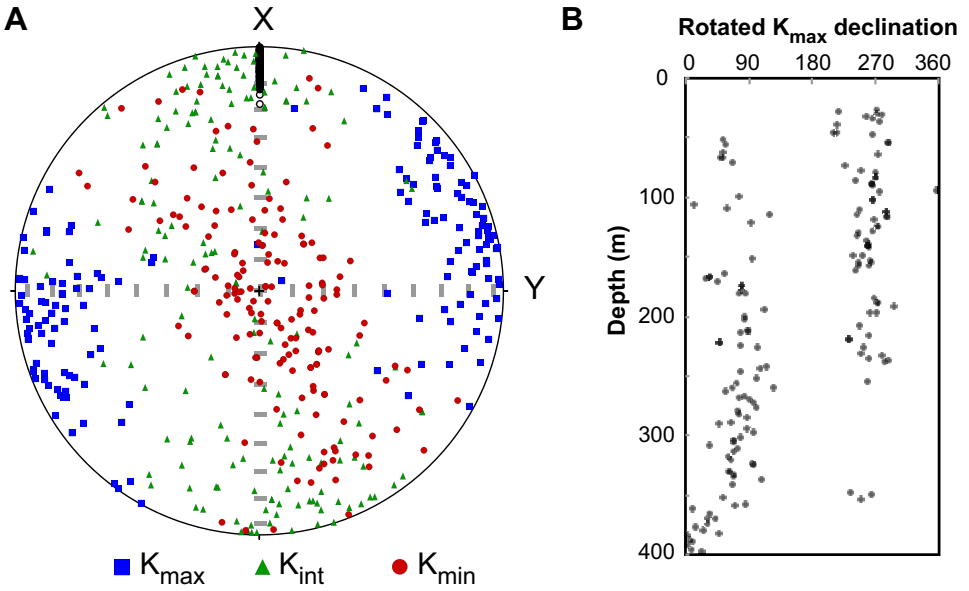

Figure F94. A. Example of primary interstitial Fe oxides occurring in association with Fe sulfide minerals (reflected light [RL]). **B, D, E.** Fine-grained oxides in altered olivine grains (RL). **C, F.** Mesh texture of opaque phases in altered olivine grains (PPL).

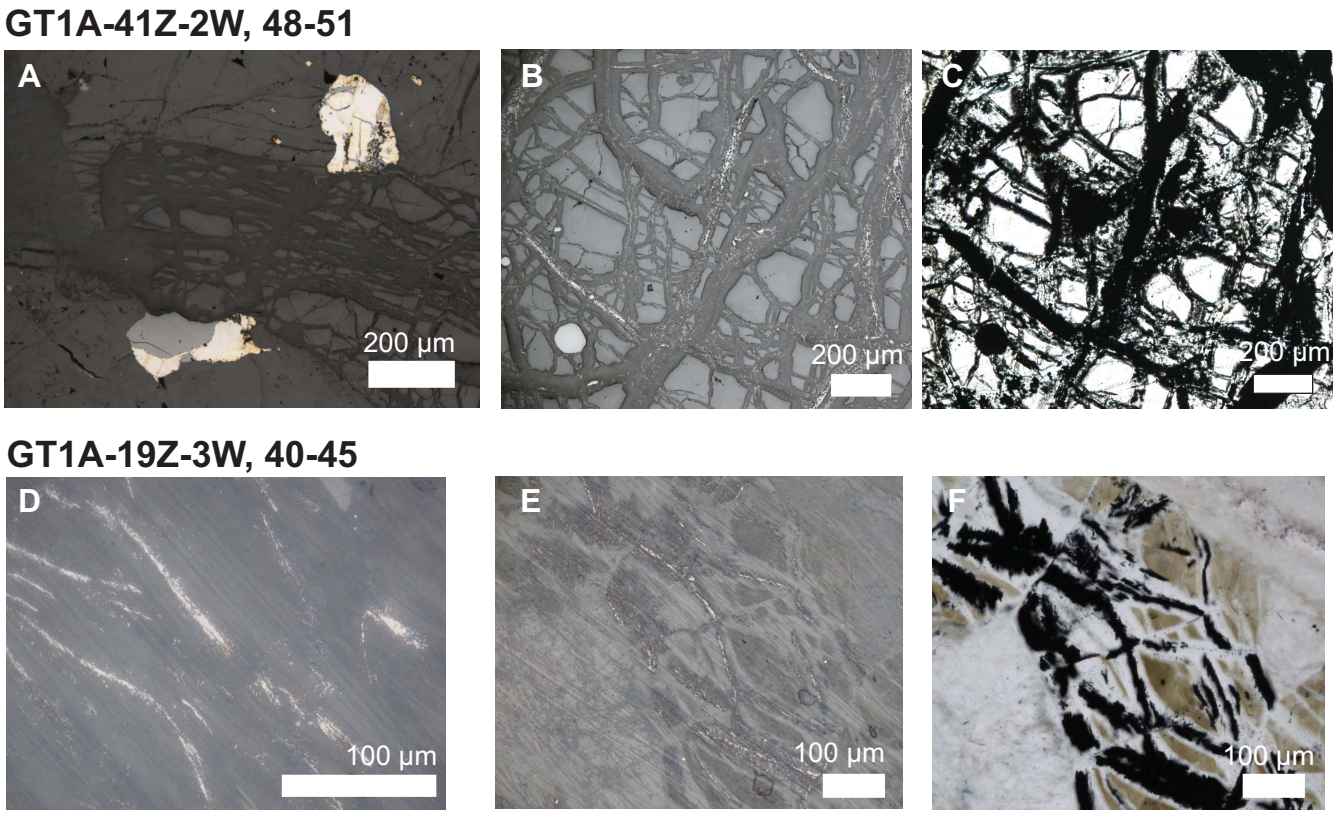

Figure F95. Downhole MS and NGR summary plot.

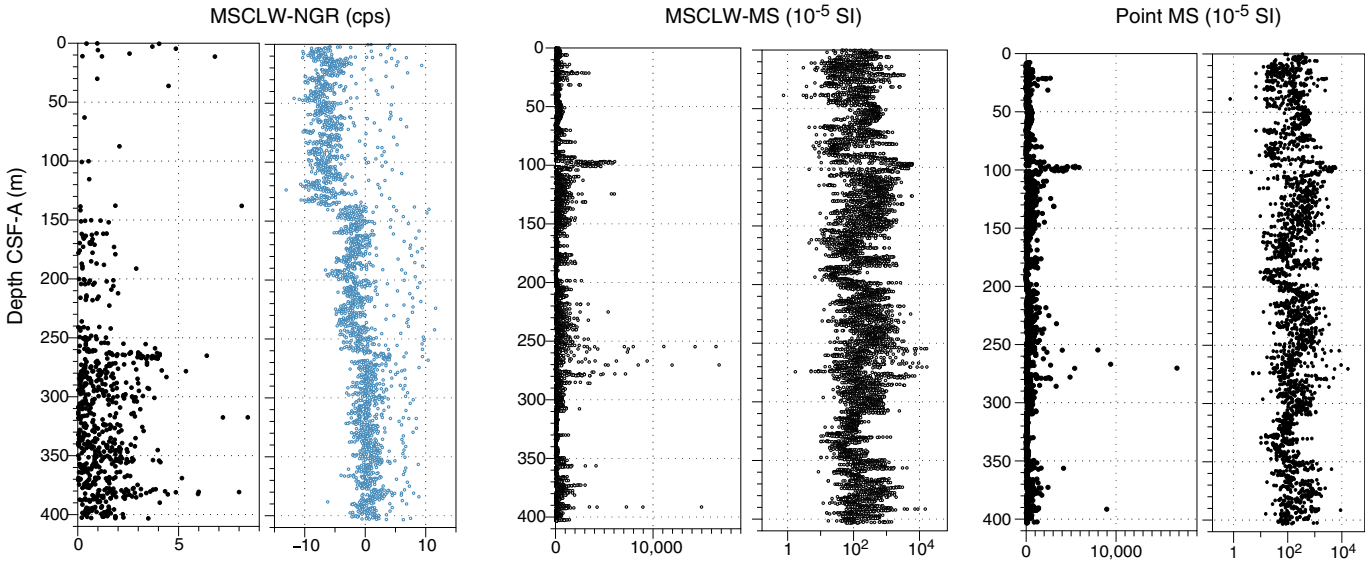

Figure F96. Examples of X-ray CT data for Sections 104Z-3 and 108Z-4. **A**, **D.** MSCL-I scanned images. **B**, **E.** Along-section XCT images. **C**, **F.** Average CT values of across-section XCT images.

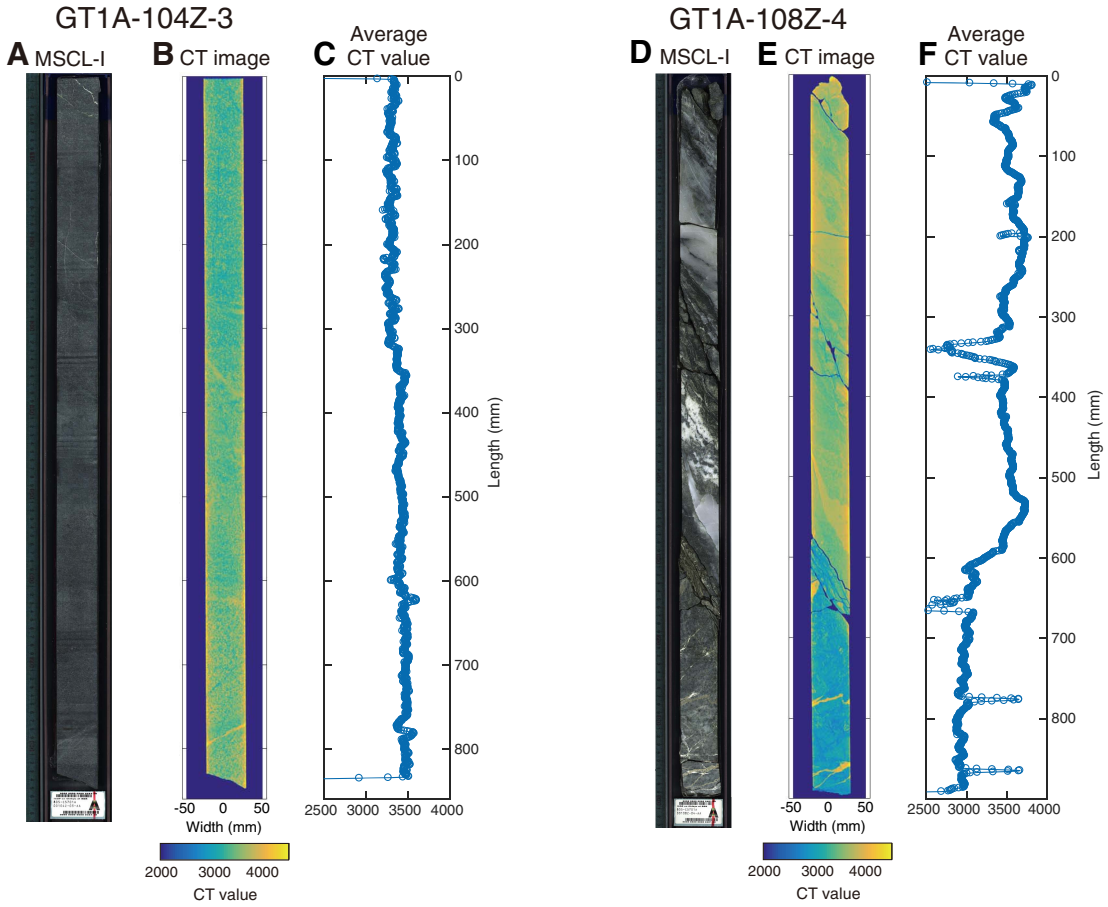

Figure F97. MSCL-Color downhole plot.

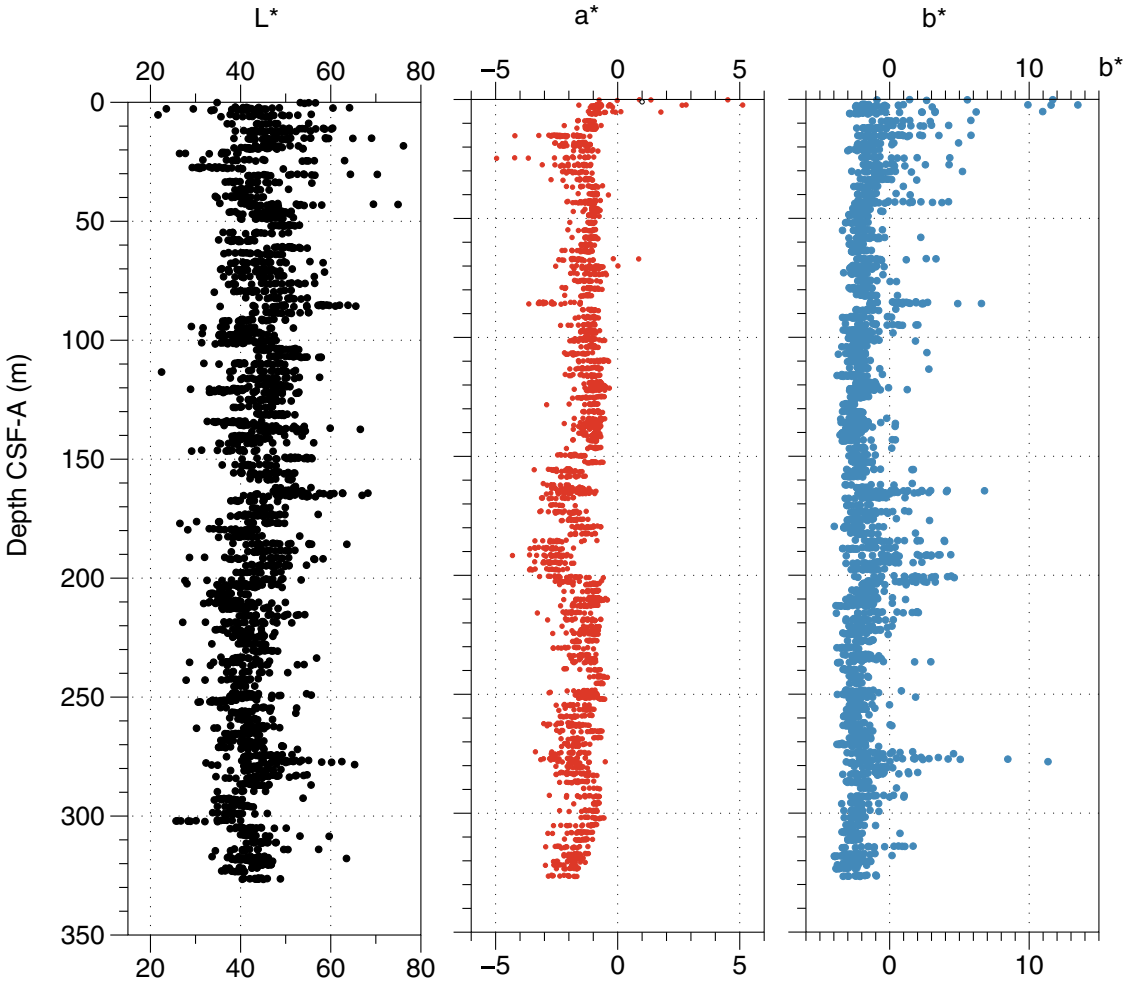

Figure F98. Selected sections for MSCL-Color and MS.

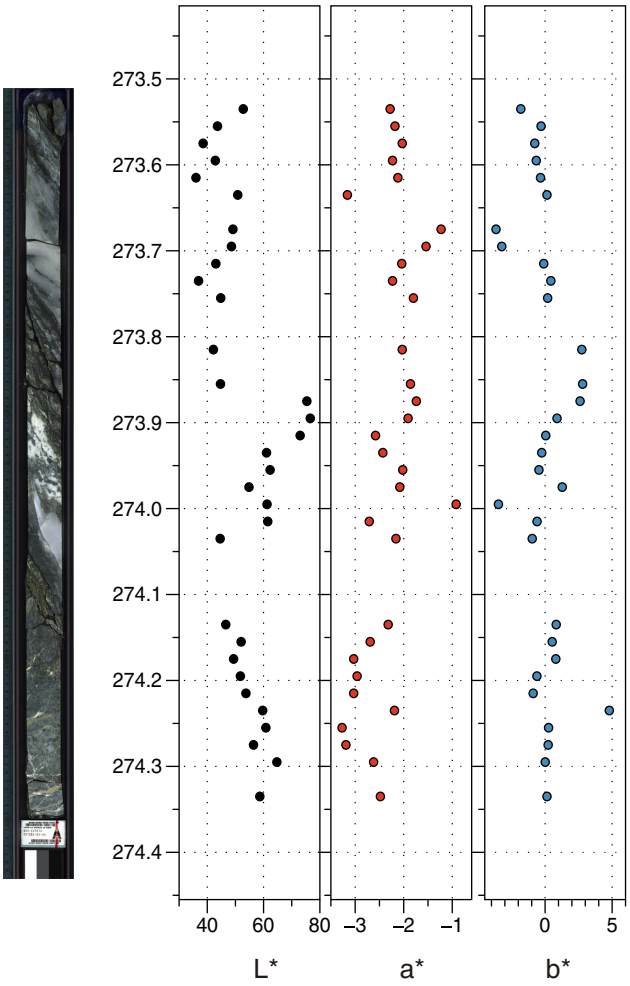

Figure F99. Downhole distribution of P-wave velocity, grain density, and porosity measured on discrete samples. Lithology of samples is that of host igneous intervals.

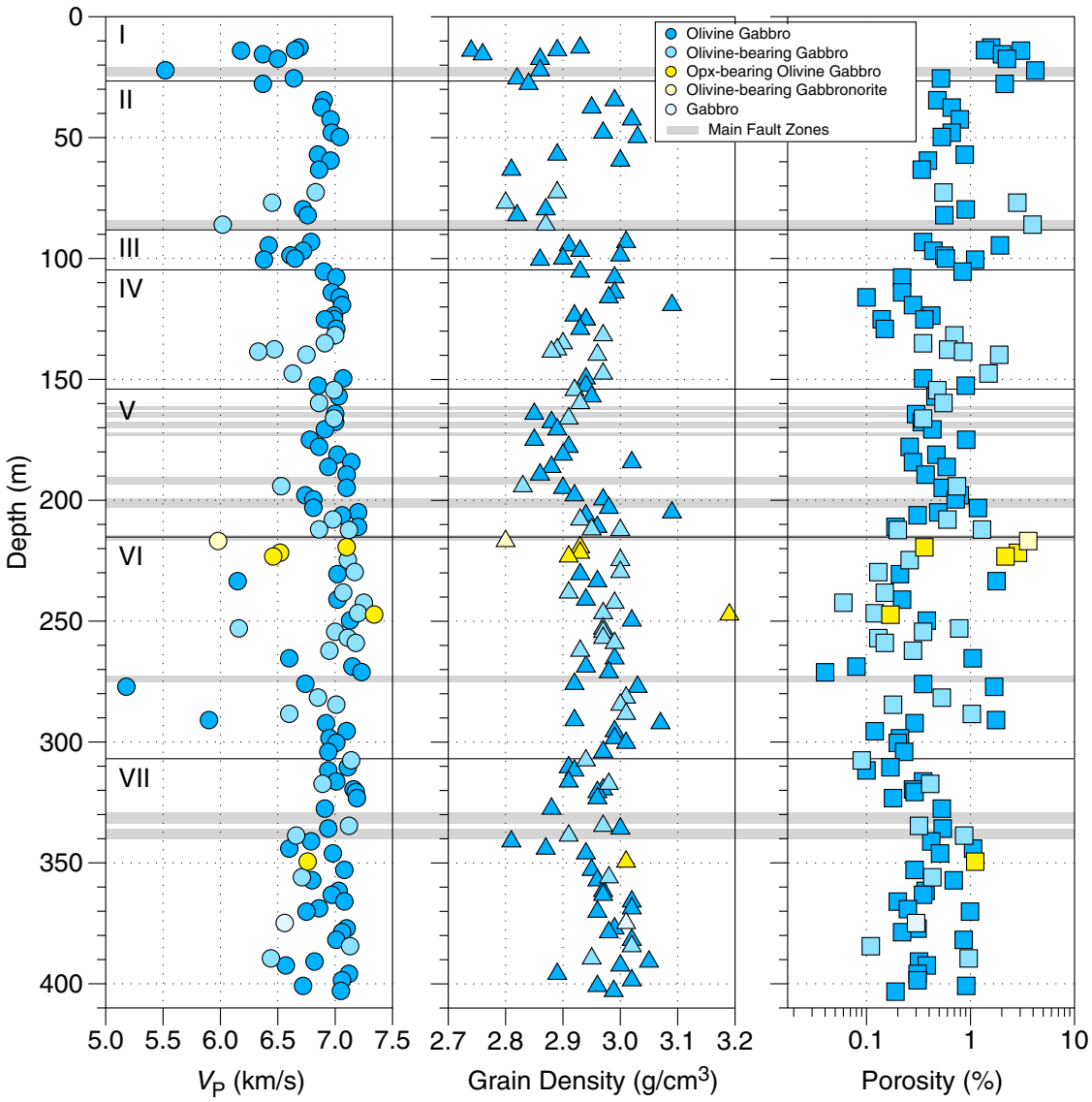

Figure F100. A. P-wave velocity vs. porosity. **B.** Bulk density vs. porosity. **C.** P-wave velocity vs. average olivine mode of host interval. **D.** Grain density vs. average olivine mode of host interval.

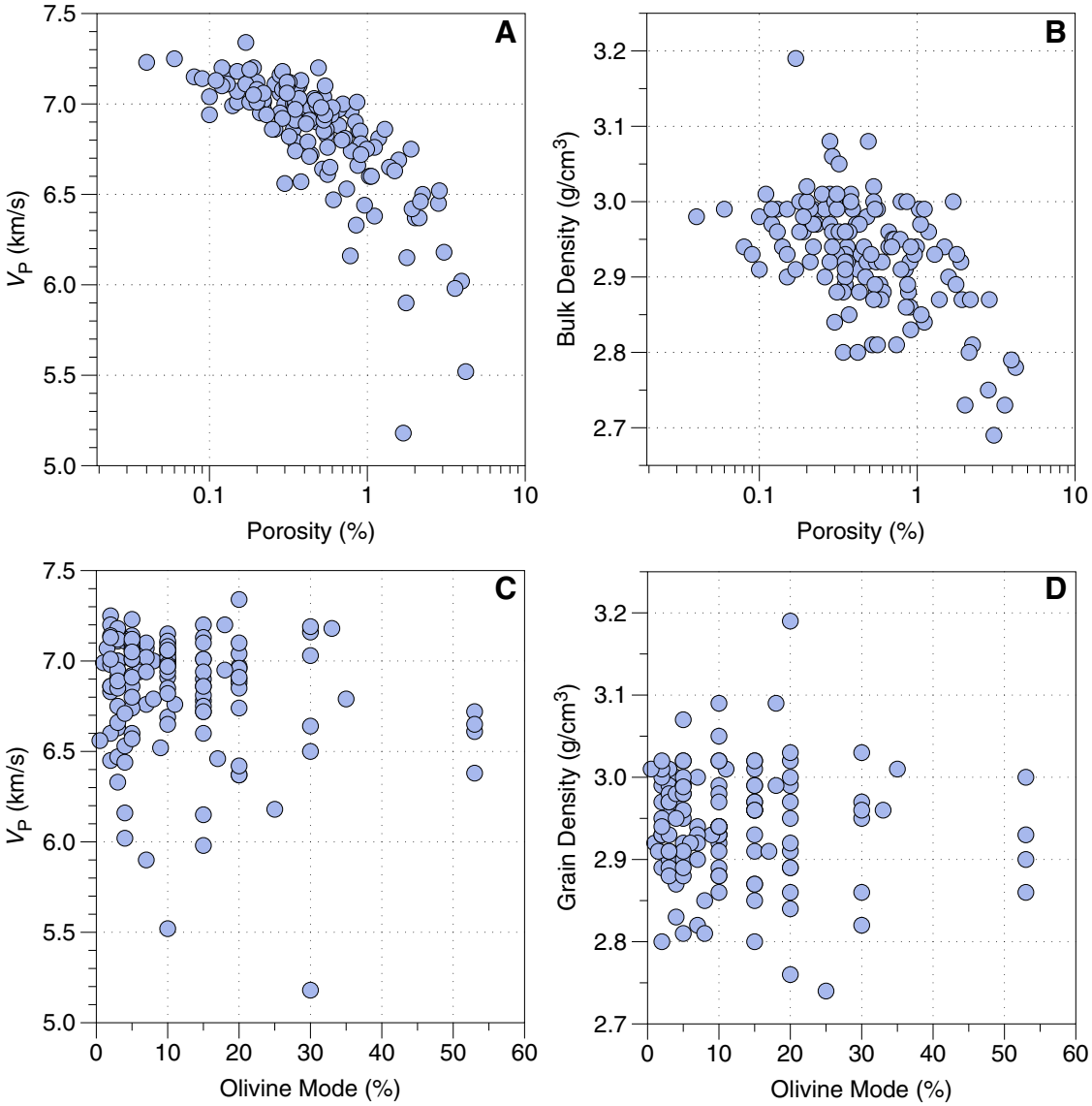

Figure F101. P-wave velocity vs. (**A**) bulk density and (**B**) grain density. Background data are from Blackman et al. (2006; Atlantis Massif), Gillis et al. (2014b; Hess Deep), and MacLeod et al. (2017; Atlantis Bank). The average Oman gabbro data in (B) is from Abers and Hacker (2016).

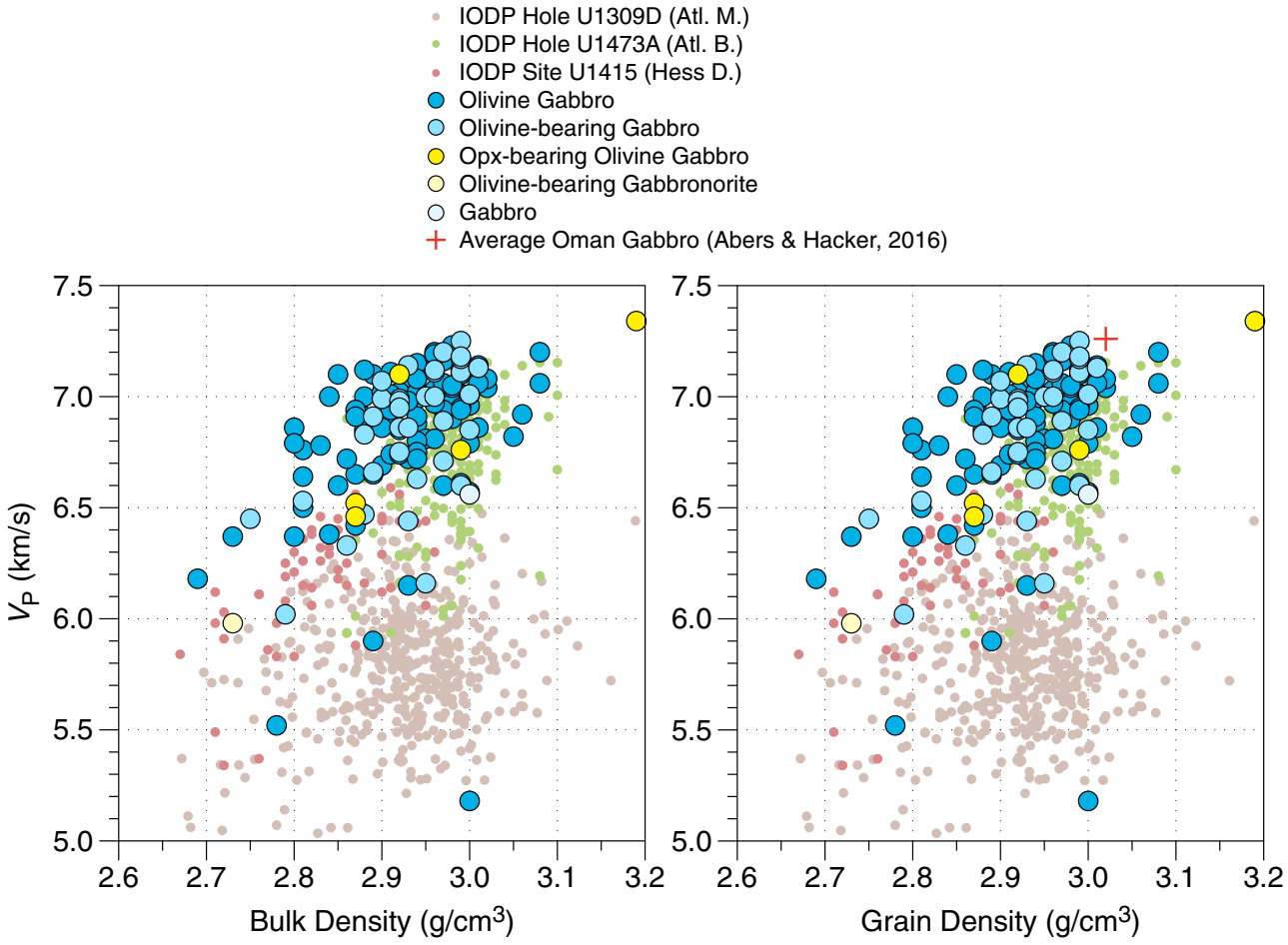

Figure F102. Downhole distribution of thermal conductivity. Sample rock types are those of the host igneous intervals.

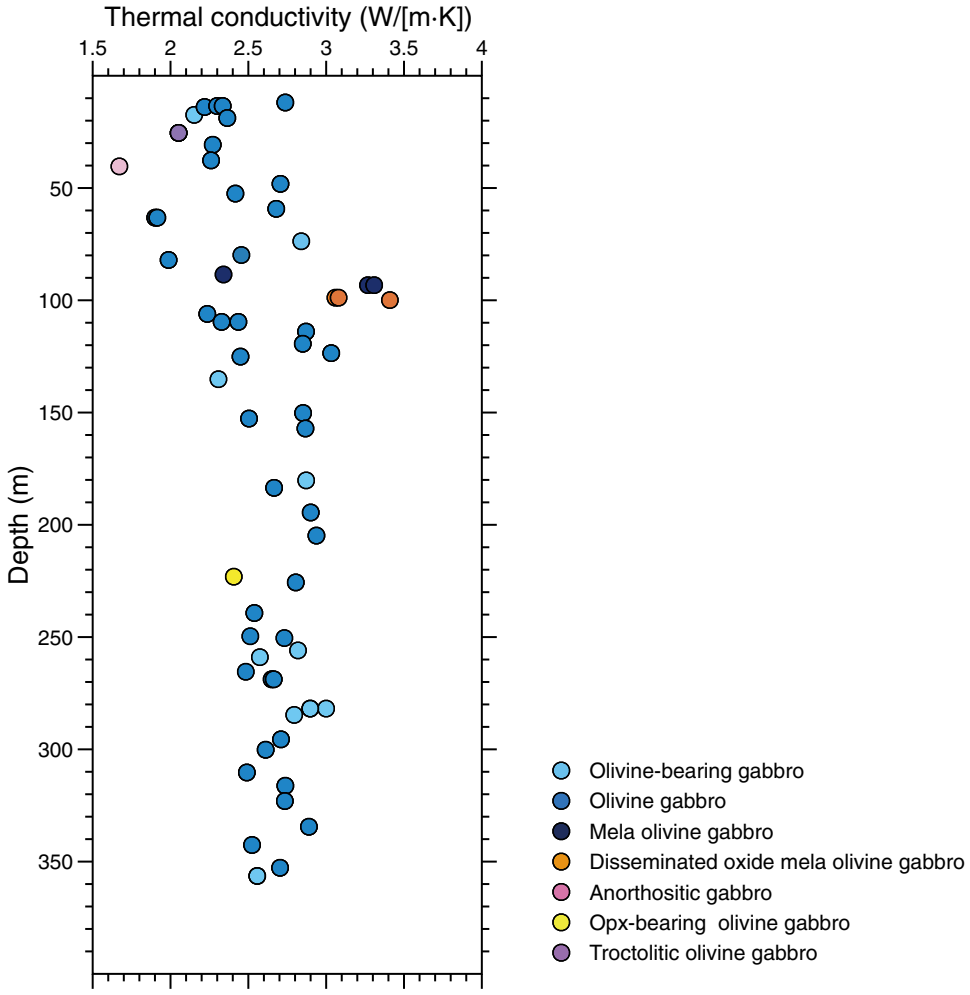

Figure F103. Thermal conductivity vs. olivine mode of host igneous interval.

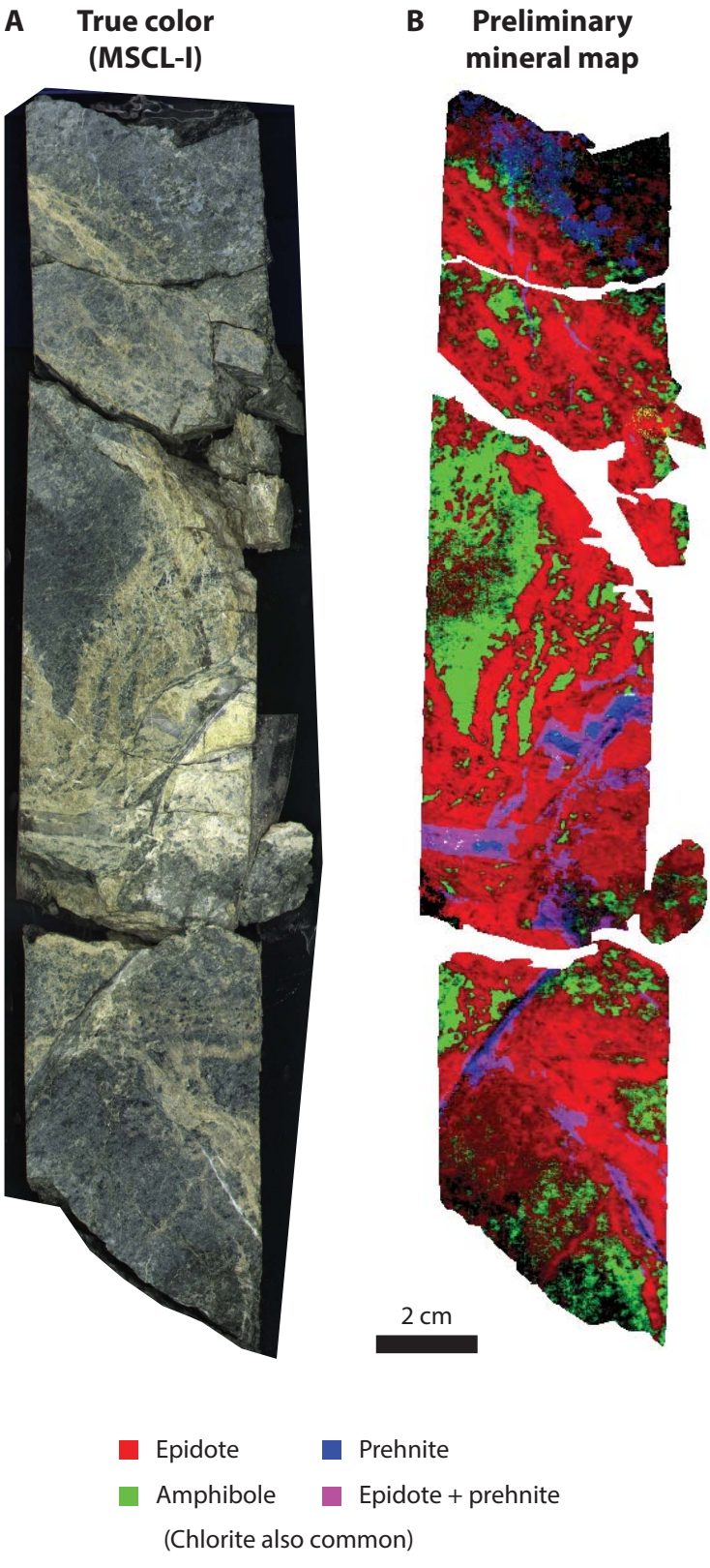

Figure F104. **A.** MSCL-I true color image of the upper part of Section 111-1. **B.** Preliminary mineral map showing some phases of interest for the same core section derived from imaging spectroscopy data. Other minerals are likely present within each pixel, and this map shows a selection of key phases.

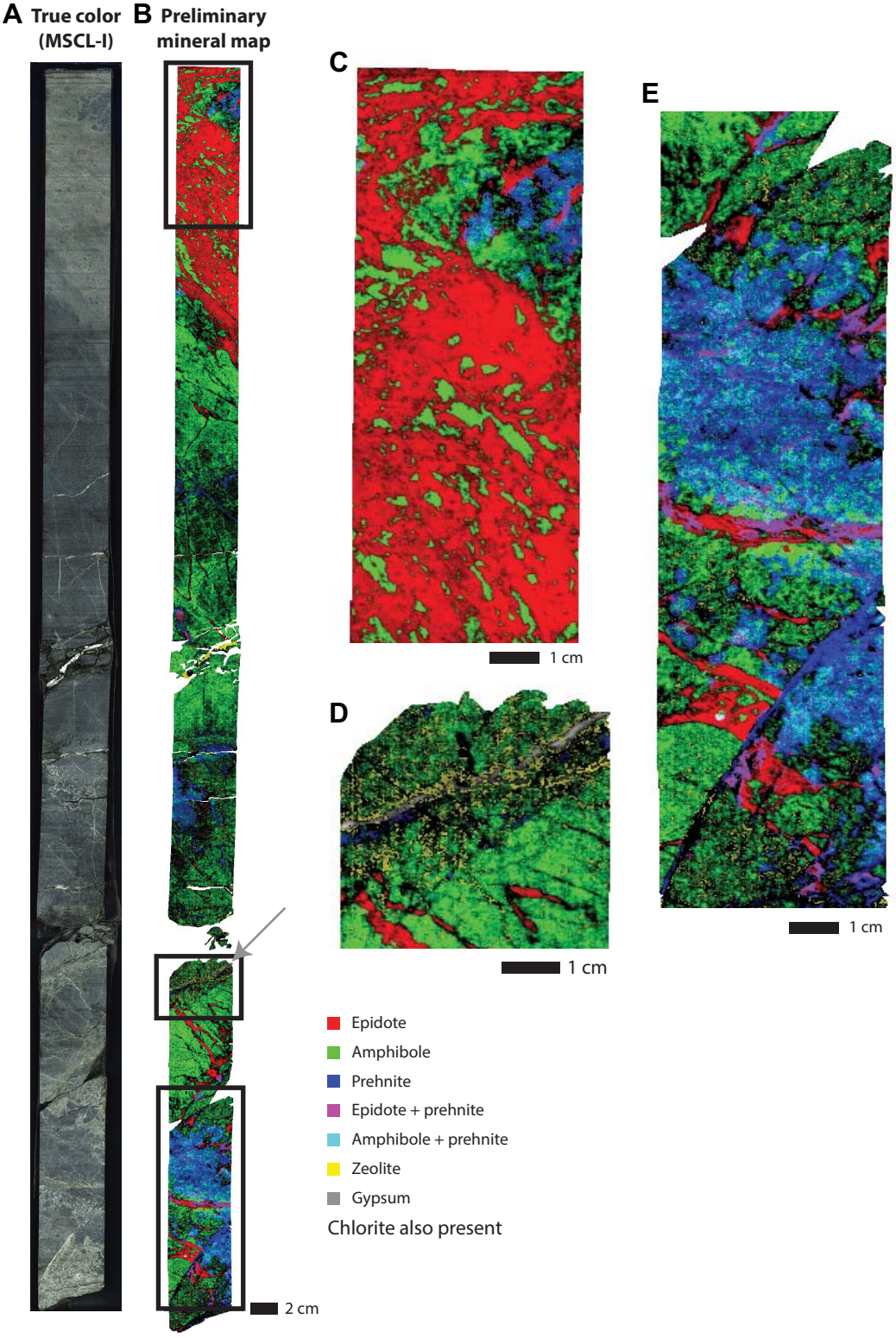

Figure F105. A. MSCL-I true color image of Section 133-2. **B.** Preliminary mineral map showing some minerals of interest for Section 133-2 derived from imaging spectroscopy data. Gray arrow = location of a gypsum vein. Void spaces are larger in the mineral map than (A) because the scans were completed at different times, and different pieces of this core section were not pushed together as tightly for the imaging spectroscopy measurements. **C, D, E.** Close-up views of portions of the mineral map shown in (B).

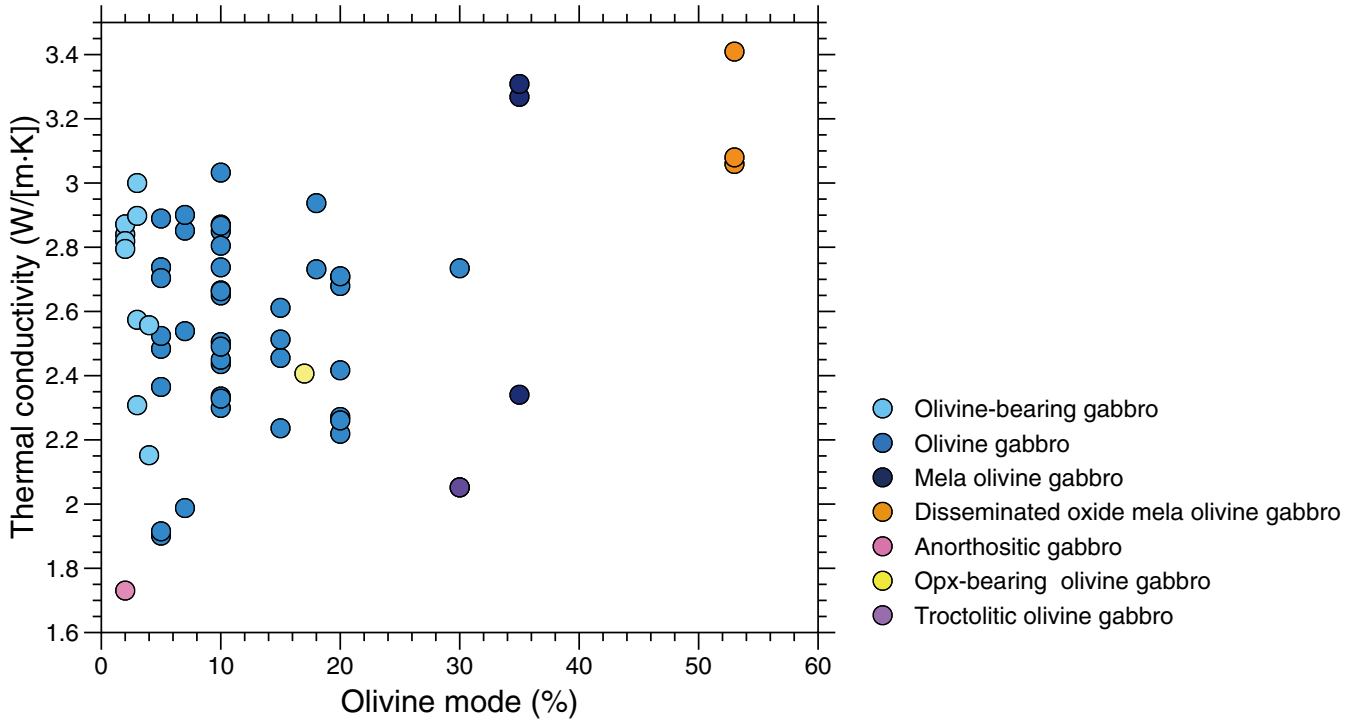

Tables

Table T1. Site GT1 operations. **This table is available in Microsoft Excel format.**

Table T2. Igneous intervals, Site GT1. **This table is available in Microsoft Excel format.**

Table T3. Thin section descriptions, Site GT1. **This table is available in Microsoft Excel format.**

Table T4. XRD secondary minerals, Site GT1. **This table is available in Microsoft Excel format.**

Table T5. Major, trace, and rare earth elements and volatile CHNS data, Hole GT1A. **This table is available in Microsoft Excel format.**

Table T6. Analyzed cores and areas measured by CS-XRF, Site GT1. Note: n = number of spots along each axis. **This table is available in Microsoft Excel format.**

Table T7. Raw analytical data for interval GT1A-38Z-3, 13–40 cm, without correction. **This table is available in Microsoft Excel format.**

Table T8. Raw analytical data for interval GT1A-53Z-4, 30–60 cm, without correction. **This table is available in Microsoft Excel format.**

Table T9. Raw analytical data for interval GT1A-90Z-1, 45–80 cm, without correction. **This table is available in Microsoft Excel format.**

Table T10. Raw analytical data for interval GT1A-100Z-3, 4.5–60 cm, without correction. **This table is available in Microsoft Excel format.**

Table T11. Raw analytical data for interval GT1A-118Z-4, 15–35 cm, without correction. **This table is available in Microsoft Excel format.**

Table T12. Raw analytical data for interval GT1A-122Z-3, 34–54 cm, without correction. **This table is available in Microsoft Excel format.**

Table T13. Raw analytical data for interval GT1A-143Z-2, 3–50 cm, without correction. **This table is available in Microsoft Excel format.**

Table T14. Average compositions with standard deviation of the studied cores, Site GT1. **This table is available in Microsoft Excel format.**

Table T15. NRM and PCA results, Site GT1. **This table is available in Microsoft Excel format.**

Table T16. Inclination statistics, Site GT1. **This table is available in Microsoft Excel format.**

Table T17. Anisotropy, Site GT1. **This table is available in Microsoft Excel format.**

Table T18. Discrete physical properties, Site GT1. **This table is available in Microsoft Excel format.**

Table T19. Velocity, density, and porosity, Site GT1. **This table is available in Microsoft Excel format.**

Table T20. Thermal conductivity, Site GT1. **This table is available in Microsoft Excel format.**

Table T21. Core sections processed for VNIR and SWIR imaging, Site GT1. **This table is available in Microsoft Excel format.**

Supplemental Table ST1. Geochemistry results, Site GT1. **This table is available in Microsoft Excel format.**

Supplemental Table ST2. MSCL-W results, Site GT1. **This table is available in Microsoft Excel format.**

Supplemental Table ST3. MSCL-C results, Site GT1. **This table is available in Microsoft Excel format.**